ASSESSMENT OF INSPECTION CRITERIA AND TECHNIQUES FOR RECERTIFICATION OF NATURAL GAS VEHICLE (NGV) STORAGE CYLINDERS

By

S. G. Ribarits

B. A. Sc. (Mechanical Engineering), The University of British Columbia, 1983

A THESIS SUBMITTED IN PARTIAL FULFILLMENT OF

THE REQUIREMENTS FOR THE DEGREE OF

MASTERS OF APPLIED SCIENCE

in

THE FACULTY OF GRADUATE STUDIES

(DEPARTMENT OF MECHANICAL ENGINEERING)

We accept this thesis as conforming

to the required standard

THE UNIVERSITY OF BRITISH COLUMBIA

April 1992

In presenting this thesis in partial fulfilment of the requirements for an advanced degree at the University of British Columbia, I agree that the Library shall make it freely available for reference and study. I further agree that permission for extensive copying of this thesis for scholarly purposes may be granted by the head of my department or by his or her representatives. It is understood that copying or publication of this thesis for financial gain shall not be allowed without my written permission.

(Signature)

Department of _MECH. ENG_

The University of British Columbia
Vancouver, Canada

Date _APRIL 1992_

Abstract

In-service natural gas vehicle (NGV) storage cylinders are subject to various forms of damage which can degrade structural integrity. In recognition of this, the Canadian Transport Commission (CTC) requires that cylinders be recertified for service every five years.

Current standards for NGV cylinder recertification are based on cylinder behaviour during a hydrostatic test (pressurization to 1.67 × service pressure) and specify that a cylinder should be removed from service if either the measured plastic expansion exceeds 10 % of the total cylinder expansion or the cylinder ruptures. These criteria have been established, for the most part, to ensure a minimum cylinder wall thickness during service.

A serious deficiency of the current assessment criteria is that they do not specifically address the possibility of sub-critical crack growth that may occur between inspections due to the combined effects of aggressive environmental conditions and cyclic loading. Evidence of sub-critical crack growth in sectioned in-service NGV cylinders however, has raised concerns over the effectiveness of the current recertification criteria and points to the need to determine whether these criteria are adequate to ensure against in-service failure.

The objective of this research is to evaluate the current standards for NGV cylinder recertification.

In this investigation, various fracture mechanics based methodologies are investigated in view of their applicability to predicting cylinder rupture. Elastic-plastic finite element models of uncracked and cracked NGV cylinders are utilized to predict cylinder behaviour (volumetric expansion/crack opening displacement) during a hydrostatic test. These

analyses, in conjunction with small scale critical crack tip opening displacement (CTOD) test results and full scale burst test results indicate that a critical CTOD approach, modified by a plastic collapse analysis for small defects can be used to accurately predict cylinder rupture.

Analysis of full scale numerical and experimental results indicates that there exists a range of defect sizes which, if present in a cylinder, would not violate the current hydrostatic test acceptance criteria (i.e., volumetric expansion/rupture). This finding, in conjunction with available fatigue crack growth estimates indicates that it is possible for cylinders containing this range of defect sizes to fail in service during the subsequent five year inspection interval. This result indicates that current hydrostatic test criteria are non-conservative.

In view of the inability of current retest procedures to reject cylinders containing defects which may lead to in-service failure, the feasibility of utilizing acoustic emission (AE) techniques for NGV cylinder inspection is also investigated. Full scale cylinder AE tests indicate that it is possible for cylinders with similar defect sizes to exhibit markedly different AE characteristics (i.e, hit rate, amplitude distribution, etc.) due to other AE sources such as corrosion. However, the potential for using AE techniques for inspection of cylinders is discussed.

Table of Contents

List of Tables

List of Figures

xv

xvii

Nomenclature

a	crack depth
$2c$	crack length
d	inner diameter
z	distance to knife edges
D	outer diameter
COD	crack mouth opening displacement
CTOD	crack tip opening displacement
E	modulus of elasticity
J	J-integral
K	stress intensity factor
l	Dugdale plastic zone length
M	stress magnification factor
p	pressure
P	load
r	radial distance from the crack tip
r_p	Irwin plastic zone radius
R	mean radius
S	span
t	thickness
$\{u\}$	displacement vector
V	volume, clip gage displacement
W	width

Y form factor

Greek symbols

ε strain

λ shell parameter

ν Poisson's ratio

Φ non-dimensional CTOD

σ stress

θ angle from plane of crack

$\{\theta\}$ rotation vector

Subscripts and superscripts

el elastic

pl plastic

F   flow

θ circumferential

I   mode I

Ic   mode I critical

l   longitudinal

L   limit

LY   ligament yield

NSY   net section yield

U   ultimate tensile

S   surface flaw

T   through-wall defect

Y   yield

Miscellaneous

AE	Acoustic Emission
CCP	Center Cracked Plate
CGA	Compressed Gas Association
CT	Compact Tension
CTC	Canadian Transport Comission
SENB	Single Edge Notch Bend

Acknowledgement

Above all, the author would like to express his sincere gratitude to Dr. D. P. Romilly for his many invaluable suggestions, academic guidance and continued support throughout this project. Without his on-going efforts, completion of this thesis would not have been possible.

The author would like to thank Mr. D. Chow, Ms. C. Taggart, and Mr. R. Baerg for assistance while these individuals contributed to the on-going investigation of AE based recertification techniques. The author would also like to thank Dr. A. Akhtar, P. Eng. and Dr. G. Bhuyan, P. Eng. of Powertech Labs, Inc. for many informative discussions related to structural integrity of NGV cylinders.

Further, the author would like to express his sincere appreciation to the following research engineers/technicians for continued assistance and invaluable advice throughout the course of this investigation.

Mr. G. Rohling, P. Eng.	Research Engineer (Computing support)
Mr. A. Steeves, P. Eng.	Research Engineer (Computing support)
Mr. D. Bysouth	Technician (Instrumentation)
Mr. A. Schreinders	Machine Shop supervisor
Mr. A. Abel	Technician (Machine shop)
Mr. T. Besec	Technician (Machine shop)

The author would also to express his gratitude to the Canadian Gas Association and B. C. Science Council for funding this research.

Chapter 1

INTRODUCTION

1.1 Background

In the last decade there has been a significant increase in the use of natural gas as an alternative fuel. This trend, which can be expected to increase has resulted in a significant research effort to assess and improve the technology of natural gas fuel systems. One important aspect of this technology is the on-board storage of the product.

While the current trend is towards use of aluminum liner/composite wound cylinders, a great many existing and new natural gas fuel systems employ seamless steel cylinders for on-board storage of natural gas. Due to the susceptability of steels to corrosion, blistering and stress corrosion cracking in a natural gas environment, there exists a significant threat to the structural integity of these cylinders.

While there are no reported incidents involving NGV cylinders, there are reported failures of other classes of cylinders which were in natural gas service. Perhaps the most prominent of these failures was that of a seamless Cr-Mo steel tube trailer in 1977, which failed only one week after beginning service [28]. The cause of failure was found due to stress corrosion cracking which had resulted from a combination of a particularly harsh natural gas environment, material susceptibility and marginal wall thickness.

While a recent report has concluded that NGV cylinder material is relatively resistant to sulphide stress cracking (at 24.82 MPa (3600 psi) and current contractural limits of natural gas contaminants) [11], there is evidence to suggest that defects can develop in

NGV cylinders during service. Microcracks have been discovered in certain Italian-made cylinders and further, a more recent study indicated that crack-like defects can even be introduced into cylinders during manufacture [85].

To ensure against in-service failures, the Canadian Transport Commission requires that steel NGV cylinders be inspected and recertified every five years. The Compressed Gas Association (CGA) has set out standards for inspection and recertification of DOT-3HT seamless steel cylinders; these standards have been adopted by the Canadian Transport Commission (CTC) and are currently used to recertify NGV cylinders.

A major component of the CGA/CTC standards is a criterion which limits volumetric expansion of a cylinder during a hydrostatic test, a test which involves pressurizing a cylinder to 34.48 MPa (5000 psi) (1.67× service pressure)[1]. The reason for use of the volumetric expansion criterion is that it provides some measure of cylinder wall thickness and hence, nominal cylinder wall stress. The volumetric expansion criterion reflects an assumption in the CGA/CTC standards that the predominant mode of cylinder degredation is a uniform reduction in cylinder wall thickness due to internal corrosion. A major drawback of this assumption is that it does not specifically address the significance of very localized reductions in wall thickness.

Localized reductions in cylinder wall thickness, such as corrosion pits and stress corrosion cracks produce stress concentrations which can lead to failure at loads much less than would be calculated on the basis of the nominal stress acting over the remaining wall. In recognition of this, current standards for NGV cylinder recertification specify that the region around a localized reduction in wall thickness be ground to a depth equal to the reduction. While this procedure, known as 'reconditioning', may have merit in terms of eliminating stress concentrations, it relies on visual inspection to detect potential defects. A further drawback is that defects on the interior surface of the cylinder

---

[1]Volumetric expansion criterion and the hydrostatic test are discussed more fully in Sec. (2.4).

(where gas impurities accelerate corrosion and cracking) cannot be reconditioned.

As a means of resolving any uncertainty associated with defects that may evade visual inspection or which cannot be reconditioned, current standards rely on the hydrostatic test. In addition to providing the means to measure volumetric expansion therefore, the hydrostatic test is intended as a proof test. It is assumed that any defect that does not lead to failure (rupture) of a cylinder during a hydrostatic test can be tolerated for the next five years (following recertification) that a cylinder remains in service.

1.2 Statement of Problem

While a proof test can be utilized to ensure the integrity of a wide range of structures containing defects, one can reasonably question the use of this test to recertify NGV cylinders. A proof test, for the most part, is effective only when it is possible to ensure that defect size will remain less than critical during a given inspection interval. Because NGV cylinders are subject to an aggressive environment and alternating load (see Sec.s (2.2) and (2.3)), there exists the potential for accelerated sub-critical stress corrosion and fatigue crack growth. Evidence of this potential (i.e., crack-like defects) has been found in sectioned, previously in-service cylinders.

On the basis of these observations, and because any pre-existing defect is a potential site for the initiation of sub-critical crack growth, it becomes reasonable to question whether current standards are adequate to guard against in-service failure. The current view is that these standards (the hydrostatic test/volumetric expansion criterion) are not sufficient to guard against in-service failure.

In order to assess whether the currents standards for NGV cylinder recertification are adequate, a significant research effort has evolved to assess the significance of localized defects that can arise during NGV service. This effort has for the most part focused on

the significance of defects from the viewpoint of sub-critical crack growth [12, 13, 15]. A significant result of this research effort has been the recommendation of an alternate recertification protocol for NGV cylinders. This recertification protocol would remove cylinders from service based on the dimensions of defects detected during a scheduled 5 year inspection.

While the recommendation of an alternate recertification protocol for NGV cylinders is promising, it is important to note that there is only limited support for its implementation. This is due to the fact that to date, there have been no quantitative studies performed which quantify the conservatism of current hydrostatic test criteria when applied to cylinders containing very localized defects. Clearly such a study is required, as the expense of implementing any new recertification protocol cannot be fully justified until existing standards (i.e., current hydrostatic test criteria) have been thoroughly examined.

1.3 Objectives

In view of the need to examine and re-evaluate the current standards for NGV cylinder recertification, and develop standards which will ensure on-going cylinder integrity, the following research objectives were established.

1. To develop and verify a fracture mechanics based failure criterion suitable for assessing the structural integrity of a steel NGV cylinder containing a defect.

2. To evaluate the applicability, and degree of conservatism (if any) of the current hydrostatic test recertification criteria through comparison with the developed fracture mechanics based approach.

3. To investigate the feasibility of an acoustic emission based recertification protocol.

1.4 Scope of Research

Based on these objectives, the scope of this project encompassed the following:

Review of fracture mechanics methods applicable to NGV cylinders

The various fracture mechanics methods which might be utilized to assess NGV cylinder integrity were reviewed. Based on this review, which covered methods applicable to the full range of crack tip behaviour, a CTOD (crack tip opening displacement) approach was adopted for further investigation.

Small scale testing of steel cylinder material

A series of small scale tests were performed to determine critical CTOD of axial defects in NGV cylinders. These tests were performed in general accordance with a recognized standard for critical CTOD testing (BS 5762).

Development and verification of a computer-based model to predict volumetric expansion

A computer based finite element model of a NGV cylinder was constructed and additional software developed to predict volumetric expansion of cracked/uncracked NGV cylinders. Volumetric expansion results from this model were compared to current hydrostatic test volumetric expansion criteria to identify defect dimensions which would be considered acceptable under current standards for NGV cylinder recertification.

Development of a computer-based model to predict failure utilizing CTOD concepts

The finite element model was further developed and utilized to evaluate CTOD for various crack geometries and locations. CTOD estimates from the model were compared with critical CTOD values obtained from the small scale testing to determine the failure pressure of cylinders containing defined defect dimensions, and to establish critical defect dimensions for failure at a given cylinder pressure.

Acoustic emission testing of cracked/uncracked NGV cylinders

A series of acoustic emission tests were performed on cylinders containing representative size, artificially introduced external defects. Additional acoustic emission control tests were performed on cylinders containing no known defects. Information over a range of pressures (from operating to recertification pressure) was obtained. Data from the tests (hits, hits past previous pressure, amplitude distribution, etc.) was analysed in a variety of ways in an attempt to correlate defect severity with acoustic emission activity. To gain as much information as possible from available cylinders, an initial series of tests was followed by further fatigue cracking of cylinders and retesting.

Burst testing of cracked NGV cylinders

Cracked cylinders were pressurized to failure to obtain data to verify numerical and analytical failure predictions and to gain information on acoustic emission activity up to failure.

Correlation of analytical/numerical failure predictions with experimental results

Numerical and analytical predictions of failure pressure were compared with experimental results to determine an acceptable failure criterion for rupture type failure of NGV cylinders.

Assessment of current standards for recertification of NGV cylinders

Numerical estimates of volumetric expansion and failure pressure of cracked cylinders, and available fatigue crack growth data, were used to evaluate the conservatism of current standards for recertification of NGV cylinders.

Chapter 2

TECHNICAL BACKGROUND

Knowledge of design and service conditions is a prerequisite to an understanding of the possibility of in-service failure. For this reason, NGV cylinder geometry and material properties, environmental conditions and loading are discussed in this chapter.

2.1 Cylinder Geometry and Material Properties

Steel cylinders currently used in NGV service are available in 40, 60, and 70 liter capacities. The nominal dimensions and weights of these designations are given in Tables (2.1).

Fabrication of NGV cylinders involves deep drawing of AISI 4130X steel billets to form the bodies, followed by heating and spinning to form the end caps. The top end caps (nozzle ends) are made hemispherical, to minimize stress and the bottom caps torospherical, to minimize overall cylinder length. Details of cylinder geometry of a typical Faber 60 liter cylinder are shown in Fig. (2.1).

Mechanical properties of 4130X steel, determined from a series of tests performed by PowerTech Labs, are given in Table (2.2). The chemical composition of this steel, obtained from the manufacturer, is given in Table (2.3).

2.2 Environment

Natural gas contains, in addition to the primary constituent methane (CH_4), a number of impurities including hydrogen sulphide (H_2S), carbon dioxide (CO_2), and water

(H_2O). Experience in the oil and gas industry has shown that these impurities create an environment that promotes surface corrosion, blistering and cracking of steels. These environmentally induced forms of damage are all, in one way or another, due to the dissociation of hydrogen sulphide in water.

The increased availability of atomic hydrogen (decrease in pH) that results when hydrogen sulphide dissociates in water creates an acidic environment. This environment promotes surface corrosion through the formation of iron sulphide. Surplus atomic hydrogen adsorbs to the metal surface and, possibly catalyzed by the sulphide ion, diffuses into the matrix. Upon entering the metal matrix, the atomic hydrogen tends to migrate towards microvoids, dislocations and inclusions, or regions of high triaxial stress such as the tips of sharp defects or cracks. At microvoids, atomic hydrogen recombines to form hydrogen gas. The partial pressure of the gas is often sufficient to produce blistering of the metal surface. Atomic hydrogen that has accumulated at regions of triaxial stress decreases the cohesive strength between interatomic bonds. This reduction in strength, or 'embrittlement', reduces apparent fracture resistance often leading to sustained, sub-critical crack growth. In addition to environmental variables the rate of crack growth depends upon the magnitude of applied tensile stress. This form of sub-critical cracking, resulting from the dissociation of hydrogen sulphide and occurring due to an applied stress, is commonly referred to as sulphide stress cracking.

The susceptability of steels to sulphide stress cracking depends on a number of factors such as material properties (composition, microstructure, strength and hardness), environmental conditions (concentration of impurities, pH, temperature, etc.) and nominally applied stress levels. In general, steels of higher strength and hardness are most susceptable. One approach to controlling sulphide stress cracking therefore, has been to limit the strength and hardness of steels used in natural gas service.

Although there appears to be a threshold strength (and applied stress level) below

which sulphide stress cracking will not occur, certain low strength steels can be susceptable if the concentration of hydrogen sulphide is sufficiently high. Another approach to controlling sulphide stress cracking therefore, has been to regulate pipeline gas quality. The current Canadian contractural limits (and typical values) for the concentrations of hydrogen sulphide, carbon dioxide, and water are given in Table (2.4).

2.3 Service Loading

The relatively low critical temperature for liquification of natural gas (-82.5 C at ambient temperatures) makes on-board storage of liquid natural gas impractical. Acceptable vehicle range requires on-board storage at the relatively high pressure and thus, rated maximum service pressure for NGV cylinders is 20.69 MPa (3000 psi).

Because NGV cylinders are drained through fuel consumption and refilled throughout service, they are subject to an alternating, or cyclic, loading. Estimates of the number of cycles that a typical cylinder will experence are difficult to make, given the variablity in vehicle operating conditions. An upper bound of 25 cycles per week however, has been estimated based on taxi cab service. This figure represents approximately 6500 refilling cycles during the five year recertification period. NGV cylinders are typically refilled at approximately 2.07 MPa (300 psi) resulting in a cyclic R ratio (ratio between maximum and minimum service pressures) equal to 0.1.

2.4 Current Standards for NGV Cylinder Recertification

2.4.1 Minimum Wall Thickness Requirement

Current standards for certification of NGV cylinders (Section 73.34(e) of CTC regulations for the transport of dangerous goods [26]) are based on a minimum allowable service wall thickness approach. The standards limit the reduction in wall thickness that can occur

during service, and specify that a cylinder should be removed from service when the wall thickness is reduced by

$$\frac{1}{2}(t - t_{min}) \tag{2.1}$$

where t is the 'as-received' wall thickness and t_{min} is the 'minimum allowable' wall thickness. The minimum allowable wall thickness is determined from a condition of general yield, i.e., it is the wall thickness at which the cylinder suffers complete plastic collapse at hydrostatic test pressure. Prediction of the pressure at which plastic collapse occurs is made using the Bach Formula [32, 34]:

$$P = S\frac{D^2 - d^2}{1.3D^2 + 0.4d^2} \tag{2.2}$$

where P is the test pressure (1.67× service pressure), S is the allowable wall stress, D is the outer diameter, and d is the inner diameter. This equation, derived using the St. Venant maximum principal strain yield condition and the Lamé solution for stresses in a long cylinder [67], can be used to obtain an expression for the minimum wall thickness t_{min},

$$t_{min} = \frac{D}{2}\left[1 - \left(\frac{S - 1.3P}{S + 0.4P}\right)^{\frac{1}{2}}\right] \tag{2.3}$$

The minimum service wall criterion for cylinder recertification assumes that during service the wall thickness is decreased uniformly, i.e., the cylinder wall is reduced by the same amount at all locations. This assumption is valid when the only mode of cylinder degradation is surface corrosion (the formation of iron sulphide). The aggressive NGV environment, however, can produce more local forms of damage such as corrosion pits, lines and crevices, and sulphide stress cracks. Stress concentrations associated with such discontinuities result in stresses greater than would be calculated on the basis of the nominal stress acting over the remaining ligament, or net section. The nominal stresses required for yielding of the net section are therefore usually much less that those required

for yielding of a 'smooth' wall of equivalent thickness. While there is some recognition of this in the current standards, no formulation is provided to assess the significance of localized defects; hydrostatic testing, as required by current regulations, is assumed to be sufficient to remove the uncertainty associated with such defects.

2.4.2 Hydrostatic Testing

Cylinder wall thickness can be determined using a variety of techniques. Direct measurement can be made using mechanical, electrical, ultrasonic, or radiographic methods. The time and expense involved in the use of these methods however, makes them impractical for cylinder recertification. A practical alternative to direct measurement of wall thickness is an indirect measurement based on volumetric expansion during a hydrostatic test [31]. This test determines wall thickness indirectly, through a measurement of cylinder compliance (the change in volume due to internal pressure). As noted previously, the hydrostatic test is also intended as a proof test, that is defects and cracks that do not become critical under test pressure are considered safe until the next inspection.

Hydrostatic testing involves measurements of volumetric expansion while pressurizing a cylinder to 1.67 times the service pressure. Volumetric expansion can be measured either by enclosing a cylinder in a water jacket and measuring the volume of water displaced (the water jacket method) or by directly measuring the volume of water forced into a cylinder (the direct method). The water jacket method, because of its relative simplicity, is most widely used.

Regardless of the method employed, when the hydrostatic test is performed, two components of expansion are typically observed: an elastic component and a plastic component. Elastic expansion is due to cylinder compliance and is therefore directly proportional to pressure. Plastic, or permanent expansion is a residual expansion due to plastic deformation during the hydrostatic test.

2.4.3 Hydrostatic Test Failure Criteria

Both the elastic and plastic component of volumetric expansion can be used to estimate the reductions in wall thickness that have occurred during service. Volumetric expansions corresponding to minimum wall thickness can therefore be used as the failure criteria during cylinder recertification.

The elastic expansion, ΔV_{el}, of a cylinder can be related to pressure using an empirical relationship; this relationship, known as the Clavarino equation is given by

$$\Delta V_{el} = KPV \frac{D^2}{D^2 - d^2} \tag{2.4}$$

where K is a constant, P is the test pressure (1.67 X service pressure), V is the cylinder volume, D is the outer diameter, and d is the inner diameter. The constant K, the 'K-factor', represents the constraint imposed by the cylinder end caps and is determined experimentally from 'as-manufactured' cylinders. The Bach Formula, given by equation (2.2), can be used in conjunction with the Clavarino equation to derive a relationship giving elastic expansion at minimum allowable wall thickness. The result is the Bach-Clavarino formula given by

$$\Delta V_{el} = KV \frac{S + 0.4P}{1.7} \tag{2.5}$$

This equation provides the failure criterion based on elastic expansion. According to CGA standards [32], cylinders with elastic expansion in excess of ΔV_{el} no longer meet the minimum wall thickness requirement, and should be condemned.

Plastic expansion cannot be written directly in terms of variables such as allowable wall stress, test pressure, and cylinder geometry. Therefore, rejection plastic expansion cannot be determined absolutely. Experience with a large number of cylinders however, has shown that when permanent expansion exceeds 10 % of the measured total expansion,

i.e., when

$$\Delta V_{pl} > 0.10 \Delta V_{total}$$

where $\Delta V_{total} = \Delta V_{el} + \Delta V_{pl}$, wall thickness has been reduced to the minimum allowable.

In theory, both elastic and plastic expansion failure criteria could be applied to NGV cylinder recertification. However, current Canadian regulations based on standards prepared by the Compressed Gas Association (CGA) specify that only the plastic component of expansion be used as a criterion in NGV cylinder recertification. Under section 73.34(e) of the CTC regulations, a cylinder is considered unfit for further service when permanent expansion exceeds 10 % of total (elastic plus permanent) expansion.

Chapter 3

FRACTURE MECHANICS METHODS APPLICABLE TO NGV CYLINDERS

Over the years, a variety of fracture mechanics techniques have been developed which can be used to assess structural integrity of NGV cylinders. In this chapter, these techniques are reviewed as they apply to a range of material behaviours (i.e., linear-elastic, elastic-plastic, etc.). Also discussed are some design practices which have been established which may have potential as standards for NGV cylinder recertification.

3.1 General Concepts

Fracture mechanics assessments are based on the comparison of an applied parameter which quantifies the severity of a defect to an associated material property which quantifies resistance to crack extension. Failure is predicted when the applied fracture mechanics parameter exceeds some critical material value. The applied fracture mechanics parameter is a function of defect/structure geometry and applied load; the critical value of this parameter is a material property (which can often be determined in a small scale test of a representative section). To date, a variety of techniques have evolved for evaluating both applied and critical fracture mechanics parameters. Application of these techniques, in conjunction with the use of modern non-destructive testing methods to estimate defect size, provide the means to assess the severity of defects in a wide range of structures and materials and make 'fitness for purpose' assessments.

Before examining these techniques it should be noted that, in general, fracture mechanics methods fall into three categories as illustrated diagrammatically in Fig. (3.1). These categories, linear-elastic fracture mechanics (LEFM), elastic-plastic fracture mechanics (EPFM) and plastic collapse methods apply to low, moderate and high toughness materials respectively. Materials of low toughness require relatively low energy to initiate failure. These materials typically fail in a 'brittle' manner due to cleavage along crystallographic planes. Materials of increased toughness require greater energy to initiate failure. This energy is associated with plastic flow and consequently, moderate toughness materials typically fail in a 'ductile' manner due to formation, growth and coalescence of microvoids at the crack tip. Materials of very high toughness require the greatest energy to initiate failure. Failure of these materials does not occur due to crack extension, but rather, to rupture due to complete plastic collapse.

3.2 Linear-Elastic Fracture Mechanics

Linear-elastic fracture mechanics is based on the elasticity solution for stresses near a crack tip. This solution, due to Westergaard (1939) has the general form

$$\sigma_{ij} = \frac{K_I}{\sqrt{2\pi r}} f_{ij}(\theta) \tag{3.1}$$

where K_I is a stress intensity factor[1]. For an arbitrarily cracked body, the stress intensity factor is a function of structure/defect geometry and applied loading. In the original analysis, it was shown, using dimensional analysis, that $K_I = \sigma \sqrt{c}\beta$, where c is the crack length and β is a factor which depends only on geometry. For an infinite plate with a through thickness defect subject to remote tension, $\beta = \sqrt{\pi}$.

Since the time that the concept of a stress intensity factor was introduced, it has been customary in LEFM to utilize the same basic solution (i.e., that for an infinite plate)

---

[1]The subscript I is used here to distinguish mode I (opening) from modes II (sliding) and III (tearing).

modified by a 'form' factor, Y, to account for specific structure/defect geometry and loading. Hence, most solutions for stress intensity factor are given as

$$K_{\mathrm{I}} = \sigma\sqrt{\pi c}\, Y\left(\frac{c}{W}\right) \tag{3.2}$$

where W is a generalized size parameter.

Since all the terms in Equ. (3.1) except the stress intensity factor are independent of the specific geometry under consideration, the asymptotic behaviour in the near crack tip region (i.e., strength of the singularity) for different cracked bodies differs in proportion to the ratio of the stress intensity factors. This implies that the stress intensity factor is a similitude parameter which can be used to relate the severity of defects in different geometries. Hence, if failure of one cracked body occurs at some critical value of K_{I} (i.e., at K_{Ic}), failure of another cracked body (of the same material) will occur when

$$K_{\mathrm{I}} > K_{\mathrm{Ic}} \tag{3.3}$$

where K_{Ic} is a material property called fracture toughness. It should be noted that, for Equ. (3.3) to apply, there must be similitude between the state of stress (i.e., plane stress or plane strain) at the crack tip. This makes it necessary, in specifying fracture toughness, to distinguish between material plane strain and plane stress fracture toughness[2]. In most practical applications of LEFM, it is desirable to employ plane strain fracture toughness since this will yield the most conservative estimate of failure stress.

From the preceeding discussion, it can be seen that to apply LEFM it is necessary to have knowledge of both the material fracture toughness and applied stress intensity factor for the particular structure/defect geometry and loading of interest. Most often, material fracture toughness is determined in a standardized test (e.g., ASTM E399 [3] or BS 5447 [22]) which will require that certain validity requirements are to be met

---

[2]It is usual to denote plane strain fracture toughness with a roman I, i.e., K_{Ic}, and plane stress fracture toughness with an arabic 1, i.e., K_{1c}.

to ensure that measured fracture toughness is in fact plane strain fracture toughness. Stress intensity factors for most geometries and loadings of interest can be found in the literature. Because of the widespread use of pressure vessels, there exists a number of solutions for stress intensity factors for through-wall and surface defects in cylinders which may be applicable to NGV cylinders. These solutions are discussed in the next section.

3.2.1 Stress Intensity Factors for Through-Wall and Surface Defects in Cylinders

As noted, it is customary in fracture mechanics to utilize the same basic form of the stress intensity factor (i.e., the flat plate result given by Equ. (3.2)) and relate this to a specific geometry and loading through a geometry factor. Hence, most solutions for stress intensity factors in cylinders are given as the ratio of the stress intensity of a cylinder, K_{cyl}, to that of a wide plate, K_{plate},

$$M_{T,S} = \frac{K_{cyl}}{K_{plate}}$$

where the subscripts T and S denote a through-wall or surface defect respectively (see Fig. (3.2)). In solutions of this form, the remote stress σ in Equ. (3.2) is replaced by circumferential stress, pR/t. Because induced bending tends to increase the stress intensity in cylinders, the ratio $M_{T,S}$ is always greater than one and is commonly referred to as a stress magnification factor.

Analytical solutions for stress magnification factors for axial through-wall defects have been derived by several investigators [44, 47]. These factors are typically given as a linear combination of a membrane component and a bending component. The membrane and bending components, in turn, are given in terms of a shell parameter λ,

$$\lambda = \frac{c}{\sqrt{Rt}}$$

Erdogan and Kibler [44] give

$$M_T = G_m + \frac{2z}{t}G_b \tag{3.4}$$

where G_m and G_b are the membrane and bending components respectively (see Fig. (3.3)), z is the distance from the cylinder midplane and t is the cylinder wall thickness. Folias [47] gives

$$M_T = \left[I^2 + \frac{(33 + 6\nu - 7\nu^2)(1 + \nu)}{3(9 - 7\nu)} J^2 \right]^{\frac{1}{2}} \tag{3.5}$$

where again, I and J are the membrane and bending components respectively. Folias gives the components in graphic form for a range of λ. For small values of λ however, Equ. (3.5) can be written in the following approximate form.

$$M_T = \left[1 + 1.61 \left(\frac{c^2}{Rt} \right) \right]^{\frac{1}{2}}$$

While stress magnification factors for through-wall defects in cylinders are given in terms of the stress intensity factor for a through-wall defect in a wide plate, stress magnification factors for surface defects in cylinders are typically given in terms of the stress intensity factor for an elliptical defect in a wide plate; this solution, from Irwin [54] is,

$$K_I = \frac{\sigma\sqrt{\pi a}}{E(k)} \left(\sin^2 \varphi + \frac{a^2}{c^2} \cos^2 \varphi \right) \tag{3.6}$$

where $E(k)$ is the complete elliptical integral of the second kind, most often given approximately by

$$E(k) \approx \frac{\pi}{8} \left(3 + \frac{a^2}{c^2} \right)$$

and a, c, and φ are defined as shown in Fig. (3.4).

The simplicity of Equ. (3.6) sometimes makes it desirable to apply this equation directly to cylinders. although strictly speaking it is valid only for plates. This is usually acceptable provided λ is small. Some sources have also suggested simple modifications to Equ. (3.6) to increase its applicability to cylinders. These modifications include replacing

the term pR/t by $p(R/t + 1)$ for internal defects to account for pressure on the crack faces [25] and multiplying by M_T for external defects [48]) to account for outward bulging.

A more accurate approach however, would be to multiply Equ. (3.6) by a stress magnification factor derived specifically for surface defects in cylinders. Such stress magnifiation factors have been developed by Kobayashi (and co-workers) [60, 61] and have been presented in the form

$$M_S(\varphi) = M_c(\varphi)M_{KS}(\varphi) \tag{3.7}$$

where M_c is a factor which accounts for various effects including the non-linear stress distribution over the defect, induced bending, and internal pressure on the faces of internal defects. The factor M_{KS} is a front free surface correction that accounts for the proximity of the free surface ahead of the crack.

In addition to analytical solutions for stress intensity factors for surface flaws, a number of numerical solutions utilizing spring-line [40] and finite element methods [17, 75] have been developed. Perhaps, the most popular of these numerical solutions is that of Newman and Raju [75], who give present results for internal and external defects for a range of a/c, a/t, t/R and φ ($0.2 < a/c < 1.0$, $0.2 < a/t < 0.8$, $0.1 < t/R < 0.25$ and $0 < \varphi < \pi/2$).

While LEFM solutions are relatively well developed and understood, they are of limited applicability to NGV cylinders due to the relatively high toughness of NGV cylinder material. Use of LEFM relationships will, in general, provide over-conservative estimates of burst pressures due to lack of consideration to the energy associated with plastic deformation at the crack tip. LEFM relationships do however provide a means of predicting fatigue crack growth and leak before break (LBB) behaviour.

3.3 Plasticity Corrected LEFM

Plasticity corrected LEFM evolved in an attempt to extend the applicability of LEFM solutions to situations where small scale yielding occurs. The fundamental ideas behind the approach were first proposed by Irwin and have been shown to be consistent with the small scale approximations of models dealing with larger scale plasticity due to Dugdale and Barenblatt [25].

Plasticity corrected LEFM solutions are based on some approximation of the plastic zone at the crack tip. Irwin [53] reasoned that the plastic zone could be approximated by a circular disk of radius r_p (see Fig. (3.5)) and derived

$$r_p = \frac{K_I^2}{2\pi(\lambda_1\sigma_Y)^2} \tag{3.8}$$

where the factor λ_1 was introduced to account for the constraint at the crack tip; Irwin suggested that

$$\lambda_1 = \begin{cases} 1 & \text{Plane stress} \\ \sqrt{2\sqrt{2}} & \text{Plane strain} \end{cases} \tag{3.9}$$

Dugdale [42] assumed that the plastic zone ahead of a crack could be approximated by a yielded strip of length l (see Fig. (3.6)) and derived

$$l = a\left[\sec\left(\frac{\pi}{2}\frac{\sigma}{\sigma_Y}\right) - 1\right] \tag{3.10}$$

Expanding the sec term in the LHS of Equ. (3.10) and noting that for small scale yielding (i.e., $\sigma/\sigma_Y \ll 1$) all but the first term can be neglected, gives

$$l = \frac{\pi}{8}\frac{K_I^2}{\sigma_Y^2} \tag{3.11}$$

which is within 20 % of Irwin's plane stress plastic zone correction.

In formulating plasticity corrected LEFM, Irwin reasoned that due to crack tip plasticity the crack effectively behaves as if it is slightly longer, i.e.,

$$a_{\text{eff}} = a + r_p \tag{3.12}$$

Using this crack length provides a plasticity corrected expression for the stress intensity factor. For example, substituting Equ. (3.12) into Equ. (3.6) and rearranging, gives [36]

$$K_1 = \sigma\sqrt{\frac{\pi a}{Q}} \left(\sin^2 \varphi + \frac{a^2}{c^2} \cos^2 \varphi \right) \qquad (3.13)$$

where Q, denoted the flaw shape parameter, is

$$Q = \sqrt{E(k)^2 - 0.212\frac{\sigma}{\sigma_Y}}$$

Multiplying this result by a stress magnification factor (see Sec. 3.2.1) gives a plasticity corrected solution which can be used to analyse surface defects in cylinders.

Although they extend the applicability of LEFM relationships, plasticity corrected LEFM concepts are of limited value since there is no real justification for predicting elastic-plastic behaviour using relationships derived on the basis of linear elasticity. Another difficulty with the approach is that one must typically solve for the stress intensity factor iteratively. Despite these limitations, plasticity-corrected LEFM concepts have proved of value since they have provided insight into development of another fracture mechanics parameter more suited to predicting failure in the elastic-plastic regime, the crack tip opening displacement.

3.4 Elastic-Plastic Fracture Mechanics

3.4.1 The CTOD Approach

General Concepts

The crack tip opening displacement (CTOD) approach was first proposed by Wells [96] as a means of predicting failure in the elastic-plastic regime. The approach is based on the concept that it is crack tip strain and hence, crack tip displacement, which controls failure. As with all fracture mechanics approaches, the CTOD approach predicts failure when the controlling parameter (i.e., crack tip displacement) exceeds some critical value.

A simple argument to justify the CTOD approach can be made on the basis of the state of stress and strain at the crack tip. Ignoring the effects of material hardening, once a condition of general yield is reached, stress in the near crack tip region will increase very little with increasing load. Strain on the other hand, will continue to increase until ultimately, sufficient plastic strain has accumulated to initiate failure. If crack tip strain is assumed equivalent to crack tip displacement, it follows that in general, failure occurs when some critical value of crack tip displacement is exceeded.

A relationship for CTOD can be derived using the LEFM solution for crack opening displacement (COD) in a wide plate (see Fig. (3.7)),

$$\text{COD} = \frac{4\sigma}{E}\sqrt{a^2 - x^2} \tag{3.14}$$

and the Irwin plastic zone correction. Substituting Equ. (3.12) into Equ. (3.14) and defining CTOD as the COD at $x = a$ gives (assuming that $r_p \ll a$),

$$\text{CTOD} = \frac{4\sigma}{E}\sqrt{2ar_p}$$

which can be written (c.f. Equ. (3.2))

$$\text{CTOD} = \frac{4}{\pi}\frac{K^2}{E\sigma_Y} \tag{3.15}$$

A somewhat different relationship for CTOD is derived using the Dugdale plastic zone correction; this relationship is [21]

$$\text{CTOD} = \frac{8\sigma_Y a}{\pi E}\ln\sec\frac{\pi\sigma}{2\sigma_Y} \tag{3.16}$$

It should be noted that, in accordance with the assumed plastic zone corrections, Equ.s (3.15) and (3.16) each have limits of applicability in terms of the scale of yielding. While Equ. (3.15) is valid only for small scale yielding (i.e., $r_p \ll a$), Equ. (3.16) is apparently valid for more extensive yielding[3]. For small scale yielding however, it can be

---

[3]See Sec.s (3.6.2) and (3.6.3).

shown by expanding the ln sec term and neglecting all but the first term, that Equ. (3.16) reduces to

$$\text{CTOD} = \frac{\pi\sigma^2 a}{E\sigma_Y} = \frac{K^2}{E\sigma_Y}$$

Because this expression differs from Equ. (3.15) only by a constant factor $(4/\pi)$ which reflects the assumed plastic zone approximation, in general

$$\text{CTOD} = \frac{K_I^2}{E'\lambda_2\sigma_Y} \tag{3.17}$$

where

$$E' = \begin{cases} \dfrac{E}{1-\nu^2} & \text{Plane strain} \\ E & \text{Plane stress} \end{cases}$$

A survey of numerical and experimental studies which have attempted to quantify λ_2 [25] indicates that this factor is a function of the exact position where the CTOD is measured, constraint at the crack tip (i.e., plane stress or plane strain) and possibly, work hardening characteristics. Depending on these factors, $1 < \lambda_2 < 2.14$.

While the CTOD approach has proved of great value in understanding and predicting failure in the elastic-plastic regime, it should be noted that practical application of the approach is not without drawbacks. One drawback is that relatively few analytical models exist which predict CTOD when large scale yielding occurs, thus one cannot usually solve directly for a critical crack length. CTOD at failure however, does provide a measure of material toughness and therefore can used to compare fracture resistance of different materials. Another drawback of the CTOD approach is disagreement in the literature over how CTOD should be defined. This disagreement has arisen, in large part, due to discrepancies between crack tip profiles predicted by analytical models and those observed in experimental and numerical studies [37]. While attempts have been made to define CTOD empirically, the most consistent definition remains the crack opening displacement at the original crack tip, as indicated in Fig. (3.7).

Despite these drawbacks, the CTOD approach has gained considerable acceptance. With this acceptance has come continued refinement of analytical/numerical solutions to predict CTOD and the development of experimental techniques to determine critical CTOD. In addition, the CTOD approach has been incorporated into a design standard, BSI PD 6493 [24], which can be used to assess structural integrity of a wide range of structural components. These topics are discussed in the following sections.

Experimental Measurement of CTOD

Direct experimental measurement of CTOD requires the use of relatively sophisticated techniques (e.g., silicone infiltration, radiography, etc.). Such techniques are difficult to implement and for this reason, in practice, CTOD is measured indirectly. This is done using expressions which relate CTOD to COD, a quantity which can be measured with relative ease somewhere along the crack faces (typically at the crack mouth as shown in Fig. (3.8)).

Critical CTOD for a given material is most often evaluated utilizing a small scale test specimen. Of the various configurations which can be employed, the three point bend specimen is most common. For this geometry, the relationship between CTOD and COD is (see Fig. (3.9))

$$\text{CTOD} = \frac{r(W-a)}{r(W-a)+a}\text{COD} \tag{3.18}$$

where r is a factor (rotational factor) which accounts for rotation of the crack face once a plastic hinge has formed. Using infiltration techniques, Robinson and Tetelman found that $r = 0.0472 + 0.0939\text{CTOD} + 0.00931\text{CTOD}^2 + 0.00037\text{CTOD}^2 \text{ in}^{-1}$ [25].

Another (and to date the most accepted) expression relating CTOD to measured COD was proposed by Wells [96]. In this expression,

$$\text{CTOD} = \frac{K_I^2}{2\sigma_Y E'} + \frac{0.4(W-a)V_p}{0.4W + 0.6a + z} \tag{3.19}$$

CTOD is separated into elastic and plastic compontents (c.f. Equ.s (3.17) and (3.18)) and a constant rotational factor $r = 0.4$ is assumed. While the assumption of a constant rotational factor may be justified, Anderson et al. [6] have pointed out that the value $r = 0.4$ may not be appropriate for all materials. These investigators have suggested that a more accurate estimate of r can be obtained from

$$r = \frac{1}{W - a} \left[\frac{V_p W}{q_p} \left(1 - \frac{q_p}{16W} \right) - a + z \right]$$

where q_p is the plastic component of load line displacement.

In addition to relationships for the three-point bend configuration, relationships have been derived which relate CTOD to measured COD in other geometries (e.g., the center-cracked plate). A review of these relationships can be found in Ref. [79].

Finite Element Estimation of CTOD

Modelling the Crack Tip

Of the various numerical techniques which can be used to solve problems in fracture mechanics, the finite element method is perhaps the most popular. This popularity is due, in large part to the versatility of the method which has facilitated the development of specialized approaches to deal with the various regimes of crack tip behaviour. Early investigations were concerned mainly with the suitability of the finite element method for predicting LEFM parameters such as stress intensity factor and energy release rate. More recent investigations have been concerned with the suitability of the method for predicting elastic-plastic parameters such as J-integral and CTOD. A common challenge in the application of finite element method to both LEFM and EPFM has been modelling of the crack tip region.

As noted, LEFM solutions predict a $r^{-\frac{1}{2}}$ singularity in stress and strain at the crack tip. Early attempts to deal with this singularity employed models that focused a large

number of simple elements, e.g. constant strain triangles, at the crack tip. This approach, although justified by convergence theorems, has two main drawbacks. The first was cost; the second was that computational error increased with mesh density. These drawbacks ultimately led to the development of other, more efficient means of modelling problems in LEFM.

One approach to more efficient modelling of problems in LEFM is the non-uniform mesh refinement method. This method is based on techniques that equalize the discretization error in elements near a singularity. These techniques make element size a function of the order of the singularity and of the element shape function. The results of numerical experiments performed by Johnson [55] indicate that non-uniform mesh refinement is a very efficient means of modelling problems in LEFM.

Another more efficient approach is the use of specially constructed singularity or 'crack tip' elements. This approach followed from reasoning that fewer elements would be required overall if an inverse square root singularity could be incorporated into elements at the crack tip. This reasoning led to the development, by a number of different investigators (e.g., Blackburn [16]) of special elements which are constructed with shape functions that produce an inverse square root singularity at the crack tip. Although relatively successful, these elements sometimes lacked the rigid body modes and constant strain states that guarantee convergence. This drawback was overcome however, by the discovery (by Henshell and Shaw [52], and Barsoum [8]) that an inverse square root singularity could be produced in a standard eight-node isoparametric element by collapsing one face and moving the mid-side nodes on adjacent faces to the quarter-point position.

Given the relative ease with which an inverse square root singularity can be obtained, finite element modelling of problems in LEFM has become an accepted approach. More recent studies have focused on extending finite element methods to problems in elastic-plastic fracture mechanics. This has lead a number of investigators to focus attention

on development of crack tip elements which reproduce EPFM singularities. Formulation of these elements however, was more complicated due to the fact that in high toughness materials, the strain field near the crack tip is a function of material hardening characteristics. For materials that obey a power law hardening rule,

$$\frac{\tau}{\tau_Y} = \left(\frac{\gamma}{\tau_Y/G}\right)^n$$

(where $\tau = (s_{ij}s_{ij}/2)^{1/2}$, $\gamma = (2e_{ij}e_{ij})^{1/2}$ and s_{ij}, e_{ij} are, respectively, the deviatoric components of stress and strain), the elastic-plastic crack tip singularities are

$$\sigma_{ij} = \frac{C_1}{r^{\frac{n}{n+1}}}p_{ij}(\theta), \qquad \varepsilon_{ij} = \frac{C_2}{r^{\frac{1}{n+1}}}q_{ij}(\theta)$$

It should be noted that for $n = 1$, (linear-elastic behaviour) the singularities reduce to the inverse square root singularities predicted by LEFM.

Despite the difficulties involved, several investigators (e.g., Tracey [93]) have successfully developed a class of two- and three-dimensional crack tip elements which embody the above singularities. An important feature of these elements is that they possess non-unique degrees of freedom at the crack tip. This facilitates accurate modelling of crack tip blunting, which as has been noted, occurs due to plasticity at the crack tip.

A special case of power law material hardening is perfectly plastic behaviour. For this behaviour, $n = 0$, and the singularities given by Equ.s (3.4.1) become

$$\sigma_{ij} = \frac{C_1}{r^0}p_{ij}(\theta), \qquad \varepsilon_{ij} = \frac{C_2}{r^1}q_{ij}(\theta)$$

Levy et al. [65] have shown that these singularities can be reproduced in a standard four node (linear) isoparametric element by collapsing one face and allowing the nodes on this face to move independently. Latter, Barsoum [9] demonstrated that these same singularities could be reproduced in standard eight (two-dimensional) and 20 node (three-dimensional) isoparametric elements in a similar manner.

To verify the accuracy of modified isoparametric elements in predicting perfectly plastic behaviour, both Levey et al. and Barsoum compared their finite element results for small scale yielding to the Prandtl slip line field. In these comparisons, the angular variation of stress around the crack and the distribution of stress ahead of the crack were investigated. Agreement between the element models and the slip line solution was good, and would appear to justify the use of collapsed isoparametric finite element methods in EPFM.

While these results support the use of collapsed isoparametric elements in EPFM, it should be noted that there is evidence which suggests that in some cases, standard elements (such as the constant strain triangle) may be equally as accurate. In a study of near crack tip displacement fields, Amstuiz and Seeger [2] investigated the effects of element type, mesh refinement, load incrementization and to a limited extent, material hardening. Employing constant strain triangles (CSTs), these investigators constructed a finite element model of a through thickness cracked plate. An analysis was first performed assuming perfectly-plastic (n = 0) behaviour. In this analysis, the displacement field near the crack tip was compared to that predicted by the Dugdale strip yield model (Equ. (3.16)). Differences between the finite element and analytical results were found to depend strongly on the number of load steps, with better agreement occurring as the number of load steps was increased. While a great number (on the order of 50) of load steps were required, good agreement with the analytical solution was ultimately obtained. Using the same model, Amstuiz and Seeger also performed an analysis assumed hardening (n = 3.33) behaviour. In this analysis, the displacement field near the crack tip was compared to that predicted by HHR (Hutchinson, Rosengren and Rice) field solutions. Differences between the finite element results and these solutions were found to follow the same trend (with respect to load incrementization) as was observed for elastic-plastic behaviour. Final agreement between the finite element results and the analytical

solution was also found to be very good. In the same study, Amstuiz and Seeger went on to investigate the displacement field of a model constructed with isoparametric elements. In this model, collapsed isoparametric elements (HPEs) were employed at the crack tip. Assuming perfectly-plastic behaviour, and similarly comparing the displacement field of the finite element model with that predicted by the Dugdale solution, it was again found that differences between the finite element results and analytical solution decreased as the number of load steps was increased. It should be noted however that when the HPEs were employed, much fewer (10) load steps were required and that final agreement between the finite element results and the Dugdale solution was much better (than that obtained with CSTs). Assuming hardening behaviour, Amstuiz and Seeger went on, in the final stage of the investigation, to compare the displacement field of the HPE model with that of the HRR solutions. In this case, it was found that agreement between the finite element results and analytical solutions was poor.

The results of Amistuiz and Seeger indicate that, although efficiency is sacrificed, it is possible to accurately model the crack tip with a fixed node element such as the CST when behaviour is perfectly plastic. These results also indicate that, while it is possible to accurately model the crack tip with a fixed node element when hardening occurs, it is not possible to model the crack tip with a collapsed isoparametric element when hardening occurs. While this finding is somewhat expected, given that there is no theoretical basis for modelling the crack tip with collapsed isoparametric elements when hardening occurs, it should be noted that this is often what is done in practice.

In closing the discussion on finite element modelling of the crack tip, it should be noted that as yielding becomes more extensive, there may be less need to accurately model crack tip singularities. This follows from intuitive reasoning that the singularities will become lost in a large plastic zone and that, ultimately, plastic instability mechanisms will become more important. Some support for this follows from a study performed by

Worswick and Pick [98]. This study involved finite element analysis of a circumferentially cracked pipe subjected to a moment loading. Three crack sizes (relatively short/shallow, short/deep and long/shallow) were analysed. Because material hardening was assumed, singularity elements were not employed. In the analysis, load was increased until the plastic zone extended well beyond the cracked region of the pipe. Asymptotic load-COD behaviour was used to predict the failure moment. The failure moments predicted by the finite element model were compared to failure moments predicted by an analytical model [4]. Although poor for the long/shallow defect, agreement between the finite element and analytical model was found to be within several percent for the short/shallow and short/deep defects. Reviewing the results presented by Worswick and Pick indicates that relative to defect size, the plastic zone was larger for the small defects than for the large defect. This would appear to suggest that when the plastic zone is large compared to defect size, sophisticated modelling of the crack tip region may not be necessary.

Experimental Verification of Finite Element CTOD Estimates

Several investigators have also attempted to correlate finite element and experimental results. These correlations however, have been mainly limited to small scale fracture mechanics specimens and other relatively simple geometries (e.g., [81, 4, 19]. These studies have typically involved comparisons of measured and finite element crack opening profiles, or measured and finite element load-COD records. For example, Schmitt and Hollstien [81] performed both two- and three-dimensional finite element analysis of compact tension specimens and compared computed crack open profiles to measured results. Agreement between the finite element and measured results was, in general, good. It should be noted however, that experimental points were limited mainly to the

---

[4]Details of this analytical model are not given in Ref. [98]. The authors note however, that the analytical model is supported by a considerable body of experimental evidence. On this basis, the analytical model was considered an accurate benchmark in the comparison of results.

crack flanks, and that no detailed comparisons were made between profiles at the crack tip. Anderson [4] similarly compared finite element and measured crack profiles for a grooved bar. This comparison however, showed only qualitative agreement between the finite element and measured results. Bleakley and Luxmoore [19] performed a round robin comparison of elastic-plastic finite element solutions with experimental data. In this investigation, a number of contributors were asked to perform finite element analysis of compact tension (CT), single edge notch bend (SENB) and center cracked plate (CPP) geometries. Depending on the particular geometry, several sets of results i.e., load versus COD, load versus J, crack opening profile, etc. from each of the analyses were compared with existing experimental data. While some variability between the finite element solutions and the experimental data was observed, there was in general, good agreement between the finite element and experimental results. Unfortunately, no experimental results for the crack opening profile were available. Hence, while it was possible to compare the various finite element crack opening profiles, it was not possible to compare experimental and numerical crack opening profiles.

Unfortunately, perhaps due the cost of carrying out a program of full scale numerical and experimental analysis, there are relatively few studies along these lines. One study which did compare full scale numerical finite element failure predictions with experimental results was performed by Wellman et al. [95]. In this study, five cylinders containing axial surface defects were pressurized to failure. Four of the cylinders ($D = 378$ mm, $t = 12.4$ mm, $l = 122$ m and $\sigma_Y \approx 800$MPa) contained extended axial notches and one ($D = 686$ mm, $t = 152$ mm, $l = 1.27$ m and $\sigma_Y \approx 487$MPa) contained an elliptical fatigue crack. In conjunction with the burst tests, a number of small scale CTOD tests were performed on the cylinder material to establish critical (initiation) CTOD. These small scale tests were performed according to BS 5762. Following the experimental full

and small scale tests, a finite element analysis was performed. Two-dimensional analysis was performed for the cylinders containing the extended flaws and three-dimensional analysis was performed for the cylinder containing the elliptical flaw. The crack tip region was modelled using collapsed isoparametric (perfectly plastic singularity) elements discussed previously. To reduce the size of the analysis, the non-linear region near the crack tip was sub-structured. The finite elements models were incrementally loaded until the analysis failed to converge. After the analysis was performed, pressure versus CTOD curves were constructed for each of the cylinders. The pressures corresponding the critical CTOD (from the small scale tests) on these curves were compared to the actual burst pressures. Agreement between the predicted and actual failure pressures was found to be very good; three of the cylinders failed within 1 % of the predicted failure pressure and two within 7 % of the predicted failure pressure. While these results are promising (in terms of finite element CTOD failure predictions), it should be noted that during the burst tests Wellman et al. failed to measure COD. Further comparison of finite element and experimental results was therefore impossible.

Correlation Between Analytical and Finite Element Estimates of CTOD

There exists relatively few analytical solutions which predict CTOD when large scale yielding occurs. For this reason, comparisons between analytical and finite element results given here will be limited to the small scale yielding regime, that is, in the regime where Equ. (3.17) holds. A useful means of making comparisons between CTOD predicted by Equ. (3.17) and finite element results is to rewrite this equation

$$\lambda_2 = \frac{K_I^2}{E'\sigma_Y}$$

and compare λ_2 predicted by theory with that predicted by finite element analysis. In making such comparisons however, it should be noted that variability exists even among

the analytical estimates of λ_2. The Irwin and Dugdale solutions discussed in Sec. 3.4.1 give $4/\pi$ and 1 respectively; J-integral computations by Rice [78] give 1.47.

An initial comparison of analytical and finite element estimates of λ_2 can be made using the results of two-dimensional analysis. Examples of such analysis are the investigations (discussed previously) of Tracy [93], Levey et al. [65] and Barsoum [9]. In these investigations λ_2 was found to be 1.85, 2.14, and 1.72 respectively. These values, which vary considerably and are somewhat greater than the analytical estimates of λ_2, suggest that finite element analysis will yield a conservative estimate of CTOD.

Further comparison of analytical estimates and finite element estimates of λ_2 can be made using the results of full three-dimensional finite element analysis. These comparisons however, should be made with care since one must ascertain the state of stress (i.e., plane strain or plane stress) in the structure which was modelled. In cylinders, one can be reasonably certain that a state of plane strain exists along edge cracks, or at the deepest point of a surface crack. Ranta-Maunus and Talja [76] performed an elastic-plastic finite element analysis of an edge cracked cylinder. In this investigation, J-integral and CTOD were analysed over the full elastic-plastic range and it was found that $J = 1.06\sigma_Y\text{CTOD}$. Comparing this result to the LEFM relationship between J and K_I [25],

$$J = \frac{K^2}{E'} \tag{3.20}$$

gives $\lambda_2 = 1.06$. Aurich et al. [7] and deLorenzi [41] performed a similar analysis of surface (elliptically) cracked cylinders. The results of these investigations indicate that $J \approx 1.0\sigma_Y\text{CTOD}$ and that $\lambda_2 \approx 1.0$.

3.4.2 J-integral Methods

Another elastic-plastic fracture mechanics parameter which has been proposed is the J-integral. This parameter, although not utilized in this research, has received a great deal

of attention and therefore will be discussed here for completeness.

The J-integral approach is based on the concept that the energy available for crack extension controls failure. Formally, the J-integral is defined by the following path independent integral [25].

$$J = \int_{\Gamma} \left(W dy - T \frac{\partial u}{\partial x} ds \right) \tag{3.21}$$

where $W = \int_0^{\varepsilon} \sigma_{ij} d\varepsilon_{ij}$. This integral represents a balance between the strain energy within the contour Γ and that crossing the contour Γ. It can be shown that if the contour Γ is closed, $J = 0$; alternately, if the contour is not closed, i.e., if it is penetrated by a crack as shown in Fig. (3.10), $J > 0$.

This property, and that of path-independence noted previously, make it possible to utilize J to predict failure in the elastic-plastic regime. Rice [78] has shown that the energy difference between a closed contour and one penetrated by a crack is equivalent to the potential energy per unit of crack extension

$$J = -\frac{\partial V}{\partial a}$$

Since J is path independent, it can be evaluated along a contour outside the plastic zone at the crack tip where behaviour is elastic.

When material behaviour is linear-elastic, J is equivalent to the energy release rate G. On the basis that elastic-plastic behaviour can be approximated by non-linear elastic behaviour, it has been suggested that J can be used to predict failure in the elastic-plastic regime. This implies, in analogy with LEFM concepts discussed previously, that failure will occur when J exceeds some critical value, i.e., when

$$J_{applied} \geq J_{Ic} \tag{3.22}$$

where J_{Ic} is a material property.

Practical application of the J-integral approach requires a solution to Equ. (3.21) for a particular structural/defect geometry and loading. While solutions for relatively simple geometries (e.g., the SENB specimen) exist, the complexities of solving Equ. (3.21) often makes it necessary to employ some numerical scheme (e.g., finite element analysis, spring-line methods, etc.).

Application of the J-integral approach also requires some means of estimating J_{Ic}. To this end, multispecimen and single specimen techniques have been developed which can be utilized to establish J_{Ic} for a given material. A review of these techniques can be found in Ref. [79]

While a complete discussion cannot be given here, it should be noted that certain restrictions apply to the use of the J-integral approach. One restriction, which follows from the use of non-linear elasticity to approximate elastic-plastic behaviour is that no unloading should occur. The consequence of this restriction is that the J-integral approach is valid only for stationary cracks since, typically, some unloading will occur at the flanks of advancing cracks. Other restrictions on the use of J-integral also exist. These restrictions are to ensure similarity between different structural configurations so that Equ. (3.22) remains valid.

In closing this section, it should be noted that relationships exist between J-integral and the fracture mechanics parameters (K and CTOD) discussed previously. Due to the equivalence of J and the energy release rate, G, the relationship between J and stress intensity factor K is

$$J = \frac{K_I^2}{E'} \tag{3.23}$$

From Equ.s (3.23) and (3.17), the relationship between J and CTOD is

$$J = \lambda_3 \sigma_Y \text{CTOD} \tag{3.24}$$

where λ_3 is a constant, generally taken to be

$$\lambda_3 = \begin{cases} 1 & \text{Plane stress} \\ 1.6 & \text{Plane strain} \end{cases}$$

The restrictions with apply to Equ.s (3.23) and (3.24) should be noted. Equation (3.23) is valid only when behaviour is linear-elastic; Equ. (3.24) is valid throughout the elastic plastic regime.

3.5 Plastic Collapse Methods

3.5.1 Limit Load Analysis

Structural components containing cracks may be so resistant to fracture that failure does not occur due to crack extension, but rather due to complete plastic collapse. While this situation arises due to very high toughness, it can also occur if defect dimensions are small compared to section thickness, or alternately if defect dimensions are very large compared to section thickness.

To predict failure due to plastic collapse, a limit load solution must be employed. These solutions are, in general, derived from the upper and lower bound theorems of plasticity. These theorems state that failure will occur when a mechanism can be found in which either: 1, the rate of internal plastic work done becomes less than the rate of work done by external forces or 2, internal stresses cannot be redistributed such that they are less than yield.

Due to the complexities involved in accounting for material hardening behaviour, most limit load solutions have been derived assuming elastic-perfectly plastic behaviour where the yield stress is normally replaced by flow stress. Although flow stress can be

determined empirically (see Sec. 3.6.3), it is most often taken to be [27]

$$\sigma_F = \begin{cases} \frac{1}{2}(\sigma_Y + \sigma_U) & \text{Plane stress} \\ \frac{1.15}{2}(\sigma_Y + \sigma_U) & \text{Plane strain} \end{cases}$$

where the factor 1.15 in the plane strain definition reflects the apparent elevation of flow stress resulting from transverse (out of plane) constraint in this condition.

A number of plastic collapse solutions of practical importance have been developed. For the single edge notch bend (SENB) specimen [6]

$$P_L = L\sigma_F \frac{(W - a)^2 B}{S} \tag{3.25}$$

where the factor L is the notch constraint factor. This factor accounts for the geometrical constraint produced by plastic strains near the crack tip. McClintock [69] assumed a slip line field for the SENB and calculated $L = 1.543$. Romilly et al. [80], in experimental work, used $L = 1.543$ for calculations when SENB specimens contained sharp cracks, but a somewhat lower value, $L = 1.261$ when specimens contained blunt notches.

Due to the practical importance of cylindrical pressure vessels, there exists a number of plastic collapse solutions for this geometry. For extended axial cracks, Chell [27] gives

$$P_L = \sigma_F \frac{(t - a)}{(R_i + a)} \tag{3.26}$$

$$P_L = \sigma_F \frac{(t - a)}{R_o} \tag{3.27}$$

for internal and external flaws respectively. Chell suggests however, that these relationships may be over-conservative for elliptical defects and recommends the term $(t - a)$ be replaced by

$$\frac{(t - a)}{1 - \frac{a}{t\left(1 + 2\frac{c^2}{t^2}\right)^{-\frac{1}{2}}}}$$

It should be noted that the effects of outward bulging have not been included in equation (3.27). A relationship which accounts for these effects is [92]

$$P_L = \sigma_F \frac{t}{R} \left(\frac{a/t - 1}{a/t - 1/m} \right) \tag{3.28}$$

where

$$m = 1 + \left[0.263 \frac{(2c)^2}{Rt} \right]^{\frac{1}{2}}$$

As can be seen, for small values of $(2c)^2/Rt$ this relationship predicts failure when the hoops stress reaches the material flow stress.

3.5.2 Analytical and Numerical Estimates of CTOD for Surface Flaws in the Large Scale Yielding Regime[5]

A number of investigators have investigated the problem of developing solutions for the CTOD of surface flaws when large scale yielding occurs. While the approaches taken are somewhat varied, a common theme in the solutions is the equivalence of the uncracked ligament of a surface flaw to certain closure forces (and possibly, moments). The advantage of this approach is that the surface flaw becomes equivalent to a through-wall defect with the same closure force acting over some region of the crack faces. This equivalence makes it possible to develop solutions for surface flaws by modifying solutions for through-wall defects which are more developed.

Critical CTOD Approach

In the critical CTOD approach developed by Irwin [70], it is assumed that the uncracked ligament of the surface flaw has fully yielded (see Fig. (3.11)a). This is assumed to occur

---

[5]The approaches discussed in Sections (3.5.2), (3.5.3) and (3.5.4) although not utilized in this research are discussed for completeness.

when the nominal stress acting over the ligament reaches the material flow stress; the corresponding closure force is then

$$F_c = 2c(t - a)\sigma_F$$

The surface flaw thus becomes equivalent to a through-wall defect with closure stress

$$\sigma_c = \frac{F_c}{2ct}$$
$$= \left(1 - \frac{a}{t}\right)\sigma_F$$

acting over the crack faces. Assuming that this closure stress will effectively reduce the CTOD of the through-wall defect by an amount

$$\text{CTOD} = \frac{4\sigma c}{E}$$

The CTOD for the surface flaw becomes

$$\text{CTOD} = \frac{4(\sigma - \sigma_c)c}{E}$$

Irwin went on to refine the model by accounting for plasticity at the ends of the defect. Replacing the actual crack length c by an effective crack length $c_{\text{eff}} = c + r_p$ (c.f. Equ.s (3.8) and (3.12)), and substituting for σ_c gives

$$\text{CTOD} = \frac{4(c + r_p)}{E}\left[\sigma - \left(1 - \frac{a}{t}\right)\sigma_F\right]$$

which is Irwin's final result for CTOD of a surface defect in the large scale yielding regime.

Modified Critical CTOD Method

Recognizing that the critical CTOD method neglects elastic contributions to the CTOD, Cheng et al. proposed the modified CTOD method [77] which separates the CTOD

into elastic and plastic components. The elastic component is evaluated from LEFM solutions and the plastic component is based on Irwin's CTOD solution. Based on the premise that the LEFM solution remains valid to ligament yield, and that the critical CTOD solution is valid between ligament yield and net section yield, the modified critical CTOD approach gives

$$\text{CTOD} = \frac{K_I^2}{E\sigma_F} \tag{3.29}$$

for

$$\sigma \leq \left(1 - \frac{a}{t}\right)\sigma_F$$

and,

$$\text{CTOD} = \text{CTOD}_{\text{LY}} + \frac{4(c + r_p)}{E}\left[\sigma - \left(1 - \frac{a}{t}\right)\sigma_F\right] \tag{3.30}$$

for

$$\left(1 - \frac{a}{t}\right)\sigma_F < \sigma \leq \left(1 - \frac{ac}{tW}\right)\sigma_F$$

where CTOD_{LY} is the elastic component of CTOD (i.e., Equ. (3.29)) evaluated at σ_{LY}.

3.5.3 Erdogan and Ratwani Formulation

A limitation of the critical and modified critical CTOD approaches is that they do not account for out-of-plane bending due to the eccentrically loaded crack. While this limitation may not be severe when the models are applied to defects in flat plates, it may be significant when the models are applied to defects in cylinders, where curvature further intensifies out-of-plane bending effects.

A model which more accurately predicts the CTOD of surface defects in cylinders has been developed by Erdogan and Ratwani [45, 46]. This model formulation is analagous to the critical CTOD approach in that the surface is modelled as a through-wall defect with closure stress acting over the the crack faces. In contrast to the critical CTOD method however, it is assumed that in addition to acting on the actual crack faces, the

closure stress acts beyond the ends of the defect (see Fig. (3.11b)). The surface defect is thus redefined as a through-wall defect with an effective length $c_\rho = c + \rho$ where ρ is a plastic zone correction which must be determined. To determine ρ, Erdogan and Ratwani assume a yield condition based on a plastic strip at the ends of the defect. This yield condition (which can be derived on the basis of simple beam theory[6] is

$$\frac{N}{t\sigma_F} + \frac{6M}{t^2\sigma_F} = 1 \tag{3.31}$$

where N and M are defined as shown in Fig. (3.11b). To complete the formulation, two additional equations are derived on the basis of assumptions regarding finiteness of stresses at $c + c_\rho$; these assumptions lead to two equations of the form

$$K_m(c_\rho) = 0 \tag{3.32}$$

$$K_b(c_\rho) = 0 \tag{3.33}$$

Examination of these equations (given in their full form in Ref. [45]) reveals that both K_m and K_b consist of terms representing the stress intensity due to internal pressure and the closure force and moment, N and M, at the ends of the defect. These two equations, in addition to Equ. (3.31) provide three non-linear equations for ρ, N and M which Erdogan and Rawtani solve numerically.

Some results of the solution, in terms of the non-dimensional parameter $c/(c + \rho)$ are plotted against the shell parameter λ in Fig. (3.12). Utilizing ρ, N and M, and a displacement solution which follows from their analysis, Erdogan and Rawtwani calculate the CTOD. These results, plotted against λ are shown in Fig. (3.13).

Erdogan and Ratwani compared their analytical result with experimental results for burst tests of 2014-T6 aluminum and titanium (Ti-5Al-2.5Sn-ELI) cylinders. This comparison generally verified the analytical model and the failure criterion CTOD = CTOD$_c$.

---

[6]Maximum plastic load carrying capacity at the outmost fibers of a beam subject to a combination of axial load and bending; a slightly different result is obtained if a plastic hinge condition is assumed.

3.5.4 Line-Spring Models

The line-spring method offers yet another means of estimating CTOD for a range of elastic-plastic behaviour. The approach, originally utilized by Rice and Levy to determine LEFM stress intensity factors [59], has gained popularity due to the considerable accuracy which can be obtained with minimal computational resources (i.e., in comparison to full three-dimensional elastic-plastic finite element analysis). Against the economy of the approach however, is relatively greater effort and sophistication in formulating the required equations. Due to the complexities inherent in the approach, only an overview will be given here.

In analogy with the formulations discussed previously, the principal behind the line-spring approach is that a surface defect can be modelled as a through-wall defect with certain closure forces and moments acting on its faces. These closure forces and moments constrain displacement and rotation of the faces of the through crack. To relate closure forces and moments to displacement and rotation, compliance expressions are derived from the plane strain solution for an edge crack which is equal in depth (locally) to the surface crack.

In formulation of the line-spring model, mathematical complexities arise due to the fact that the displacement and rotation of every point on the crack faces is a function of the displacement and rotation of every other point. This leads, in general, to a set of non-linear integral equations which must be solved numerically or alternately, using a specially modified finite element scheme.

A simplification which eliminates the need to solve such equations has however been proposed by King [59]. In this formulation, which serves to illustrate line-spring concepts, the surface crack is assumed to have a constant depth a. This assumption simplifies the equations for displacement, Δ, and rotation, θ, (see Fig. (3.14)) of the crack faces to a

set of linear algebraic equations,

$$\Delta = \frac{2(1-\nu)t}{E}\left(a_{11}\sigma_c + a_{12}m\right) \tag{3.34}$$

$$\theta = \frac{12(1-\nu^2)t}{E}\left(a_{12}\sigma_c + a_{22}m\right) \tag{3.35}$$

where $\sigma_c = N/t$, $m = 6M/t^2$, ν is Poisson's ratio and a_{ij} are compliance coefficients derived from the solution for an edge crack.

For a through crack with σ_c and m acting on the crack faces, the expressions for Δ and θ are

$$\Delta = \frac{4c}{E}\left(\sigma - \sigma_c\right) \tag{3.36}$$

$$\theta = \frac{-8(1+\nu)}{(3+\nu)}\frac{c}{Et}m \tag{3.37}$$

Equating these expressions to Equ.s (3.34) and (3.35) gives

$$\sigma_c = \alpha\sigma$$

$$m = -\beta\sigma$$

where α and β are funtions of a/t, ν and the compliance coefficents a_{ij}. Having derived expressions for σ_c and m, Equ.s (3.36) and (3.37) can be used to determine Δ and θ. From the geometry shown in Fig. (3.14) the CTOD of the surface defect is given by

$$CTOD = \Delta + \theta(t - 2a)$$

To complete the formulation, King adopted an approach similar to that employed in the critical CTOD/modified critical CTOD models. That is, the CTOD remains elastic up to ligament yield, which is assumed to occur when the nominal stress reaches the material flow stress. CTOD beyond ligament yield is calculated assuming no further rotation of the crack faces once the ligament has yielded. King also employed an effective

crack length to account for plasticity at the ends of the defect. The final solution is

$$\text{CTOD} = \frac{4\sigma c}{E}\left[1 + \frac{2(1-\nu)}{(3+\nu)}\left(1 - \frac{2a}{t}\right)\beta - \alpha\right]$$

for

$$\sigma \leq \frac{1}{\alpha}\left(1 - \frac{a}{t}\right)$$

and

$$\text{CTOD} = \frac{4(c+r_p)}{E}(\sigma - \sigma_{\text{LY}}) + \text{CTOD}_{\text{LY}}\left(1 + \frac{c}{r_p}\right)$$

for

$$\frac{1}{\alpha}\left(1 - \frac{a}{t}\right) < \sigma \leq \sigma_{\text{F}}\left(1 - \frac{2ac}{Wt}\right)$$

While King's formulation of the line-spring is admirable because of its simplicity, it should be noted that due to out-of-plane bending the approach may not be accurate for surface flaws in cylinders. King suggests that when applied to cylinders, use of the model be restricted to $c/\sqrt{Rt} > 1$. Parks [74] however, has applied line-spring concepts to a general class of plates and shells. This approach however, is somewhat more sophisticated in that for post yield behaviour, the equations relating diplacement and rotation to closure forces and moments are written in incremental form and solved based on an assumed slip line field (rather than average stress over the ligament). In addition, Parks suggest certain constitutive refinements to account for material hardening.

As noted, popularity of line-spring methods has arisen chiefly as a result of the considerable accuracy which can be obtained with minimal computational resources in comparison to full three-dimensional elastic-plastic finite element analysis. While expense remains an important factor in any analysis, it appears that with the decreased costs of computing and increased availability of proprietary finite element packages, the trend in recent years has been to more fully exploit finite element methods to analyse fracture problems. This is particularly true for critical components where the cost of a detailed finite element analysis can be justified.

3.6 Design Methods

3.6.1 The CTOD Design Curve

The CTOD Design Curve was developed as a means of applying the CTOD approach to practical engineering problems and is based on a non-dimensional CTOD, Φ, given by

$$\Phi = \frac{\text{CTOD}E}{2\pi a \sigma_Y} \tag{3.38}$$

Initial motivation for the design curve was due to the the work of Burdekin and Stone [21]. These investigators reasoned that by utilizing an equation of the form given by Equ. (3.38), a maximum defect size could be established once material critical CTOD is known. It remained however, to find an acceptable form for Φ which, to be of practical value, would be conservative over the range of material yield stress. In the original formulation, Burdekin and Stone utilized the Dugdale strip yield CTOD solution (Equ. (3.16)). However, as experimental results became available the CTOD design curve underwent several empirical adjustments [39]. These adjustments, made to maintain conservatism and ease of use resulted in the following form of design curve, which is in use today.

$$\Phi = \begin{cases} \left(\frac{\varepsilon}{\varepsilon_Y}\right)^2 & \frac{\varepsilon}{\varepsilon_Y} \leq 0.5 \\ \frac{\varepsilon}{\varepsilon_Y} - 0.25 & \frac{\varepsilon}{\varepsilon_Y} > 0.5 \end{cases} \tag{3.39}$$

Equating this equation to Equ. (3.38) and rearranging, gives the following expressions for the maximum allowable defect.

$$\bar{a}_{max} = \begin{cases} \dfrac{\text{CTOD}_c E \sigma_Y^2}{2\pi\sigma^2} & \frac{\sigma}{\sigma_Y} \leq 0.5 \\ \dfrac{\text{CTOD}_c E}{2\pi(\sigma - 0.25\sigma_Y)} & \frac{\sigma}{\sigma_Y} > 0.5 \end{cases} \tag{3.40}$$

The CTOD design curve has been incorporated into a document, BSI PD 6493 [24] which can be used to assess the severity in a wide range of structural components. To extend the usefulness of the approach, i.e., to make it possible to utilize a single curve

to analyse geometries other than through-wall defects, LEFM shape factors are utilized to relate through-wall to surface and buried defects (see Fig.s (3.15) and (3.16)). This provides an equivalent through-wall defect ($\bar{a}$) which can be compared to the maximum allowable given by Equ.s (3.40). Although not strictly valid, this procedure follows a suggestion by Dawes that under constrained yielding, use of LEFM relationships can be justified [39]. For plates, Fig.s (3.15) and (3.16) can be used directly; for cylinders however, due to outward bulging effects which have been noted previously, PD 6493 requires that the equivalent crack length be further reduced by the factor D shown in Fig. (3.17).

One drawback with the CTOD design curve approach is that no explicit formulation is given for behaviour near plastic collapse. In recognition of this, PD 6493 requires that surface defects be recategorized as through-wall defects (of the equivalent length) when the net section stress reaches the material flow stress, i.e., when

$$a \leq t \left(1 - \frac{\sigma}{\sigma_F}\right) \tag{3.41}$$

An important point to note is that the CTOD design curve approach provides a maximum allowable and not a critical defect size. Due to the assumption of unconstrained yielding and the nature of applied loading, maximum allowable defect size will possess an inherent factor of safety. Based on a study performed by Dawes [38], a factor of safety of approximately 2.5 on crack sizes was estimated at a 95.4 % confidence level.

It should be noted that while a factor of safety of 2.5 is generally accepted, in certain instances (i.e., at high net section stresses), a much more variable factor of safety can be observed [5]. This observation, which relates to the fact that the upper region of the curve is empirical, in addition to the one noted previously (i.e., that plastic collapse is not an integral part of the formulation) means that the CTOD design curve cannot in general be used to perform a critical engineering assessment. To resolve these difficulties,

a three tier assessment (which utilizes a reference stress methodology to predict post yield behaviour) has been proposed. Details of this approach, which should provide a more universal means of assessing the significance of defects in structural components, can be found in Ref. [5].

3.6.2 The Central Electricity Generating Board R6 Method

In a study of the significance of defects in structural components, Dowling and Townley suggested the 'two criteria approach' to failure assessment. The approach was subsequently supported by other investigators (Harrison et al. and Milne et al.) and ultimately used by the Central Electricity Generating Board (CEGB) to develop the R6 failure assessment diagram [84].

The principal behind the two criteria approach is that failure will occur when the applied load reaches either: 1, the load to cause brittle fracture, P_K, or 2, the load to cause plastic collapse, P_1. The two criteria approach therefore assumes failure to be either toughness controlled or flow stress controlled. This assumption is clearly not always valid; it is however, a conservative one given that actual failure load is usually bounded by either P_K or P_1.

Dowling and Townley found that even in the transition from toughness controlled to flow stress controlled behavior, failure loads could be predicted to within 20 % using the two criteria approach. Although this order of accuracy was considered reasonable in view of the simplicity of the approach, Dowling and Towley noted that increased accuracy could be achieved using the Dugdale strip yield model to interpolate between LEFM and plastic collapse failure criteria. This refinement of the two criteria approach ultimately led to the development of a more comprehensive means of predicting failure—the CEGB R6 method.

The CEGB R6 method [27, 84] is based on the generalized failure assessment diagram

shown in Fig. (3.18). The ordinate and abscissa of this diagram, S_r, K_r, are given by the following non-dimensional parameters.

$$S_r = \frac{\sigma}{\sigma_1} \tag{3.42}$$

$$K_r = \frac{K_1}{K_c} \tag{3.43}$$

These parameters reflect the degree to which either toughness or flow stress control failure. It is assumed that the range of behaviour between fully toughness controlled, $(S_r = 0, K_r = 1)$ and fully flow stress controlled $(S_r = 1, K_r = 0)$ can be interpolated using the Dugdale strip yield model. This leads to

$$K_r = \left[\frac{8}{\pi^2 S_r^2} \ln \sec \left(\frac{\pi}{2} S_r \right) \right]^{-\frac{1}{2}}$$

which corresponds to the locus of points (S_r, K_r) for which failure is expected to occur. Equations (3.42) and (3.43) can be used to determine an assessment point for a cracked body. If this point lies on or outside the assessment curve, a prediction of failure is made.

A feature of the R6 method is that a quantitative assessment of structural integrity can be made based on the proximity of a point $((S_r, K_r)$ to the failure curve. This makes it possible to perform sensitivity analysis with respect to variables such as applied load, defect geometry, and material properties.

3.6.3   AGA Model (Battelle Empirical Analysis)

A number of investigators at the Battelle Memorial Institute have worked towards development of a model to predict failure of cylinders containing through wall and surface defects. This model, developed for the American Gas Association (AGA) was derived on theoretical grounds and subsequently refined using the results of large scale tests. These empirical adjustments have been found to improve the accuracy of the model throughout the range of toughness controlled to flow stress controlled behaviour.

In formulating the AGA model, Hahn et al. [50] reasoned that flat plate expressions could be utilized to predict failure stress in a cylinder if a correction was made for outward bulging. Combining Equ. (3.16) (the Dugdale strip yield model) with Equ. (3.17), these investigators arrived at

$$\sigma_\theta = \frac{K_{1c}}{(\pi c \phi)^{\frac{1}{2}}} M^{-1} \tag{3.44}$$

where ϕ is a plasticity correction, given by

$$\phi = \left(\frac{\pi M \sigma_\theta}{2\sigma_F} \right)^{-2} \ln \left[\sec \left(\frac{\pi M \sigma_\theta}{2\sigma_F} \right) \right]^2 \tag{3.45}$$

and M is a stress magnification factor. Hahn et al. chose

$$M = \left[1 + 1.61 \left(\frac{c^2}{Rt} \right) \right]^{\frac{1}{2}} \tag{3.46}$$

which, as noted in Sec. 3.2.1, is due to Folias.

To assess the validity of Equ. (3.44), Hahn et al. drew upon a number of experimental studies of pressure vessel failure. These studies included a range of materials (ductile and brittle steel, as well as alumimum and titanium alloys), and various defect geometries (c^2/Rt ratios). Equation (3.44) was used to determine the fracture properties of the materials used in experimental studies. These properties were found to be in agreement with fracture properties determined from flat plates of the same material. It was concluded that Equ. (3.44) could be used to predict both toughness controlled and flow stress controlled failure.

A similar conclusion was drawn by Maxey et al. [68] and Kiefner et al. [58] in studies of intermediate to high toughness pipeline steels. These investigators however, recast Equ.s (3.44) and (3.45) into the following non-dimensional form.

$$\frac{K_{1c}^2 \pi}{8 c \sigma_F^2} = \ln \sec \left(\frac{\pi M_{T,P} \sigma_\theta}{2\sigma_F} \right) \tag{3.47}$$

where

$$M_T = \left[1 + 1.1.255\left(\frac{c^2}{Rt}\right) + 0.0135\left(\frac{c^4}{R^2t^2}\right)\right]^{\frac{1}{2}} \tag{3.48}$$

for through-wall defects and

$$M_P = \frac{1 - a/t}{1 - a/M_T t} \tag{3.49}$$

for surface flaws.

Equation (3.47) relates a non-dimensional toughness parameter to a non-dimensional flow parameter, and represents the locus of points along which failure can be expected to occur. Maxey et al. and Kiefner et al. found, when comparing the experimental results with Equ. (3.47) that good agreement could be obtained if flow stress was taken to be

$$\sigma_F = \sigma_Y + 69 \text{ MPa}$$

Maxey et al. and Keifner et al. noted that the transition from toughness controlled to flow stress controlled behavior occurs at

$$\frac{K_{1c}^2 \pi}{8c\sigma_F^2} \approx 4 \tag{3.50}$$

and that beyond this transition, the failure criterion, Equ. (3.47) effectively becomes

$$\sigma_\theta M_{T,P} = \sigma_F$$

The Battelle methodology discussed in this section and other elastic-plastic fracture mechanics approaches discussed previously in this chapter were considered in view of their potential to predict failure of NGV cylinders. Choice of any one methodology (or number of methodologies) as a basis for assessing in-service integrity of NGV cylinders however, required greater understanding of the fracture resistance of NGV cylinder material. For this reason a series of small scale CTOD tests were performed. These tests are discussed in the following chapter.

Chapter 4

INVESTIGATION OF SMALL SCALE BEHAVIOUR

Material test results which were available when this investigation was begun [1, 13] indicated that NGV cylinder steel (AISI 4130 X) is a moderately tough material. Since materials of this nature typically exhibit some plasticity prior to failure, it was considered necessary, in this investigation, to employ elastic-plastic fracture mechanics methods to predict failure. Consideration was therefore given to the relative merits of adopting either J-integral or crack tip opening displacement (CTOD) based methods. Although use of the J-integral technique is applicable to this material behaviour, a fundamental drawback is that this parameter cannot in general be measured experimentally. For this reason, it was decided to adopt the CTOD approach. While the CTOD cannot be measured directly, it can be estimated from the crack opening displacement (COD), a quantity that can be measured experimentally (see Sec. 3.4.1). Another motivation for use of the CTOD to predict failure was that a design methodology based on the CTOD approach is somewhat established and has been incorporated into a proposed standard, BSI PD 6493 [24].

In order to apply the CTOD approach to predict failure of NGV cylinders, it was necessary to initially establish the critical value of CTOD for AISI 4130 X steel. One of the first stages of this investigation therefore, was small scale critical CTOD bend specimen testing. This testing was performed in general accordance with British Standard 5762 (BS 5762) [23], an accepted standard for critical CTOD testing.

4.1 Numerical Modelling of CTOD Specimens

4.1.1 Specimen Design

NGV cylinder steel was expected to exhibit considerable anisotropy due to the deep drawing process used in the manufacturing process. Critical CTOD in turn, was expected to be highly dependent on defect orientation. Since interest in this investigation was in axial defects and because BS 5762 requires a full thickness specimen, it was necessary to employ a curved CTOD specimen.

The nominal stress field acting over an axially oriented defect in a pressurized NGV cylinder (a thin walled vessel) is biaxial tension. This stress field produces a high constraint condition at the crack tip. To reproduce this condition in the small scale specimens, a three point bend loading configuration was employed. Guidelines for the final design (see Fig. (4.1)) were found in the literature and British Standard BS 5762.

While there are no inherent difficulties in employing curved fracture CTOD specimens, it does make a number of standardized relationships given in BS 5762 suspect, as they were derived assuming a straight fracture mechanics specimen. Since handbook solutions for curved fracture mechanics specimens were unavailable, an alternate means of determining the stress intensity and compliance of this unique CTOD specimen was required. This led to the use of a finite element analysis to model the curved CTOD specimens. It should be noted that in addition to providing data necessary to calibrate the small scale test procedure, the finite element analysis of the curved fracture mechanics specimen provided experience in the modelling aspects of fracture mechanics problems. This experience was of value in the latter stages of this project, where a finite element analysis of full scale NGV cylinders containing defects was performed.

4.1.2 Mesh, Boundary Conditions, and Loading

As noted above, the purpose of finite element analysis in this stage of the investigation was to determine stress intensity factors and specimen compliance for a range of crack depth in the curved CTOD specimen. To facilitate this analysis, the finite element model was constructed to permit crack length a to be input as a parameter. This parameter was varied so that the specimen a/W ratio ranged between 0.4 and 0.9.

Figure (4.3) shows the finite element mesh for the CTOD specimen; this figure also shows the boundary conditions and applied load. The finite element mesh was constructed using the eight-node (quadratic) isoparametric element of Zienkiewicz [99][1]. Since specimen width was sufficient for a condition of plane strain, stiffness matrices were formulated with a plane strain elasticity matrix. Note in Fig. (4.3) that due to symmetry, it was possible to perform the analysis with a model of one-half of the actual specimens. To model symmetry across $x = 0$, nodes were constrained against displacement in the x-direction. To model the roller supports of the bend fixture (see Fig. (4.2)), the node at $x = 50.8$ mm was constrained against displacement in the y-direction. Specimen load was modelled by a point force acting in the $-y$ direction.

As noted in Sec. 3.4.1, an inverse square root singularity is produced when the mid-side node of an isoparametric element is moved to the quarter-point position. Since this modification more accurately represents the stress distribution in the crack tip region, the mid-side nodes of the four elements near the crack tip were moved to the quarter point position (see Fig. (4.3b)).

Finite element modelling of the small scale CTOD specimens (and subsequent full scale cylinders) during this investigation was performed using the commercial finite element program ANSYS[2]. The ANSYS input file is listed in Appendix C. The analysis

---

[1]This element is described in Appendix A.

[2]ANSYS was developed and is distributed by Swanson Analysis Systems, Inc..

described in this phase was run on an Apollo DN 4000 workstation. Computer CPU time per specimen analysis was approximately 2 minutes.

4.1.3 Numerical Results

After the finite element models were created and submitted, solution files were post-processed to extract stress intensity, crack opening displacement and specimen compliance values. This was accomplished by employing a user written subroutine which utilized the ANSYS command KCALC to compute stress intensity factor (K_I) and the following relationships to compute crack opening displacement (Δ) and specimen compliance (C)

$$\Delta = 2u$$
$$C = \frac{P}{v}$$

where u is the x-displacement of the node at the crack mouth, P is the load, and v is the y-displacement of the node to which the load was applied (see Fig. (4.4)).

To aid in identifying trends in the numerical results, the following relationships were employed

$$K_I = \sigma\sqrt{\pi a}F\left(\frac{a}{W}\right) \tag{4.1}$$

$$\Delta = \frac{4\sigma a}{E}V_1\left(\frac{a}{W}\right) \tag{4.2}$$

$$v = \frac{\sigma}{E}SV_2\left(\frac{a}{W}\right) \tag{4.3}$$

where σ is the maximum bending stress ($3PS/2W^2t$), E is the modulus of elasticity, S is the load span and F, V_1 and V_2 are non-dimensional shape factors which are functions of a/W.

To assess the differences in the compliance relationships, the results of the finite element analysis have been plotted in terms of the non-dimensional shape factors, F,

V_1 and V_2 as shown in Fig.s (4.5) through (4.7). Superimposed on these figures are analytical solutions from Ref. [91] calculated based on a straight specimen of dimensions equivalent to those of the curved CTOD specimen for comparison. Overall, the results from the finite element analysis suggest that the curvature effects of the cylinder CTOD specimen are relatively insignificant. This is particularly evident in the figures that compare stress intensity and crack opening displacement results for the two specimen geometries (Fig.s (4.5) and (4.6)). For these results, the effect of curvature becomes significant only when $a/W > 0.8$, with the maximum difference between the finite element estimates and analytical solution being 9 % for the crack tip stress intensity and 5 % for the crack opening displacement. Increased differences between the finite element estimates and analytical solution over the range of crack size can be seen in Fig. (4.7) which shows the results for point load displacement. For these results, a maximum difference between the finite element estimates and analytical solution was 16 %.

From the finite element analysis of the CTOD specimen, it was concluded that the effects of curvature of the specimen up to $a/W < 0.8$ could be neglected thus validating the BS 5762 guidelines for CTOD testing. Hence, in subsequent small scale testing described in the next section, the standardized relationships given in BS 5762 were employed.

4.2 Experimental Measurement of Critical CTOD

4.2.1 Specimen Preparation

A total of 6 specimens were cut and prepared from a sectioned NGV cylinder. To facilitate fatigue precracking, a 0.15 mm slitting saw was then used to produce a notch. After the specimens were notched, they were cycled in three point bending to grow a fatigue crack approximately 0.125 mm (0.05 in) in length. To ensure uniformity in fatigue crack length, crack propagation gauges were mounted on the specimens to monitor crack growth. The

location of these gauges are shown in Fig. (4.2). This figure also indicates the position of the potential drop probes used to measure crack growth in the subsequent CTOD testing.

Fatigue crack growth data collected during fatigue precracking has been plotted in Fig.s (4.8) and (4.9).

4.2.2 Test Procedure

After each CTOD specimen was precracked, it was fitted with knife edges and a double cantilever type clip gauge to monitor COD, and potential drop leads to monitor crack growth. The locations of the knife edges and potential drop leads are shown in Fig. (4.2). The specimen was then placed in the three point bend fixture of the test machine and loaded under displacement control at a ramp displacement rate of approximately 0.025 in/min. Loading of each specimen proceeded well beyond the attainment of maximum load. This resulted in CTOD tests that lasted approximately three to four minutes. During the CTOD tests, data from from the clip gauge and the load cell of the test machine were collected on a DAS 20 data acquisition board installed in an IBM AT. Potential drop data was collected using an MDT DC potential drop system. Unfortunately, at the time of testing, it was not possible collect load and COD, and potential drop data utilizing a single system. This made it necessary to design a system which would enable matching of load/COD data and potential drop data. A system was therefore designed to monitor potential drop power pulses to the specimen and send these pulses to the DAS 20 board. After the tests, pulses recorded on the DAS 20 board were matched to potential drop data recorded on the MDT board.

To facilitate integration and analysis of load, COD and potential drop data files, a FORTRAN progam (CODREAD) was written. This program, listed in Appendix C, reads and merges binary DAS 20 and ASCII MDT files, applies calibration factors and outputs the results for further examination. The potential drop data are converted to

crack length using Johnson's equation [81]:

$$\frac{V}{V_0} = \frac{\cosh^{-1}[\cosh(y/2W)/\cos(a/2W)]}{\cosh^{-1}[\cosh(y/2W)/\cos(a_0/2W)]}$$

where V is the voltage drop corresponding to the crack length a, V_0 is the voltage drop corresponding to the original crack length a_0, y is the length across which V and V_0 are measured and W is the specimen width.

After the CTOD tests, the specimens were immersed in liquid nitrogen and broken open to reveal the fracture surfaces. The fracture surfaces were then examined under an optical microscope for evidence of cleavage and/or stable crack growth. With the aid of a travelling table and a precision scale mounted on the base of the microscope, fatigue precrack lengths, a_0, were measured.

4.2.3 Small Scale Test Results

Depending on the material crack growth resistance, several different types of material behaviour may be observed during a critical CTOD test. The various material response behaviour, i.e., cleavage, stable crack growth prior to failure, attainment of a maximum load plateau, etc., have been classified in BS 5762 according to characteristics of the load-COD as shown in Fig. (4.10). This figure also illustrates the point (or points) on each load-COD record at which critical CTOD can be calculated. As has been noted, it was of interest in this investigation to determine CTOD at initiation (subscript i in Fig. (4.10)).

Determining critical CTOD at true crack initiation is, from a practical viewpoint, very difficult. It can be seen from Fig. (4.10) that, while the points of instability or maximum load on the various load-COD curve (subscripts u and m) are well defined, the onset of crack initiation is not easily determined. At the present time, there are no accepted analysis techniques for estimating the point of initiation. Where stable crack growth is

suspected, BS 5762 outlines a multi-specimen method for developing a resistance curve that can be used to determine crack opening displacement at initiation. This method however, requires further testing and a minimum of four (but preferably six) additional specimens. An alternative to the use of the multi-specimen technique is to monitor crack growth directly as was done in the test described here.

One approach to utilizing crack growth data to estimate CTOD at initiation is given by Romilly [79] and was employed in this study. The approach makes use of a plot of load, P, versus crack growth, Δa. From this plot the load at the onset of stable crack growth, i.e., at $\Delta a = 0$ can be determined. This load is then transferred to the load-crack opening displacement curve to determine the plastic component of crack opening displacement, V_P. CTOD at initiation, CTOD_i is then calculated using (ref. Sec. 3.4.1)

$$\text{CTOD}_i = \frac{K^2(1 - \nu^2)}{2\sigma_Y E} + \frac{0.4(W - a)V_p}{0.4W + 0.6a + z} \tag{4.4}$$

where K is the stress intensity factor, ν is the Poisson's ratio, E is the modulus of elasticity, W is the specimen width, a is the crack length, and z is the distance between the specimen and the point at which the COD is measured.

Critical CTOD Analysis

Referring to Fig. (4.10) discussed previously, analysis of the load-crack opening displacement records of all of the CTOD specimens showed the behaviour of this material to be similar to those of Type I and Type III in Fig. (4.10), indicating either cleavage or some stable crack growth prior to failure. Comparison of the load-crack opening displacement curves suggested that appreciable stable growth prior to failure had occurred in only one specimen, Specimen 5. This can be observed in Fig. (4.11), where the load-crack opening displacement record of Specimen 1 is compared to that of Specimen 5. (The load-crack opening displacement records of the other specimens are similar to that of Specimen 1

and have therefore been omitted from Fig. (4.11) for clarity.) Visual records made during testing supported the assumption that, with the exception of Specimen 5, only limited crack growth occurred prior to failure.

In order to verify the visual records, crack growth (Δa) was plotted against load (P) as shown in Fig.s (4.12) and (4.13). These figures indicated that, with the exception of Specimen 5, initiation of crack growth occurred at maximum load. Following the procedure outlined in the previous section, initiation CTOD was calculated using the load-COD curves. The loads and crack lengths used in these calculations are given in Table (4.1). Initiation CTOD was found to range from 0.027 to 0.049 mm, with a mean of 0.039 mm and a standard deviation of 0.008 mm (see Table (4.2)).

To verify the small scale test results, a correlation between J-integral and CTOD was employed. This correlation (ref. Sec. 3.4.2) is

$$J = m\sigma_{\mathrm{F}}\mathrm{CTOD}$$

where J is the J-integral corresponding to CTOD, m is a non-dimensional constant of proportionality ($= 1.6$ for plane strain) and σ_{F} is the material flow stress ($\sigma_{\mathrm{F}} = (\sigma_{\mathrm{Y}} + \sigma_{\mathrm{U}})/2 = 885$ MPa). Substituting the value of flow stress and the average value for initiation CTOD for the cylinder material into the above equation gives

$$
\begin{aligned}
J &= (1.6)(885 \text{ MPa})(0.039 \text{ mm}) \\
&= 55.2 \text{ N/mm}
\end{aligned}
$$

which is nearly identical to $J_{\mathrm{Ic}} = 54$ N/mm reported by Powertech Labs, Inc. [13]. This close agreement would appear to support the small scale CTOD results of the present investigation and further, suggests that the J-CTOD correlation is valid and useful for this material.

Limit Load Analysis

The limit load, P_L for three point bend specimens (ref. Sec. 3.5.1) is

$$P_L = 1.543\sigma_{\mathrm{F}}\frac{(W - a)^2 B}{4S}$$

This expression was used to calculate the limit load for the five CTOD specimens. The calculated limit load and the ratio of maximum test load to limit load (P_{max}/P_L) for each specimen has been entered in Table (4.3). As indicated in this table, the mean of the results for P_{max}/P_L was 0.83 with a standard deviation of 0.02. These results indicate that all of the specimens failed significantly below the predicted limit load. The results of the limit load analysis confirm that unstable crack growth rather than plastic collapse controlled failure of the small scale specimens. Although not conclusive, this suggests that plastic collapse methods may not be well suited to predicting large scale NGV cylinder behaviour in the presence of sharp defects.

The critical CTOD results obtained from this small scale testing were subsequently utilized in FEM modelling to predict the full scale behaviour of NGV cylinders containing cracks. This is discussed in Chapters 5 and 6.

Chapter 5

NUMERICAL INVESTIGATION OF FULL SCALE BEHAVIOUR

As noted in Chapter 1, the major goal of this investigation was to assess the current standards for NGV cylinder recertification. The approach adopted to achieve this goal was to predict cylinder behaviour during recertification, i.e., during a hydrostatic test, and following recertification, during the five years a cylinder remains in service. An overview of this approach is shown in Fig. (5.1). As noted in Chapter 1, a significant portion of the study involved finite element analysis of NGV cylinders. This analysis is discussed in this chapter.

The goal of the finite element analysis was to predict volumetric expansions and failure (burst) pressures of cylinders containing a range of defect sizes. Finite element analysis was intended therefore, to predict cylinder behaviour during a hydrostatic test. The results of the analysis make it possible to determine whether or not a defective cylinder will fail recertification, that is, whether or not a defective cylinder will exceed volumetric expansion limits or rupture. As will be seen in Chapter 8, this information, together with available fatigue crack growth estimates (which predict whether or not a cylinder will fail during service) provides the means to assess the current standards for NGV cylinder recertification.

Before discussing the numerical analysis, it should be noted that a CTOD approach was adopted to predict failure (burst) pressure. To this end, the critical CTOD material data from the small scale tests as discussed previously in Chapter 4 were employed.

61

5.1 Model Description

5.1.1 Material Properties

To perform the finite element analysis and subsequently analyse the results, it was necessary to know both the tensile and fracture properties of NGV (AISI 4130X) steel. At the time this investigation was begun, a series of tensile tests had been performed at Powertech Labs, Inc. These tests, as reported in Ref. [13], indicated that the yield strength, ultimate tensile strength and elongation of AISI 4130X steel are 822 MPa, 948 MPa, and 20 percent respectively. As discussed in Chapter 4, the fracture properties for this material were determined by a series of small scale tests performed during present investigation and indicated that the average critical CTOD for the initiation of crack growth (L-R direction) is 0.039 mm.

For the purpose of finite element modelling, the stress-strain behaviour of the 4130X steel was idealized as linear strain hardening as shown in Fig. (5.2). Plasticity was assumed to be governed by the von Mises yield criteria, associative (Prandtl-Reuss) flow rule and kinematic hardening rule[1].

5.1.2 Cylinder/Defect Geometry

The geometry of the 60 liter cylinder that was analysed is shown in Fig. (5.3). Nominal outside diameter and wall thickness of this capacity cylinder are 316.6 mm and 7.5 mm respectively; nominal length is 972.8 mm. The orientation of the defect considered is also shown in Fig. (5.3). Note that an elliptical crack shape and axial orientation were assumed. This geometry and orientation corresponds to a fatigue crack subjected to the highest principal wall stress (i.e., the hoop stress), and hence represents the most severe type of defect encountered in service.

---

[1]A explanation of these laws, which come from plasticity theory, is given in Appendix B.

To assess cylinder behaviour, i.e., fracture resistance, volumetric expansion, etc., over a range of defect size, defects of various a/t and a/c ratios were considered. Each defect size was investigated as both an interior and exterior defect. The matrix of computer analyses performed (run designation and crack size) is given in Table (5.1). Note from this table that the crack size was varied from short and shallow to relatively long and deep.

5.1.3 Finite Element Mesh

Shell to Solid Submodelling

Due to a relatively small thickness to radius ratio (i.e., t/R), NGV cylinders can be classified as thin walled, shell structures. The logical approach to finite element analysis of such structures is to utilize elements which have been derived from thin shell theory, i.e., shell elements. Shell elements are by nature, two-dimensional entities since only in-plane forces and moments have been assumed in their derivation.

Because shell elements are well suited to analysis of NGV cylinders, it was desirable to use this type of element in the analysis. This, however, presented a difficulty as the ultimate goal was to analyse surface defects in the cylinders. As surface flaws are three-dimensional, some form of solid element was required. While it was possible to construct a mesh for a defective NGV cylinder exclusively with solid elements, this was not considered feasible due to the demands which would be placed on the computer CPU and memory. An alternate approach, known as shell to solid submodelling was therefore employed. In shell to solid submodelling, a technique developed specifically to analyse stress concentrations in shell structures, two finite element models are constructed. The first model, referred to as the coarse model, represents the structure of interest and is constructed with shell elements. The second model, referred to as the submodel,

represents some region of the structure (i.e., a stress concentration) and is constructed with solid elements.

The basis for shell to solid submodelling is the specified boundary displacement approach discussed by Kelley [57]. In this approach, an analysis is first performed with the coarse model. This analysis yields a displacement solution which is used to specify displacements at the boundary of the submodel. Displacements of a node at the boundary of the submodel ($\{u\}_s$) are specified using the following result, which accounts for translation and rotation of elements in the coarse model [89].

$$\{u\}_s = \{u\} + \{\theta\} \times \{r\}$$

where $\{u\}$ is the translation vector of a point on the coarse model, $\{\theta\}$ is the rotation vector of a point on the coarse model, and $\{r\}$ is the position vector from the coarse model to a node on the boundary of the submodel.

Because the displacement field of the submodel is made to match that of the coarse model, the stress field should also match. This will not be the case however, if the dimensions of the submodel have not been made sufficiently large for any local disturbances within it to dissipate at the boundary[2]. It is therefore critical in shell to solid submodelling that the dimensions of the submodel be sufficient for any local disturbances produced within this region to dissipate prior to reaching the boundaries.

Coarse Model

Following the shell to solid submodelling approach, a coarse model representing an NGV cylinder plus a number of submodels representing defects in the cylinder were constructed. The coarse model mesh is shown in Fig. (5.4). This mesh was constructed using the eight node isoparametric shell element of Cook [35] (see Appendix A). Note in Fig. (5.4), that

---

[2]Dissipation of any local effects is guaranteed by Saint-Venant's principal.

due to symmetry, it was possible to employ a mesh of one-quarter of the actual cylinder. This was accomplished with the aid of symmetry boundary conditions which were applied to nodes along the planes $x = 0$ and $z = 0$. These boundary conditions constrained nodal displacements perpendicular to the plane of symmetry and nodal rotations parallel and perpendicular to the element planes. In addition to the symmetry boundary conditions, an additional set of boundary conditions were applied to the nodes along the $y = 0$ plane to constrain the model against rigid body motion in the y-direction. Although possible to apply this last set of boundary conditions at any point in the y-direction, they were applied at the mid-section to permit use of symmetry boundary conditions in the submodel (see Sec. 5.1.3).

In a non-defective NGV cylinder, plasticity does not occur at pressures below 41.37 MPa (6000 psi) (the maximum pressure in the analysis–see Sec. 5.1.4). For this reason, finite element analysis of the coarse model was performed assuming linear-elastic material properties.

Several refinements in the finite element mesh were performed prior to achieving the desired order of accuracy. The final version, as shown in Fig. (5.4), contained 300 elements and approximately 4500 active degrees of freedom. Run time on an Apollo DN 4000 workstation was approximately 15 minutes. The ANSYS input file for the coarse model is listed in Appendix C.

To gain some idea of the accuracy of the coarse model, membrane and bending stresses (in the circumferential and longitudinal directions) were compared with an analytical solution given by Coates [30]. This comparison is shown in Fig.s (5.5) and (5.6), were membrane and bending stress from the finite element model and from Coates' solution have been plotted as functions of s/l, where s is distance (measured from the nozzle end) along the cylinder wall and l is cylinder length. As can be seen, there is generally good agreement between the finite element and analytical solution. Differences between the

two solutions appear mainly in the top end cap, near the nozzle, and in the bottom end cap. These differences however, should not necessarily be attributed to the finite element model, as Coates' solution does not account for the constraint imposed by a nozzle and further, is based on an elliptical, rather than a torospherical end cap.

Submodel

The submodel mesh (for the 5 × 10 mm defect) is shown in Fig. (5.7). This mesh was constructed with the twenty-node isoparametric element of Zienkiewicz [99] (see Appendix A). In the view of the submodel given in Fig. (5.7), the defect lies in the lower right hand corner of the mesh on the plane $z = 0$. This region of the mesh has been enlarged and is shown in Fig. (5.8(a)). The near crack tip mesh is shown in Fig (5.8(b)).

To facilitate analysis of a range of defect sizes (ref. Sec. 5.1.2), the elliptical transformation

$$
\begin{aligned}
x' &= x\sqrt{1 + \frac{c^2 - a^2}{x^2 + y^2}} \\
y' &= y \\
z' &= z
\end{aligned}
$$

was employed. This transformation, illustrated diagrammatically in Fig. (5.10), made it possible to employ a single semi-circular mesh (representing a crack of depth a and length $2a$) for each crack length $2c$. The advantage of using this transformation was that for each three crack lengths, it was necessary to construct only one submodel. The semi-circular crack submodels for each crack depth were constructed with the aid of the solid modelling capabilities of ANSYS. It should be noted that while in general, solid modelling greatly simplifies construction of a finite element mesh, initial attempts to construct an elliptical crack profile utilizing solid modelling exclusively were disappointing due to current limitations of ANSYS solid modelling capabilities. Use of the above

transformation however, made it possible to take full advantage of solid modelling, as construction of a semicircular mesh is relatively straight forward.

To further reduce the need to construct a large number of submodels, an additional transformation was employed to change the curvature of each submodel so that a single submodel (i.e., for a given crack depth a and crack length $2c$) could by utilized for both interior and exterior defects.

To reduce the size of the submodel, symmetry boundary conditions were applied to nodes along the planes $y = 0$ and $z = 0$. These boundary conditions constrained displacement normal to the planes of symmetry. To generate the defect on $z = 0$, the displacement constraints on the elliptical crack plane were released. Boundary conditions on the other two boundaries of the submodel consisted of specified displacements as discussed previously. Submodel boundary conditions, and the geometric relationship between the submodel and the coarse model are illustrated diagramatically in Fig. (5.9).

Development of a submodel that would accurately predict volumetric expansion and CTOD required preliminary studies to determine the dimensions of the submodel and the number of elements to employ in the submodel. To determine submodel dimensions, membrane and bending stresses at the boundary were examined as the dimensions h and s (see Fig. (5.7)) of the submodel with the largest defect were varied over the range $75 < h < 150$ mm, $40 < s < 80$ mm. Based on the observation that membrane and bending stresses at the boundary were within several percent of those shown in Fig.s (5.5) and (5.6), the submodel dimensions $h = 100$ mm and $s = 80$ mm were chosen.

Following the initial study to determine correct dimensions for the submodel, a study was performed to determine the number of elements to employ in the submodel. To illustrate the approach taken to determine the number of elements to focus at the crack tip, some results are plotted in Fig. (5.11). In this figure, which represents the final stages of mesh refinement, non-dimensional LEFM stress intensity factors (c.f. Equ. (3.6)) are

plotted as functions of $2\varphi/\pi$ for three levels of refinement of the mesh near the crack tip
(5 × 30 mm defect) [3]. As can be seen, there is little variation in the stress intensity factor
with increased degrees of freedom. This was taken to indicate that the near crack tip
mesh was sufficiently refined and based on this observation, the mesh shown in Fig. (5.7)
was chosen.

The final version of the submodel mesh shown in Fig (5.7) contained approximately
500 elements and 7000 active degrees of freedom. Run time for this model on an Apollo
DN 10000 was approximately six hours. The ANSYS input file for the submodel is listed
in Appendix C.

5.1.4 Loading

To load the finite element model in a manner consistent with actual service loading,
uniform pressure was applied to the element faces on the interior of the model. This
pressure was applied to the element faces in both the coarse model and submodel; pressure
was also applied to the faces of the interior defects.

The model was loaded to 41.37 MPa (6000 psi), a pressure 6.90 MPa (1000 psi)
greater than the maximum pressure that a cylinder experiences during a hydrostatic
test. Because the analysis was non-linear, it was necessary to step incrementally through
the loading history. Since the greatest plasticity was expected for the largest defect
(5×30 mm), the submodel for this defect was used to determine the correct loading
sequence. Based on the load at which yielding first occurred, the first load step for this
and all other submodels was set equal to 10.34 MPa (1500 psi). To determine the size of
subsequent load steps and convergence within a load step, criteria based on the maximum
plasticity ratio were employed. The plasticity ratio (at an integration point) is defined

---

[3]φ is defined in Fig. (3.4).

by

$$\frac{\Delta\varepsilon^{pl}}{\varepsilon^{el}}$$

where $\Delta\varepsilon^{pl}$ is the change in plastic strain (between load steps) and ε^{el} is the elastic strain (in the current load step). Based on a maximum plasticity ratio of 0.015, the load step increment was set equal to 1.72 MPa (250 psi). Within each load step, the solution was considered converged when the maximum plasticity ratio was equal to 0.005.

Several solution methods (the Newton-Raphson, modified Newton-Raphson and initial stiffness methods) were investigated as a means of solving the non-linear problem. It was found that per load step, the Newton-Raphson and modified Newton-Raphson methods required relatively few (three to four) iterations to converge, and that the initial stress method[4] required considerably greater number (up to 15) of iterations to converge. The time taken per iteration in the Newton-Raphson and modified Newton-Raphson methods however, actually made these methods slower than the initial stress method. To minimize run time therefore, the initial stress method was employed throughout the analyses.

5.1.5 Calculation of COD, CTOD, and Volumetric Expansion

To predict failure of NGV cylinders and assess the current standards for cylinder recertification, it was necessary to extract COD, CTOD and volumetric expansion data from the finite element analysis. The methods used to calculate these quantities are described in this section. It should be noted that, since there were no provisions for calculating COD, CTOD and volumetric expansion in the version of ANSYS (Ver. 4.3/4.4) used for the analysis, it was necessary to develop several ANSYS subroutines (macros) and FORTRAN programs for this purpose.

In fracture mechanics literature, various definitions for CTOD have been suggested.

---

[4]A discussion of the initial stress method is given in Appendix B.

These definitions include the displacement at the original crack tip, the crack tip radius, and the displacement at the elastic plastic boundary. [25]. The most often used, and perhaps the most consistent definition of CTOD is the displacement at the original crack tip. This definition of CTOD was adopted in this investigation.

Employing this definition of CTOD, an approach was developed for extracting CTOD from the finite element analysis. This approach is illustrated in Fig. (5.12). This figure represents the displacement of nodes perpendicular to the plane of the defect. Note that due to symmetry only one-half of the actual defect is represented. Indicated on Fig. (5.12) are the points at which COD and CTOD were measured. Note that the actual COD is twice the displacement of the node at the crack mouth, and that the CTOD is twice the distance to a line projected from the crack faces.

To extract the volumetric expansion from the finite element analysis, an approach was developed based on concepts typically employed in Computer Aided Design/Engineering (CAD/E). In CAD/E, it is often necessary to find the volume of an arbitrarily shaped, three-dimensional object. One approach often utilized is to subdivide the object into a number of tetrahedra [71]. The volumes of the tetrahedron are then calculated and summed to find the total object volume.

Following this approach to find the cylinder volume, tetrahedra were defined by the origin and three points on element faces as shown in Fig. (5.13). Note in this figure that two points of the tetrahedron (on the element face) correspond to nodal points while the remaining point (on the element face) corresponds to the center of the element face. The center point was defined using element shape functions to map the element center from local to global coordinates. The volume of the incremental tetrahedra were calculated using

$$V_{incr} = \frac{1}{6}[\{r_I\} \cdot (\{r_M\} \times \{r_C\})]$$

where $\{r_I\}$, $\{r_M\}$ and $\{r_C\}$ are position vectors of points on the element face.

To facilitate cylinder volume calculations, a FORTRAN program (see Appendix C) was written to perform the above vector operations and sum the incremental volumes. At each load step in this program, the nodal displacements are added to nodal coordinates to update the position vectors.

As noted in Chapter 2, there are typically two components which contribute to the volumetric expansion. The first component is elastic and due to cylinder compliance; the second component is plastic and due to deformation of the cylinder walls. Since the current recertification criterion is based on plastic expansion, it was necessary to isolate this component of expansion from total cylinder expansion. This operation was performed as shown in Fig. (5.14). This figure illustrates diagrammatically the change in cylinder volume (i.e., from the initial unpressurized volume) as a function of pressure. In Fig. (5.14), it can be seen that with increasing pressure there is an increase in the rate of change in cylinder volume. This non-linear behaviour results in permanent cylinder expansion since any unloading will occur along the elastic loading line. Hence, to calculate plastic expansion at each load, the elastic loading line was projected from the P–ΔV curve to $P = 0$.

5.2 Numerical Results

5.2.1 Crack Opening Displacement (COD)

Figure (5.15) shows the COD versus pressure for the 5 × 30 mm (deep long), 3.5 × 20 mm (intermediate) and 2 × 10 mm (shallow short) interior cracks; Fig. (5.16) shows the COD versus pressure for the corresponding exterior cracks[5]. From these figures it can be seen that significant differences exist in the growth of the COD over the range of crack sizes analysed. COD versus pressure for the shortest cracks is nearly linear. This suggests that for these cracks, yielding is relatively confined. In contrast, COD versus pressure for the largest cracks is approaching asymptotic with increasing pressure. This suggests that for these cracks, yielding is much more extensive.

Figure (5.17) shows the COD as a function of crack size at 20.69 MPa (3000 psi) (NGV cylinder service pressure). This figure shows that, as crack depth increases, COD varies more with crack length. Figure (5.17) illustrates the differences between COD for the interior and exterior defects. It was found that the COD for smaller exterior cracks is less than that for the corresponding interior cracks. The opposite of this trend is observed for larger cracks. These differences in COD between interior and exterior cracks can be explained in terms of the differences in secondary loading. Induced bending tends to close an internal crack and open an external crack. The faces of an internal crack however, are subject to internal pressure which tends to open the crack. From Fig. (5.17), it appears that when the crack size is small, loading due to internal pressure is more significant than induced bending. Hence, COD for small internal cracks is greater than for corresponding external cracks. When crack size is large however, induced bending becomes more significant. Hence, COD for large external cracks is greater than for large

---

[5]These crack sizes are plotted in Fig.s (5.15) and (5.16) (and elsewhere) to illustrate behaviour over the range of crack sizes analysed.

internal cracks.

Figure (5.18) shows the COD as a function of crack size at 34.48 MPa (5000 psi) (hydrostatic test pressure). This figure exhibits trends similar to those of Fig. (5.17). The secondary effects discussed previously are however, significantly more evident at 34.48 MPa (5000 psi) than at 20.69 MPa (3000 psi).

5.2.2 Development of the Plastic Zone

To quantify the extent of yielding and determine whether a condition of instability might be expected for larger cracks, the development of the plastic zone was analysed. Figures (5.19) and (5.20) show the percentage of the ligament that yields as a function of the COD for interior and exterior cracks. From these figures it can be seen that in several cases the plastic zone had extended to either the inner or outer wall of the cylinder. Both the size and location of the defect appear to influence the development of the plastic zone. Location of the defect, that is interior or exterior, appears to be particularly significant. This is most evident for the case of the intermediate size crack; the plastic zone extending from the exterior crack penetrates through the wall while the plastic zone extending from the interior crack did not.

It is of interest to note that the curves shown in Fig.s (5.19) and (5.20) are discontinuous. For each crack size, a point is reached in the development of the plastic zone at which the rate of change of COD decreases. The reason for this is not entirely clear. Comparison of Fig.s (5.19) and (5.20) with Fig.s (5.15) and (5.16) indicates that discontinuities in COD versus $r_p/(t - a)$ correspond roughly to points at which COD versus pressure becomes nonlinear.

Although of considerable interest, an in-depth study of the development of the plastic zone was beyond the scope of this investigation. This topic will be the subject of future work.

5.2.3 Crack Tip Opening Displacement (CTOD)

Figure (5.21) shows the CTOD versus pressure for the 5 × 30 mm, 3.5 × 20 mm, and 2 × 10 mm interior cracks; Fig. (5.22) shows the CTOD versus pressure for the corresponding external cracks. These figures exhibit trends similar to those discussed for the COD versus pressure; however the CTOD appears to increase somewhat more rapidly than the COD. This behaviour is attributed to blunting and stretching of the crack tip.

Figure (5.23) shows the CTOD as a function of crack size at 20.69 MPa (3000 psi) (NGV cylinder service pressure). Figure (5.24) shows corresponding results at 34.48 MPa (5000 psi) (hydrostatic test pressure). Note that as with the COD, the CTOD for cracks of the same depth varies more significantly as crack size increases. The effects of secondary loading can also be observed.

At 20.69 MPa (3000 psi) (Fig. (5.23)), the maximum CTOD for any of the cracks analysed is less than approximately 0.033 mm, indicating that none of the cracks investigated would be critical during service. (Recall that the critical CTOD for initiation of crack growth is estimated at 0.039 mm.) At 34.48 MPa (5000 psi) however, the CTOD of five of the cracked cylinders does exceed 0.039 mm[6]. Cylinders containing these cracks would therefore be expected to fail (rupture) during a hydrostatic test.

For each defect size analysed, failure pressure was predicted using the CTOD versus pressure plots. These predictions, based on the pressure at which CTOD becomes equal to 0.039 mm are listed in Table (5.2).

Further use was made of the CTOD versus pressure plots to predict the dimensions of defect which will lead to failure at 34.48, 37.92 and 41.37 MPa (5000, 5500 and 6000 psi). These defect dimensions are shown in Fig. (5.25). As will be seen in Chapter 8, the curve corresponding to failure at 34.48 MPa (5000 psi) is of particular interest, as it

---

[6]CTOD of the 2 × 15 mm cracks is only slightly less that the critical value and should, given numerical and experimental error, be considered critical.

predicts the defect dimensions which will lead to rupture type failure of a cylinder during a hydrostatic test.

5.2.4 Volumetric Expansion

Figure (5.27) shows the finite element modelling result for elastic expansion of a NGV cylinder. Also shown in Fig. (5.27) are the experimentally measured results. These results were obtained from hydrostatic tests performed on two as received (uncracked) NGV cylinders. Agreement between the predicted and measured results is within 5 % indicating that both the finite element model and that computational method used to calculate volumetric expansion were accurate.

Figure (5.28) shows the finite element results for plastic expansion of cylinders containing 5 × 30 mm, 3.5 × 20 mm and 2 × 10 mm interior defects. Figure (5.29) shows the results for cylinders containing corresponding exterior defects. Most significant is the magnitude of the results shown in these figures. Comparison of Fig.s (5.28) and (5.29) with Fig. (5.27) indicates that the plastic expansion was, in all cases, several orders of magnitude less than the cylinder elastic expansion. Note however that the plastic expansion for the larger defects was becoming asymptotic.

Figure (5.30) shows the plastic expansion as a function of crack size at 34.48 MPa (5000 psi) (recertification pressure). From this figure, it can be seen that the plastic expansion versus crack size follows a trend similar to the COD/CTOD versus crack size relationships. That is, the plastic expansion for a given crack depth varied increasingly as crack length increased. Also similar to the COD/CTOD results was that, in general, plastic expansion of cylinders containing exterior defects was greater than for interior cracks when defect depth size was large (i.e., $a \geq 3.5$mm, $c \geq 10$mm).

As noted in Chapter 2, current standards for NGV cylinder recertification require that a cylinder should be removed from service if the plastic expansion measured during

a hydrostatic test exceeds 10 % of the total (elastic plus plastic) expansion, i.e., when

$$\Delta V_{pl} > 0.10 \Delta V_{total} \tag{5.1}$$

Noting that $\Delta V_{total} = \Delta V_{el} + \Delta V_{pl}$, this criterion can be written

$$\Delta V_{pl} > 0.11 \Delta V_{el} \tag{5.2}$$

to give the volumetric expansion criterion in terms of elastic expansion.

Equation (5.2) can be used to predict which defects investigated would be considered tolerable under current standards for recertification. As noted, elastic expansions results (Fig. (5.27) predict that elastic expansion is 360 cc at hydrostatic test pressure (34.48 MPa (5000 psi)). This means that to be considered unfit for service under current standards, cylinder plastic expansion should exceed 40 cc. Plastic expansion results (Fig. (5.30)) however, predict plastic expansions that are significantly less (by a factor of 100) than this.

Thus, based the volumetric expansion criterion, finite element results indicate that for the crack size range investigated, all defects would be considered tolerable under the current standards for cylinder recertification.

Chapter 6

EXPERIMENTAL INVESTIGATION OF FULL SCALE BEHAVIOUR

In this stage of the investigation, a series of full scale hydrostatic tests were performed. These tests were conducted for several reasons. The primary reason was to gather data which could be used to verify numerical predictions of cylinder behaviour (failure pressures and volumetric expansions). The second reason for the large scale tests was to investigate the feasibility of an acoustic emission based recertification protocol for NGV cylinders.

6.1 Introduction to Acoustic Emission

Processes at the crack tip, such as sudden crack extension or plastic deformation release elastic energy. This energy is propagated in the form of longintudinal and transverse waves. As these waves approach and are reflected from a free surface, they cause finite displacement of the surface. This displacement can, with proper transducers and instrumentation, be measured. Because P- and S-waves are effectively sound waves in a solid medium, they are commonly referred to as acoustic emission.

In a manner analagous to seismology, acoustic emission techniques are based on the analysis/interpretation of the surface displacements which result due to remote processes (i.e., at the crack tip). The fundamental concept behind the approach is that acoustic emission can be used to quantify the severity of the emitting source (i.e., defect). To this end, a great deal of theoretical (e.g. [72]) and empirical (e.g. [18, 10]) research has been done in an attempt to correlate fracture mechanics parameters (i.e., stress intensity

factor, plastic zone size, etc.) with AE signal characteristics. While progress in this endeavor has been made, there is to date no unified approach to AE testing due to the variables which influence AE (material properties, loading, etc.) and AE detection (frequency response of sensors, acoustic coupling of sensors to structure, background noise, etc.). For this reason, interpretation of AE is often based on empirical correlations for a given configuration and the experience of the AE technician.

Despite noted drawbacks of AE testing, there are a number of advanges which make the method a desirable non-destructive testing technique. The primary advantage is the ability to passively monitor all regions of a structure remotely. This means, in the case of pressurized components with must be periodically hydrotested, that recertification can be done in-situ, eliminating the need for disassembly. This can mean a significant saving in cost due to the elimination of labour and component down-time.

While a great deal of research on AE of pressurized components has been performed, perhaps the most significant from the point of view of the present investigation, is that of Blackburn and Rana [18] and Barthélémy [10] who, independently, have studied the use of AE based recertification of seamless steel cylinders. Blackburn and Rana studied AE in DOT 3AAX and 3T cylinders. Employing a 40 dB threshold, these investigators were able to isolate flaws which, based on available fatigue growth rates, would grow to critical during the following inspection interval. Based on the strength of these findings, the U.S. Department of Transport currently permits the use of AE testing for recertification in lieu of hydrostatic testing. Barthélémy has studied AE of defects in a similar class of cylinders (in service in Europe) and noted the onset of AE from defects at pressures above approximately 1.5 × service pressure. While this investigator recommends use of AE in addition to a standard hydrotest, he notes that on the basis of AE test results, the recertification interval could be doubled.

Given the potential for application of AE techniques for recertification of NGV cylinders, it was decided to conduct a series of full scale AE tests prior to burst testing of cylinders. These tests are described in the following sections.

6.2 Experimental Setup and Procedure

6.2.1 Hydrostatic Testing Equipment

A Galiso Hydroclose Model MAK-6B hydrostatic testing system with automatic controls was used for pressurizing cylinders. This system, illustrated schematically in Fig. (6.1), consists of a test chamber and a control console, and utilizes an air driven two stage pump capable of delivering up to 68.95 MPa (10,000 psi) pressure. The test chamber is constructed of heavy gauge steel, a feature considered essential to provide protection in the event of cylinder failure during planned tests. Cylinders are suspended within the test chamber by means of a special high pressure spud attached to the lid of the test chamber. The lid itself is sealed in place by a pressurized rubber diaphram. The automatic controls of the system permit choice of a variety of loading sequences, including extended hold at a given pressure and cyclic pressurization/depressurization.

To facilitate planned AE tests, the test chamber of the Hydroclose unit was modified to permit passage of low noise signal cables from the cylinders to the Locan Acoustic Emission (AE) system (described in Sec. 6.2.2). The control console was also modified to permit acquisition of a pressure signal from the unit's pressure transducer.

6.2.2 Acoustic Emission Monitoring Equipment

A Physical Acoustics Corporation Locan AT based system was used to collect, and store acoustic emission (AE) data. This system is capable of collecting AE data from up to six channels, and parametric (voltage) inputs from up to four channels. Acoustic emission

data arrives at the Locan from sensors attached to the structure under investigation (see inset, Fig. (6.2)). These sensors are essentially displacement transducers which utilize a piezoelectric crystal to sense motion beneath a wear-plate. Various types of AE sensors, with different resonant frequencies are available; in this investigation, 150 kHz sensors, with integral 40 dB preamplifiers were employed.

Figure (6.3) shows the signal waveform of a typical acoustic emission event (or 'hit'). Also indicated on this figure are a number of parameters which quantify a hit; these parameters are:

Time of hit
The time of the first threshold crossing; recorded with a resolution of 250 nanoseconds.

Energy count
A measure of the area under the rectified signal envelope; recorded with a resolution of 1 energy count.

Duration
The time difference between the first and last threshold crossing; recorded with a resolution of 1 micosecond.

Counts
The number of threshold crossings between the first and last threshold crossings.

Rise Time
The time difference between the first threshold crossing and the signal peak; recorded with a resolution of 1 microsecond.

Amplitude
The amplitude of the AE signal referenced to 1 microvolt at the sensor; recorded with an accuracy of 1 dB.

The Locan unit processes each hit to extract these quantities and writes this information to a disk file. Hence, it is the characteristics of a hit (i.e., time of hit, energy count, duration, etc.), not the actual signal waveform which is recorded. Due to reflection or an anomalous waveform, it is possible in some instances to record the same hit twice. To reduce this possibility, the Locan provides several additional settings which can be used to isolate incoming hits; these parameters are:

Peak Definition Time (PDT)

The length of time that the system will continue to sample for a peak after detecting a local peak. Used to determine the true peak of the AE waveform; preset to within 1 microsecond.

Hit Definition Time (HDT)

The length of time that the system continues to sample for threshold crossings. Used to isolate one hit from the next; preset to within 1 microsecond.

Hit Lockout Time (HLT)

The length of time that the system 'locks out' after recording a hit. Used in conjuction with HDT to eliminate signal reflections; preset to within 2 microseconds.

The Locan AT operates under MS-DOS, with test settings such as threshold amplitude, HDT, etc. software selected. During a test, incoming data is written to a disk file, for later analysis, and to a CTR screen for real time analysis. The Locan software however, provides only limited support for post-processing. To overcome this limitation, specialized software was written in the C programming language to allow AE data to be downloaded from a Locan AT data file to an APOLLO DN 3000 workstation. This software also makes it possible to filter the AE data based on hit characteristics such as time of hit, energy, etc. and allows for more versatile batch style processing of data files.

6.2.3 Test Cylinder Preparation

Precracking

Six NGV cylinders in total were tested in the experimental investigation of large scale behaviour. Four of the cylinders were defective and two were 'as received'. All of the cylinders were manufactured by Faber Industries of Italy. The four cracked test cylinders (manufactured in 1981) had previously been in NGV service; the two uncracked control cylinders (manufactured in 1986) were new.

The four cracked cylinders each contained an external, axially oriented elliptical surface crack near the cylinder midpoint. These cracks were artificially introduced[1] by first electrode discharge machining a starter notch, then pressurizing under cyclic hydrostatic pressure (ranging between 2.41 and 20.69 MPa (350 and 3000 psi)) to produce a sharp fatigue crack. The four cracked cylinders were originally prepared and utilized as part of a parallel investigation[2] of acoustic emission sponsored by the Canadian Gas Association.

Before defects were introduced, the four test cylinders were visually examined. No evidence of external surface corrosion, denting, gouging or external cracks, other than those artificially introduced, was found. While it was not possible to perform a detailed examination of the interior of cylinders, it was apparent that some corrosion of the interior walls had occurred. After the cylinders were examined, they were designated Tanks A–D; Table (6.1) lists the corresponding fatigue precrack sizes[3].

Acoustic Emission Sensor and Clip Gauge Placement

The general arrangement of the experimental setup is illustrated diagrammatically in Fig. (6.2). As indicated, four sensors mounted in a rectangular pattern were employed in each AE test. This arrangement placed the known defect in the center of the pattern. Two sensors where located approximately 32 cm above the defect, each 90 degrees around the cylinder from the defect. The remaining two sensors were located approximately 32 cm below the defect, again 90 degrees around the cylinder from the known defect.

To ensure proper transmission of AE during the tests, the sensor mounting area was first cleaned (using a combination of coarse (150 grit) and fine (400 grit) sandpaper) to remove rust and paint. After cleaning the sensor area, sensors were mounted on the cylinders using specially designed magnetic holders. These holders applied the force required

---

[1] This operation was performed at PowerTech Labs, Inc.

[2] In which the author was involved.

[3] Measured during post burst test examination of the cylinders.

to ensure good transmission of AE signal from the cylinder to the sensor (approximately 2 lb$_f$), and eliminated lateral movement of the sensors due to cylinder expansion. To further ensure good transmission of AE, an ultrasonic couplant was applied to each sensor wear-plate before the sensors were mounted. Prior to each test, an AE pulser unit was used to check the response of each sensor and ensure proper acoustic coupling.

Crack opening displacement during the AE tests was monitored using a double cantilever type clip gauge. This gauge was fixed between two knife edges which were bonded to the cylinder with an epoxy adhesive. The distance between the knife edges (see Fig. (6.2)) was approximately 0.125 in. Output from the clip gauge was first run through a DC amplifier and then balanced using a bridge amplifying meter (BAM). After balancing the clip gauge, output from the BAM was fed to one of the Locan AT parametric channels. Before each test, the clip gauge was calibrated using a specially designed sliding block/caliper fixture.

Once the sensor and clip gauge placement and all calibrations were complete, the cylinder was hung inside the test chamber of the Hydroclose for testing. This chamber, as noted in Sec. 6.2.1, is constructed of heavy gauge steel. This feature, in addition to that of a rubber diaphram (to secure the lid of the test chamber) and flexible tubing (to supply pressure to cylinders), isolated the cylinders from extraneous noise which may have interfered with recording of the AE data.

With all instrumentation ready and the cylinder in place, the AE test was begun. These tests were performed in accordance with a specially designed procedure, which is discussed in the following section.

6.2.4 Procedure

The testing procedure was designed to provide information to assess both the feasibility of acoustic emission as an inspection technique, and the validity of hydrostatic test criteria.

Since both acoustic emission, and volumetric expansion are load history dependent, it was necessary to select suitable measurement techniques and correctly sequence the test procedures to ensure valid data. This made necessary a relatively elaborate procedure, which would normally not be required in standard cylinder recertification.

Acoustic Emission Test Procedure

A common observation in AE testing is relatively low levels of AE activity at loads less than a previously attained maximum. This effect (known as the Kaiser effect), was considered a constraint when designing the procedure, as it would degrade the quality of results which could be obtained from a cylinder subsequent to the application of given pressure. Hence, to realize greatest economy from available cylinders, it was necessary to design a procedure which would yield the maximum amount of data in a single test.

In designing the procedure, it was also recognized (for safety reasons), that in any potential AE recertification protocol, it would be desirable to utilize a pressure as close to operating pressure as possible. That is, it would be desirable to utilize a recertification pressure of 1.1 to 1.3 × operating pressure (22.75 to 26.89 MPa (3300 to 3900 psi)), rather that the current 1.67 × operating pressure (34.48 MPa (5000 psi)). Without a prior knowledge of the AE characteristics of NGV cylinders however, it was not possible to ascertain a suitable test pressure in advance. Hence, it was decided to monitor AE up to the current hydrostatic test pressure. To investigate the feasibility of utilizing a lower recertification pressure however, it was desirable to design a procedure which yielded valid AE data at a number of pressure increments which would be some fixed percentage (i.e., 110, 120, etc.) of normal service pressure.

The procedure ultimately decided upon, with consideration to gaining the maximum data from available cylinders and to assessing the feasibility of utilizing a lower recertification pressure, was to pressurize cylinders from 20.69 to 34.48 MPa (3000 to 5000 psi)

in increments of 2.07 MPa (300 psi). To eliminate residual AE at each pressure increment (i.e., Felicity ratio), cylinders were pressurized to each peak pressure a total of three times. Following this procedure resulted in an AE test which lasted approximately 2 hours.

Volumetric Expansion Test Procedure

To determine whether test cylinders would be recertified under current standards, it was necessary to determine both total (elastic plus plastic), and plastic cylinder expansion at 34.48 MPa (5000 psi). In practice (see Sec. 2.4.2), this would be done by noting the quantity of water displaced from the test chamber as a cylinder is pressurized to 34.48 MPa (5000 psi), and the volume of water displaced after the cylinder is depressurized. Since during planned AE tests, cylinders would be pressurized to 34.48 MPa (5000 psi), it was desirable to measure volumetric expansion simultaneously as the AE tests were being performed. Difficulties in isolating the piezoelectric sensors from water however, made this impossible.

Since previous pressurization to a given pressure does not affect elastic expansion measured during a subsequent pressurization, it was possible to measure elastic expansion of the cylinders following the AE tests. Elastic expansion therefore, was measured during a hydrostatic test performed after the AE tests. Plastic expansion of each cylinder was measured indirectly, by calculating the difference in cylinder volume before and after the AE tests. Cylinder volumes were determined from the mass of water which cylinders held. The following result was used to relate cylinder mass before and after the AE tests to plastic expansion.

$$\Delta V_{pl} = V_1 \left(\frac{\rho_1}{\rho_2} - 1 \right) - \frac{1}{\rho_2} \left(m_1 - m_2 \right)$$

where V_1 is the inital cylinder volume, given by

$$V_1 = \frac{m_1 - M}{\rho_1}$$

and M is the mass of the empty cylinder, m_1 is the mass of the cylinder and water before the AE test, m_2 is the mass of the cylinder and water after the AE test, ρ_1 is the density of water before the AE test, ρ_2 is the density of water after the AE test, and M is the mass of the cylinder. The densities ρ_1 and ρ_2 correspond to the temperature of the water when the cylinders were weighed.

Summary of Test Procedure

1. Visually inspect cylinder for damage (cuts, gouges, etc.) and corrosion.

2. Fill cylinder with water and allow temperature to equalize. Weigh cylinder and record water temperature.

3. Prepare cylinder for AE test (prepare sensor mounting area, mount knife edges, etc.).

4. Mount AE sensors, verify sensor output using artificial source (pulser), calibrate and mount clip gauge. Insert cylinder into test chamber.

5. Perform AE test according to the following schedule. Pressurize three times to each peak pressure and hold for two to five minutes at each peak pressure.

Pressure range	% of OP
0–20.69 MPa (0–3000 psi)	100
0–22.75 MPa (0–3300 psi)	110
0–24.82 MPa (0–3600 psi)	120
0–26.89 MPa (0–3900 psi)	130
0–28.96 MPa (0–4200 psi)	140
0–31.03 MPa (0–4500 psi)	150
0–33.10 MPa (0–4800 psi)	160
0–34.48 MPa (0–5000 psi)	167

6. Remove cylinder from test chamber. Remove sensors and clip gauge.

7. Reweigh cylinder and record water temperature (to determine plastic expansion).

8. Perform hydrostatic test (to determine elastic expansion).

Retest/Burst Test Procedure

To gather additional data which could be used to more clearly identify AE characteristics of defective NGV cylinders, it was decided to retest the defective cylinders. Due to unexplainably high levels of AE observed during the initial test of control Tank Z, it was also decided to retest this cylinder.

It was expected that, due to pressurization to 34.48 MPa (5000 psi) during the initial tests, some plasticity at the crack tip occurred. On the assumption that this plasticity would contribute to the Kaiser effect and significantly degrade AE activity during planned retests, it was decided to cycle cylinders between 2.41 and 20.69 MPa (350 and 3000 psi) to grow and sharpen the artificial defects. Hence, upon completion of the initial AE tests, each of the cracked cylinders was cycled between 2.41 and 20.69 MPa (350 and 3000 psi) pressure.

Fatigue cracking of cylinders was done in the Hydroclose unit described previously. After placing the cylinders in the test chamber, the automatic controls were set to pressurize to 20.69 MPa (3000 psi), hold for one second, and depressurize to 2.41 MPa (350 psi). The duration of each cycle was approximately one minute. During fatigue cracking, crack opening displacement was monitored via the clip gauge described previously. Pressurization/depressurization was continued until the clip gauge indicated an increase in crack opening displacement. This increase was taken as an indication that the crack had grown through the plastic zone, as due to crack tip plasticity, a latent period of constant crack opening displacement would be expected. An increase in crack opening diplacement was observed for all cylinders except Tank A, which was cycled 3000 times with no apparent crack growth.

When fatigue cracking of the cylinders was complete, the AE retests were performed according to the procedure described previously. At the end of the each AE retest, cylinders were monotonically pressurized to failure. During these burst tests, AE was monitored in the same manner as during cyclic AE tests. To perform the burst tests, the Hydroclose pump was simply allowed to operate at maximum capacity until the pressure was sufficient to rupture the cylinders.

6.2.5 AE Settings

As noted in Sec. 6.2.2, AE signals generated by an emission source are detected by means of sensors which are constructed to take advantage of the mechanical resonance of the a piezoelectric crystal. To maximize sensitivity when testing steels, 150 KHz sensors are typically employed. Hence, 150 kHz sensors with integral 40 dB preamplifiers were employed in the test performed in this investivation. To minimize noise, (i.e., to maximize the signal to noise ratio), shielded cables and Locan band-pass filters were employed.

Locan setting for the AE tests were selected on the basis of settings reported in the

literature (e.g. [18]) and through discussions with investigators at Powertech Labs, Inc.[4] These settings, listed below were held constant for all tests to ensure consistency in subsequent comparison the AE results for the different cylinders.

Amplitude threshold	30 dB
Gain	58 dB
PDT	500 microseconds
HDT	1000 microseconds
HLT	1000 microseconds
Time driven data sampling	2 seconds

A Locan AT threshold amplitude of 30 dB was selected to allow acquisition of events associated with crack tip plasticity, expected to have an amplitude of between 30–40 dB [18]. Preliminary AE test performed on discarded cylinders indicated that hydraulic noise (due to pressurization) was significant at low pressures due to associated high flow rates, but negligible above approximately 10.34 MPa (1500 psi). To eliminate this noise, all AE data obtained and presented in this report has been filtered to exclude any hits which occurred at pressures less than 6.90 MPa (1000 psi). The AE data presented has also been filtered to exclude any hits with a total count of one, since these hits were believed to be noise (i.e., a signal which just exceeded the threshold amplitude).

To allow the greatest flexibility in the data analysis, incoming AE data was not filtered on any AE characteristic or parametric input (e.g., pressure, COD) other than those noted above. In subsequent analysis, the C program (noted in Sec. 6.2.2) was employed to download and filter the AE results based on selected AE hit characteristics. As the data was obtained over three pressure cycles, data from each cycle was first isolated, analysed and then compared with data from the other cycles.

---

[4]During this investigation, AE testing of steel NGV cylinders was simultaneously performed at Powertech Labs, Inc. as part of the CGA sponsored project noted previously.

6.3 Results

6.3.1 Hydrostatic Test Results

Elastic expansion results for the four test cylinders and the two control cylinders are given in Fig. (6.4). The figure shows results scattered about two straight lines; one line representing the test cylinders, the other the control cylinders. Regression analysis on the data gives

$$\Delta V_{el} = (7.76 \times 10^{-2})p - 2.93$$

for the test cylinders, and

$$\Delta V_{el} = (6.99 \times 10^{-2})p - 2.28$$

for the control cylinders. Comparison of the slopes indicates that the compliance of the test cylinders is approximately 11 percent greater than that of the control cylinders. Maximum elastic expansions (elastic expansions measured at 34.48 MPa (5000 psi), 1.67 $\times$ service pressure) are given in Table (6.2); average values are 387.8 cc for the test cylinders and 348.5 cc for the control cylinders. The elastic expansion for which the cylinders would be rejected was calculated and found to be 472.6 cc. The measured maximums are all less than the rejection elastic expansion indicating that all test cylinders would be recertified using the elastic expansion failure criteria.

Plastic expansion results for three of the test cylinders and the two control cylinders are given in Table (6.3). (Temperature, used in the calculation of plastic expansion, was not measured for Tank A, therefore plastic expansion measurements for this tank have been omitted.) Plastic expansion ranged from 21.7 to 27 cc for the test cylinders and from 0 to 0.9 cc for the control cylinders. The insignificant plastic expansion of the control cylinders is due to the previous hydrostatic testing to 34.48 MPa (5000 psi) during quality control, prior to delivery as part of factory inspection. The rejection

plastic (10 % of total (elastic plus plastic) expansion) was calculated and is also listed in Table (6.3). Reviewing the results in this table indicates that all of the cylinders would be recertified under current CTC regulations as all measured plastic expansions are less than the corresponding rejection values.

6.3.2 Acoustic Emission Results

The AE data was analyzed and plotted in a number of ways in an attempt to identify a useful parameter or criteria for correlating the data to defect severity. The following sections present and compare the results, and identify areas where correlation and possible use as inspection criteria may be possible.

AE Hits Past Previous Pressure

As hit activity is often considered a parameter which correlates with defect severity, AE data was initially reviewed for trends in the number of hits up to peak pressure in each cycle. This analysis suggested that the Kaiser effect had occurred between cycles. This effect, as noted previously, tends to eliminate hit activity below a previously attained peak pressure. As the Kaiser effect had tended to eliminate hit activity below the previously attained pressure, it was deemed appropriate to plot and analyse hits past previous pressure. This approach was also considered more consistent, as it would effectively filter cycle to cycle variations of the Kaiser effect (i.e., cycle to cycle Felicity ratio).

Hits past previous pressure for the full amplitude range of hits (30 to 70 dB) for the initial test first, second and third cycles are plotted in Fig.s (6.5), (6.6) and (6.7) respectively; corresponding results for the retests are plotted in Fig.s (6.8), (6.9) and (6.10). (Note that the data from the initial test of cylinder A, the first test in the series, was tested at pressures based on an operating pressure of 24.13 rather that 20.69 MPa (3500 rather than 3000 psi) and that the points are at intervals of 2.41 MPa (350 psi) rather

than 2.07 MPa (300 psi)). Hits past previous pressure for the filtered amplitude range (40 to 70 dB) of hits are plotted in Fig.s (6.11) through (6.16).

Initial review of these figures does not yield any easily recognizable, generally increasing or decreasing trend. The results indicate a highly non-linear relationship between hits past previous pressure and peak pressure which is not reproduced from cycle to cycle or upon retesting the cylinders.

First cycle results

Focusing attention on intial test first cycle results for cylinders having approximately the same size defect (Tanks B, C, and D) shown in Fig. (6.5), it can be seen that there is no clear correlation between the results for the different cylinders. Varied levels of AE hits emitted by Tank D below 28.96 MPa (4200 psi) tended to increase above 28.96 MPa (4200 psi). This contrasts the low levels of AE hits emitted by Tank B (which contained a slightly larger defect that Tank D), which tended to increase in the midrange pressures and decrease again at higher pressures, and the relatively constant levels (20–30) of AE hits emitted by Tank C throughout the pressure range. Turning attention to the first cycle retest results shown in Fig. (6.8), it can be seen that there is some weak correlation between the results for the different cylinders. High levels of AE hits emitted by all cylinders at low pressures ($<\approx$24.82 MPa (3600 psi)) tended to decrease to some minimum in the midrange pressures and increase again at higher pressures.

Further review of the results in Fig.s (6.5) and (6.8) reveals that the levels of hits emitted by the control cylinders varied significantly. Relatively constant and low levels of AE hits emitted by Tank Y, contrast the varied and typically greater levels of AE hits emitted by Tank Z. Hits emitted by Tank Z tended to be high at low pressures, somewhat less in the midrange and greater again in the high pressure range. Comparison with the data for the cracked cylinders indicates that activity of Tank Z was for the most part,

greater than that of cracked cylinders.

At the particular time of testing Tank Z, mechanical problems with the hydrotest pump were experienced and it was suspected that the high levels of AE observed might be due to mechanical noise. After full reconditioning and testing of the pump, Tank Z was retested [5]. Comparing figures for the inital and retest results indicates that during the retests, Tank Z reproduced the high levels and varied distribution of AE observed during the initial tests. In an attempt to resolve this clearly anomalous behaviour, Tank Z was sectioned and microscopically examined following the tests. This examination revealed a large number of microcracks in the wall on the interior of the cylinder. These microcracks are believed responsible for the high levels of AE observed for Tank Z.

Disregarding Tank Z results, it can be seen with reference to Fig.s (6.5) and (6.8) that control (Tank Y) cylinder AE hits emitted were generally less than the cracked cylinder AE hits emitted. This suggests, although far from conclusively, that some threshold level of AE hits exists. Additionally, the general trend for cracked cylinder AE hits emitted to reach some minimum in the midrange pressures (at $\approx$28.96 MPa (4200 psi)), and subsequently increase suggests that cracked cylinder response is different from uncracked cylinder response, as this trend was not observed in Tank Y results. While there is a need for more substantiative results, these observations clearly enhance the potential for hits past previous pressure as an inspection criterion.

An analysis of initial and retest first cycle amplitude filtered to retain only those hits between 40 and 70 dB (Fig.s (6.11) through (6.14)) indicates reduced levels of AE hits, and thus suggests that the majority of hits emitted were of relatively low amplitude. These results however, still do not reveal a clear trend or threshold level of AE hits. While the relevence of filtering the data cannot be established, it clearly reduces and

---

[5]As Tank Z was retested, retest results for this cylinder appear with retest results for the cracked cylinders in all the figures referred to in this chapter.

condenses the results and thus may in itself have merit.

Second and third cycle results

These results, shown in Fig.s (6.6) and (6.7) (initial tests) and Fig.s (6.9) and (6.10) (retests), indicate a significant reduction in AE hits past previous pressure emitted by all cylinders throughout the pressure range. In comparison to the results for the cracked cylinders, relatively few hits were emitted by Tank Y. This would appear to support earlier comments that a threshold in hits past previous pressure may exist. Although there are several data points (e.g., Tank B (24.82 MPa (3600 psi)), Tank C (28.96–33.10 MPa (4200–4800 psi)), Tank D retest (22.75 and 33.10 MPa (3300 and 4800 psi)), etc.) which clearly do not support this observation, it would appear to enhance the potential for utilizing AE hits past previous pressure as an inspection criterion.

Unfortunately, amplitude filtering of second and third cycle results (Fig.s (6.12), (6.13), (6.15) and (6.16)) as described previously did not yield any further useful information. As identification of a threshold level becomes even more uncertain, amplitude filtering is for these results, not beneficial.

AE Hit Rate/Pressure Increase

Further review of hit data suggested that hit rates (slopes of hits versus pressure curves) near peak pressures might have potential as an inspection criterion. This concept appeared justified on the grounds that hit activity which might occur due to crack extension would likely occur near peak pressure of a given cycle, whereas hit activity resulting from other sources (i.e., corrosion) would likely occur throughout the pressure cycle.

Adopting this approach, hit rates for the final 0.69 MPa (100 psi) of each cycle were calculated. The results of these calculations for the first, second and third cycles of the initial and retests (full amplitude range) are shown in Fig.s (6.29) through (6.34). Review

of these results indicates that, during the initial tests, hit rates of the cracked cylinders varied with peak pressure and that hit rate generally decreased with each load cycle. During the retests, hit rates of the cracked cylinders (all cycles) tended to decrease in the midrange pressures, reach some minimum (between approximately 26.89 and 28.96 MPa (3900 and 4200 psi)) and then increase. Hit rates during these tests tended either to remain at the same level or to increase with each cycle. Hit rates of Tank Y (initial tests), were in general less than those of the cracked cylinders during either the initial or retests.

To resolve discrepancies between the initial and retest results, hit rates were calculated using only amplitude filtered hits (i.e., hit amplitude greater than 40 dB). The results of these calculations (hit rates for the first, second and third cycles of the initial and retests) are shown in Fig.s (6.35) through (6.40). Reviewing these figures suggests that amplitude filtering is not a valid approach, as it provides little in the way of isolating trends. Moreover, comparing Fig.s (6.29) through (6.34) which indicate a general decrease and subsequent increase in hit rate, with Fig.s (6.35) through (6.40) suggests that filtering hit amplitude may actually obscure existing trends.

Comparing initial test results for control Tank Y with those for the cracked cylinders indicates that a threshold level of hit rate might exist. While this observation enhances the potential for use of hit rate as an inspection criterion, inconsistencies between initial and retest results, and difficulties in identifying threshold hit rate, clearly diminish the potential.

AE Hold Time Hits

Hold time hits is a parameter which reflects time dependent energy release processes (i.e., creep, plastic flow, incremental crack growth, strain hardening, etc.) at the crack tip. To assess the potential for use of this parameter as an inspection criterion, the number

of hits which occurred during the hold times were plotted as functions of peak cyclic pressure.

Review of initial and retest results for the first, second and third cycles (Fig.s (6.17) through (6.22)) indicates that fewer hold time hits were emitted during the initial tests than in the retests, and that hold time hits emitted by the cracked cylinders were, in general, markedly greater in number than those emitted by the control cylinders. This promising observation however, is offset by the sporadic hold time hits emitted by the control cylinders and the fact that there are no discernible trends in the number of hold time hits emitted by either the cracked or control cylinders. Further, while hold time hits emitted by the cracked cylinders are in general greater than those emitted by the control cylinders, it is evident that the presence of a crack is in itself no guarantee that hold time hits will occur (e.g. cylinder B containing a relatively large defect produced little or no hold time hits) This fact, combined with the sporadic hold time hits emitted by the control cylinders, clearly diminishes the potential for hold time hits as an inspection criterion.

To further analyse the results, amplitude filtered (i.e., amplitude greater than 40 dB) hold time hits were plotted as shown in Fig.s (6.23) through (6.28). Reviewing these figures indicates that amplitude filtering reduced the results, but did not serve to isolate any new trend which might increase the potential for hold time hits as an inspection criterion.

AE Amplitude Distribution

Hit amplitude is considered a parameter which correlates in some manner with defect severity. On the basis that hit amplitude might serve as an inspection criterion, AE hit amplitude distributions were plotted for the three cycles of the initial and retests. A review of these distributions indicated that the greatest frequency of hits was in the 30

to 45 dB amplitude range, and that no cycle to cycle trend existed. On the basis of these observations, only first cycle, 30 to 45 dB amplitude distributions will be presented.

Amplitude distributions for the first cycle of initial and re-tests are plotted for each peak pressure in Fig.s (6.41) through (6.56). A review of these figures indicates that peak frequencies varied significantly between cylinders and from peak pressure to peak pressure. Generally, initial test distributions indicate that relatively low amplitude hits were emitted. This contrasts retest amplitude distributions which indicate a significant increase in higher (i.e. 40 dB or greater) amplitude hits. Although this behaviour might be attributed to slightly larger defects during the retests, it is not believed that crack lengths were increased enough during fatigue cracking to influence amplitude distributions in this manner.

While it was anticipated that as the pressure increased, the amplitude distributions of the cracked cylinders would change to reflect some crack tip process such as plastic deformation or crack growth, it is apparent upon examining the results that no clearly defined change in fact occurred. Based on the observation that peak frequency generally fell in the 32 to 40 dB range, it would appear that amplitude distribution is independent of both crack size and peak pressure. (As noted, there were also no significant change in amplitude distributions over the three cycles.) Unfortunately, comparison of the amplitude distributions of the control cylinders with those of cracked cylinders does not serve to illuminate any trend which might be useful in further explaining results for the cracked cylinders. This clearly makes identification of specific amplitude characteristics for cracked cylinders difficult, and reduces the potential for amplitude distribution as an inspection criterion.

6.3.3 Burst Test Results

Burst Test Cummulative AE Hits

Cumulative AE hits emitted during the burst tests of Tanks A, B, C and D are plotted against pressure Fig.s (6.57) through (6.61). The data in these figures indicates relatively low levels of hits below 34.48 MPa (5000 psi), and an asymptotic increase in hits between 34.48 MPa (5000 psi) and failure pressure. A reasonable explanation for the relatively low levels of activity below 34.48 MPa (5000 psi) is the Kaiser effect. The asymptotic increase in AE hits is believed due to plastic deformation at and beyond the defects, and throughout the cylinder wall, as post-test examination of the cylinders indicated that considerable yielding had occurred prior to failure. Although impossible to confirm at this point, it appears that there is a significant correlation between the volume of yielded material and AE hit activity. If this correlation can be confirmed and quantified, it may serve as a means of predicting impending failure during AE recertification.

Burst Test Amplitude Distribution

Amplitude distributions for the cylinder burst tests are shown in Fig. (6.62). This data shows the AE data obtained as the cylinder was pressurized to failure pressure, however, as the cylinder had been previously pressurized to a pressure of 34.48 MPa (5000 psi), the majority of AE hits were emitted at pressures above 34.48 MPa (5000 psi). Thus, the amplitude distribution for the burst tests are dominated by the characteristics of the AE which occurred near failure, rather than proportionally over the full pressure range approaching failure. Reviewing this data indicates that the amplitude frequency peak occurs at approximately 32 dB, notably lower than previously observed in the lower pressure level testing. However, unlike the previous results, this burst data indicates a definite and consistent amplitude distribution and peak amplitude frequency. If, as

suggested in the previous section, AE hits emitted near failure were due to plastic defor-
mation, it would appear from these observations that a definite amplitude threshold for
plastic deformation exists.

Burst Test Crack Opening Displacement

As has been noted, the primary reason for adopting the CTOD approach in this in-
vestigation was that CTOD can be measured experimentally. This meant that actual
failure pressures during planned burst tests could be compared to analytical and numer-
ical predictions of failure pressure. Comparison of experimental results with analytical
and numerical predictions was considered important, as this would make it possible to
assess the accuracy and/or conservatism of these predictions.

Burst tests were performed by monotonically pressurizing each of the four test cylin-
ders containing defects to failure. Failure pressures and initial defect sizes for the cylinders
are given in Table (7.1). Failure of all of the cylinders during burst tests was due to prop-
agation of cracks that initiated at the artificial defects (see Figs (6.63) through (6.65)).
Post-test examination of fracture surfaces revealed that in all cases, some yielding had
occurred in the ligament, and in the wall beyond the ends of defects. The fracture sur-
face of the ligament and slightly beyond the ends of defects (2 to 3 mm) was parallel to
the plane of defects, indicating that growth of defects through-wall occurred under plane
strain conditions. Beyond this plane strain region, a 45 degree shear type fracture sur-
face was observed indicating that growth of defects parallel to the cylinder axis occurred
under plane stress conditions.

To assess the suitability of the CTOD approach in predicting failure of NGV cylinders,
burst test COD was plotted against pressure as shown in Fig.s (6.66) through (6.69). The
trend in these figures, as can be seen, is a distinct change in slope (an increase in the rate
of change in COD with pressure) prior to failure. This indicates that yielding beyond the

ends of defects and/or some stable crack growth (tearing) was occurring prior to failure. As noted above, post-test examination of the fracture surfaces indicated that yielding had occurred.

Chapter 7

CORRELATION BETWEEN EXPERIMENTAL AND NUMERICAL/ANALYTICAL FAILURE PREDICTIONS

In this chapter, failure pressures measured during the large scale tests are compared with failure predictions based both on the numerical results discussed in Chapter 5 and with failure predictions made using several of the analytical methods discussed in Chapter 3 (i.e., the CTOD design curve, the CEGB R6 method, the Battelle empirical analysis and a plastic collapse approach). The intent of this comparison is to illustrate the relative accuracy/conservatism of the various approaches to predict burst type failure of NGV cylinders. Following the comparison of experimental and numerical/analytical results, a failure criterion is identified which defines limiting defects dimensions for rupture during a hydrostatic test (i.e., at 34.48 MPa (5000 psi)). In the chapter which follows, it will be shown that this criterion relates directly to limitations of current standards for NGV recertification.

7.1 Finite Element Failure Predictions

To verify and assess the accuracy of the numerical approach adopted in this investigation, finite element results presented in Chapter 5 were used to predict COD versus pressure behaviour and failure pressures for the four test cylinders. Because the defect sizes in the test cylinders differed from those considered in the finite element analysis, it was necessary to interpolate (and in the case of Tank A, extrapolate) the numerical results. To facilitate this interpolation (/extrapolation), all surface defect dimensions were first

converted to equivalent through-wall defect dimensions using Fig. (3.15).

The predicted COD versus pressure have been plotted against observed COD versus pressure in Fig.s (6.66) through (6.69). Considering various sources of error, agreement between the numerical and measured results in the initial portion of the COD versus pressure relationships is good. The difference between these results (slopes of COD versus pressure) is less than 5 % for Tanks A and D (Fig.s (6.66) and (6.69)) and approximately 25 % for Tanks B and C (Fig.s (6.67 and (6.68)). One factor that may have contributed to differences between numerical and observed results is internal surface corrosion of the test cylinders; because corrosion reduces wall thickness, the $\bar{c}/t$ ratio of the test cylinders was likely somewhat greater than that assumed in the finite element model. This greater $\bar{c}/t$ ratio would explain the tendency in Fig.s (6.66) through (6.69) for observed COD to be greater than predicted COD.

Although initially (i.e., at lower pressures) in good agreement, differences between the predicted and observed results for all of the cylinders tends to increase as measured COD begins to increase rapidly prior to failure. It is believed that this disagreement may be due to stable crack growth occurring prior to failure of the test cylinders. Since no mechanism for stable crack growth was incorporated into the finite element model, this behaviour would not be predicted. It should be noted that differences between the measured and predicted results in both the initial and later portions of the COD versus pressure were most significant for the tanks containing the two largest defects (Tanks B and C).

To determine the accuracy and estimate the conservatism (if any) of the finite element failure predictions made in Chapter 5, numerical CTOD results were again interpolated (/extrapolated) to determine failure pressures based on the critical CTOD (0.039 mm) from the small scale testing. These predicted failure pressures (indicated on Fig.s (6.66)

through (6.69) and listed in Table (7.1)) have been plotted against actual failure pressures in Fig. (7.1)[1]. Based on the observed burst pressures, three of the four finite element/CTOD failure predictions are conservative. Predicted failure pressure for Tank A however, was 73.09 MPa (10,600 psi); although plotted on Fig.(7.1) for completeness, the point representing Tank A should in fact lie to the right of the position indicated. This cylinder however, contained a relatively small (2.2 × 5.6 mm) defect. Subsequent analyses utilizing different approaches (to be discussed) suggest that for this cylinder, plastic collapse mechanisms may have played a more significant role.

7.2 PD 6493 Failure Predictions

In Sec. (3.6.1), it was noted that the CTOD design curve has been incorporated into a design standard, PD 6493, which can be used to assess structural integrity of a wide range of structural components. To assess the applicability of PD 6493 to NGV cylinders, this standard was to predict failure pressures of the four test cylinders.

It should be noted that while it is possible to calculate failure pressure using PD 6493, the intent of the standard is to provide a means of calculating allowable defect dimensions based on given loading, structural geometry, etc. Because of a number of assumptions made in the development of the CTOD design curve, allowable defect dimensions will typically be much smaller (by up to a factor of 2.5) than critical defect dimensions. For this reason, failure pressure calculated using PD 6493 are typically very conservative.

In accordance with the PD 6493 (the CTOD design curve approach), a non-dimensional CTOD, Φ, was calculated for each defect size using

$$\Phi = \frac{CTOD_c E}{2\pi \sigma_Y \bar{c}}$$

---

[1] During the burst test of Tank D, AE data saturation caused collection of pressure data to cease at approximately 41.37 MPa (6000 psi). Actual failure pressure for this cylinder was visually noted to be 43.78 MPa (6350 psi).

where $\bar{c}$ is the length of an equivalent through-wall defect determined using Fig. (3.15). This non-dimensional CTOD was equated to the CTOD design curve, defined by

$$\Phi = \begin{cases} \left(\frac{\varepsilon}{\varepsilon_Y}\right)^2 & \frac{\varepsilon}{\varepsilon_Y} \leq 0.5 \\ \frac{\varepsilon}{\varepsilon_Y} - 0.25 & \frac{\varepsilon}{\varepsilon_Y} > 0.5 \end{cases} \tag{7.1}$$

where, from elementary theory of elasticity, the relationship between $\varepsilon/\varepsilon_Y$ and pressure, p, is given by

$$\frac{\varepsilon}{\varepsilon_Y} = \frac{pR}{\sigma_Y t}\left(1 - \frac{1}{2}\nu\right)$$

In Sec. (3.6.1) it was noted that if load is sufficient to cause yielding of the remaining ligament, PD 6493 requires that a surface defect by recategorized as through-wall defect. Accordingly, if

$$\sigma > \sigma_F \left(1 - \frac{a}{t}\right) \tag{7.2}$$

a surface defect of length $2c$ must be reclassified as a through-wall defect of length $2c$.

In making failure predictions as was done here, a defect cannot be recategorized on the basis of Equ. (7.2) since it is σ (i.e., p) which is unknown. Hence, for each cylinder, failure pressure was calculated based on both an equivalent and a recategorized crack length. The results of these calculations are shown in Fig. (7.2). The open symbols in this figure represent failure pressures calculated using a crack length $2c$ (i.e., recategorized defects) and the solid symbols represent failure pressures calculated using a crack length $\bar{c}$ (i.e., equivalent through-wall defects determined from Fig. (3.15)).

The results presented in Fig. (7.2) indicate that, with the exception of one point, the CTOD design curve provides conservative estimates of failure pressure. As can be seen, recategorization of defects significantly effects the conservatism of these predictions; failure pressures based on the recategorized defect length are on average approximately 50 % lower than those based on an equivalent defect length. It is of note that the Tank A prediction based on an equivalent crack length is non-conservative by a considerable

margin while the prediction based on an equivalent crack length is conservative. This would appear to support earlier comments that plastic collapse played an important role in the failure of this cylinder.

7.3 CEGB R6 Method Failure Predictions

To assess the applicability of the R6 method (discussed in Sec. 3.6.2) to NGV cylinders, the approach was used to predict failure pressures of the four test cylinders. It should be noted (as with PD 6493) that while possible to predict failure pressures using the R6 method, the intent of the approach is to provide a means of assessing safe operating loads for structures containing defects.

In accordance with the R6 method, the non-dimensional parameters (assessment points)

$$K_r = \frac{K}{K_{\mathrm{Ic}}} \tag{7.3}$$

$$S_r = \frac{p}{p_{collapse}} \tag{7.4}$$

were calculated for each test cylinder based on measured failure pressure and defect dimensions. K_r was calculated using the finite element results for stress intensity factors of Newman and Raju [75] and $K_{\mathrm{Ic}} = 105$ MPa$\sqrt{\mathrm{mm}}$ (from Ref. [13]). S_r was calculated using the plastic collapse solution given in Sec. 7.4.

The results of the calculations are shown in Fig. (7.4). Recalling that failure is predicted for any point that lies outside the assessment line, it can be seen that the R6 method correctly predicts failure of all the cylinders. Because both K_r and S_r are linear functions of load, the ratio OP/OP' (see construction for Tank B in Fig. (7.4)) is the ratio of actual to predicted failure pressure. Using constructions similar to that shown for Tank B, predictions of failure pressure were made for the four test cylinders. These

predictions are listed in Table (7.1). Comparing the predictions for the different cylinders suggests that the R6 method is most conservative for larger defects.

7.4 Plastic Collapse Failure Predictions

To investigate the accuracy of plastic collapse failure predictions, the collapse pressure for each cylinder was calculated using the solution given by Turner [92]. This solution (see Sec. (3.5.1) is

$$p_{collapse} = \frac{t}{R}\sigma_F \frac{t/a - 1}{t/a - 1/m} \tag{7.5}$$

where

$$m = 1 + \left[\frac{0.263(2c)^2}{Rt}\right]^{\frac{1}{2}}$$

and σ_F is the material flow stress assumed here to be

$$\begin{aligned}
\sigma_F &= \frac{1}{2}(\sigma_Y + \sigma_U) \\
&= 885 \text{ MPa}
\end{aligned}$$

The results of the calculations, shown in Fig. (7.3), indicate that for the range of defect sizes investigated, a plastic collapse approach provides a relatively accurate and conservative method for predicting burst failure of these cylinders. Noting that the point representing Tank A is within several percent of the actual failure pressure, it would appear that for small defects in NGV cylinders, plastic collapse methods are most appropriate.

7.5 Battelle Empirical Analysis

The Battelle empirical analysis (see Sec. (3.6.3)), has successfully been applied to the analysis of failure of seamless compressed gas cylinders containing cracks [28, 29]. To

assess the accuracy of this approach, it was used to predict failure pressures of the four test cylinders.

The failure criterion for the Battelle analysis is

$$\ln \sec \frac{\pi}{2} \frac{M_P \sigma_\theta}{\sigma_F} = \frac{K_{1c}^2 \pi}{8c' \sigma_F^2} \tag{7.6}$$

where M_P is

$$M_P = \frac{1 - a/t}{1 - a/M_T t}$$

and M_T

$$M_T = \left(1 + 1.255 \frac{c'^2}{Rt} - 0.0135 \frac{c'^4}{R^2 t^2}\right)$$

The term K_{1c} is the material plane stress fracture toughness and the term c' is an equivalent crack length (for surface defects) This crack length is defined in terms of the actual surface area of a part-through defect. For an elliptical defect

$$2c' = \frac{1}{2}\pi c$$

In the original formulation of the Battelle empirical analysis described in Ref. [68], plane stress fracture toughness K_{1c} was determined using a correlation with Charpy impact energy C_V. Since in the present study neither K_{1c} nor C_V data was available, a correlation between K_{1c} and plane strain fracture toughness (K_{Ic}) was employed. This correlation, from Ref. [18], is

$$K_{1c} = K_{Ic} \left[1 + \frac{1.4}{t^2} \left(\frac{K_{Ic}}{\sigma_Y}\right)^4\right]^{1/2}$$

and gives, for $K_{Ic} = 105.5$ MPa$\sqrt{\text{m}}$, $\sigma_Y = 822$ MPa and $t = 7.8$ mm, the value $K_{1c} = 205$ MPa$\sqrt{\text{m}}$.

Using the above relationships, the non-dimensional parameters $M_P \sigma_\theta / \sigma_F$ and $K_{1c}^2 \pi / 8c' \sigma_F^2$ were calculated for each test cylinder at the observed failure pressure. The results of the

calculations have been plotted in Fig. (7.5) along with the failure criterion expressed by Equ. (7.6). As can be seen, there is very good agreement (less that 2.5 % difference) between the experimental results and the curve which predicts failure.

It can also be seen in Fig. (7.5) that for all the experimental points, $K_{1c}^2 \pi / 8 c' \sigma_F^2 > 4$. Maxey [68] has suggested that when this is the case, failure is predominantly flow stress controlled. For this behaviour, the failure criterion expressed by Equ. (7.6) can be written

$$M_P \sigma_\theta = \sigma_F \qquad (7.7)$$

Based on the limited experimental results of this investigation, it appears that this simple equation may provide an acceptable failure criterion for NGV cylinders.

7.6 Choice of an Acceptable Failure Criterion for NGV Cylinders

7.6.1 Comparison of Fracture Mechanics Based Failure Predictions

The fracture mechanics based failure predictions discussed in the last section have been summarized in Table (7.1). A review of this table indicates that, with the exception of Tank A, numerical CTOD and CTOD design curve predictions of failure pressure are conservative (i.e., less than the observed failure pressures). Plastic collapse and R6 failure predictions are also conservative. Battelle empirical analysis predictions are slightly non-conservative.

Focusing attention on the conservative failure predictions, it can be seen that CTOD design curve and R6 predictions are somewhat more conservative than the finite element CTOD (ignoring Tank A) and plastic collapse failure predictions. Comparing the finite element CTOD and plastic collapse predictions indicates that, with the exception of Tank A, the finite element CTOD predictions are more accurate.

If the Tank A prediction is ignored, the overall accuracy and conservatism of the finite element CTOD failure predictions for Tanks B, C, and D supports use of the CTOD

approach to predict failure of NGV cylinders. As has been noted, Tank A contained a relatively small defect. The relative accuracy of the plastic collapse failure prediction for Tank A supports the view that this cylinder failed due to plastic collapse. This suggests that for small defects in NGV cylinders, plastic collapse analysis is appropriate.

Given the experimental support for use of the finite element CTOD approach for larger defects and a plastic collapse approach for smaller defects, it is interesting to further analyse the failure predictions made using these two approaches. Comparing the failure predictions made using the two approaches indicates that, with the exception of Tank A, plastic collapse predictions are slightly more conservative than the finite element CTOD predictions. This observation can be explained with the aid of a simple example. For a wide plate with a through thickness defect subject to remote tension, the expressions for failure stress are

$$\sigma_c = \frac{\text{CTOD}_c E \sigma_F}{\sqrt{\pi c}} \tag{7.8}$$

for elastic-plastic behaviour and

$$\sigma_c = \left(1 - \frac{c}{W}\right) \sigma_F \tag{7.9}$$

for fully plastic behaviour. If these expressions are plotted as functions of c/W as shown in Fig. (7.6), it can be seen that they cross and that to the right of the intersection (the largest range of c/W), the CTOD failure stress is most conservative. To the left of the intersection however, because materials cannot support infinite stress, plastic collapse failure stress is most conservative.

Based on the conservatism of plastic collapse failure predictions with respect to the numerical CTOD failure predictions, it would appear that the defect sizes in the test cylinders correspond roughly to the intersection of the two curves shown in Fig. (7.6). Recalling that Tank A contained a relatively small defect (see Table (6.1)), the point

representing this cylinder would (notionally) lie to the left of those representing the other cylinders. This would explain, given the asymptotic behaviour of the CTOD failure stress, why predicted failure pressure of Tank A is highly non-conservative.

7.6.2 Limiting Defect Sizes for Rupture of NGV Cylinders During a Hydrostatic Test

In the chapter to follow, an assessment is made of the ability of current standards for NGV cylinder recertification to ensure in-service cylinder integrity. For reasons which will become apparent, it was necessary, in making this assessment, to predict the defect dimensions which will lead to cylinder failure during a hydrostatic test.

In Sec. (5.2.3) numerical CTOD estimates of critical defect dimensions were employed to develop a set of curves (see Fig. (5.25)) which define critical defect dimensions (i.e., $a \times 2c$) at 34.48, 37.92 and 41.37 MPa (5000, 5500, and 6000 psi). Based on experimental support for the finite element CTOD approach, it was deemed appropriate to utilize the curve corresponding to 34.48 MPa (5000 psi) to predict the dimensions of defects which will lead to failure during a hydrostatic test. The observation that the CTOD approach may be non-conservative for small defects however, suggested that the lower region of the curve be modified. Accordingly, a curve which defines critical defect dimensions at 34.48 MPa (5000 psi) was also developed using the plastic collapse solution given by Equ. (7.5). This curve, and the CTOD based curve are plotted Fig. (7.7).

Noting that in this figure points which lie on or to the right of a respective curve represent defect dimensions which will lead to failure at 34.48 MPa (5000 psi), it can be seen that although the curves overlap, there are ranges of defects sizes for which one approach predicts failure and the other does not. As expected, plastic collapse predicts failure for relatively deep and short defects. This approach does not predict failure however, for a considerable range of shallower, longer defects (i.e., $a <\approx 5$ mm,

$2c >\approx 15$ mm). For this range of defect size, the numerical CTOD approach provides a more conservative estimate of critical defect size.

Since it is considered desirable to utilize a single curve to define critical defect dimensions at 34.48 MPa (5000 psi), a curve bounding both the critical CTOD and plastic collapse curves was constructed. This curve is plotted in Fig. (7.8) along with the dimensions of the defects analysed in the numerical and experimental investigations. As can be seen, the failure curve predicts failure of cylinders containing several of the numerical defect dimensions. Further, it can be seen that the modified curve correctly predicts no failure for the experimental cylinders. These observations, in conjuction with numerical and experimental plastic expansion results are of considerable importance from the point of view of of assessing current standards for NGV cylinder recertification. This assessment is discussed in the following chapter.

Chapter 8

ASSESSMENT OF THE CURRENT STANDARDS FOR RECERTIFICATION OF NGV CYLINDERS

8.1 Summary of Findings

In Chapter 1 it was noted that steel NGV cylinders must be recertified for service every five years. It was also noted in Chapter 1 (and further in Chapter 2) that the standards currently used to assess cylinder integrity are based on cylinder performance during a hydrostatic test. According to these standards, a cylinder is considered unfit for further service if (during a hydrostatic test) either:

1. plastic (permanent) volumetric expansion exceeds 10 % of the total (elastic plus plastic) cylinder expansion at 34.48 MPa (5000 psi) (1.67× service pressure), or,

2. the cylinder ruptures (bursts or leaks).

These hydrostatic test criteria, it will be recalled, are designed to ensure that reductions in wall thickness which may have occurred during service (due to environment) have not significantly degraded cylinder integrity. The second criterion, cylinder rupture, recognizes the existence of localized forms of damage such as cracks, and is intended to remove from service any cylinder containing a defect which may lead to failure during service. This criterion however, is not based on any quantitative fracture mechanics assessment of the various forms of sub-critical crack growth which can occur during NGV cylinder service. Several studies (discussed in the following section) which have examined sub-critical crack growth in NGV cylinders indicate that it is possible for some

112

part-through defects to grow through-wall within a five year period. The results of these studies further make it possible to predict the dimensions of a defect which will grow through-wall within a five year period (the length of time a cylinder remains in service following recertification).

Given that current standards for cylinder recertification are not based on any accepted fracture mechanics approach, it is reasonable to question whether the hydrostatic test criteria (i.e., 1 or 2 above) are adequate to ensure on-going cylinder integrity. Clearly, any recerification procedure must be capable of removing from service any cylinder which contains a defect which will grow to critical within five years. The goal of this investigation has been to address this question.

To this point in the discussion, the behaviour of defective (cracked) NGV cylinders during a hydrostatic test has been analysed and quantified. Based on numerical results (which are supported by experimental results), this behaviour can be summarized as follows:

1. Permanent Expansion

   Permanent (plastic) volumetric expansion of cylinders containing no other form of damage other than a crack is significantly less than 10 % of total volumetric expansion. Numerical results indicate that plastic expansion of a cylinder containing a defect as large as as 5 × 30 mm, is of the order of 1 % of total expansion.

2. Cylinder Rupture

   Burst failure of cylinders containing defects can occur during a hydrostatic test. Numerical CTOD results (in conjunction with small scale critical CTOD results) (modified by a plastic collapse approach for smaller defects) indicate that a range of defect dimensions exists (see Fig. (7.8)) which will lead to failure at 34.48 MPa (5000 psi).

To illustrate the significance of these findings, it is useful to consider a hypothetical hydrostatic test to recertify cylinders containing defects of the dimensions analysed in the numerical portion of the study. Several cylinders containing defects of these dimensions would rupture during such a test. The defect sizes of these cylinders are identified in Fig. (7.8), where the dimensions of defects analysed have be overlaid on the modified CTOD/plastic collapse failure curve discussed in Sec. 7.6.2. Cylinders which would not rupture, would be considered fit for service. This is because, as noted above, permanent volumetric expansion would be less than 10 % of total expansion. These cylinders would be recertified and returned to service. It should be noted that, based on observed volumetric expansion and failure pressures, all of the experimental cylinders would also be considered fit for service based on current standards.

Defects in cylinders returned to service would however, be subject to environmental and loading conditions which promote various forms of sub-critical crack growth. Studies which have investigated this form of degredation are discussed in the following section.

8.2 In-Service Failure

8.2.1 Subcritical Crack Growth

The potential for subcritical crack growth in NGV cylinders has been the subject of several investigations. An initial study considered the effects of environment [11]. In this study, the susceptability of NGV cylinder steel to sulphide stress cracking was investigated using the NACE[1] test method. The study concluded that, based on current contractual limits for natural gas contaminants and nominal service loads, NGV cylinder steel is not particularly susceptable to sulphide stress cracking.

Later studies have investigated the effects of alternating load. In on-going research

---

[1]National Association of Corrosion Engineers

at Powertech Labs, Inc. [1, 13, 14] which has involved both small and large scale testing, fatigue crack growth rates have been determined for NGV cylinder material. In a study which involved large scale testing, artificial axial defects were introduced into four cylinders. Of the four cylinders, one was monotonically loaded to failure. Three of the cylinders were cyclically loaded between pressures of 2.41 and 24.13 MPa (350 and 3500 psi) (the typical range of NGV service pressures) until fatigue cracks originating from either the artificial or natural defects grew through the cylinder wall, causing leakage of the pressurizing medium (water). During these large scale tests, crack growth in both the depth and length direction was monitored. The data obtained was fitted to relationships to predict crack growth rate and flaw shape development. These relationships were then used to construct curves to predict crack growth as a function of initial defect size (Fig. (8.1)) and the size of defect that will grow through the cylinder wall within the five years (an estimated 6500 refueling cycles) that a cylinder remains in service before the next scheduled recertification (Fig. (8.2)).

It should be noted that Fig.s (8.1) and (8.2) were constructed based on fatigue crack growth rates measured in an inert (air or water) environment. In more recent studies [12, 15] of sub-critical crack growth in NGV cylinder material, the combined effects of the natural gas environment and alternating load (including frequency and overload effects) have been investigated. In these studies, which involved measurement of fatigue crack growth rates in small scale specimens in a simulated natural gas environment, it was concluded that fatigue growth rates in a natural gas environment can be up to 60 times greater than those in air. This finding suggests that actual in-service fatigue crack growth rates in NGV cylinder may be significantly greater than those predicted by Fig.s (8.1) and (8.2). To date however, this has not been confirmed by any large scale studies of fatigue crack growth in a simulated natural gas environment.

8.2.2 Expected Mode of In-Service Failure

Sub-critical crack growth of a surface defect in a pressurized component can, in general, lead to one of two conditions. The growing surface crack can reach a critical size, resulting in instability and fast fracture (rupture) at the nominal service load. Alternately, the surface crack can grow through the cylinder wall before becoming critical. This latter condition, known as 'leak before break' (LLB) is most desirable as it makes detection of the defect possible. Removal of the component from service, or repair can be initiated before instability occurs.

Numerical CTOD results discussed in Sec. 5.2.3 (see Fig. (5.24)) indicate that, even for relatively large cracks (i.e., 5 × 30 mm, CTOD at maximum NGV service pressure (20.69 MPa (3000 psi)) is less than the critical CTOD for initiation of crack growth. These results suggest that in-service rupture of cylinders should not occur.

In the fatigue studies cited previously (i.e., Ref. [13]) it was found during the large scale tests that cylinders failed in LLB mode. Based on this observation, it was concluded that NGV cylinders fail in LLB mode. This conclusion was subsequently supported in Ref. [14] on the basis of a correlation between plane stress and plane strain fracture toughness.

8.3 Limitations of Current Standards for NGV Cylinder Recertification

To illustrate the limitations of the current standards for NGV cylinder recertification, the defects sizes (numerical and experimental) have been plotted in Fig. (8.2). From this figure, which defines defect dimensions which will grow through-wall within a five year period, it can be seen that all but two (Run 12 and Tank A defects) would lead to failure sometime during service.

The eleven cylinders containing defects which would grow through-wall should be

considered unfit for further service at time of recertification. It was noted in Sec. (8.1) however, that under current hydrostatic test criteria (i.e., permanent volumetric expansion/cylinder rupture) only four of these eleven cylinders (Run 01, 02, and 05) would be considered unfit for further service. A summary of the the two modes of cylinder failure (i.e., rupture in hydrostatic test versus in-service failure) is given in Table (8.1).

In view of the possibility that cylinders containing some defects can pass hydrostatic inspection yet still fail in service, it must be concluded that current standards for cylinder recertification are inadequate to ensure on-going cylinder integrity. To quantify the range of defects for which hydrostatic test criteria are inadequate and summarize the major findings of this investigation, the curves in Fig.s (7.8) and (8.2) have been overlaid as shown in Fig. (8.3). Recalling that defect dimensions to the right of Curve A lead to rupture of cylinders during a hydrostatic test, defect dimensions to the left of this curve will be considered tolerable under current standards for NGV cylinder recertification. Since defect dimensions to the right of curve B lead to in-service failure within five years, the defect dimensions in the hatched region represent those defects for which current standards provide no assurance of NGV cylinder integrity.

8.4   Interior versus Exterior Defects

In closing this chapter it should be noted that Fig. (8.3) was derived from results for exterior defects in NGV cylinders. A similar, and in fact stronger, conclusion as drawn in the previous section can however be made for interior defects. This can be shown if it is recalled that Curve A of Fig. (8.3) bounds the finite element CTOD solution for shallow, long defects and the plastic collapse solution for deep, short defects.

From Fig. (5.25) (discussed in Chap (5)), it can be seen that there are only several percent difference between CTOD failure curves for interior and exterior defects. For

practical purposes, these differences can be ignored. With regard to the plastic collapse solution used to construct Curve B, a comparison of plastic collapse solutions for interior and exterior defects given in Ref. [27] indicates that, for a given failure pressure, the defect dimensions of an interior crack required for failure will vary only slightly (several percent) from those of an exterior crack required for failure. Hence, given that both the CTOD failure curve and plastic collaspe failure curve vary only slightly for interior versus exterior defects, Curve A in Fig. (8.3) can, for practical purposes, be considered applicable to both interior and exterior defects.

With regard to Curve B, it should be noted that interior defects in NGV cylinders are in direct contact with the natural gas environment. This implies, based on the studies (cited in Sec. 8.2.1) of the combined effects of environment/loading, that Curve B (derived from fatigue crack growth rates measured in an inert environment), may in fact be conservative. Due to the effects of environment, it is reasonable to expect that for interior defects, Curve B will lie closer to the lower left-hand region of Fig. (8.3). If this is the case, a greater range of defect dimensions will lead to in-service failure than is predicted by the existing Curve B. This would mean that the current hydrostatic test criteria provide even less assurance against in-service cylinder failure than concluded on the basis of exterior defects.

Chapter 9

CONCLUSIONS AND RECOMMENDATIONS

9.1 Conclusions

This thesis has investigated current standards for NGV cylinder recertification in view of fracture mechanics methodologies which address the severity of defects that may develop during NGV cylinder service. Based on the results of this investigation, a number of general conclusions (i.e., related to numerical and experimental results) and more specific conclusions (i.e., related to current and potential standards for NGV cylinder recertification) can be drawn. These conclusions are:

9.1.1 General conclusions

1. A finite element model was developed in this investigation to predict volumetric expansion of uncracked NGV cylinders. Comparison of volumetric expansion results obtained from this model with experimental results has shown that the model is accurate to within ±5 %.

2. A finite element model was developed to model the behaviour of cracked NGV cylinders and was utilized to predict COD and CTOD for a range of defect sizes. This model provides a powerful tool for assessing the significance of defects that can develop during NGV cylinder service and indicates that:

   (a) Length of defects in NGV cylinders strongly influences COD and CTOD. Defects as shallow as 2 mm can lead to failure (at hydrostatic test pressure) if

119

length is in excess of 30 mm. The dependence of CTOD on defect length increases non-linearly as defect depth increases.

(b) For equivalent defect sizes, maximum crack severity shifts from an internal surface crack location for small crack dimensions to an external surface crack location for relatively larger defect dimensions as a result of induced bending effects. This trend was also reflected in the extent of plastic volumetric expansion of interior and exterior cracked cylinders.

(c) The plastic expansion of a cylinder containing defects that will grow to critical within five years is negligible; this expansion is, even for relatively large defects, of the order of accuracy that can be attained during an actual hydrostatic test, i.e. ± 0.5 cc.

(d) Hydrostatic test pressure ($1.67 \times$ service pressure) is sufficient to cause rupture of some cylinders containing defects that will grow to critical during a five year inspection interval (based on available fatigue crack growth rates). There is, however a significant range of defect sizes that will not lead to rupture during a hydrostatic test, but will lead to failure during a five year inspection interval. Cylinders containing these defects will be considered fit for service under current standards for cylinder recertification since, as noted above, plastic expansion will be less than 10 % of total expansion.

3. Burst test results for cracked NGV cylinders indicate that, over the range of defect sizes investigated, the CTOD approach provides accurate and conservative predictions of failure pressure for large defects and non-conservative predictions of failure pressure for relatively small defects. For small defects, a plastic collapse analysis provides conservative predictions of failure pressure. Over the range of defect sizes analysed, the CTOD design curve (i.e., PD 6493) and R6 failure assessment

diagram provide somewhat more conservative predictions of failure pressure than the CTOD approach; in contrast, the Battelle empirical analysis provides slightly non-conservative predictions of failure pressure.

4. Acoustic emission results for cracked, previously in-service NGV cylinders (i.e., hits past previous pressure, hold time hits, hit rates and amplitude distributions) do not, in general, follow any readily recognizable trends which can be be correlated to defect severity. Trends in this data do indicate however, potential criteria which may be used in NGV cylinder recertification and hence justify further research in the application of acoustic emission techniques to NGV cylinder recertification (see Sec. 9.2).

5. Acoustic emission hit activity results indicate that event rate increases non-linearly as failure is approached.

9.1.2 Specific conclusions regarding current and potential standards for NGV cylinder recertification

1. The potential exists for localized defects such as cracks to develop during NGV cylinder service. Further, there exists a range of defect size which will, through mechanisms of sub-critical crack growth (fatigue and stress corrosion cracking) grow through-wall within a five year inspection interval. Cylinders containing such defects should be considered unacceptable and be removed from service. Current standards for cylinder recertification which are based on hydrostatic test (volumetric expansion) failure criteria however, do not specifically address the significance of such defects. Given that internal corrosion which may occur during service more strongly influences volumetric expansion, it should be concluded that:

(a) Plastic volumetric expansion of a cylinder containing a defect (as measured during a hydrostatic test) will provide no useful information regarding the presence, or the severity of a defect.

(b) The current hydrostatic test rejection criterion (plastic expansion less than 10 % of total expansion) is not an adequate safeguard against in-service failure due to subcritical crack growth.

2. The CTOD method has been shown to accurately predict fracture behaviour in pressurized NGV cylinders and should therefore be considered a viable technique for defining critical and allowable defect sizes for NGV cylinder structural integrity assessment.

3. A combined CTOD/plastic collapse failure assessment curve has been developed which accurately predicts the defect sizes for which the current hydrostatic test criteria are insufficient to guard against in-service failure.

9.2 Recommendations

Based on the the results of this investigation and the above conclusions, there follows a number of recommendations to ensure NGV cylinder integrity, and for further work.

9.2.1 Recommendations to ensure NGV cylinder integrity

1. Current standards for NGV cylinder recertification, which are designed to ensure minimum wall thickness, should be revised in a manner which incorporates a fracture mechanics assessment of localized defects; specifically, the standards should be revised to ensure that at time of recertification:

    (a) Localized defects in cylinders are located and quantified.

    (b) Cylinders containing defects equal to or greater than the dimensions indicated in Fig. (8.2) should be removed from service[1].

9.2.2 Recommendations for further work

1. Work should be continued to specifically define an AE inspection technique and criteria for in-situ inspection. Due to the complexity of the technique, fundamental studies to isolate AE characteristics of various types of cylinder degredation must be conducted prior to this work, specifically:

    (a) Further large scale acoustic emission tests should be performed utilizing cylinders in 'as-received' condition. Such tests would hopefully eliminate variables (such as internal corrosion or possible unknown defects) which are believed to have contributed to difficulties in identifying trends in AE data from tests performed in this investigation.

---

[1]If the current five year inspection interval is to be retained.

(b) Acoustic emission tests utilizing small scale specimens should be performed. Such tests would make it possible to more closely control conditions and eliminate extraneous sources of AE leading to a better correlation between crack tip processes and AE activity (i.e. hold time hit dependence on fatigue crack growth rate).

2. In accordance with (1a) above, further research should be undertaken to develop the acoustic emission technique as a means to locate and quantify potential defects, specifically:

(a) Acoustic emission wave speed characteristics should be investigated and quantified.

(b) Existing location software (which relies on wave speed data as input) should be utilized, and if necessary modified (i.e., for wave speed dependence) to exploit and develop its potential as a means of locating defects in NGV cylinders.

3. Experimental and numerical work should be continued to more precisely define the role of stable crack growth in failure behaviour of NGV cylinder material, specifically:

(a) The numerical models should be further developed to incorporate a mechanism for stable crack growth. This would allow predictions which could be used to to further refine the definition of allowable crack size for inspection of NGV cylinders.

(b) Crack growth should be monitored in future small scale and/or large scale testing of NGV cylinders utilizing a technique such as D.C. potential drop.

Bibliography

[1] Akhtar, A. and Heenan, J., "Advanced On-Board Storage of Natural Gas," presented at the ASME Energy Sources Technology Conference and Exhibit held in Houston, TX, 1989.

[2] Amatuiz, H. and Seeger, T., "Problems of Numerical CTOD Analyses," in *The Crack Tip Opening Displacement in Elastic-Plastic Fracture Mechanics*, K. H. Schwalbe (ed.), Springer-Verlag, 1985, pp. 21–44.

[3] American Society for Testing and Materials, ASTM E399 (Standard Test Method for Plane-Strain Fracture Toughness of Metallic Materials), American Society for Testing and Materials, 1978.

[4] Anderson, D. M., "Fracture Toughness Parameters and Elastic-Plastic Analysis of Non-Moderate Fracture Conditions Using Finite Element Methods," *Eng. Frac. Mech.*, Vol. 5, 1973, pp. 223–240.

[5] Anderson, T. L., Leggatt, R. H. and Garwood, S. J.,"The Use of CTOD Methods in Fitness for Purpose Analysis," in *The Crack Tip Opening Displacement in Elastic-Plastic Fracture Mechanics*, K. H. Schwalbe (ed.), Springer-Verlag, 1985, pp. 281–313.

[6] Anderson, T. L., McHenry, H. I. and Dawes, M. G., "Elastic-Plastic Fracture Toughness Tests with Single-Edge Notched Bend Specimens," in *Elastic-Plastic Fracture Test Methods: The User's Experience, ASTM STP 856*, E. T. Wessel and F. J. Loss (ed.s), American Society for Testing and Materials, 1985, pp. 210–229.

[7] Aurich, D., Brocks, W., Noack, H. D. and Vieth, H., "Fracture Mechanics Analysis of a Pressure Vessel with a Semi-Elliptical Surface Crack Using Elastic-Plastic Finite Element Calculations," *Fracture Mechanics: Sixteenth Symposium, ASTM 868*, M. F. Kanninen and A. T. Hooper (ed.s), American Society for Testing and Materials, 1985, pp. 617–631.

[8] Barsoum, R. S., "On the Use of Isoparametric Finite Elements in Linear Elastic Fracture Mechanics," *Int. J. Num. Meth. Eng.*, Vol. 10, 1976, pp. 25–37.

[9] Barsoum, R. S., "Triangular and Quarter-Point Elements as Elastic and Perfectly-Plastic Crack Tip Elements," *Int. J. Num. Meth. Eng.*, Vol. 11, 1977, pp. 85–88.

[10] Barthélémy, H., "Periodic Inspection of Compressed Gas Cylinders and Tubes–Flaw Detection Using Acoustic Emission Testing," *J. Pres. Ves. Tech.*, Vol. 110, 1988, pp. 161–167.

[11] B. C. Hydro Research and Development, "Sulphide Stress Cracking Resistance of CNG Cylinder Materials," CGA Task Force Report, B. C. Hydro Research and Development, Surrey, B. C., 1986.

[12] Bhuyan, G. S., "Fatigue Crack Growth in NGV Steel Cylinders," presented at the NGV Seminar in Vancouver, B. C., 1989.

[13] Bhuyan, G. S., and Akhtar, A., "Assessment of Integrity of the On-Board NGV Steel Cylinders," presented at the International Conference on Structural Engineering in Los Angeles, CA, 1989.

[14] Bhuyan, G. S., Akhtar, A., Webster, C. T. L., Wong, J. Y. and Carter, D. H., "Integrity of On-Board and Ground Storage NGV Cylinders," presented at the Second International Conference, *NGV '90* in Buenos Aires, Argentina, 1990.

[15] Bhuyan, G. S. and Brezden, W. J., "Influence of Environmental Variables and Intermittent Overloadings on Fatigue Crack Growth in On-Board NGV Cylinder Steel," *Int. J. Pres. Ves. and Piping*, Vol. 40, 1989, pp. 139–149.

[16] Blackburn, W. S., "Calculation of Stress Intensity Factors at Crack Tips Using Special Finite Elements," source unknown.

[17] Blackburn, W. S. and Hellen, T. K., "Calculation of Stress Intensity Factors in Three Dimensions by Finite Element Methods," *Int. J. Num. Meth. Eng.*, Vol. 11, 1977, pp. 211–229.

[18] Blackburn, P. R. and Rana, M. D., "Acoustic Emission Testing and Structural Evaluation of Seamless, Steel Tubes in Compressed Gas Service," *J. Pres. Ves. Tech.*, Vol. 108, 1986, pp. 234–240.

[19] Bleackley, M. H. and Luxmoore, A. R., "Comparison of Finite Element With Analytical and Experimental Data for Elastic-Plastic Cracked Problems," *Int. J. of Fracture*, Vol. 22, 1983, pp. 15–39.

[20] Burdekin, F. M. and Dawes, M. G., "Practical Use of Linear Elastic and Yielding Fracture Mechanics With Particular Reference to Pressure Vessels," Proc. I. Mech. E. Conference, 1971, pp. 28–37.

[21] Burdekin, F. M. and Stone, D. E. W., "The Crack Opening Displacement Approach to Fracture Mechanics in Yielding Materials," *Journal of Strain Analysis*, Vol. 1, No. 2, 1966, pp. 145–153.

[22] British Standards Institution, BS 5447 *(Methods of Test for Plane Strain Fracture Toughness (K_{Ic}) of Metallic Materials)*, British Standards Institution, London, 1977.

[23] British Standards Institution, BS 5762 *(Crack opening displacement (COD) testing)*, British Standards Institution, London, 1979.

[24] British Standards Institution, PD 6493 *(Guidance on some methods for the derivation of acceptance levels for defects in fusion welded joints)*, British Standards Institution, London, 1980.

[25] Broek, D., *Elementary Engineering Fracture Mechanics*, Martinus Nijhoff Publishers, Dordrecht, 1986.

[26] Canadian Transport Commission, CTC Regulations of the Subject of Periodic Retesting of Compressed Gas Cylinders (Section 73.34(e)), Canadian Transport Commission, Hull, P.Q.

[27] Chell, G. G., "Elastic-Plastic Fracture Mechanics," in *Developments in Fracture Mechanics-I*, G. G. Chell (ed.), Applied Science Publishers, London, 1979, pp. 67–105.

[28] Christ, B. W., "Analysis of the Pneumatic Burst of a Large Seamless Steel Pressure Vessel in Natural Gas Service," Fracture and Deformation Division, National Bureau of Standards, Washington, DC, 1979.

[29] Christ, B. W., Smith, J. H. and Hicho, G. E., "Fracture Analysis of a Pneumatically Burst Seamless-Steel Compressed Gas Container," *Fracture Mechanics, ASTM STP 677*, C. W. Smith (ed.), American Society for Testing and Materials, 1979, pp. 734–745.

[30] Coates, W. M., "The State of Stress in Full Heads of Pressure Vessels," *Trans. ASME*, 1930, pp. 190–204.

[31] Compressed Gas Association, Pamphlet C-1 *(Methods for Hydrostatic Testing of Compressed Gas Cylinders)*, Compressed Gas Association, Arlington, VA, 1975.

[32] Compressed Gas Association, Pamphlet C-2 *(Cylinder Service Life-Seamless, Steel, High-Pressure Cylinders)*, Compressed Gas Association, Arlington, VA, 1981.

[33] Compressed Gas Association, Pamphlet C-6 *(Standard for Visual Inspection of Compressed Gas Cylinders)*, Compressed Gas Association, Arlington, VA,

[34] Compressed Gas Association, Pamphlet C-8 *(Standard for Requalification of DOT-3HT Cylinders)*, Compressed Gas Association, Arlington, VA, 1985.

[35] Cook, R. D. *Concepts and Applications of Finite Element Analysis,* John Wiley and Sons, New York, 1974.

[36] Cowan, A., "The Approach to Analysis of Significance of Flaws in ASME Section III and Section IV," source unknown.

[37] Dawes, M. G., "Elastic-Plastic Fracture Toughness Based on the COD and J-Contour Integral Concepts," in *Elastic-Plastic Fracture, ASTM STP 668,* J. D. Landes, J. A. Begley, and G. A. Clarke (ed.s), American Society for Testing and Materials, 1977, pp. 307–333.

[38] Dawes, M. G., "The COD Design Curve," *Advances in Elasto-Plastic Fracture Mechanics,* L. H. Larsson (ed.), Applied Science Publishers, London, 1979, pp. 279–300.

[39] Dawes, M. G. and Kamath, M. S., "The Crack Opening Displacement (COD) Design Curve Approach to Crack Tolerance," *Tolerance of Flaws in Pressurized Components,* I. Mech. E. Conference Publications, 1978, pp. 21–27.

[40] Delale, F. and Erdogan, F., "Application of the Line-Spring Model to a Cylindrical Shell Containing a Circumferential or Axial Part-Through Crack," *ASME Journal of Applied Mechanics,* Vol. 49, 1982, pp. 97–102.

[41] deLorenzi, H. G., "Elastic-Plastic Analysis of the Maximum Postulated Flaw in the Beltline Region of a Reactor Vessel," source unknown.

[42] Dugdale, D. S., "Yielding of Steel Sheets Containing Slits," *J. Mech. Phys. Solids,* Vol. 8, 1960, pp. 100–104.

[43] Erdogan, F., Irwin, G. R. and Ratwani, M., "Ductile Fracture of Cylindrical Vessels Containing a Large Flaw," *Cracks and Fracture, ASTM STP 601,* American Society for Testing and Materials, 1976, pp. 191–208.

[44] Erdogan, F. and Kibler, J. J., *Int. Journ. of Fracture Mech.,* Vol. 5, 1969, pp. 229.

[45] Erdogan, F. and Ratwani, M., "Fracture of Cylindrical and Spherical Shells Containing Cracks," *Nuclear Engineering and Design,* Vol. 20, 1972, pp. 265–286.

[46] Erdogan, F. and Ratwani, M., "Plasticity and Crack Opening Displacement in Shells," *Int. Journ. of Fracture Mech.,* Vol. 8, 1972, pp. 413–426.

[47] Folias, E. S., "On the Theory of Fracture of Curved Sheets," *Engineering Fracture Mechanics,* Vol. 2, 1970, pp. 151–164.

[48] Gordon, J. R., "A Comparison of Methods of Calculating Stress Intensity Factors for Cracks in Pipes and Thin Walled Cylinders," *Int. J. Pres. Ves. and Piping*, Vol. 36, 1989, pp. 341–358.

[49] Greer, J. B., "Factors Affecting The Sulfide Stress Cracking Performance of High Strength Steel," Corrosion /73—A Forum Devoted Exclusively to the Protection and Performance of Materials, Anaheim, CA, 1973, pp. 55/1–55/22.

[50] Hahn, G. T., Sarrate, M. and Rosenfield, A. R., "Criteria for Crack Extension in Cylindrical Pressure Vessels," *Int. Journ. of Fracture Mech.*, Vol. 5, 1969, pp. 187–210.

[51] Hellen, T. K., "Numerical Methods in Fracture Mechanics," in *Developments in Fracture Mechanics-I*, G. G. Chell (ed.), Applied Science Publishers, London, 1979, pp. 145–181

[52] Henshell, R. D., and Shaw, K. G., "Crack Tip Finite Elements are Unnecessary," *Int. J. Num. Meth. Eng.*, Vol. 9, 1975, pp. 495–507.

[53] Irwin, G. R., "Plastic Zone Near a Crack and Fracture Toughness," Proc. 7th Sagamore Conf., 1960, p. IV-63.

[54] Irwin, G. R., "Crack-Extension Force for a Part-Through Crack in a Plate," *ASME Journal of Applied Mechanics*, 1962, pp. 651–654.

[55] Johnson, A. R., "On the Accuracy of Polynomial Finite Elements for Crack Problems," *Int. J. Num. Meth. Eng.*, Vol. 17, 1981, pp. 1835–1842.

[56] Kane, R. D., "The Roles of H_2S in the Behaviour of Engineering Alloys," *Symp. on the Effects of Hydrogen Sulphide on Steels*, Edmonton, Alta, The Canadian Institute of Mining and Metallurgy, 1983, pp 2–6.

[57] Kelley, F. S., "Mesh Requirements for the Analysis of a Stress Concentration by the Specified Boundary Displacement Method," Proceedings of the Second International Computer Engineering Conference held Aug. 15–19, 1982 in San Diego, CA. (Computer Engineering Division, ASME.)

[58] Kiefner, J. F., Maxey, W. A., Eiber, R. J. and Duffy, A. R., "Failure Stress Levels of Flaws in Pressurized Cylinders," in *Progress in Flaw Growth and Fracture Toughness Testing, ASTM STP 536*, American Society for Testing and Materials, 1973, pp. 461–481.

[59] King, R. B., "Elastic-Plastic Analysis of Surface Flaws Using a Simplified Line-Spring Model," *Engineering Fracture Mechanics*, Vol. 18, No. 1, 1983, pp. 217–231.

[60] Kobayashi, A. S., "A Simple Procedure for Estimating Stress Intensity Factor in Region of High Stress Gradient," *Significance of Defects in Welded Structures*, T. Kanazawa and A. S. Kobayashi (ed.s), University of Tokyo Press, 1974, pp. 127–143.

[61] Kobayashi, A. S., Polvanich, N., Emery, A. F. and Love, A. J., "Inner and Outer Cracks in Internally Pressurized Cylinders," *ASME Journal of Pressure Vessel Technology*, 1977, pp. 83–89.

[62] Kobayashi, A. S., Ziv, M. and Hall, L. R., "Approximate Stress Intensity Factor for an Embedded Elliptical Crack Near Two Parallel Free Surfaces," *Int. Journ. of Fracture Mech.*, Vol. 1, 1965, pp. 81–95.

[63] Kumar, V. and German, M. D., "Studies of the Line-Spring Model for Nonlinear Crack Problems," *ASME Journal of Pressure Vessel Technology*, Vol 107, 1985, pp. 412–420.

[64] Kumar, V., German, M. D. and Schumacher, B. I., "Analysis of Elastic Surface Cracks in Cylinders Using the Line-Spring Model and Shell Finite Element Method," *ASME Journal of Pressure Vessel Technology*, Vol. 107, 1985, pp. 403–411.

[65] Levy, N., Marcal, P. V., Ostergren, W. J. and Rice, J. R., "Small Scale Yielding Near a Crack in Plane Strain: A Finite Element Analysis," *Int. Journ. of Fracture Mech.*, Vol. 7, 1971, pp. 143–156.

[66] Maddox, S. J., "An Analysis of Fatigue Cracks in Fillet Welded Joints," *Int. Journ. of Fracture*, Vol. 11, 1975, pp. 221–243.

[67] Martin, A. R., "A Review of Current Design Formulae Applied to High Pressure Aluminium Alloy Gas Containers," I. Mech. E. Publication, 1980.

[68] Maxey, W. A. Kiefner, J. F. Eiber, R. J. and Duffy, A. R. "Ductile Fracture Initiation, Propagation, and Arrest in Cylindrical Vessels," *Fracture Toughness: Proceedings of the 1971 National Symposium on Fracture Mechanics, Part II, ASTM STP 514*, American Society for Testing and Materials, 1972, pp. 70–81.

[69] McClintock, F. A., "Plasticity Aspects of Fracture," in *Fracture–An Advanced Treatise, Vol. III (Engineering Fundamentals and Environmental Effects)*, H. Liebowitz (ed.), Academic Press, New York, 1971, pp. 47–225.

[70] McHenry, H. I., Read, D. T. and Begley, J. A., "Fracture Mechanics Analysis of Pipeline Girthwelds," *Elastic-Plastic Fracture, ASTM STP 668*, J. D. Landes. J. A. Begley and G. A. Clarke (ed.s), American Society for Testing and Materials, 1979, pp. 632–642.

[71] Mullineux, G., *CAD: Computational Concepts and Methods*, pp. 186–188.

[72] Nabil, M., "Macroscopic Origins of Acoustic Emission," *Nondestructive Testing Handbook, Vol. 5-Acoustic Emission Testing*, American Society for Nondestructive Testing, 1987, pp. 45–61.

[73] Pandey, R. K., Pratap, C. R. and Chinadurai, R., "Significance of Rotational Factor r in CTOD Determination and the Effect of Material and Loading Geometry on r," *Eng. Frac. Mech.*, Vol. 31, No. 1, 1988, pp. 105–118.

[74] Parks, D. M., "The Inelastic Line-Spring: Estimates of Elastic-Plastic Fracture Mechanics Parameters for Surface-Cracked Plates and Shells," *ASME Journal of Pressure Vessel Technology*, Vol. 103, 1981, pp. 246–254.

[75] Raju, I. S. and Newman, J. C., "Stress-Intensity Factors for Internal and External Surface Cracks Cylindrical Vessels," *ASME Journal of Pressure Vessel Technology*, Vol. 104, 1982, pp. 293–298.

[76] Ranta-Maunus, A. and Talja, H., "Elasto-Plastic Analysis of a Cracked Ductile Cylinderical Pressure Vessel," *Int. J. Pres. Ves. and Piping*, Vol. 13, 1983, pp. 169–182.

[77] Read, D. T., McHenry, H. I. and Petrovski, B., "Elastic-Plastic Models of Surface Cracks in Tensile Panels," *Experimental Mechanics*, Vol. 29, No. 2, 1989, pp. 226–230.

[78] Rice, J. R., "A Path Independent Integral and the Approximate Analysis of Strain Concentration by Notches and Cracks," *J. Appl. Mech.*, 1968, pp. 379–386.

[79] Romilly, D., "Failure Initiation From Circumferential Defects In Large Diameter Pipelines," PhD Thesis, University of Waterloo, 1984.

[80] Romilly, D., Pick, R. J., Burns, D. J. and Coote, R. I., "Ductile Failure of High Toughness Line Pipe Containing Circumferential Defects," in *Modelling Problems in Crack Tip Mechanics*, University of Waterloo, 1983, pp. 297–306.

[81] Schmitt, W. and Hollstein, T., "Numerical Evaluation of Crack Tip Opening Displacements: 2D and 3D Applications," in *The Crack Tip Opening Displacement in Elastic-Plastic Fracture Mechanics*, K. H. Schwalbe (ed.), Springer-Verlag, 1985, pp. 3–20.

[82] Schwalbe, K. H. and Hellmann, D., "Application of the Electrical Potential Method to Crack Length Measurements Using Johnson's Formula," *Journal of Testing and Evaluation*, 1981, pp. 218–220.

[83] Shah, R. C. and Kobayashi, A. S., "Stress Intensity Factors for an Elliptical Crack Approaching the Surface of a Semi-Infinite Solid," *Int. Journ. of Fracture*, Vol. 9, 1973, pp. 133-146.

[84] Simpson, L. A., Hosbons, R. R., Davies, P. H. and Chow, C. K., "Fracture Control Using Elastic-Plastic Fracture Mechanics," in Proceedings of the International Symposium on Fracture Mechanics held Aug. 23-26 in Winnipeg, Canada, W. R. Tyson and B. Mukherjee (eds.), Pergamon Press, Toronto, 1988, pp. 49-63.

[85] Southwest Research Institute, "A Proposal for Control of Corrosion Fatigue Damage in CNG Vehicle Fuel Cylinders," (SwRI Proposal No. 06-4794), Southwest Research Institute, San Antonio and Houston, 1986.

[86] Swanson Analysis Systems, ANSYS (Rev. 4.4) Users Manual, Vol. 1, Swanson Analysis Systems, Houston, PA.

[87] Swanson Analysis Systems, ANSYS (Rev. 4.4) Users Manual, Vol. 2, Swanson Analysis Systems, Houston, PA.

[88] Swanson Analysis Systems, ANSYS (Rev. 4.2) Theoretical Manual, Swanson Analysis Systems, Houston, PA.

[89] Swanson Analysis Systems, ANSYS (Rev. 4.2) Seminar Notes, *Substructures and Submodels*, Swanson Analysis Systems, Houston, PA.

[90] Swanson Analysis Systems, ANSYS (Rev. 4.4) Tutorial, *Fracture Mechanics*, Swanson Analysis Systems, Houston, PA.

[91] Tada, H., Paris, P. C. and Irwin, G. R., *The Stress Analysis of Cracks Handbook*, Del Research Corporation, Hellertown, PA, 1973.

[92] Turner, C. E., "Design Methods," in *Post-yield Fracture Mechanics, 2d ed.*, Elsevier Applied Science Publishers, London and New York, 1984, pp. 319-431.

[93] Tracey, D. M., "On the Fracture Mechanics Analysis of Elastic-Plastic Materials using the Finite Element Method," PhD Thesis, Brown University, 1973.

[94] Wellman, G. W. and Rolfe, S. T., "Engineering Aspects of Crack-Tip Opening Displacement Fracture Toughness Testing," in *Elastic-Plastic Fracture Test Methods: The Users Experience, ASTM STP 856*, E. T. Wessel and F. J. Loss (eds.), American Society for Testing and Materials, 1985, pp 230-262.

[95] Wellman, G. W., Rolfe, S. T. and Dodds, R. H., "Failure Prediction of Notched Pressure Vessels using the CTOD Approach," *Welding Research Council Bulletin 229*, Nov. 1984, pp. 26-35.

[96] Wells, A. A., "Unstable Crack Propagation in Metals—Cleavage and Fast Fracture," Proc. Crack Propagation Symposium, Cranfield, 1961, pp. 210–230.

[97] Willougby, A. A. and Garwood, S. J., "Application of Maximum Load Toughness to Defect Assessment in a Ductile Pipeline Steel," *Fracture Mechanics: Sixteenth Symposium, ASTM STP 868*, M. Kanninen and A. T. Hopper (eds.), American Society for Testing and Materials, 1985, pp. 632–655.

[98] Worswick, M. J. and Pick, R. J., "Investigation of Plastic Instability Criteria for Fracture of Pipeline Girth Welds Containing Defects," in Proceedings of the International Symposium on Fracture Mechanics held Aug. 23–26 in Winnipeg, Canada, W. R. Tyson and B. Mukherjee (eds.), Pergamon Press, Toronto, 1988, pp. 215–226.

[99] Zienkiewicz, O. C., *The Finite Element Method*, McGraw-Hill, London, 1977.

[100] Zienkiewicz, O. C. and Cheung, *The Finite Element Method in Structural and Continuum Mechanics*, McGraw-Hill, London, 1967.

Capacity (l)	Weight (kg)	Outer Dia., D (mm)	Wall Thickness, t (mm)	Length (mm)
50	54.0	268.0	7.5	889.1
60	62.6	316.6	7.8	972.8
70	70.8	317.5	7.8	972.8

Table 2.1: Nominal weights and dimensions of steel NGV cylinders.

Property	Value
Yield strength	822 MPa
Tensile strength	948 MPa
Elongation	20 %
Hardness	R_C 36
K_{Ic}	105.5 MPa$\sqrt{mm}$
J_{Ic}	54 N/mm

Table 2.2: Material properties of NGV cylinder (AISI 4130X) steel.

Element	Percent by weight
C	0.33
Mn	0.61
P	0.026
S	0.018
Si	0.4
Cr	1.1
Mo	0.28

Table 2.3: Chemical composition of NGV cylinder (AISI 4130X) steel.

Impurity	Maximum	Typical
Hydrogen Sulphide (H_2S)	1 grain/100 SCF	0.05 grain/100 SCF
Carbon Dioxide (CO_2)	3 % by volume	0.4 % by volume
Water (H_2O)	7 lbs/MMCF	2 to 4 lbs/MMCF

Table 2.4: Maximum contractural and typical levels of natural gas contaminants.

Specimen	a_i (mm)	P_i (N)	COD_i (mm)
1	4.4	2000	0.039
2	4.4	2100	0.034
3	4.4	2100	0.042
4	4.2	2300	0.034
5	4.4	2100	0.026

Table 4.1: Initiation load and COD for small scale test specimens.

Specimen	$CTOD_i$ (mm)
1	0.043
2	0.040
3	0.050
4	0.038
5	0.027
	0.039 (Mean)
	0.008 (Stnd. Dev.)

Table 4.2: Initiation CTOD for small scale test specimens.

Specimen	P_L (N)	P_{max} (N)	P_{max}/P_L
1	2506	2000	0.80
2	2506	2100	0.84
3	2506	2100	0.84
4	2809	2300	0.82
5	2506	2250	0.84
			0.83 (Mean)
			0.02 (Stnd. Dev.)

Table 4.3: Limit loads and ratios of maximum test load to limit load for small scale test specimens.

Run	Depth, a (mm)	Length, $2c$ (mm)
01	5	30
02	5	20
04	5	10
05	3.5	30
06	3.5	20
08	3.5	10
09	2	30
10	2	20
12	2	10

Table 5.1: Run designation and defect sizes analysed in finite element analysis of full scale cylinder behaviour.

Depth, a (mm)	Length, $2c$ (mm)	Failure Pressure Predicted (MPa)	
		Interior Defect	Exterior Defect
5	30	24.13	23.51
5	20	28.75	28.82
5	10	39.37	40.13
3.5	30	29.17	29.37
3.5	20	33.16	33.92
3.5	10	41.37	>41.37
2	30	35.30	36.82
2	20	38.13	39.72
2	10	>41.37	>41.37

Table 5.2: Predicted failure pressures (finite element analysis of full scale cylinder behaviour).

Tank	Defect Size (mm)
A	2.2×5.6
B	4.2×12.4
C	4.1×10.5
D	3.5×9.9

Table 6.1: Test cylinder designation / defect sizes.

Tank	Elastic Expansion (at 34.48 MPa)
A	381.5
B	394.4
C	390.6
D	384.5
Y	349.4
Z	347.0

Table 6.2: Measured test cylinder elastic expansion at 34.48 MPa (5000 psi).

Tank	Plastic Expansion (cc)	
	Measured	Rejection
A		38.2
B	21.8	41.6
C	27.0	41.8
D	21.7	40.6
Y	1.8	35.2
Z	0.0	34.8

Table 6.3: Measured and rejection test cylinder plastic expansions.

Tank	Observed Burst Press. (MPa)	Predicted Burst Press. (MPa)				
		FEM	CTOD Curve	Pl. Coll.	R6 Meth.	Battelle Empir.
A	44.13	73.09	25.37 (68.81)	43.30	42.82	44.68
B	43.09	38.27	18.13 (33.23)	33.78	35.30	45.23
C	43.44	41.09	19.24 (36.75)	38.82	37.16	45.02
D	43.78	43.78	19.65 (39.51)	40.40	38.41	44.89

Table 7.1: Measured and predicted cylinder burst pressures.

Tank	Cycles to Failure ($\times 10^3$)	Years to Failure
A	11	8.5
B	5	3.8
C	5	3.8
D	7	>5.0

Table 7.2: Number of cycles/years to failure for test cylinders.

Depth, a (mm)	Length, 2c (mm)	Failure During Recertification	Failure During Service
5	30	Yes	Yes
5	20	Yes	Yes
5	10	No	Yes
3.5	30	Yes	Yes
3.5	20	Yes	Yes
3.5	10	No	Yes
2	30	Yes	Yes
2	20	No	Yes
2	10	No	No

Table 8.1: Comparison of expected modes of cylinder failure (finite element analysis of full scale cylinder behaviour).
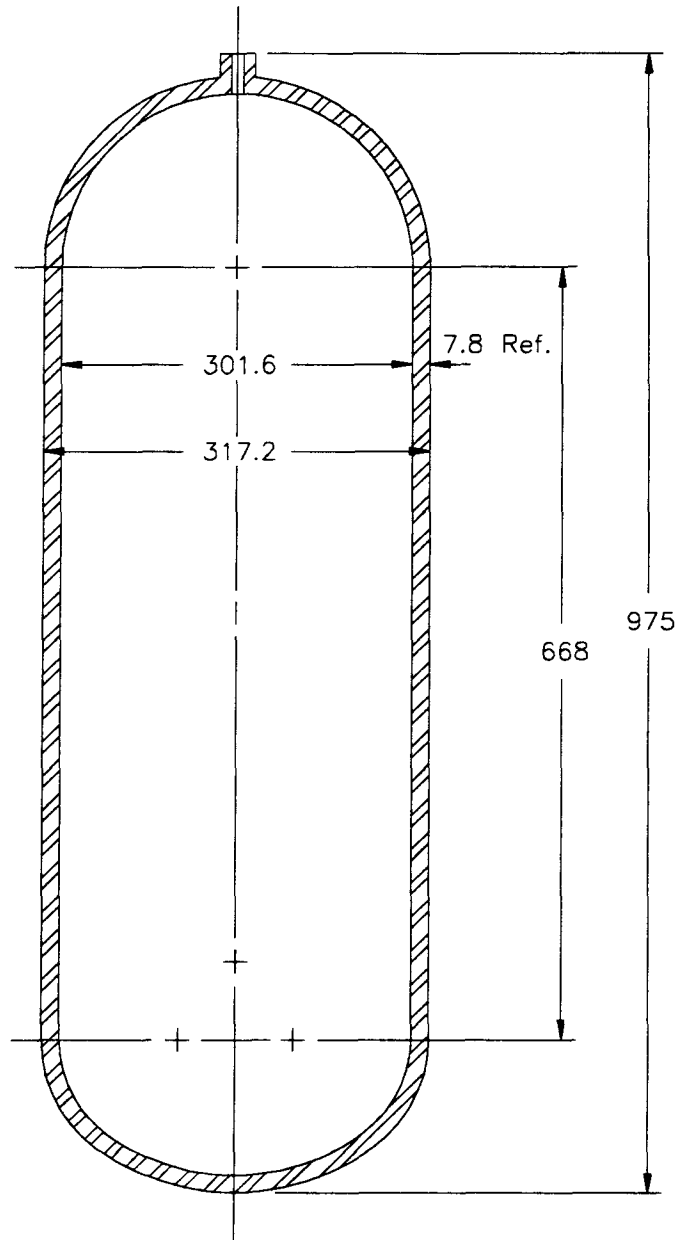
Figure 2.1: 60 liter NGV cylinder geometry.
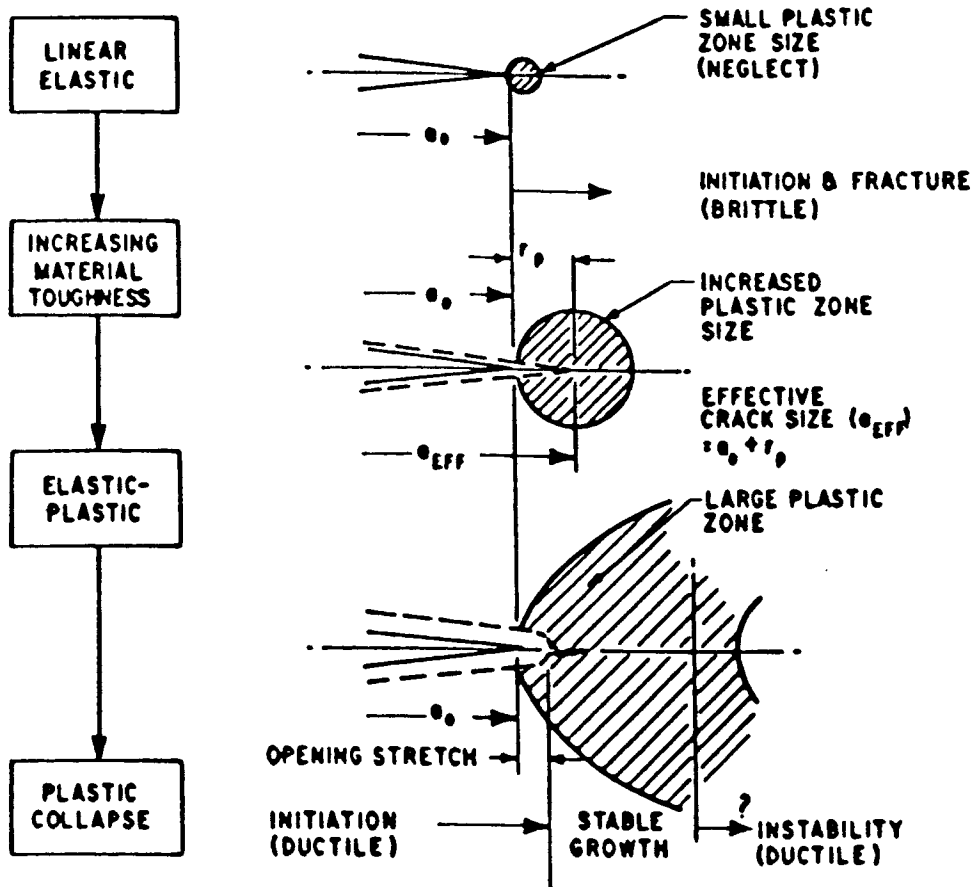
Figure 3.1: Regimes of crack tip behaviour [79].

$$\sigma = p \frac{R}{t}$$

$$M_{T,S} \, K_{plate} = K_{cyl}$$

Plate

Cylinder

Through wall defect
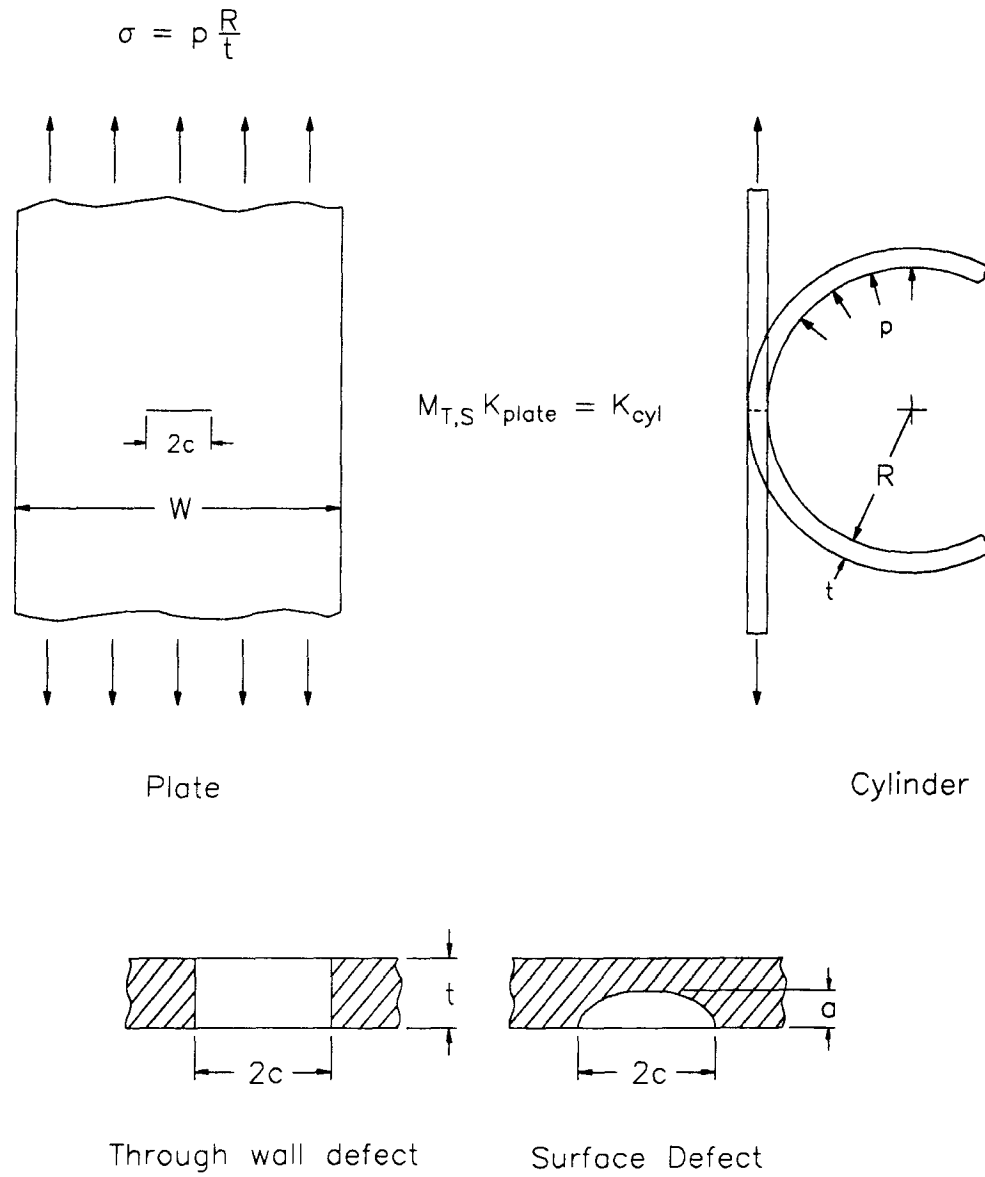
Surface Defect

Figure 3.2: Diagramatic illustration of approach used to analyse defects in cylinders.
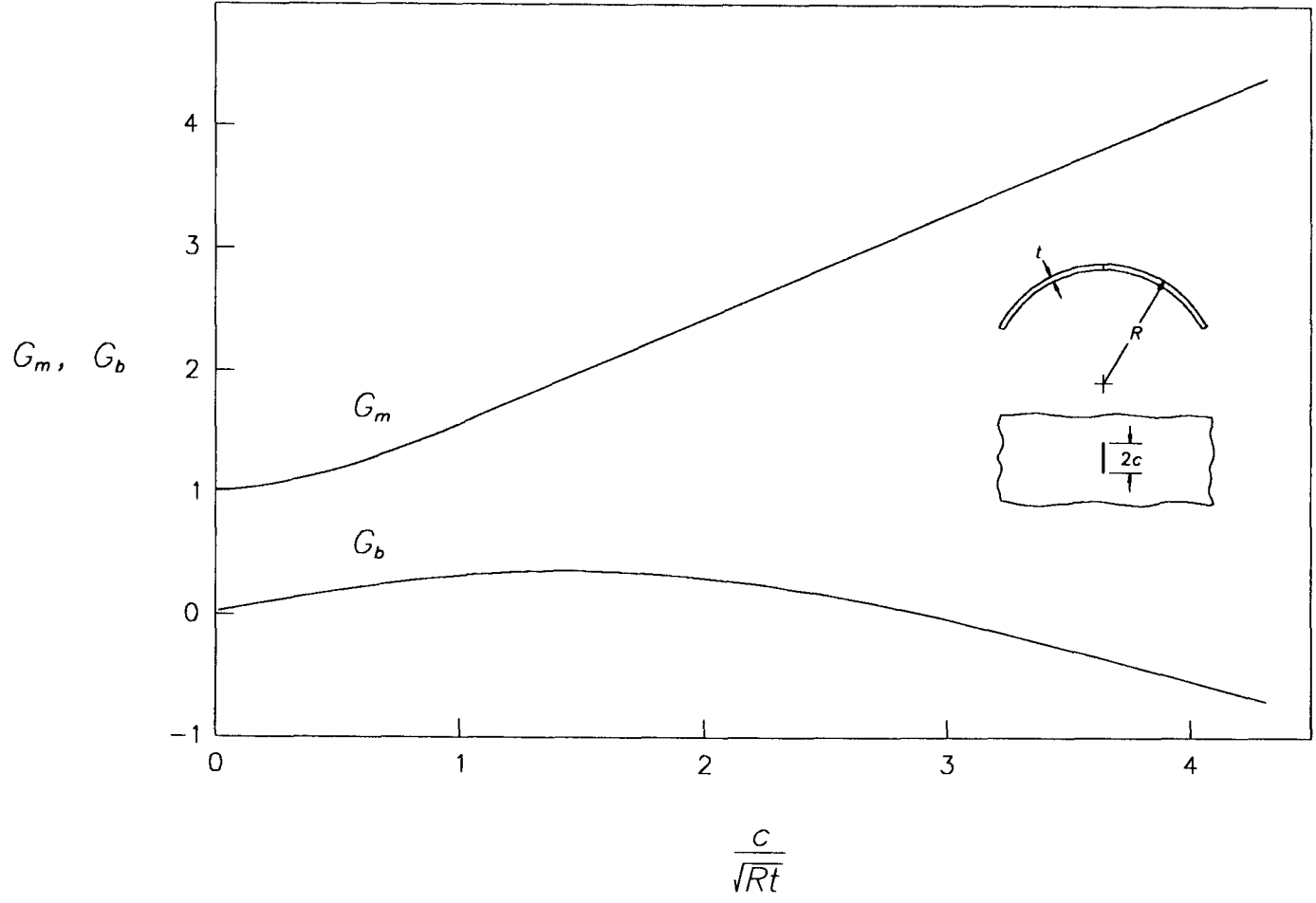
Figure 3.3: Membrane and bending components of stress magnification factor for through-wall defects in cylinders [44].
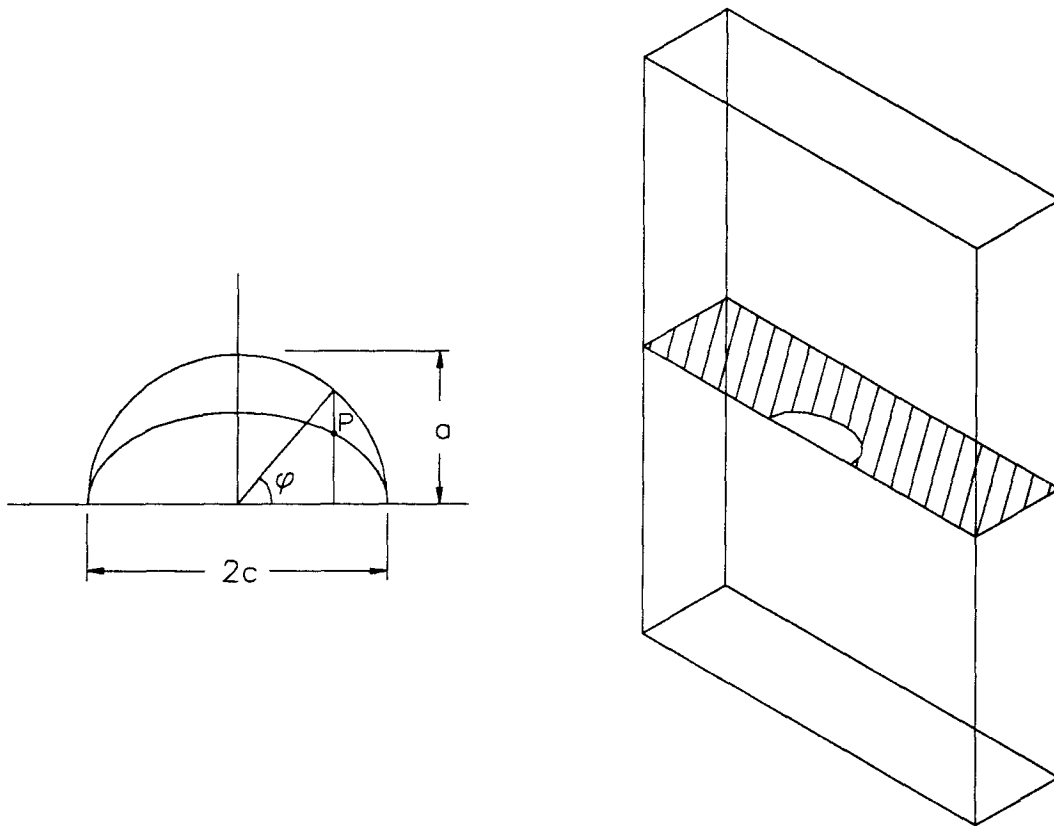
Figure 3.4: Elliptical surface defect in a wide plate.
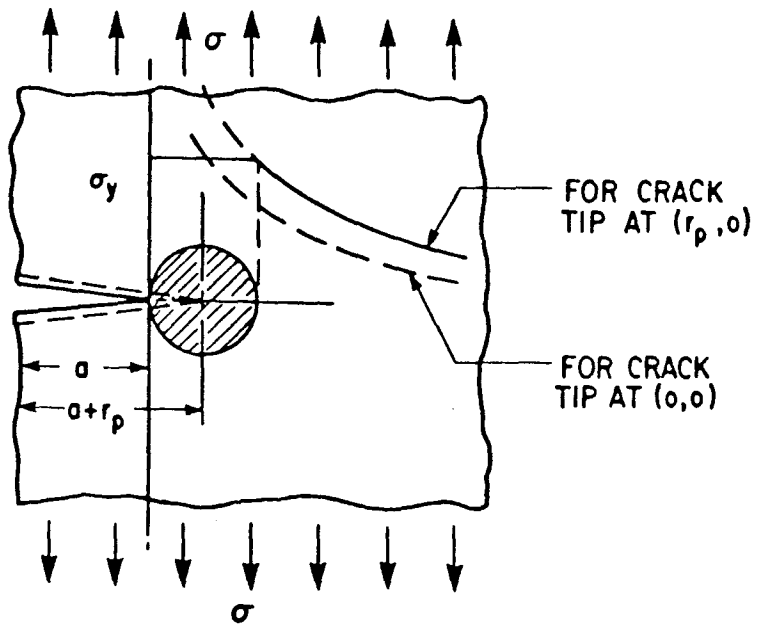
Figure 3.5: Irwin plastic zone correction [53].
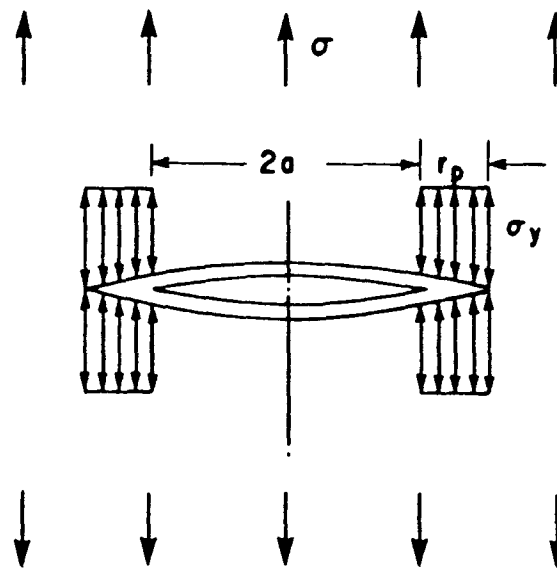
Figure 3.6: Dugdale plastic zone correction [42].
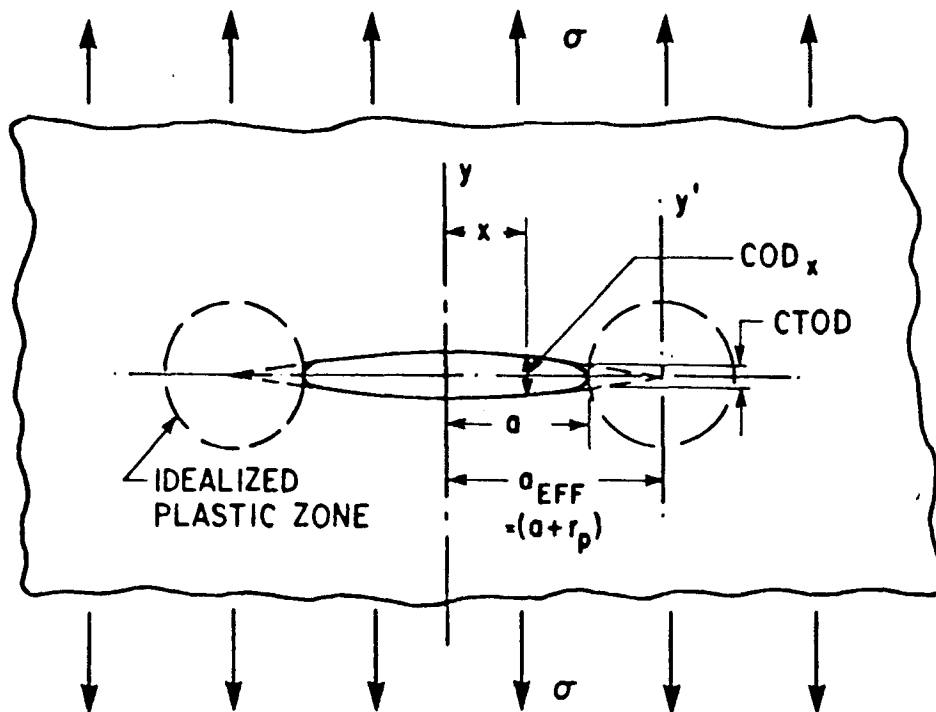
Figure 3.7: Center cracked plate geometry.
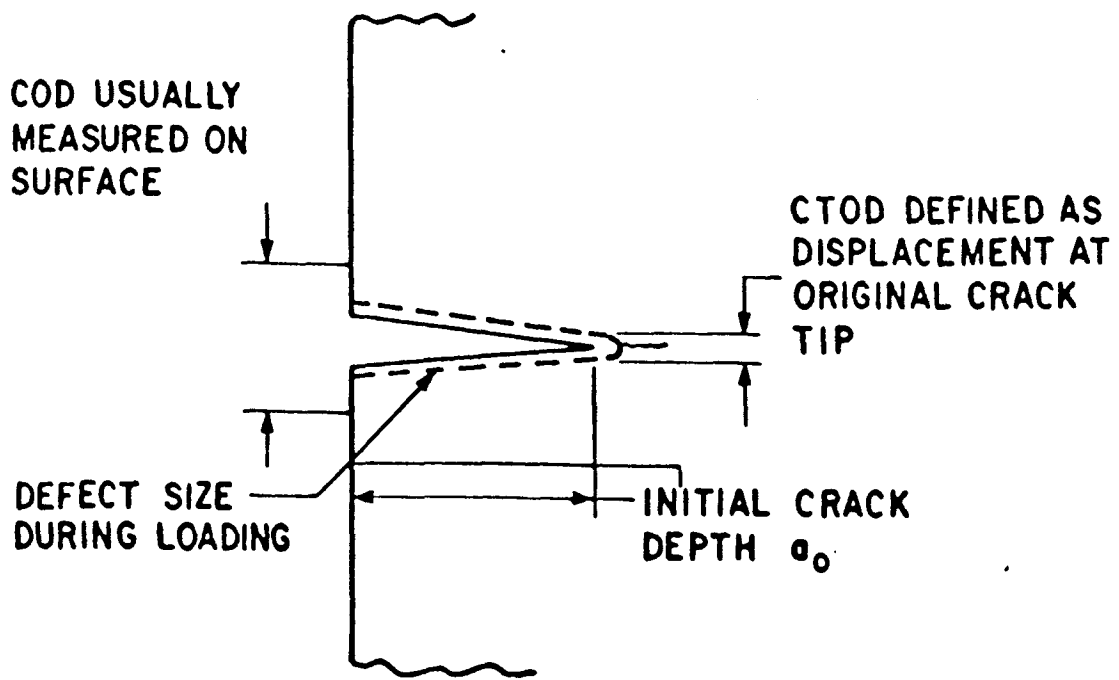
Figure 3.8: Crack tip opening displacement (CTOD) and crack opening displacement (COD).
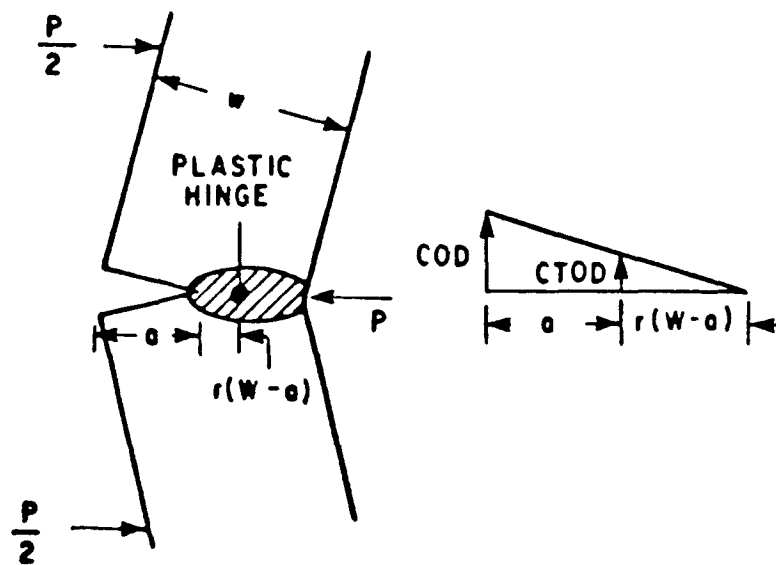
Figure 3.9: Single edge notch bend specimen (SENB) geometry.

$$J = \int_{\Gamma} (\omega\, dY - T \cdot \frac{\partial u}{\partial x}\, ds)$$
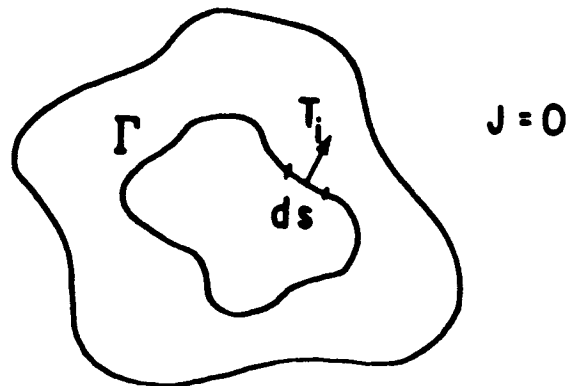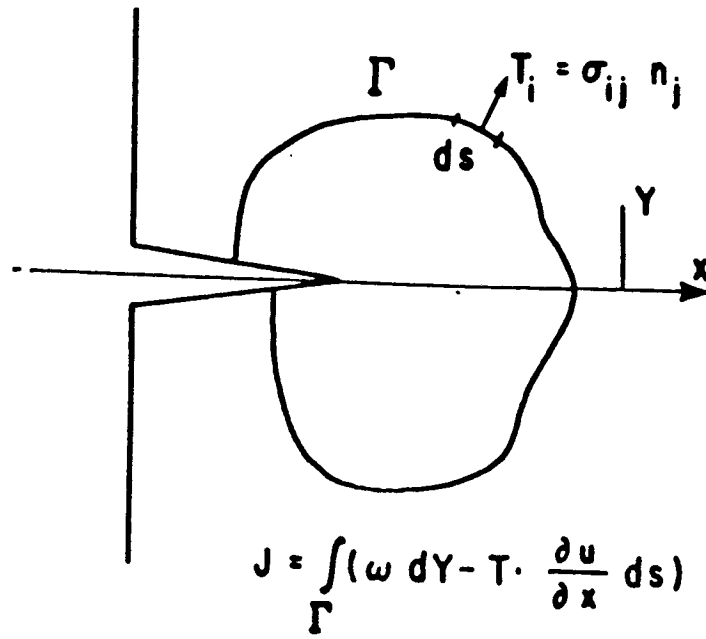
Figure 3.10: The J-integral.
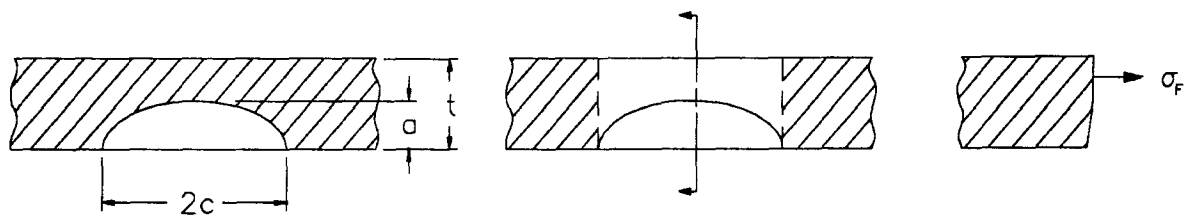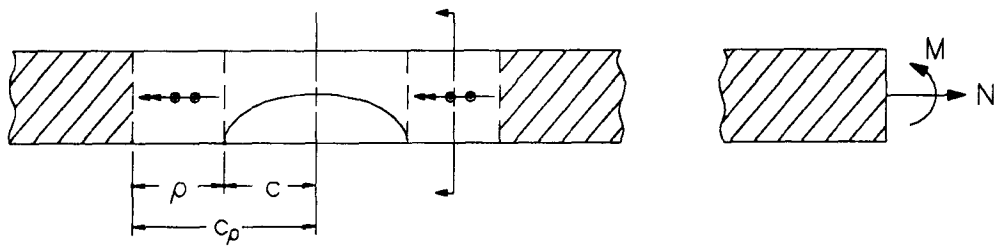
Figure 3.11: Models for CTOD in large scale yielding.
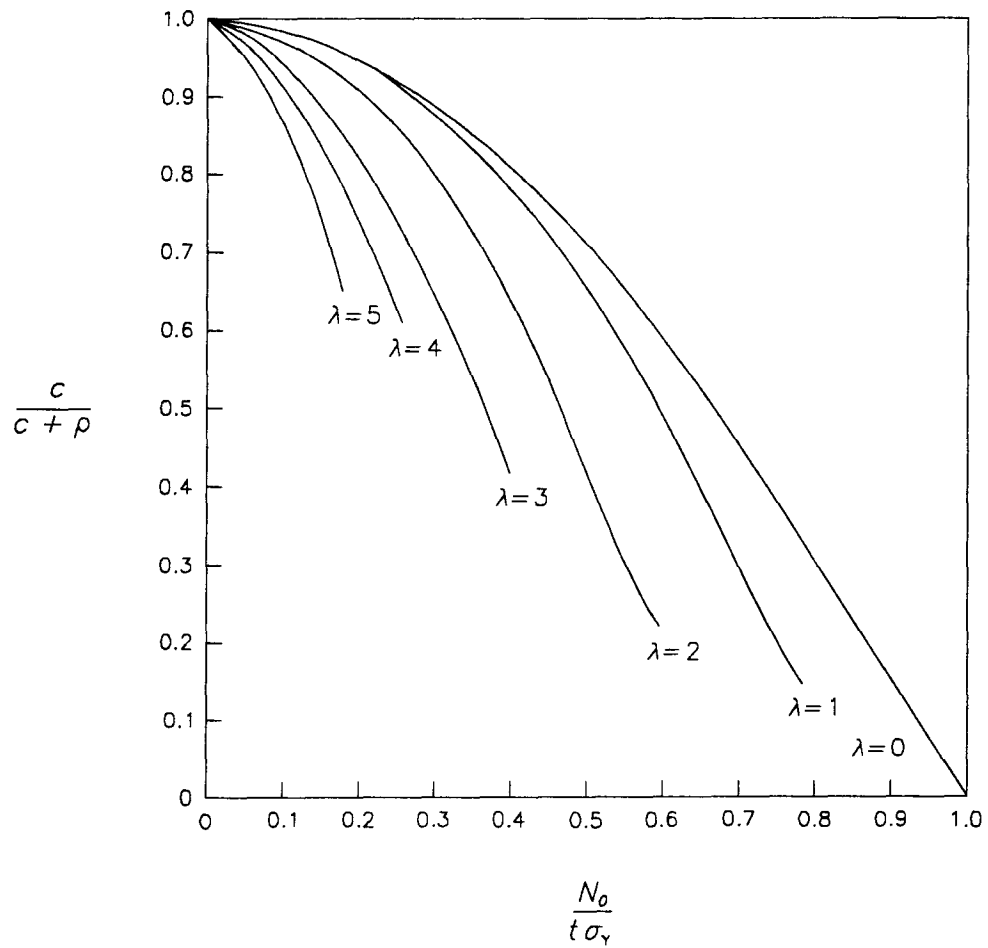
Figure 3.12: Plastic zone correction from Erdogan and Ratwani formulation [45].
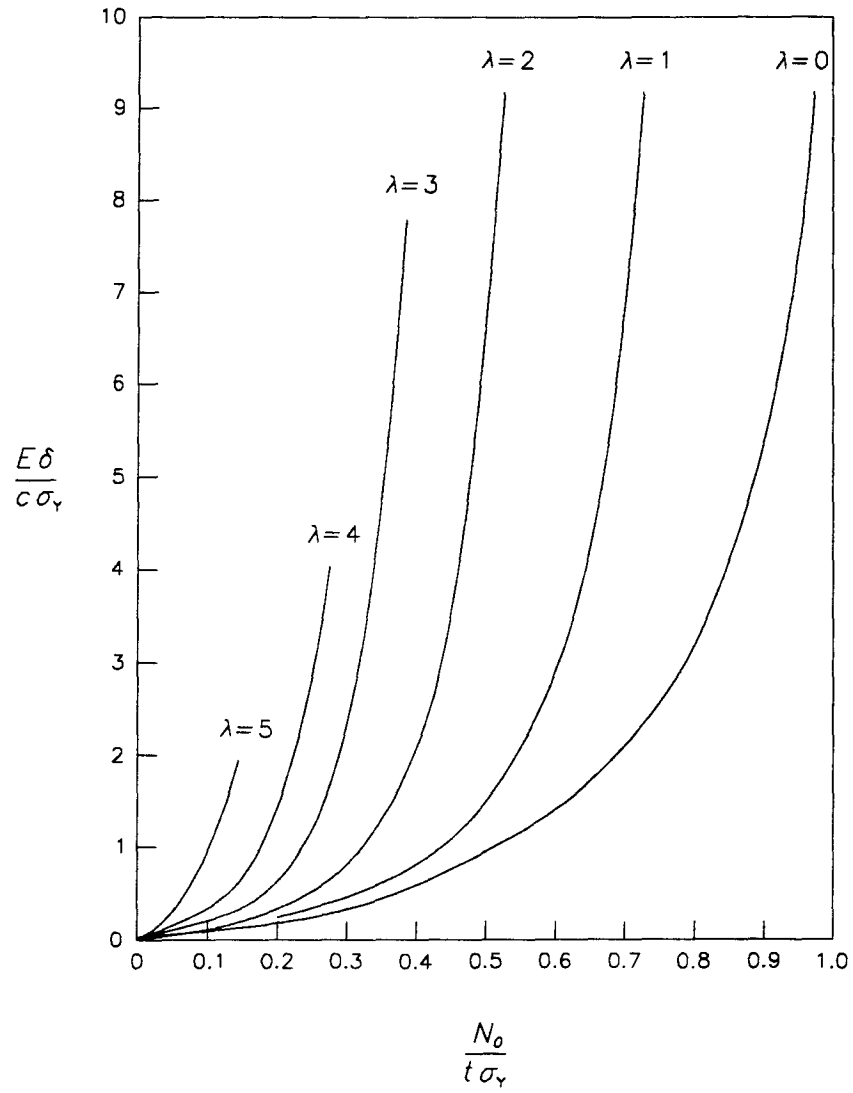
Figure 3.13: Crack tip open displacement from Erdogan and Ratwani formulation [45].

Actual crack
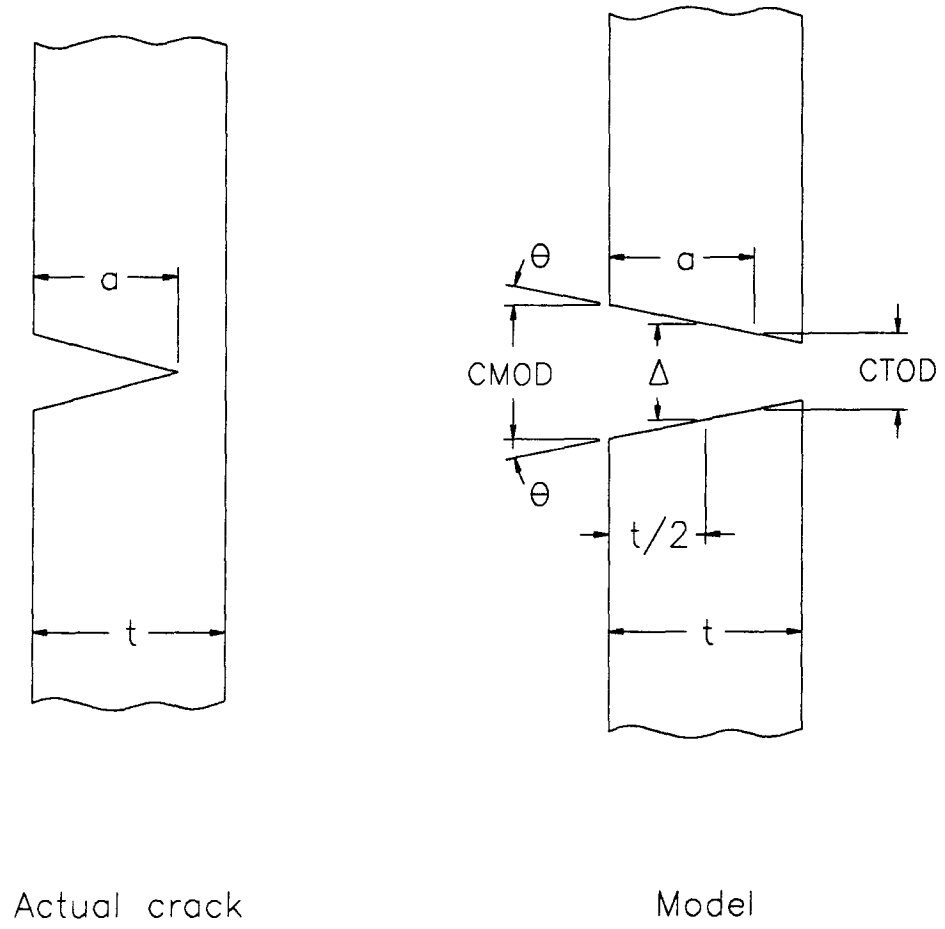
Model

Figure 3.14: Line spring model geometry [59].
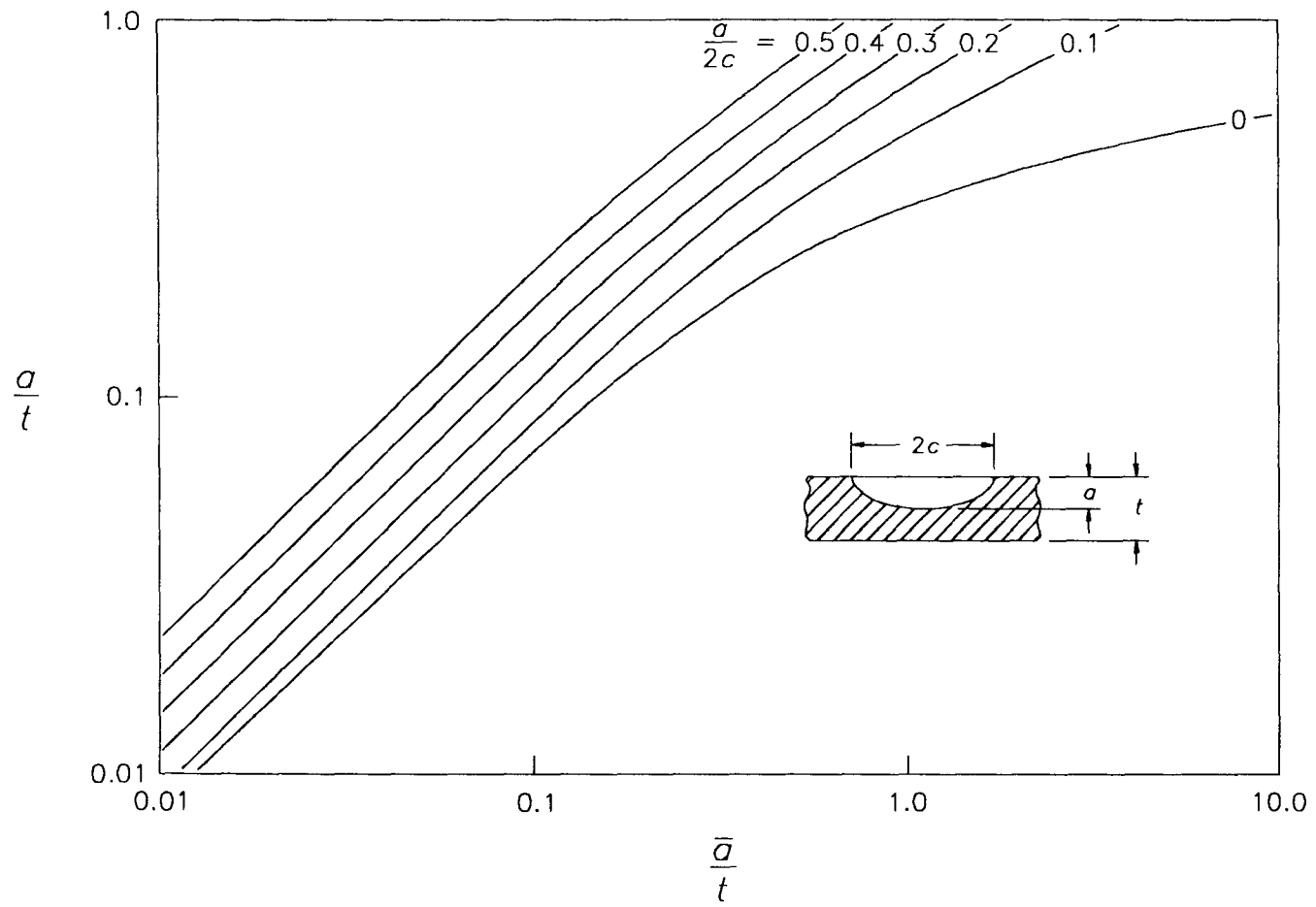
Figure 3.15: Relationship between actual defect dimensions and the parameter $\bar{a}$ for surface defects [24].
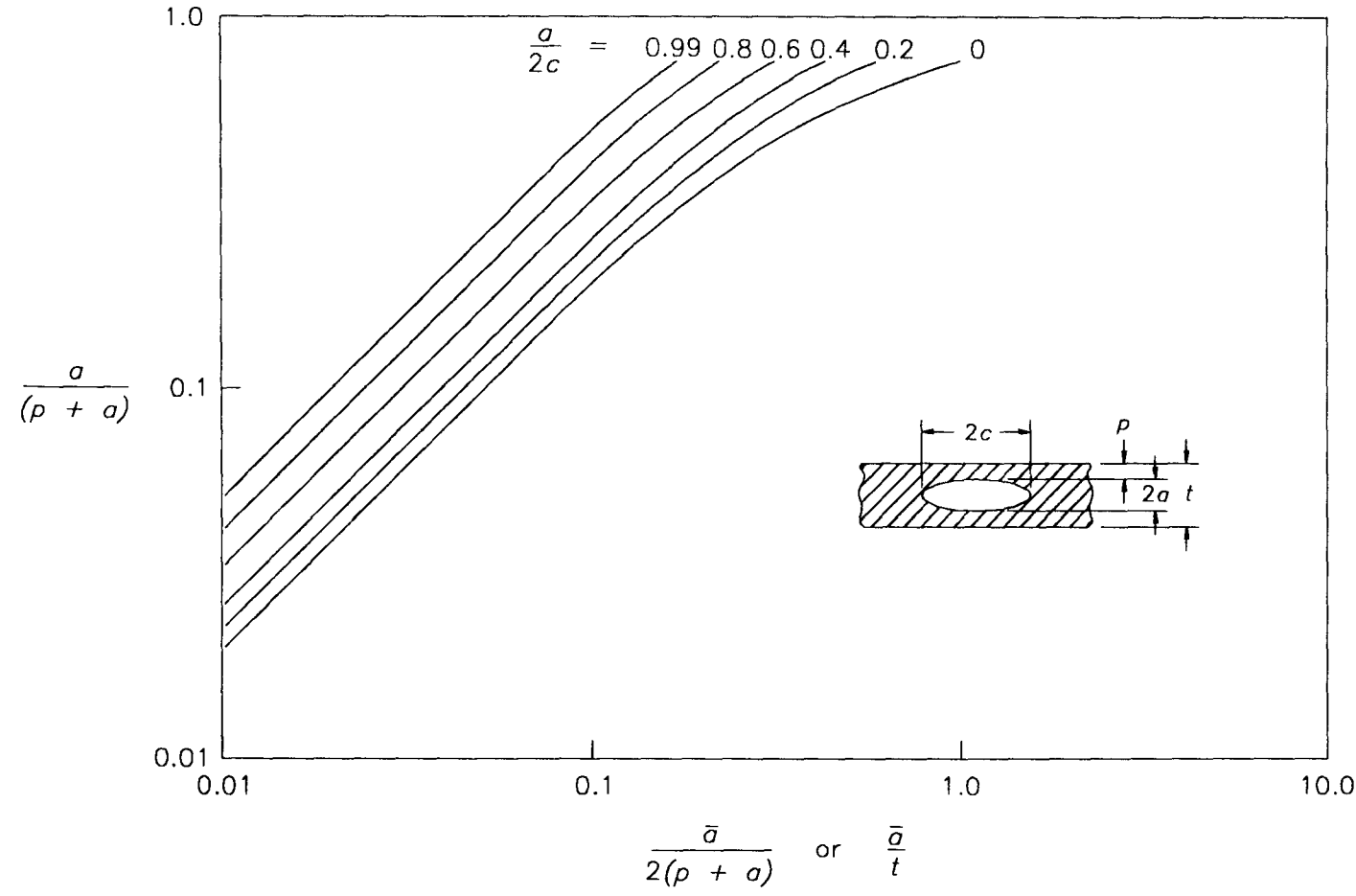
Figure 3.16: Relationship between actual defect dimensions and the parameter $\bar{a}$ for embedded defects [24].
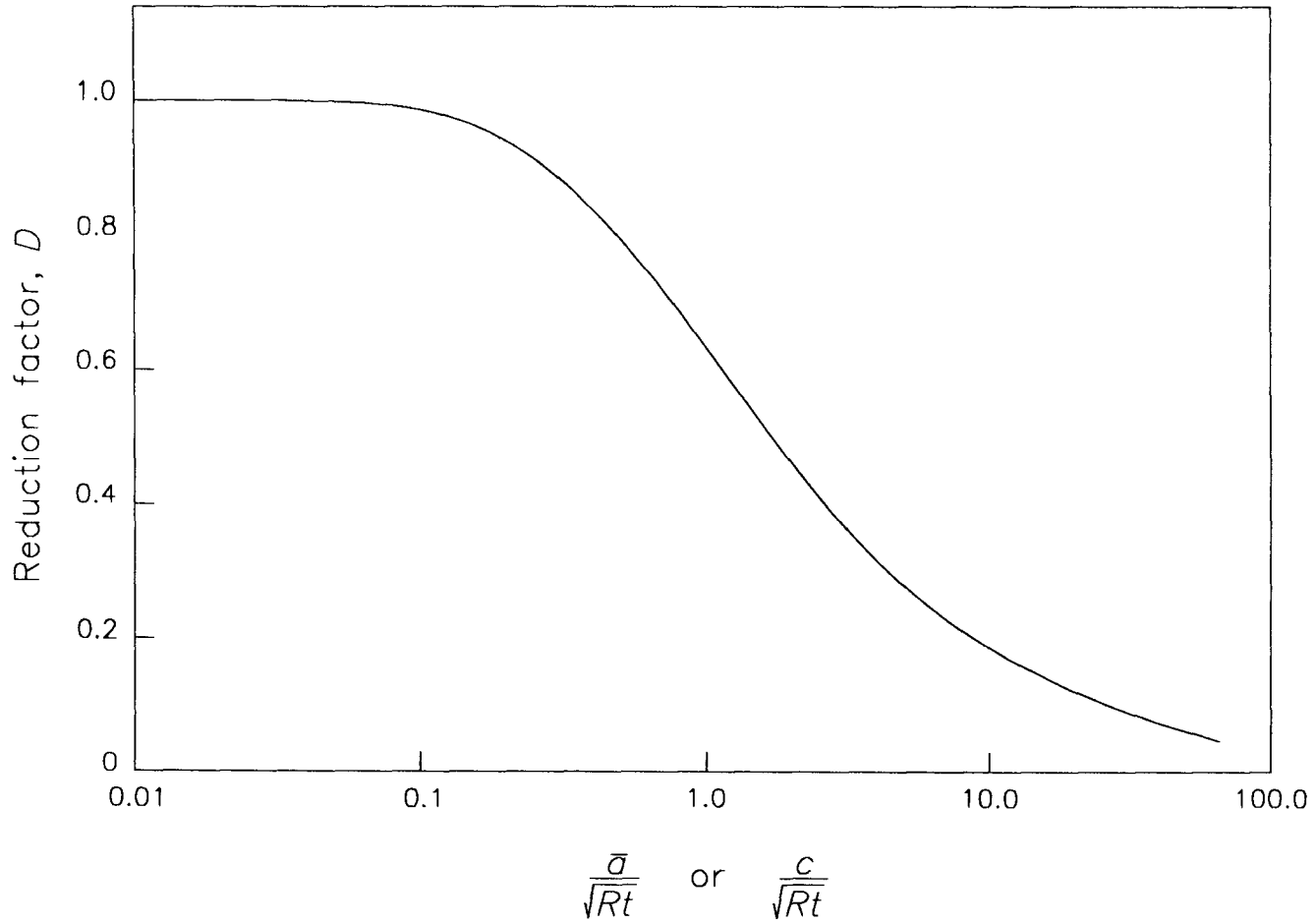
Figure 3.17: Reduction factor for long defects in curved shells containing pressure [24].
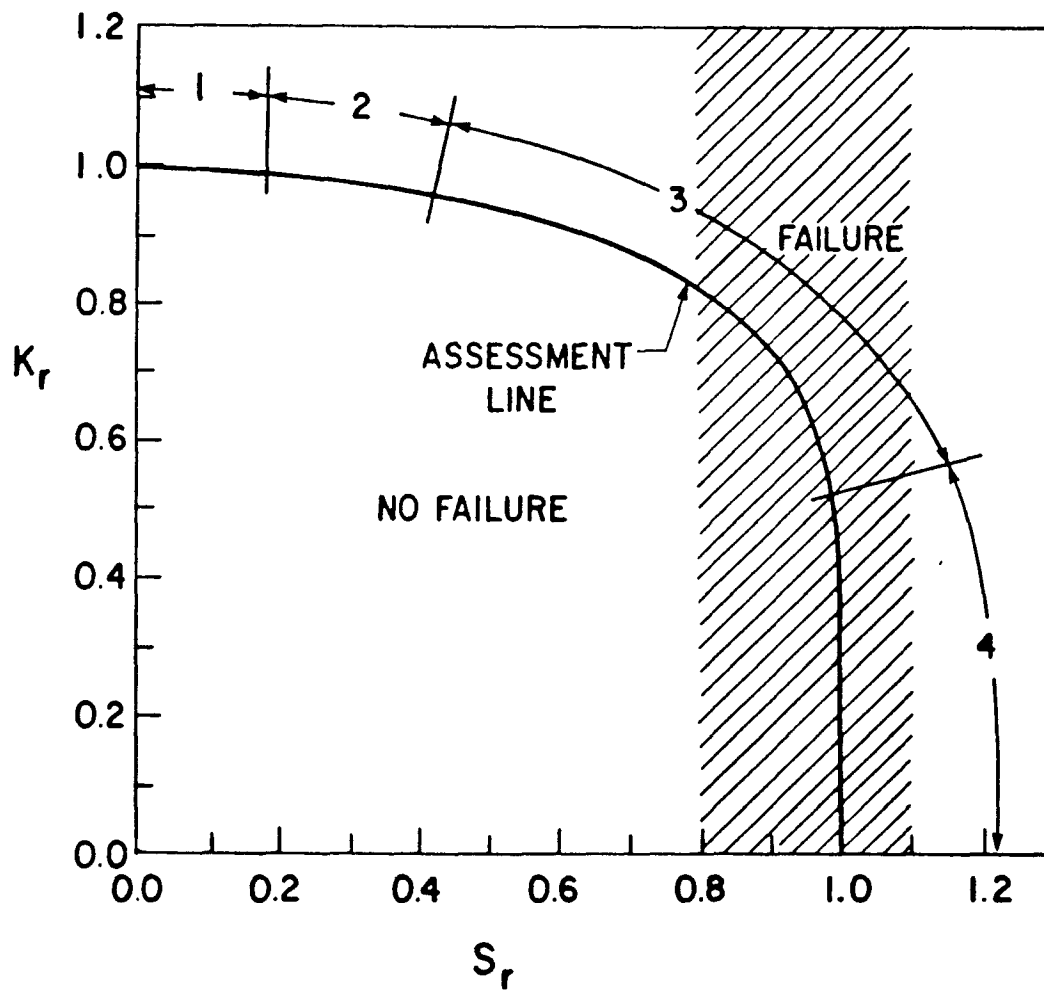
Figure 3.18: The CEGB R6 failure assessment diagram [27].
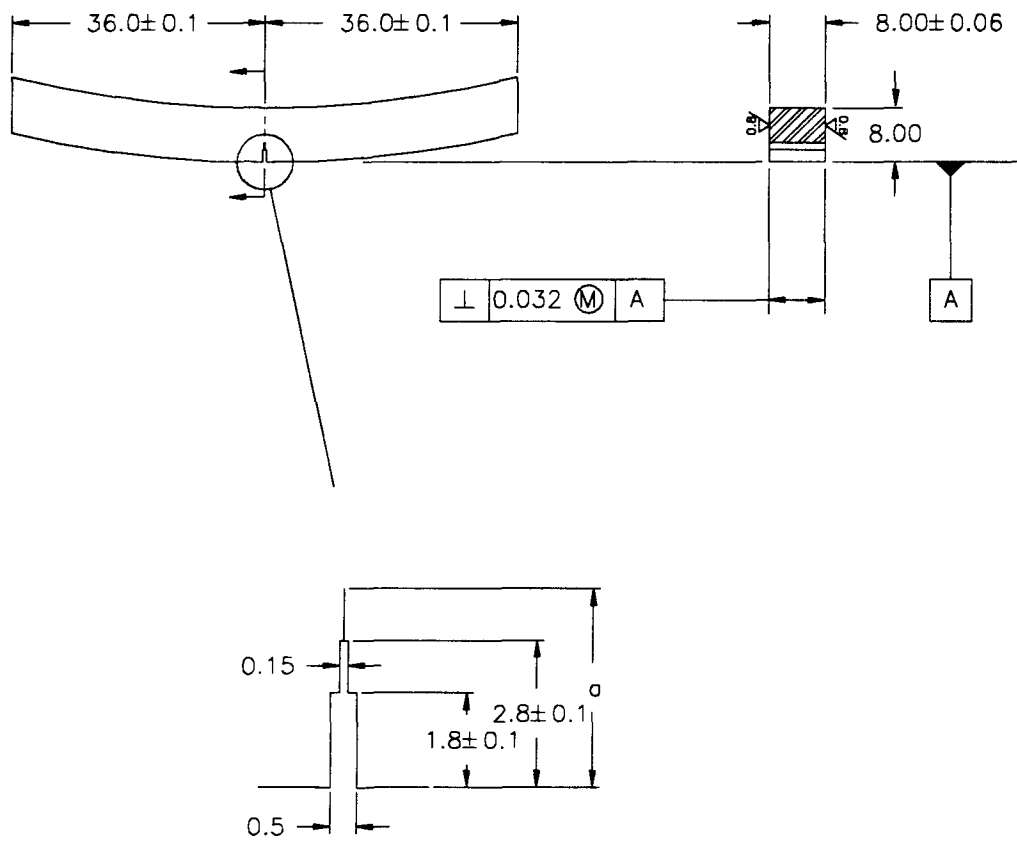
Figure 4.1: Small scale CTOD specimen geometry.
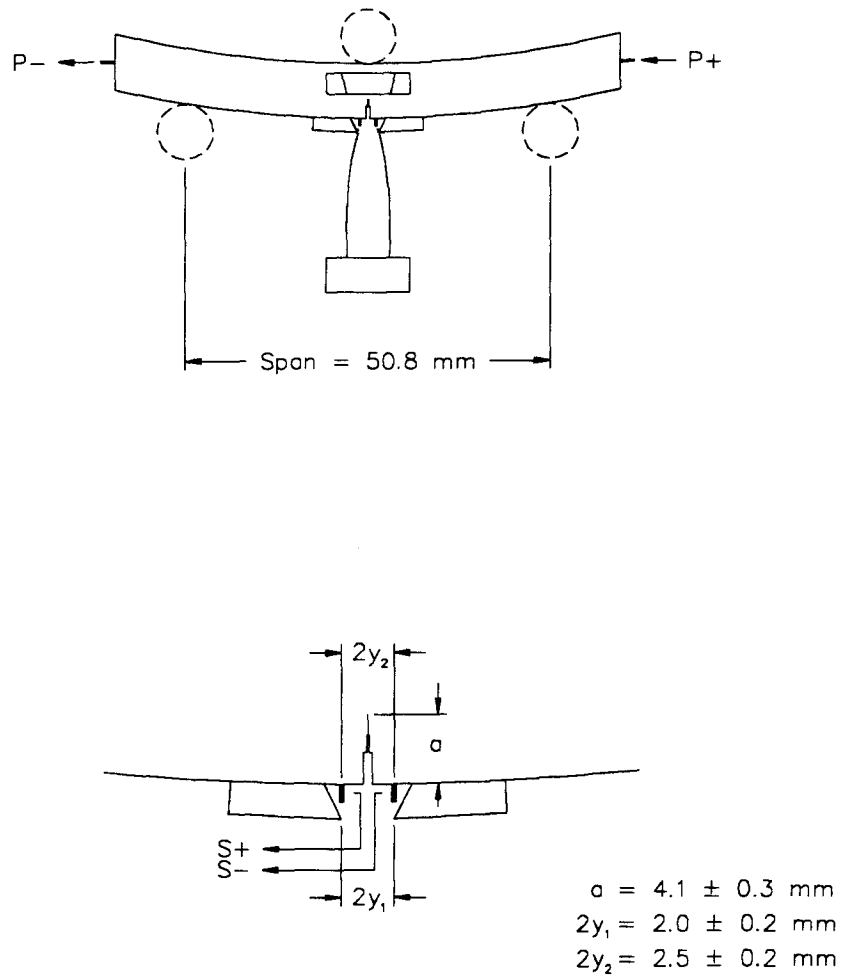
Figure 4.2: Small scale CTOD specimen clip gauge and potential drop lead locations.
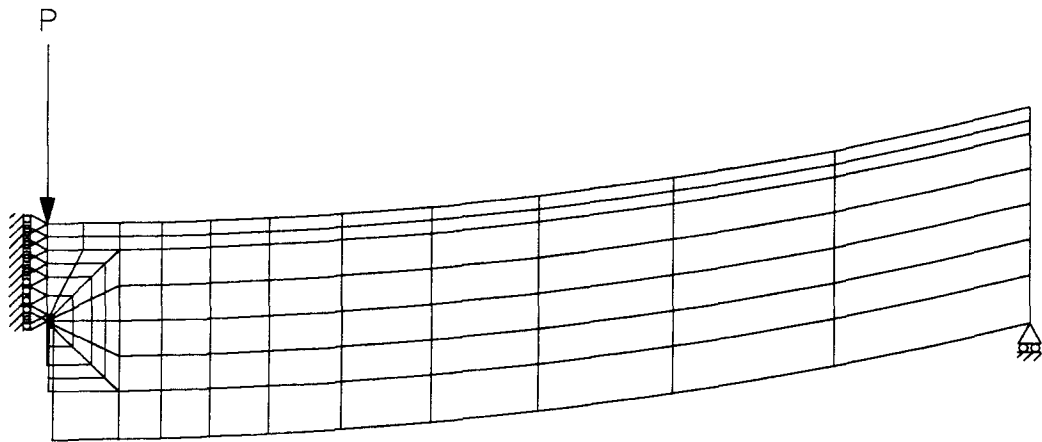
(a) CTOD specimen finite element mesh
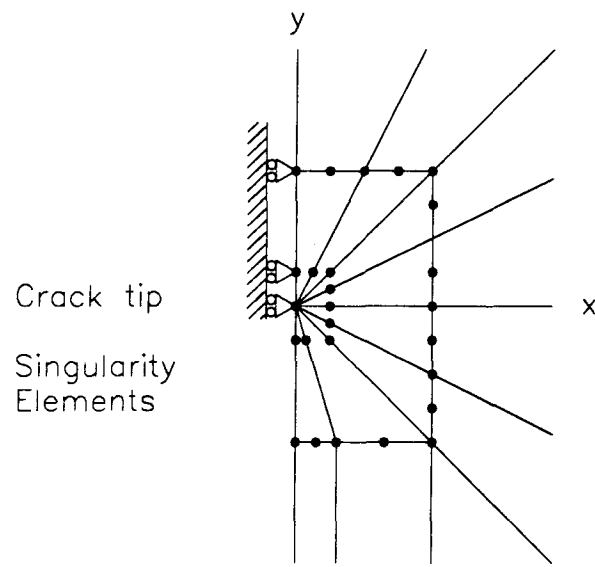
(b) Near crack tip mesh

Figure 4.3: Finite element mesh for small scale CTOD specimen.
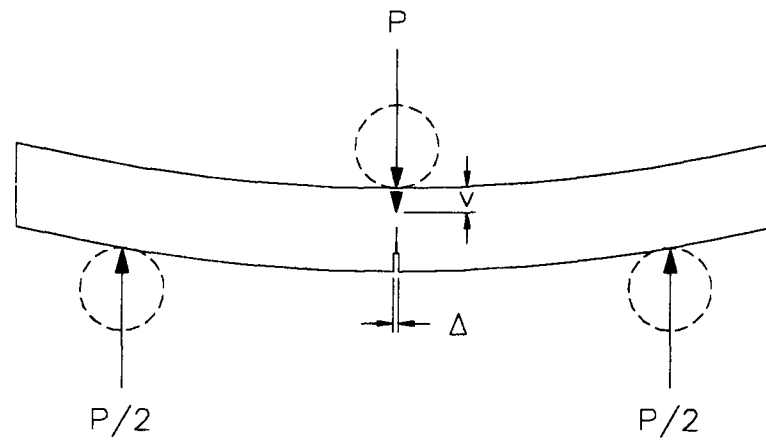
Figure 4.4: Small scale CTOD specimen COD and point load displacement.
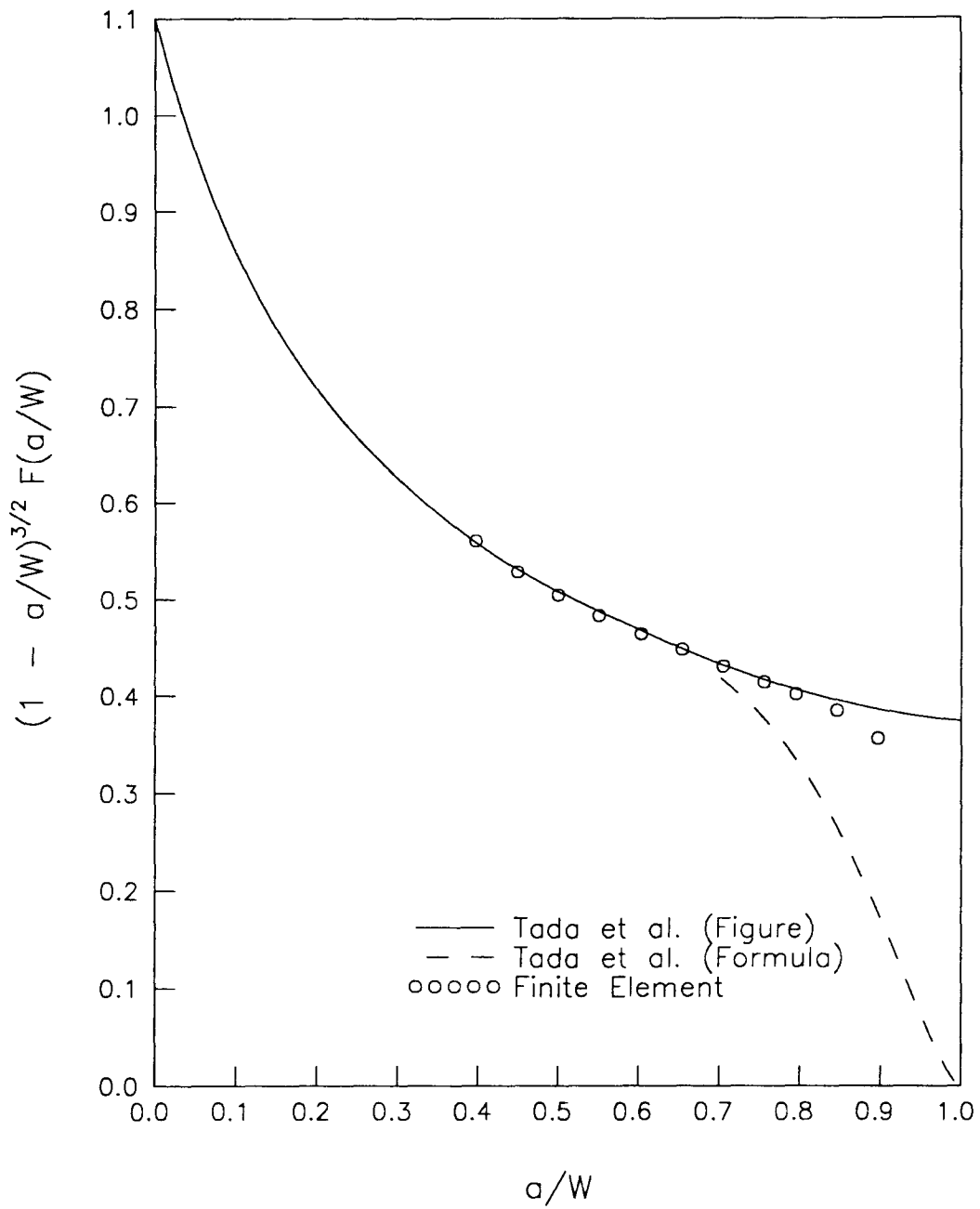
Figure 4.5: Non-dimensional stress intensity shape factor for small scale CTOD specimen.
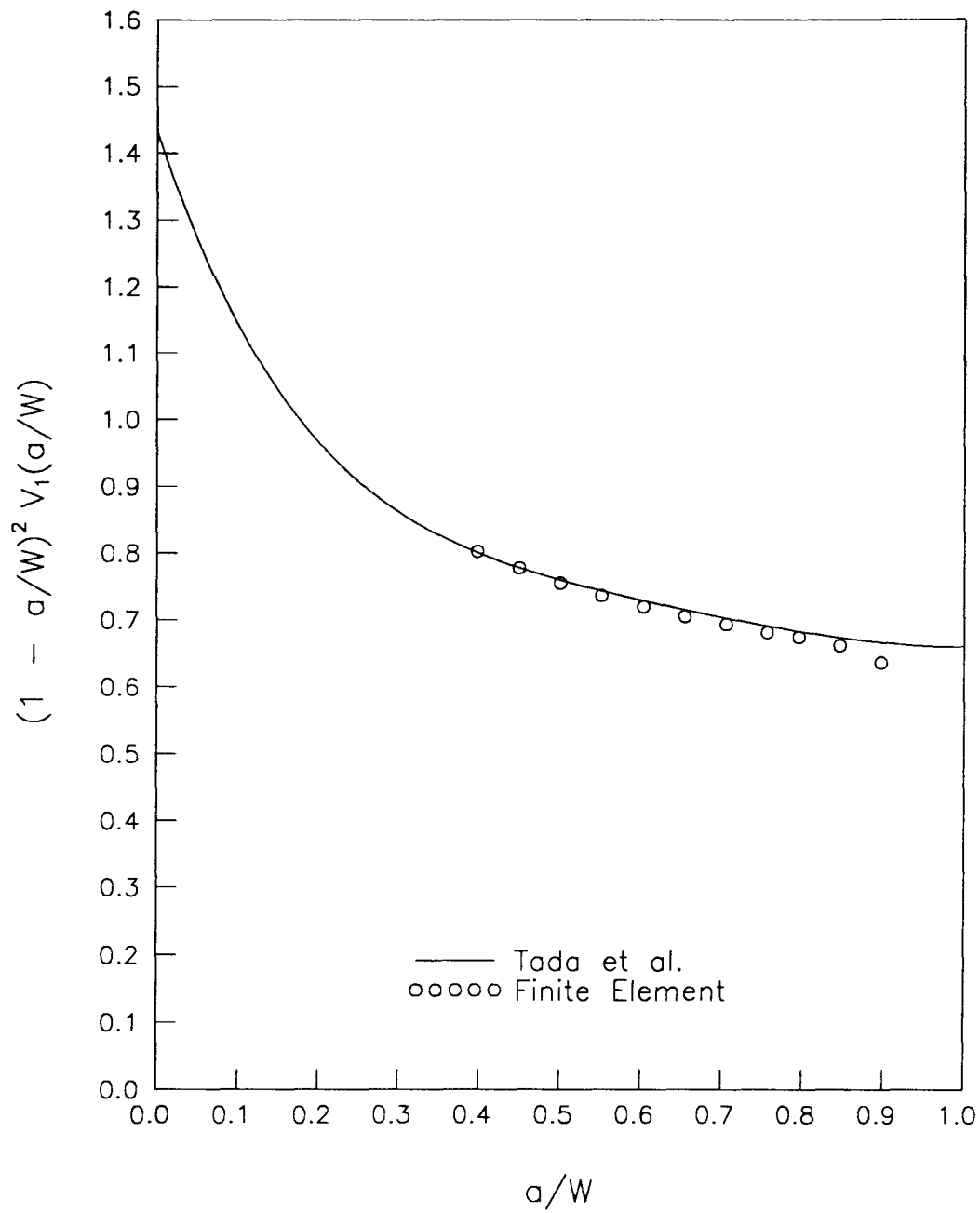
Figure 4.6: Non-dimensional crack opening displacement shape factor for small scale CTOD specimen.
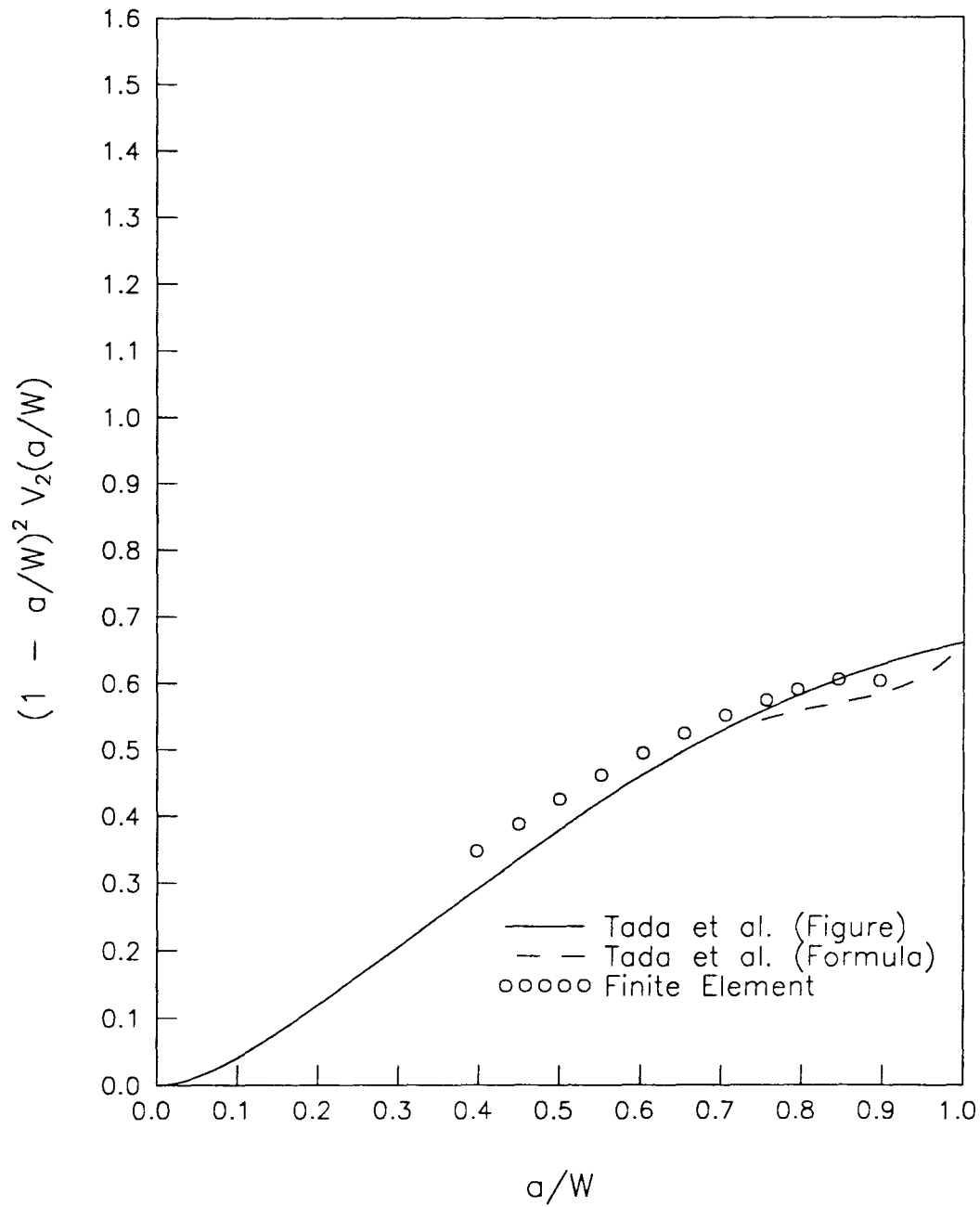
Figure 4.7: Non-dimensional point load displacement shape factor for small scale CTOD specimen.
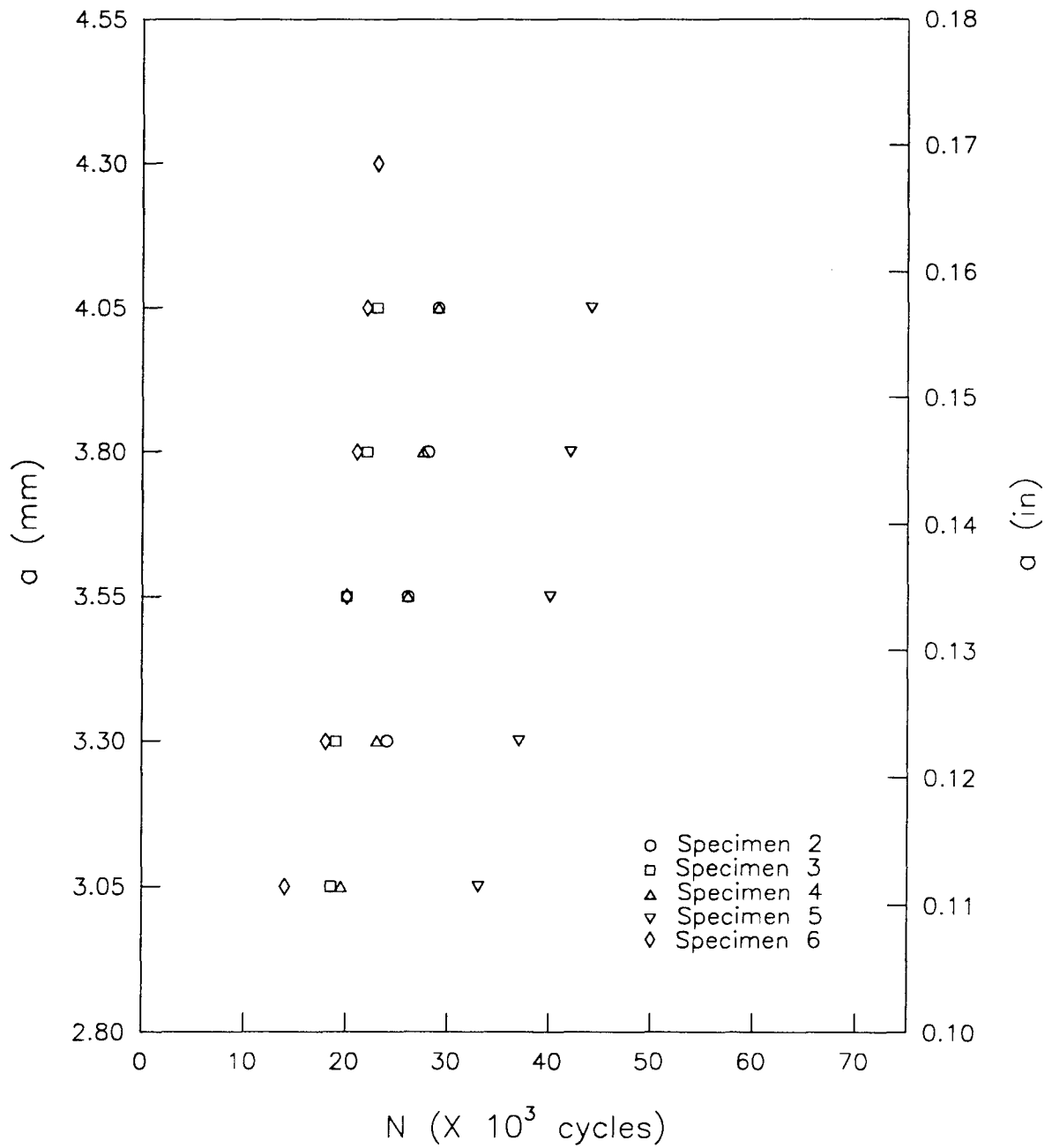
Figure 4.8: Crack depth versus number of cycles for small scale CTOD specimen.
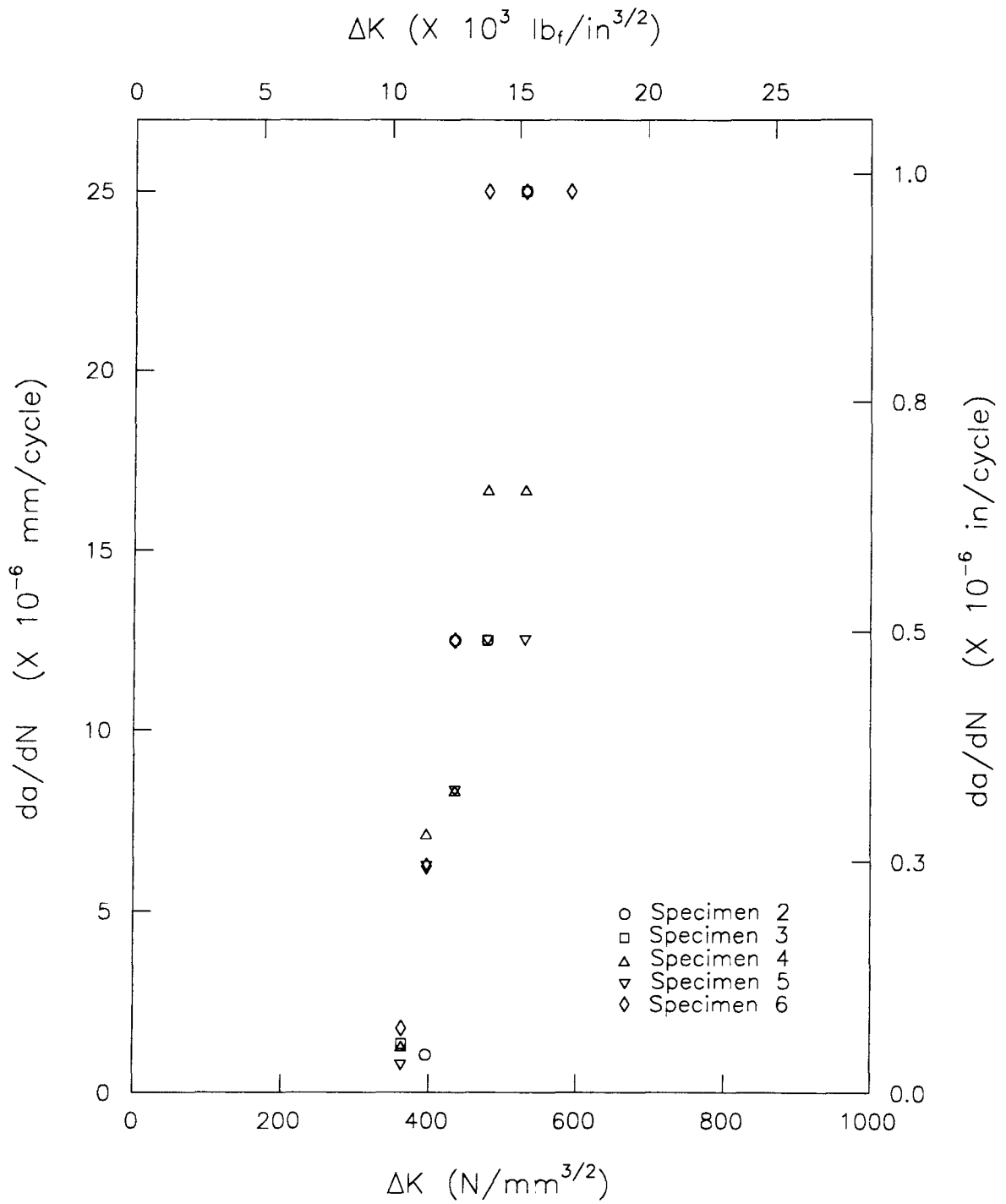
Figure 4.9: *da/dN* versus ΔK for for small scale CTOD specimen.
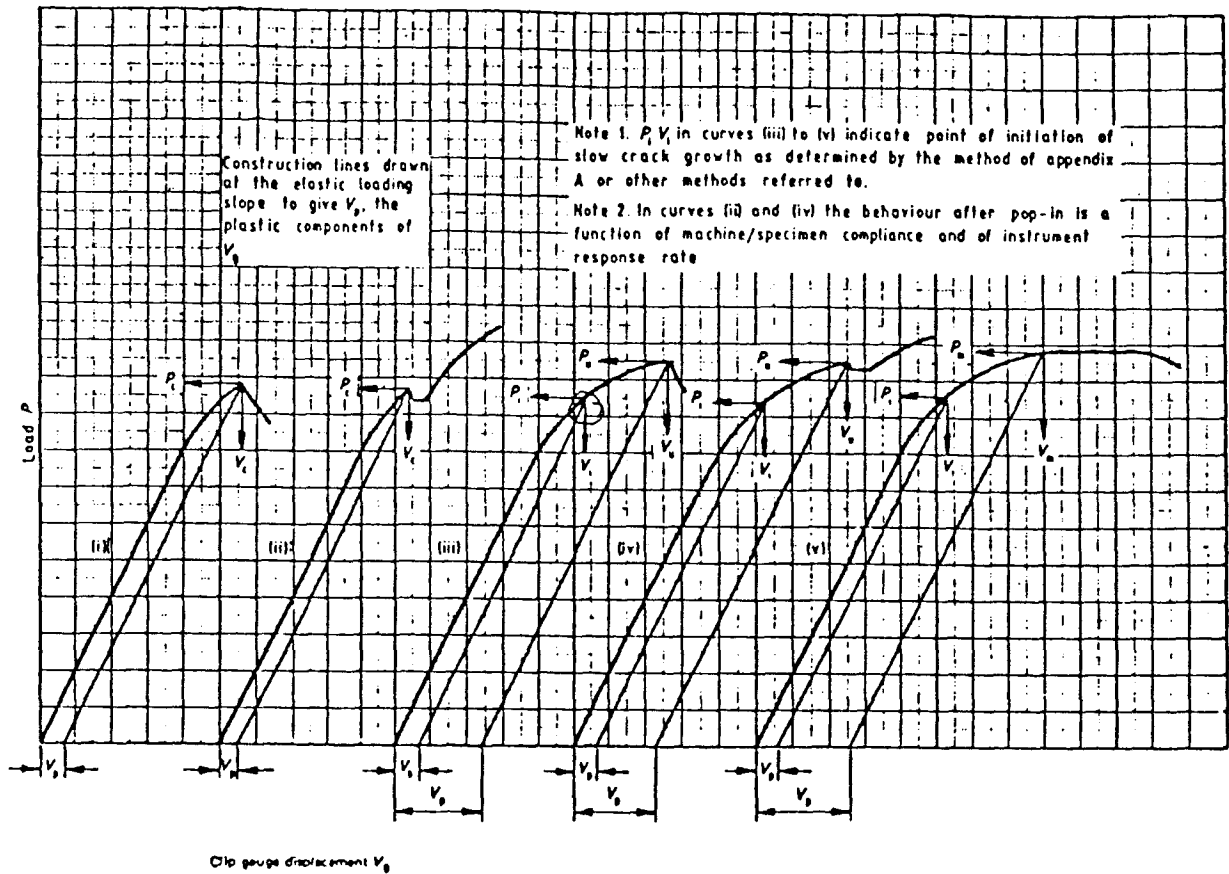
Figure 4.10: Types of load-COD records: i, cleavage, ii, crack arrest (pop-in), iii, stable crack growth, iv, stable crack growth followed by crack arrest, v, attainment of maximum load plateau [23].
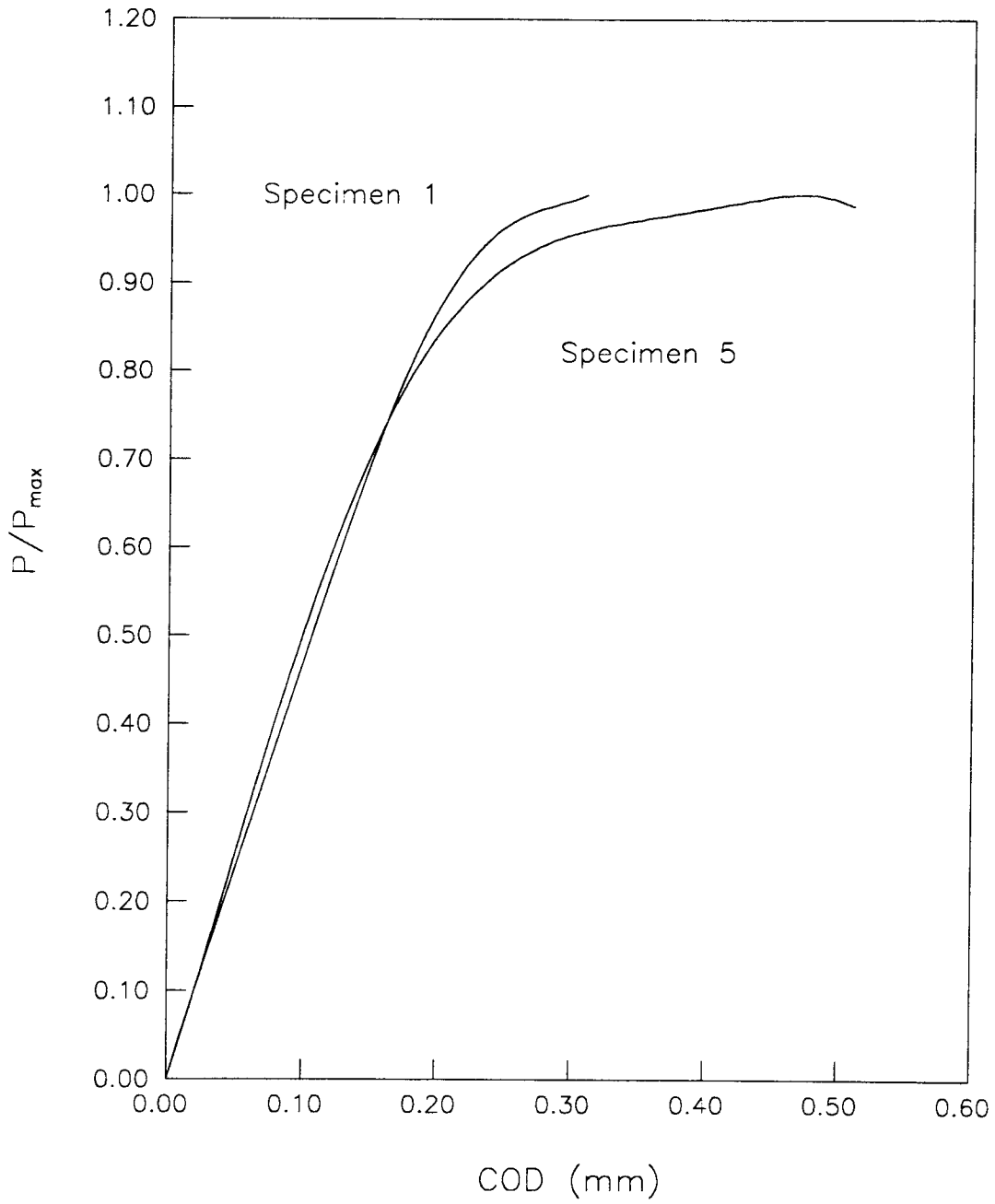
Figure 4.11: Normalized load versus COD for Specimens 1 and 5.
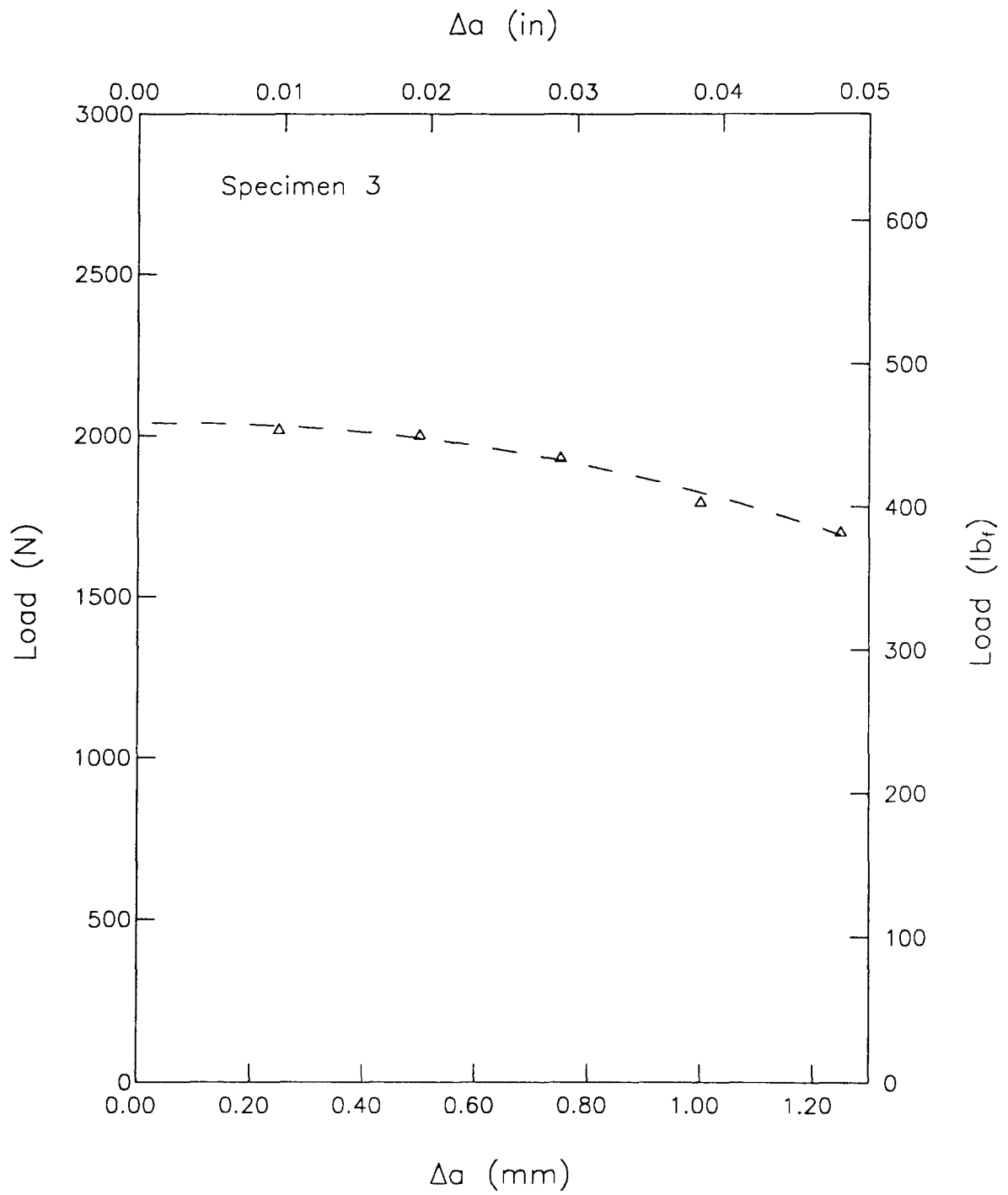
Figure 4.12: Crack growth versus load for Specimens 3.
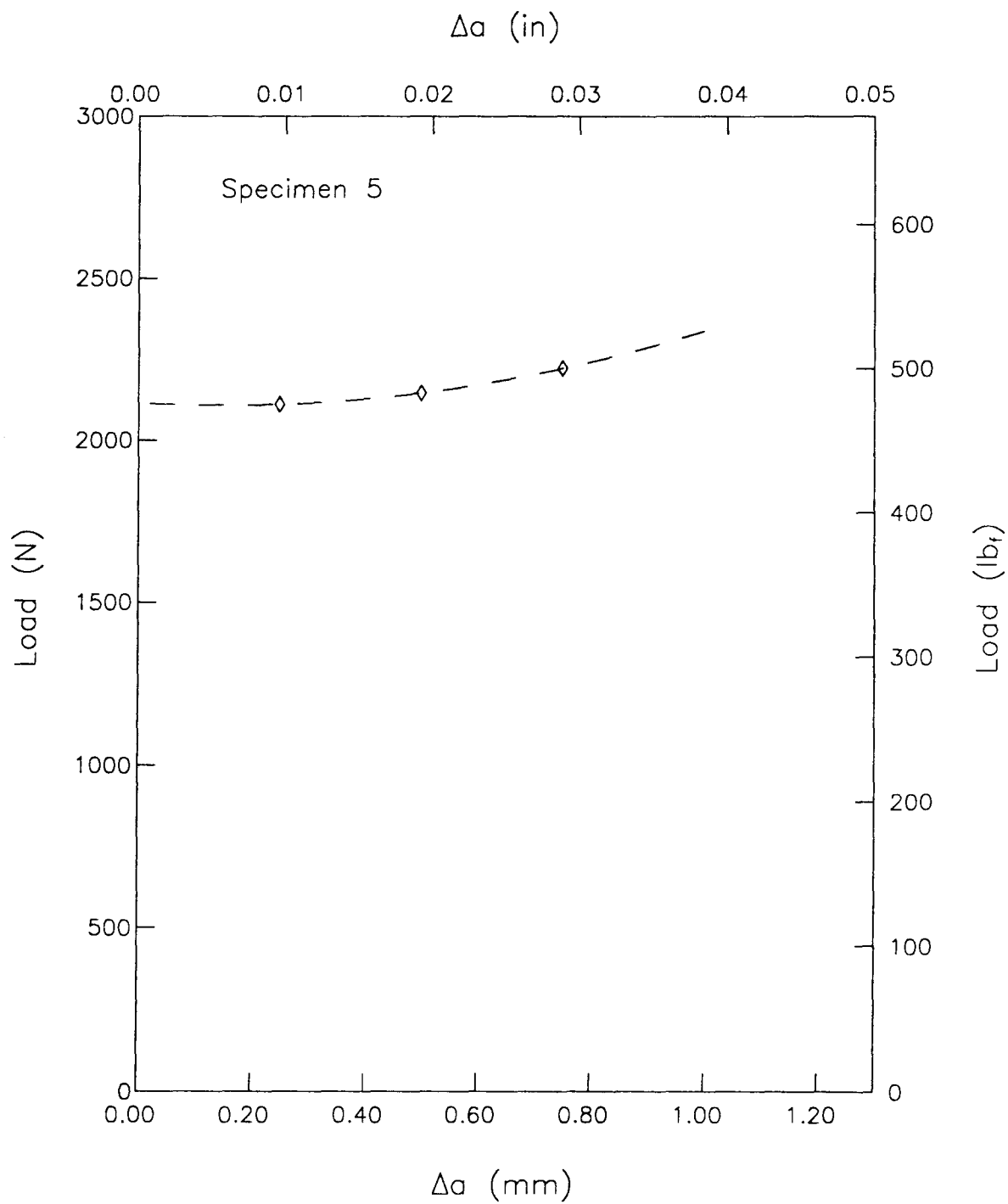
Figure 4.13: Crack growth versus load for Specimens 5.
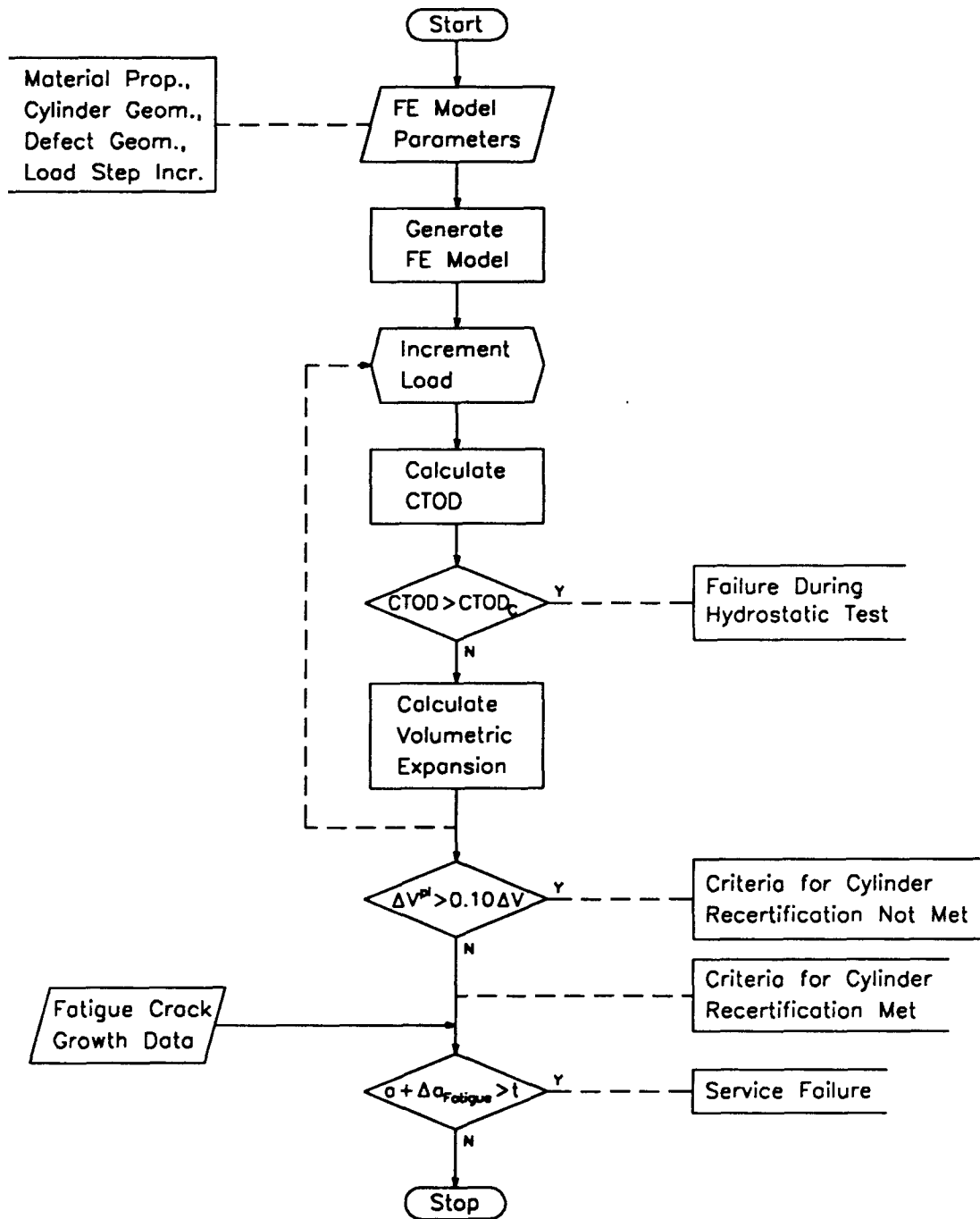
Figure 5.1: Flowchart illustrating approach to assess criteria for NGV cylinder recertification.
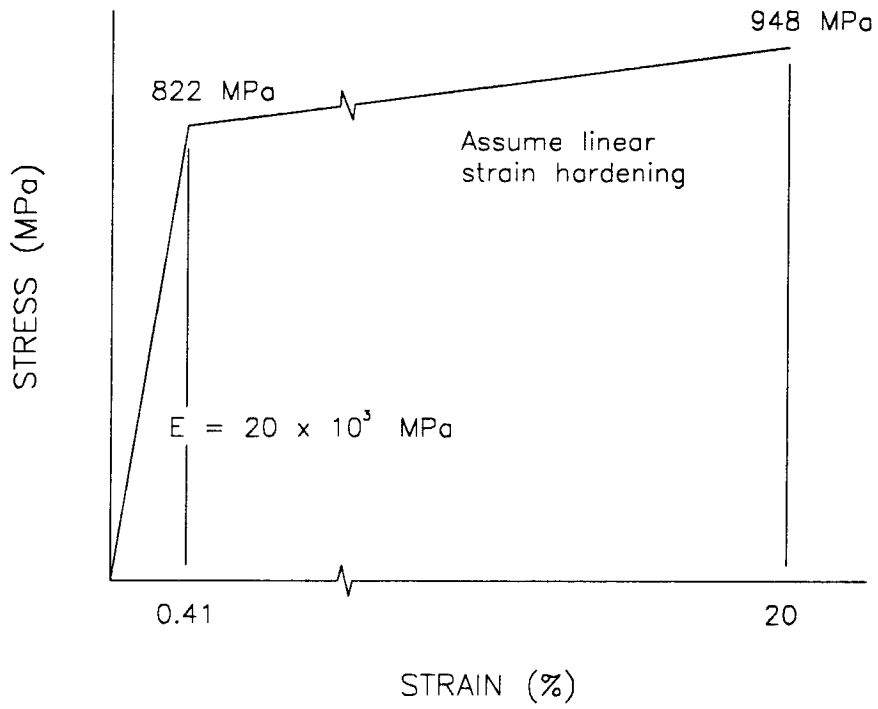
Figure 5.2: Idealized stress-strain relationship for 4130X NGV cylinder steel.
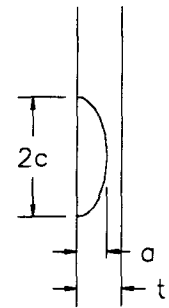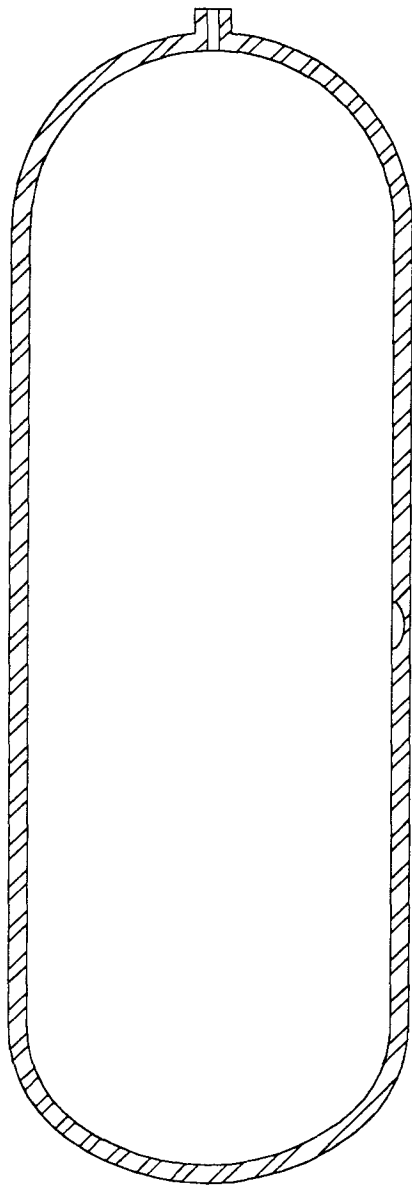
Defect Geometry

Figure 5.3: NGV cylinder/defect geometry.
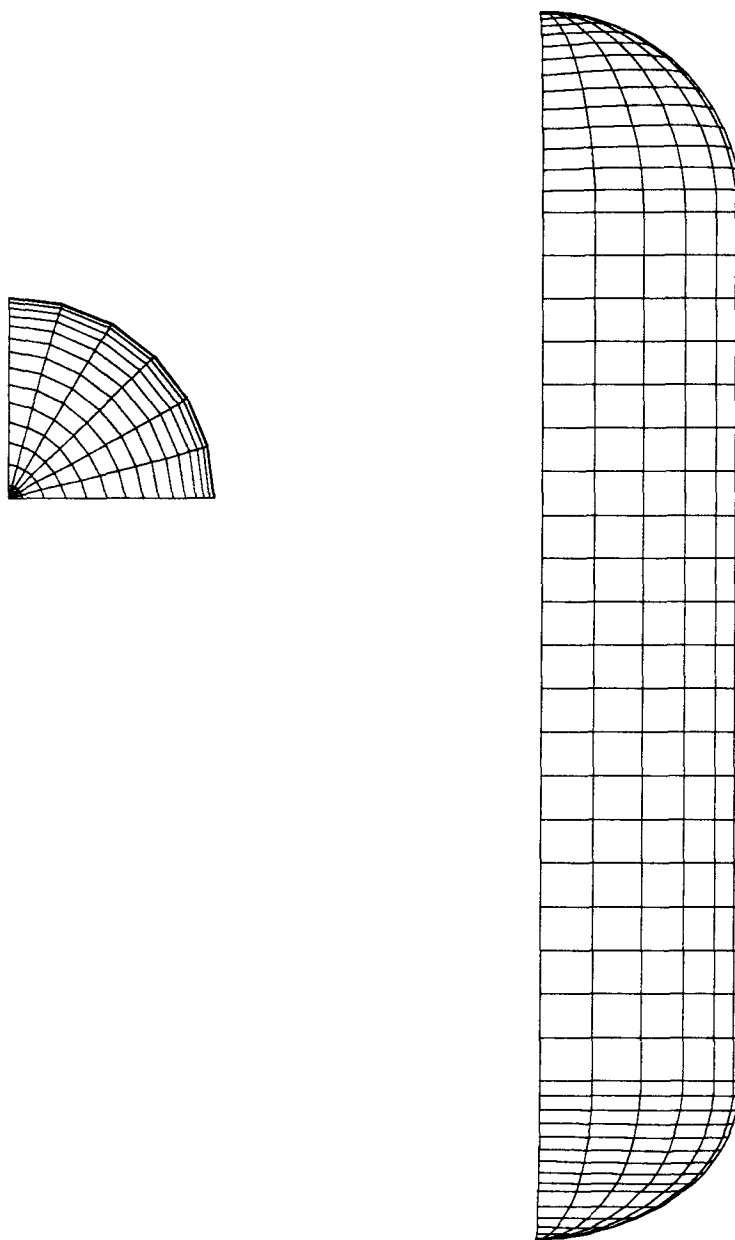
Figure 5.4: Finite element mesh for cylinder.
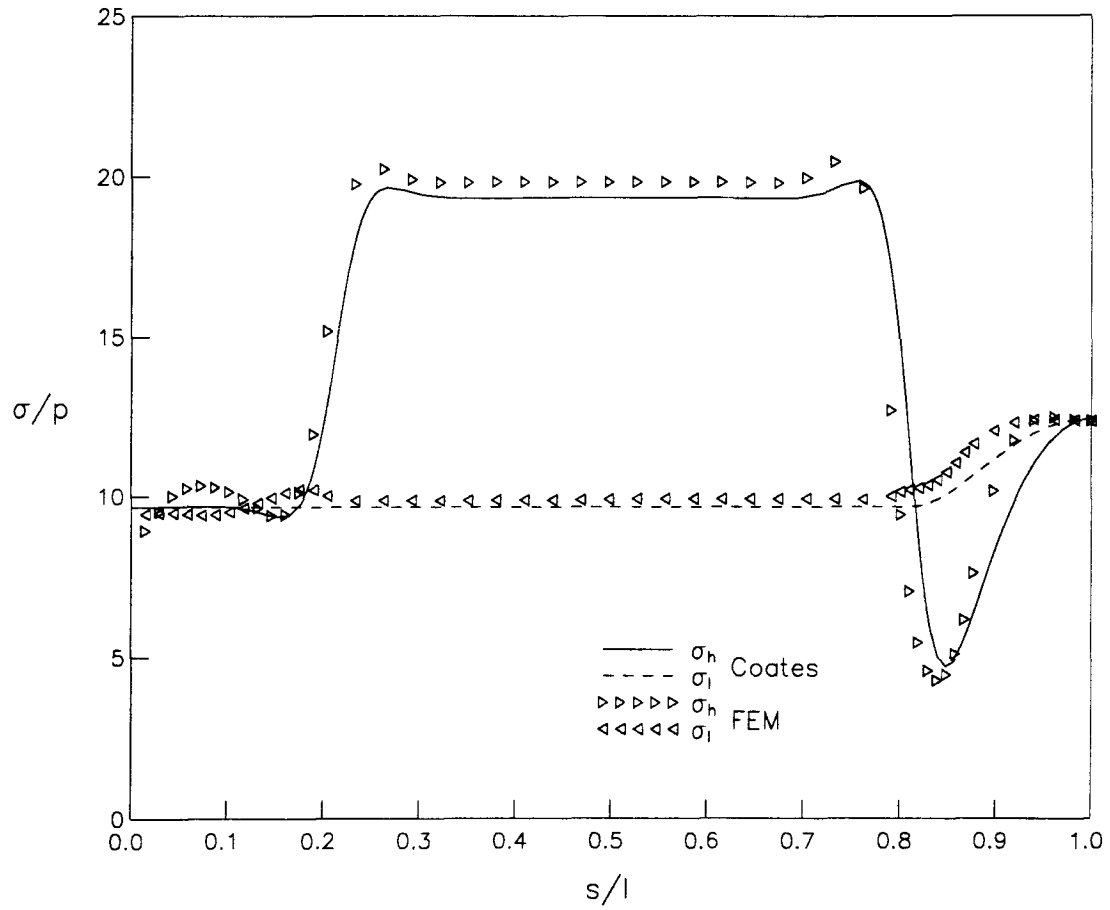
Figure 5.5: Finite element longitudinal and hoop membrane stress ($s/l = $ non-dimensional distance from nozzle end of cylinder).
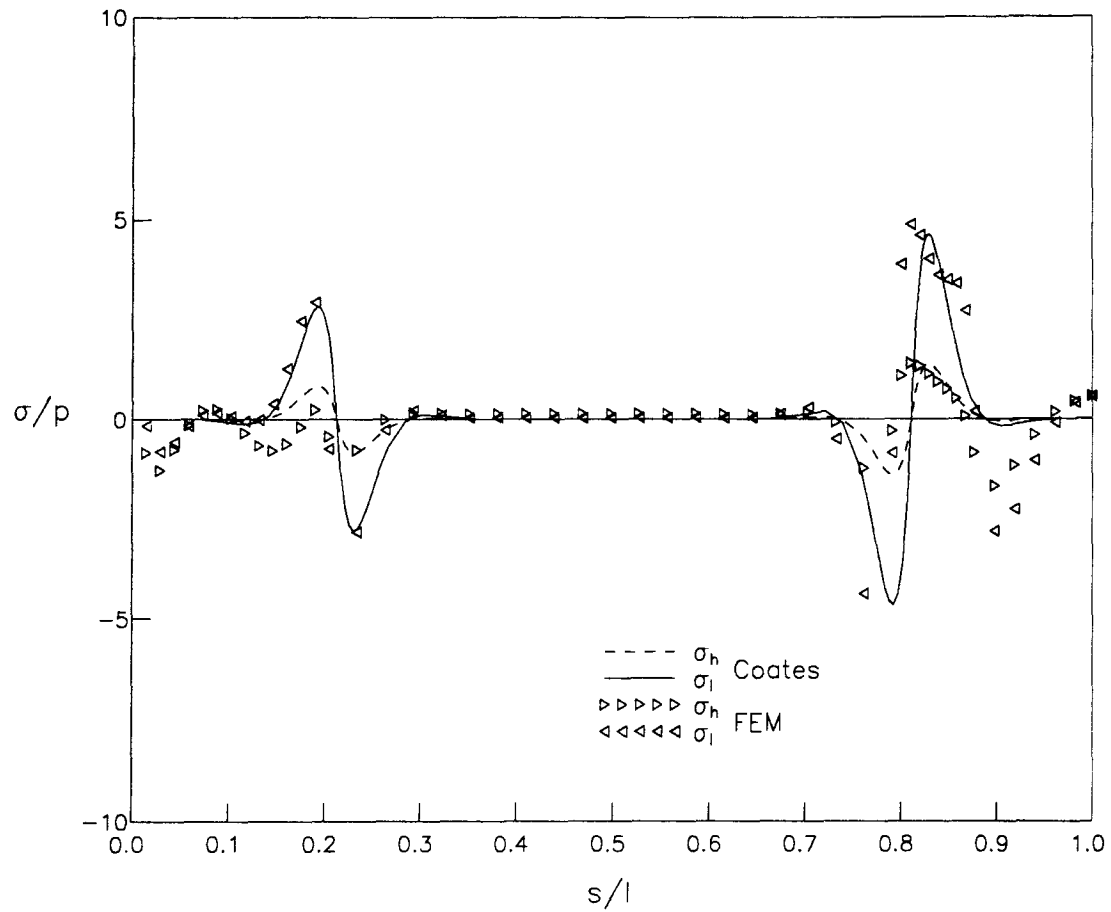
Figure 5.6: Finite element longitudinal and hoop bending stress ($s/l =$ non-dimensional distance from nozzle end of cylinder).
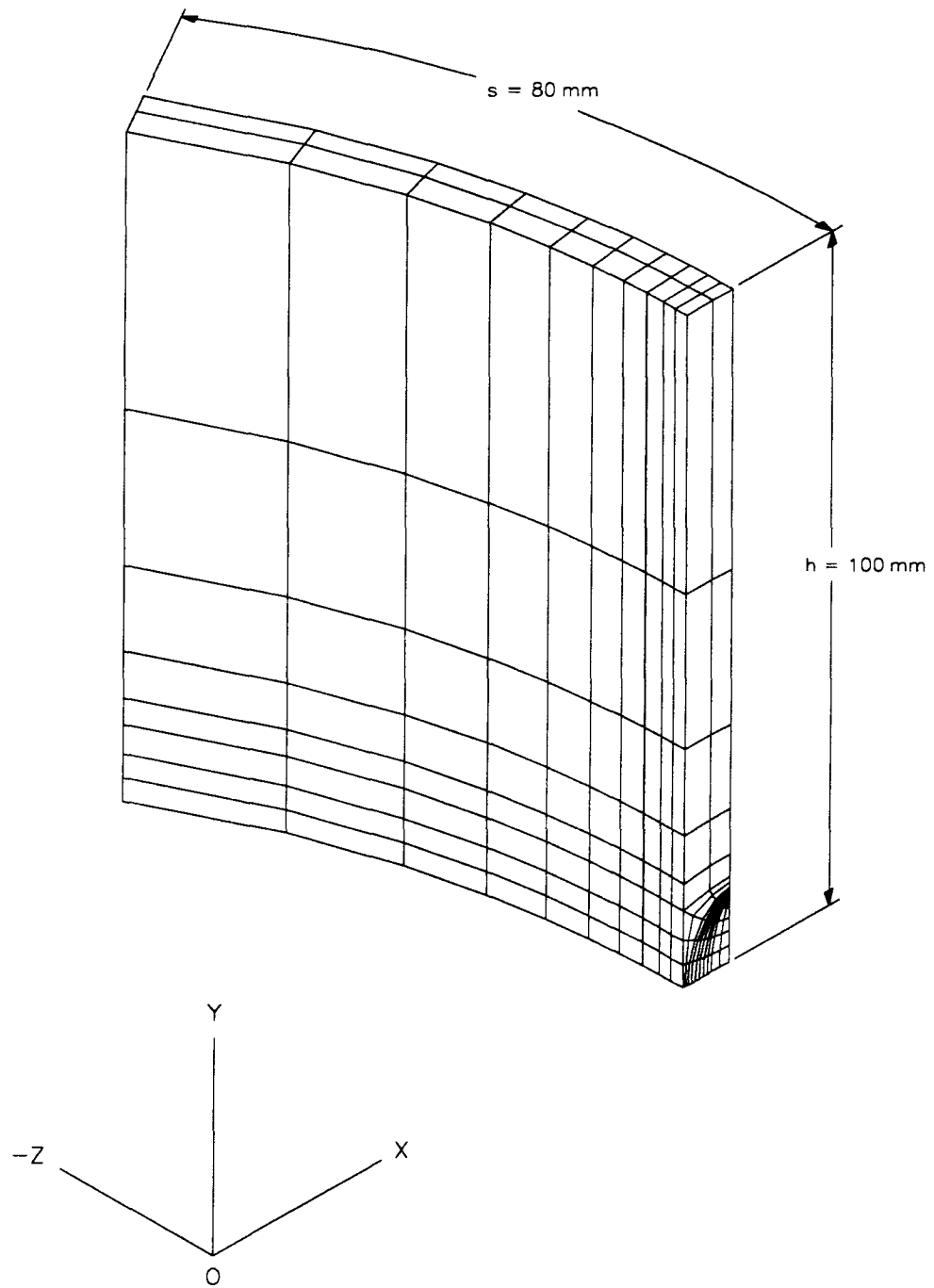
Figure 5.7: Finite element mesh for submodelled region of cylinder.
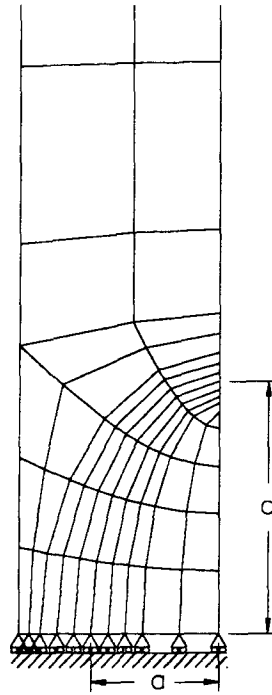
(a) Crack plane $(Z = 0)$
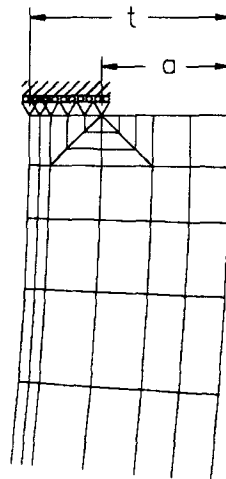
(b) Crack tip $(Y = 0)$

Figure 5.8: Elliptical crack profile and crack tip (finite element mesh for submodelled region of cylinder).

$$\{u\}_s \;=\; \{u\} \;+\; \{r\} \;\times\; \{\theta\}$$

$u_z = 0$

$u_Y = 0$

Solid Submodel

Shell Model
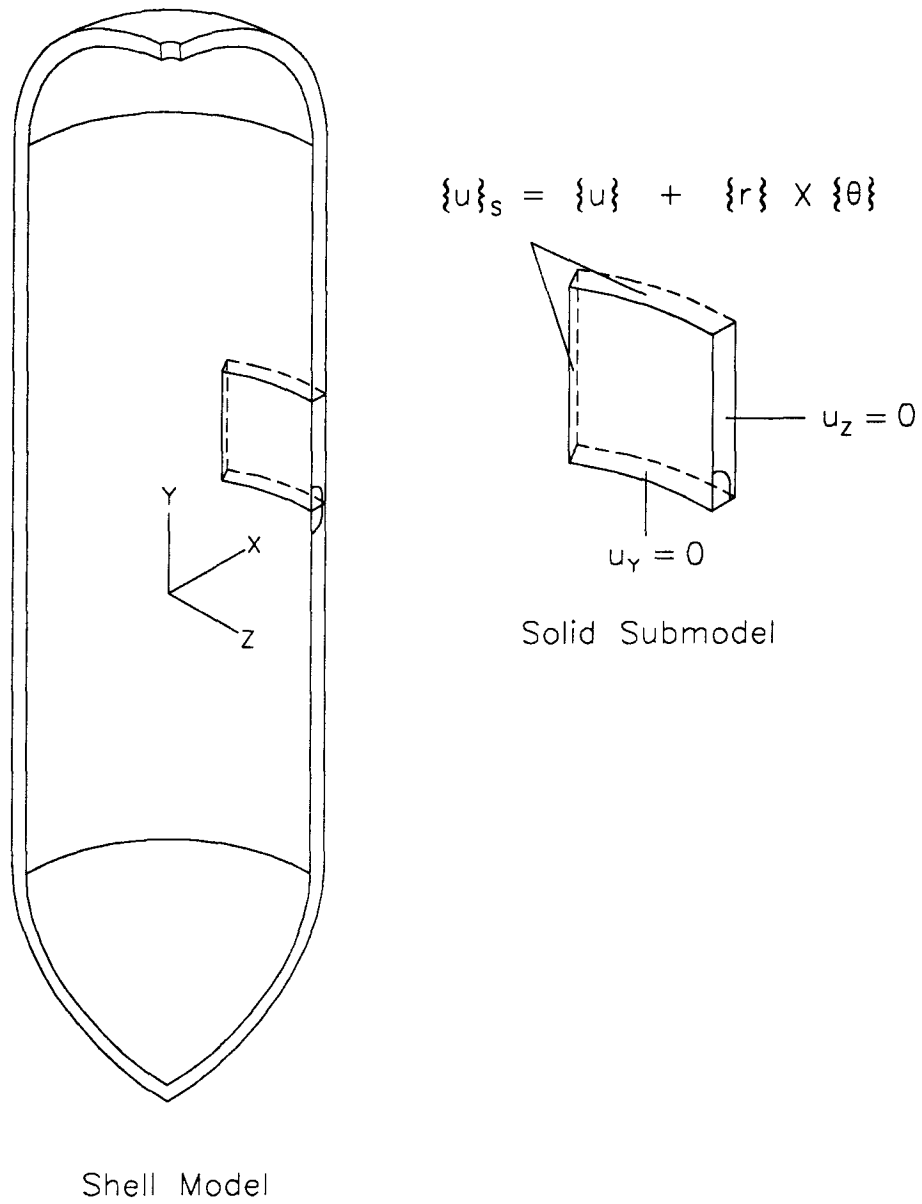
Figure 5.9: Submodelled region of cylinder.

$$x' = x \sqrt{1 + \frac{c^2 - a^2}{x^2 + y^2}}$$

$$y' = y$$
$$z' = z$$
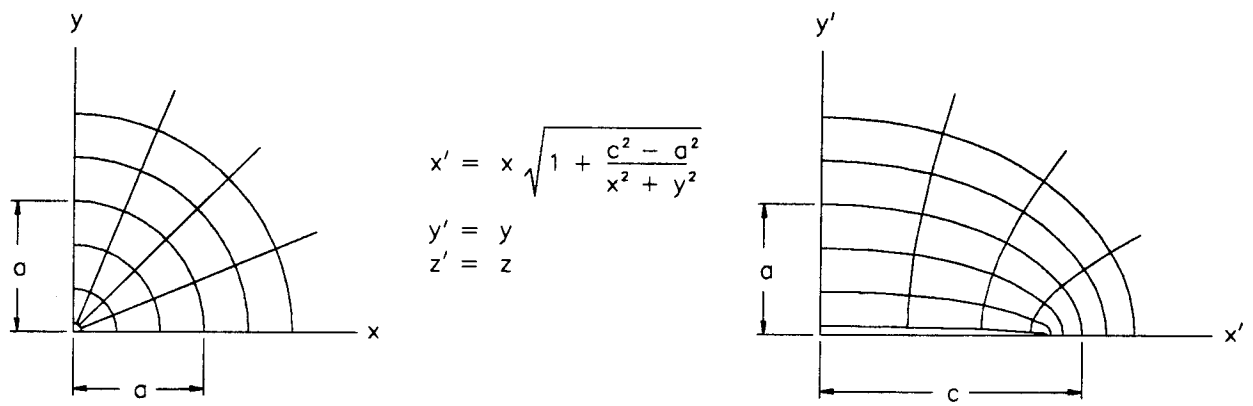
Figure 5.10: Elliptical transformation used in construction of submodel mesh.
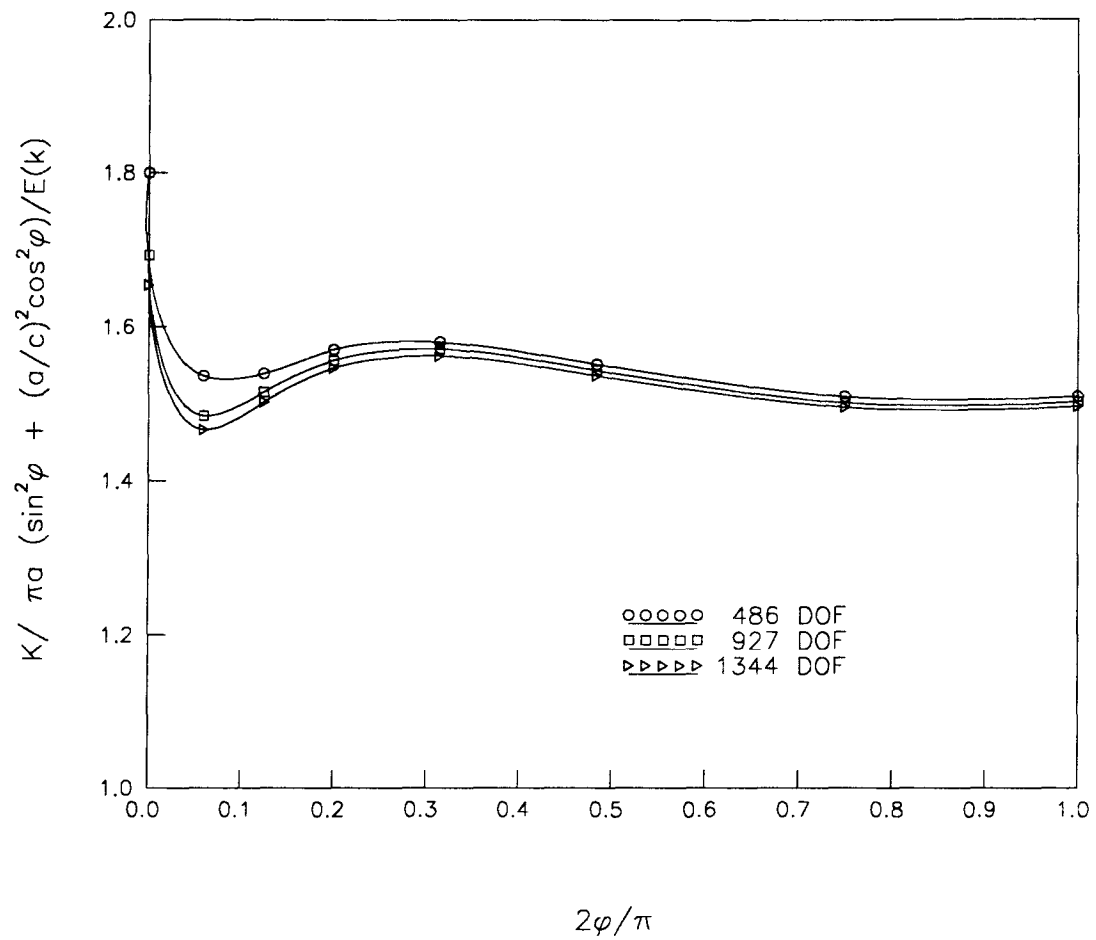
Figure 5.11: Non-dimensional stress intensity factors for the 5 × 15 mm defect.
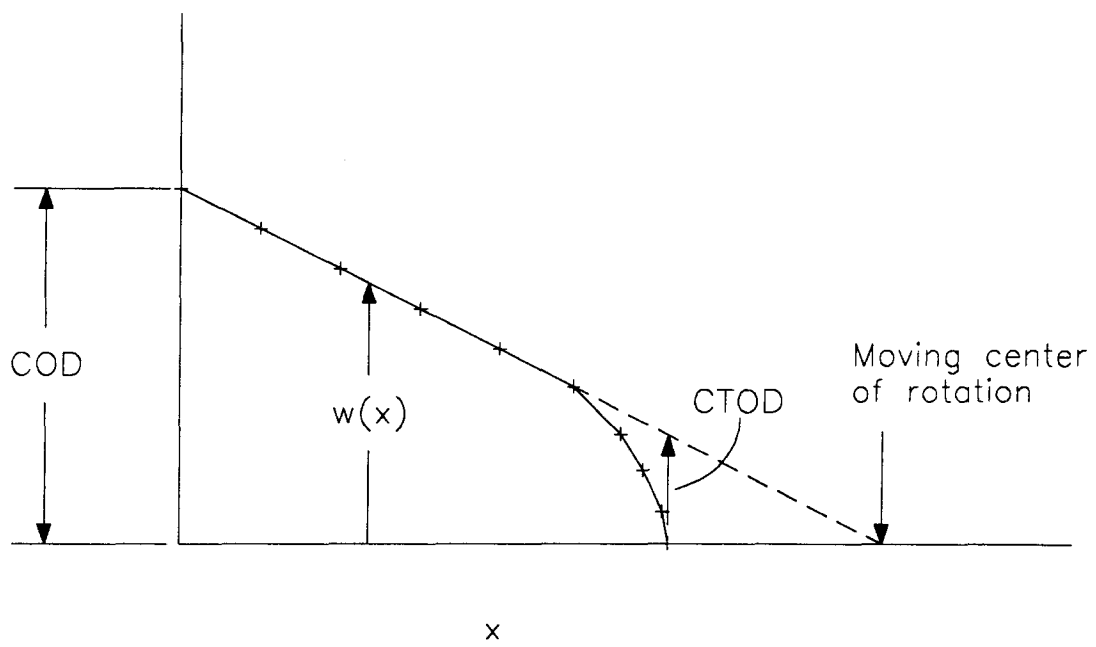
Figure 5.12: Calculation of COD, CTOD and point of rotation.
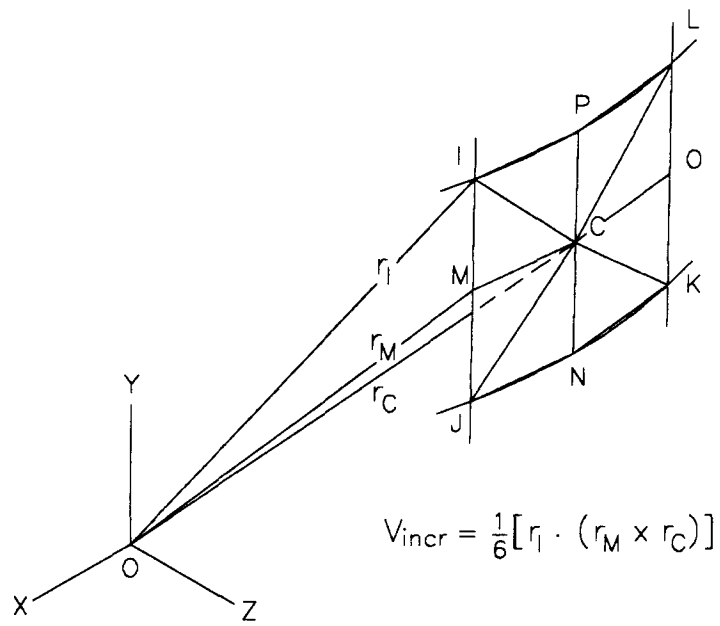
Figure 5.13: Incremental volume bounded by origin and three points on element face.
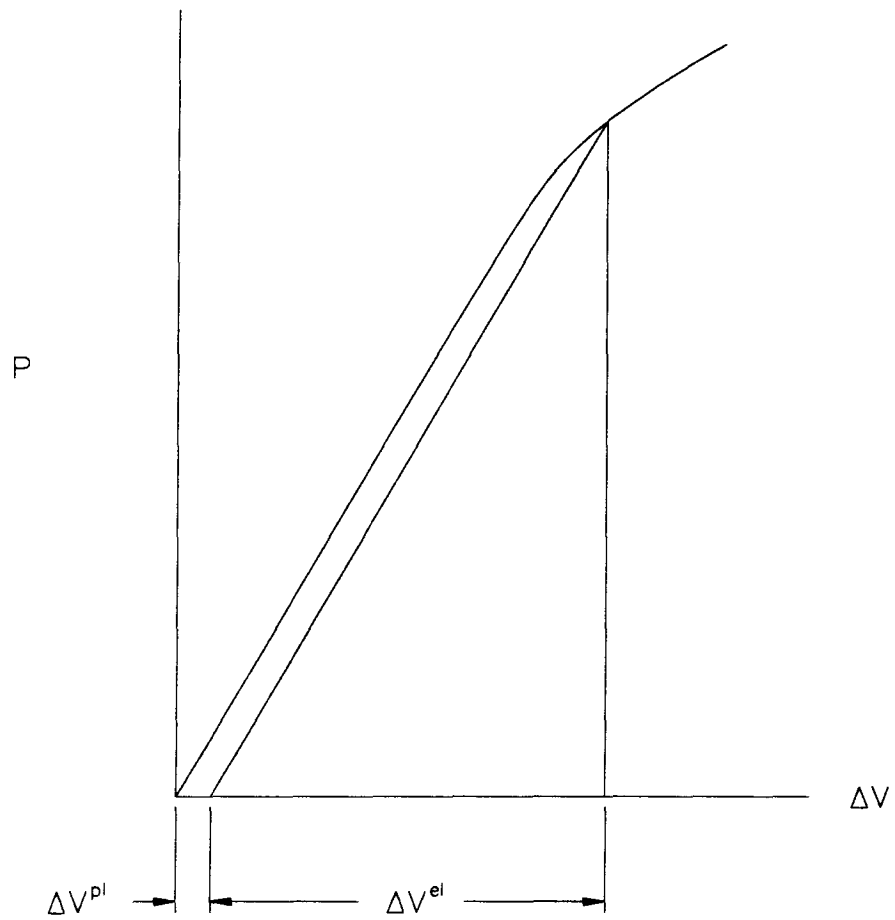
Figure 5.14: Elastic and plastic expansion components of total expansion.
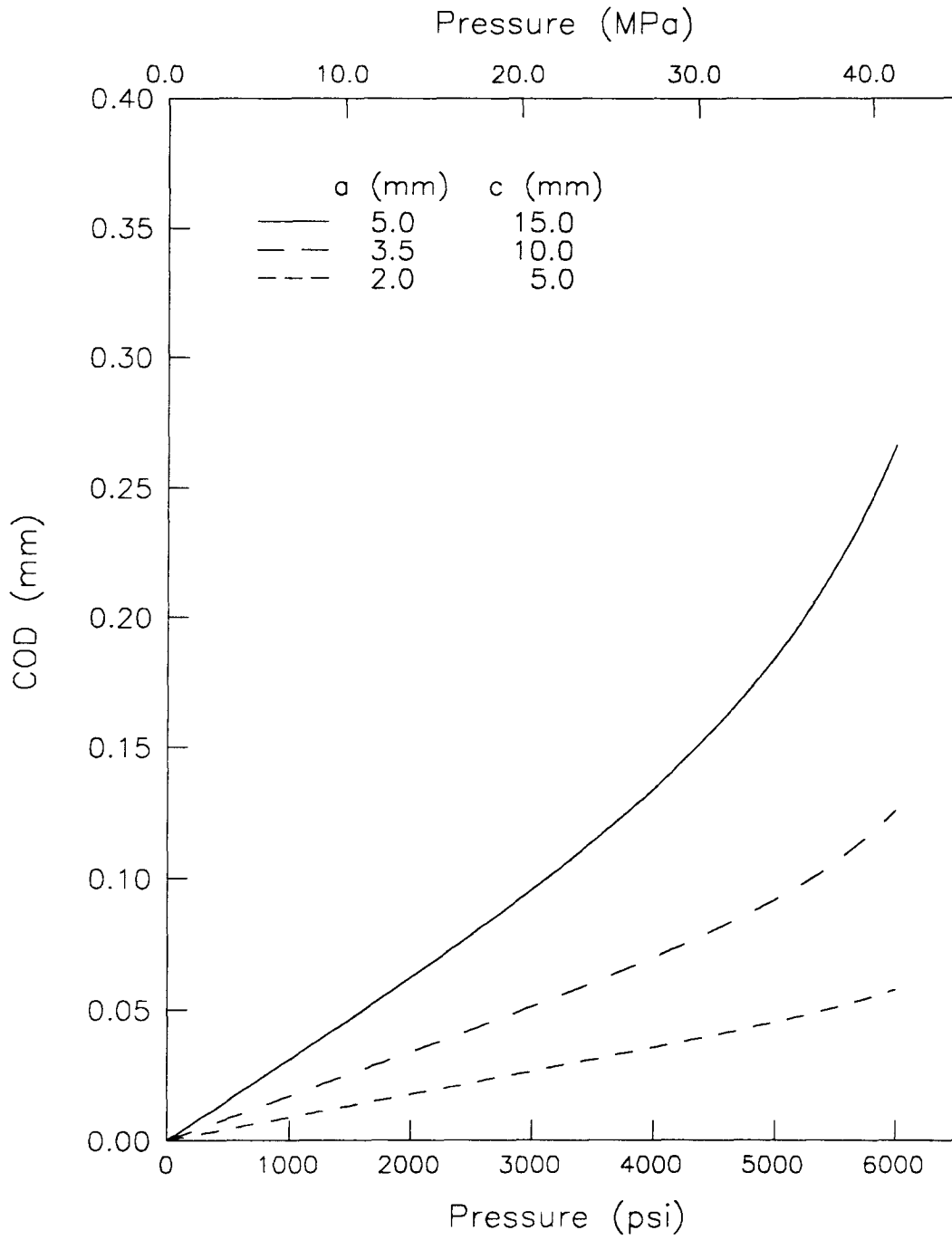
Figure 5.15: Crack opening displacement versus pressure for interior cracks.
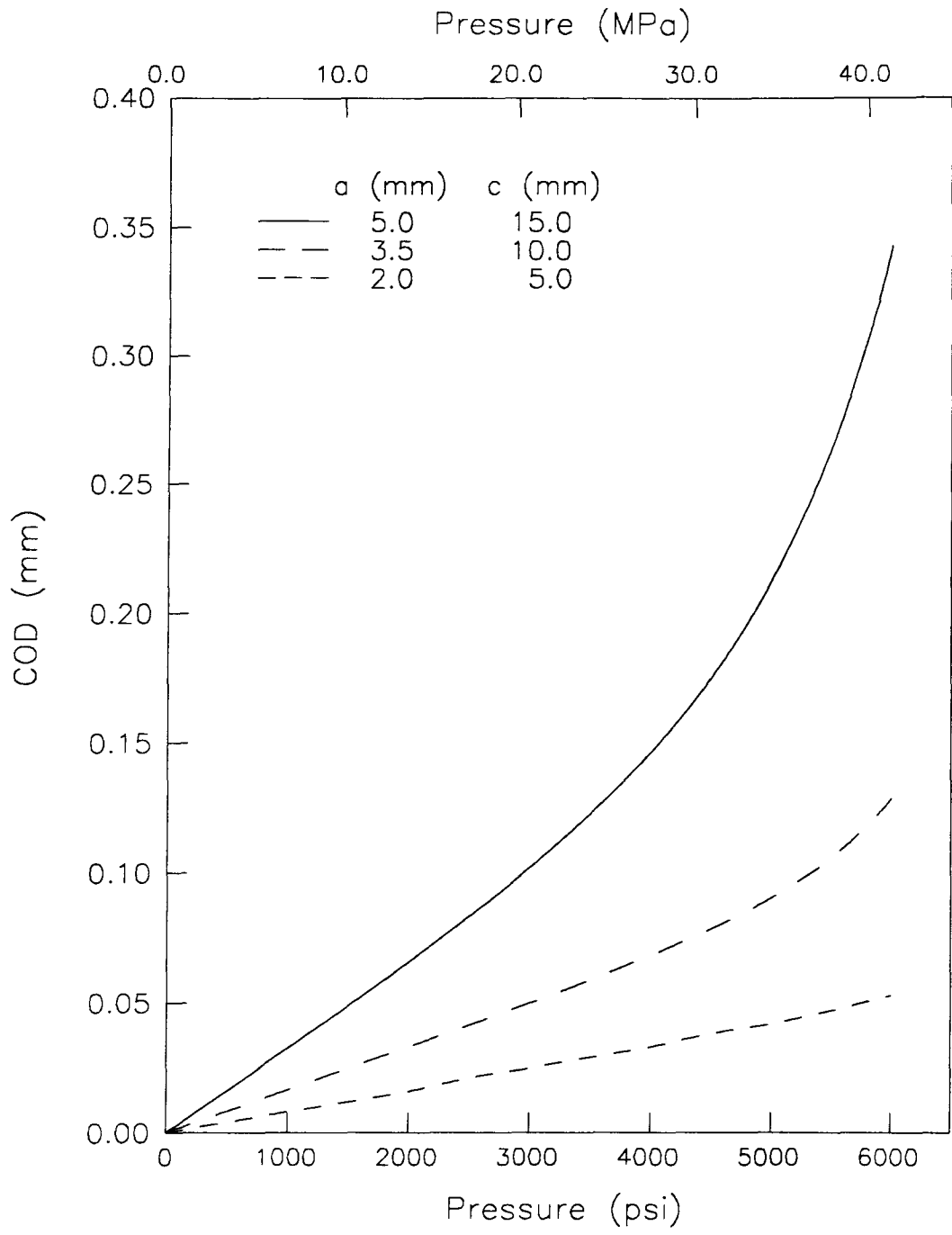
Figure 5.16: Crack opening displacement versus pressure for exterior cracks.
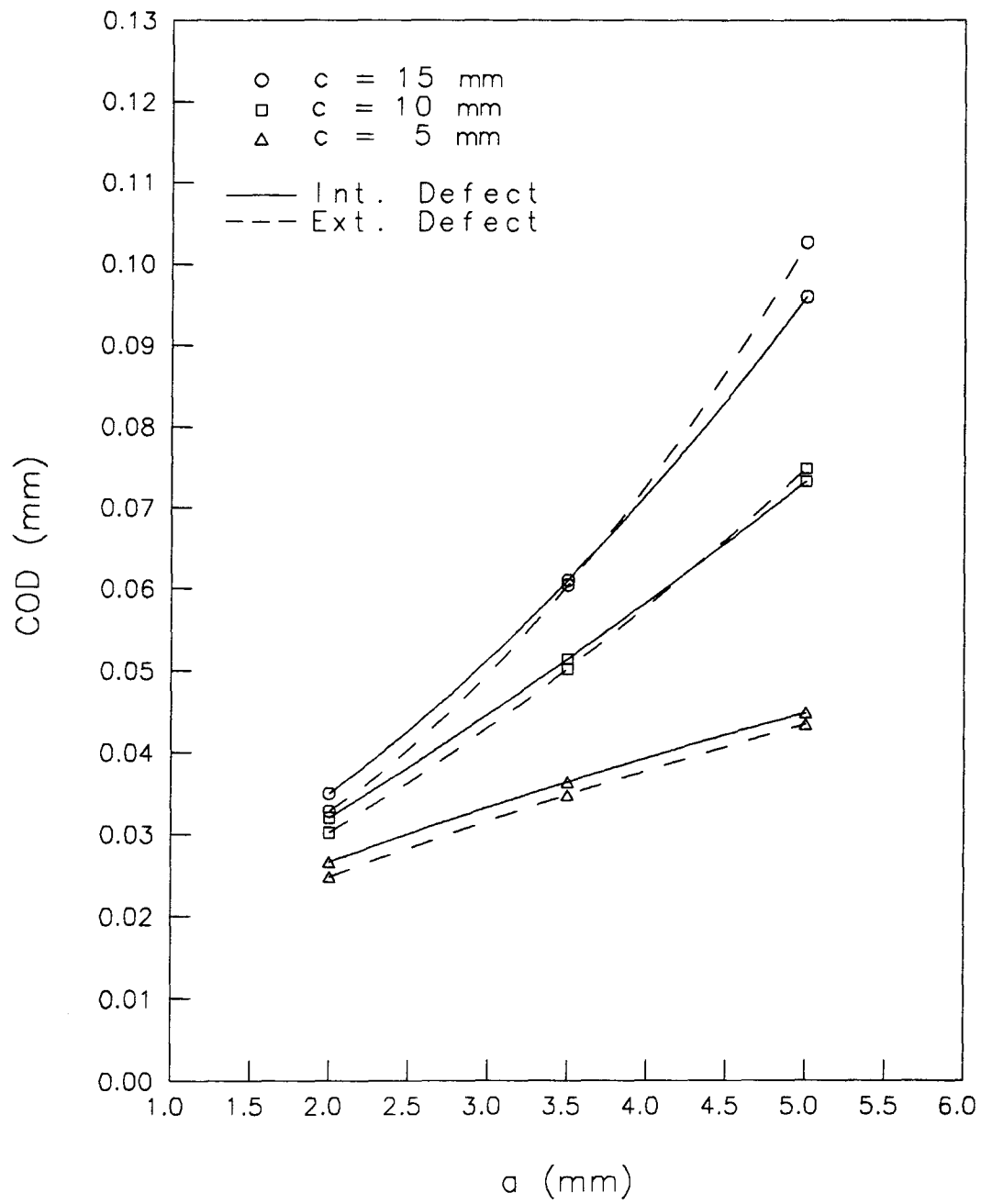
Figure 5.17: Crack opening displacement as a function of crack size at 20.69 MPa (3000 psi).
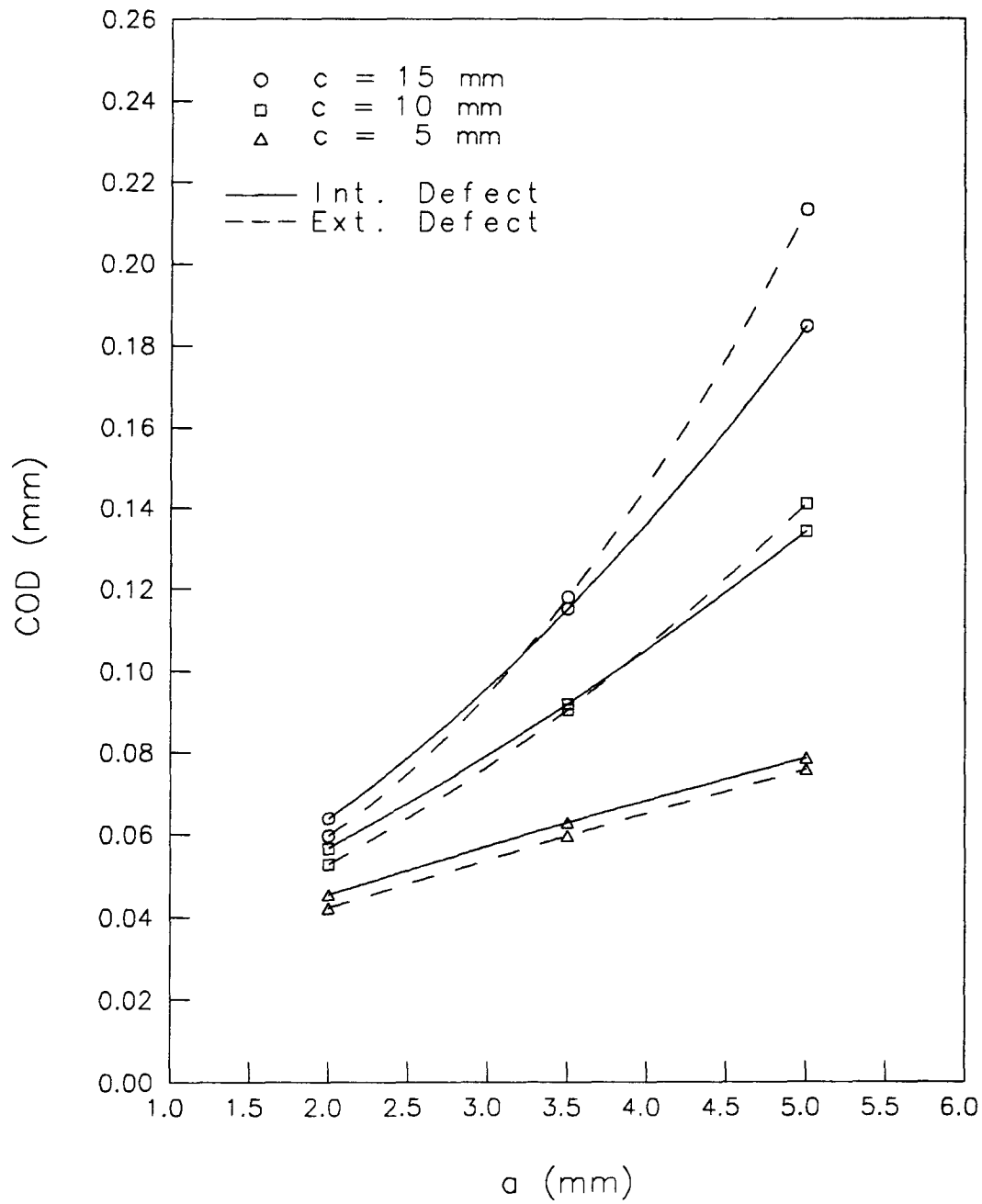
Figure 5.18: Crack opening displacement as a function of crack size at 34.48 MPa (5000 psi).
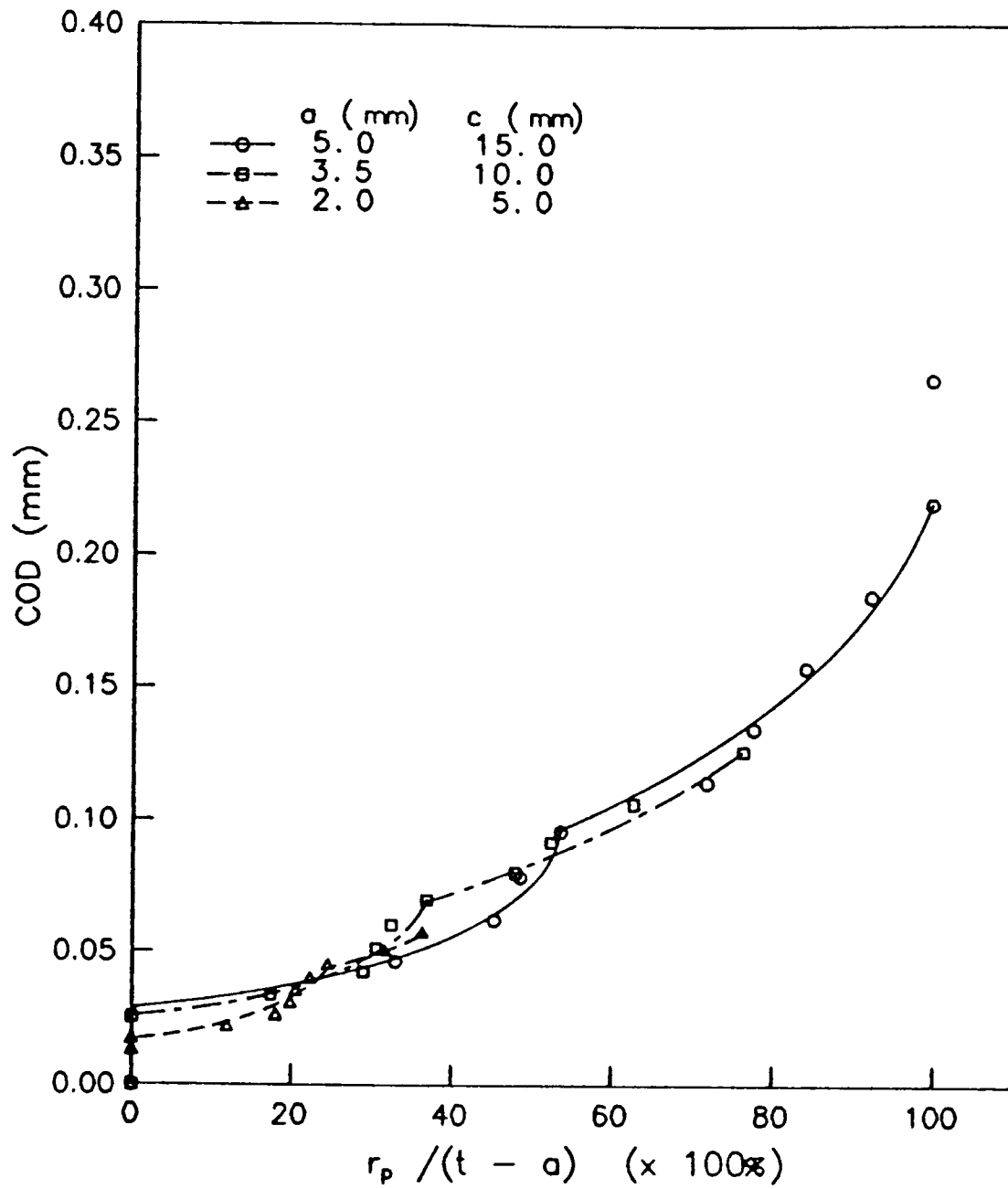
Figure 5.19: Development of plastic zone for interior cracks.
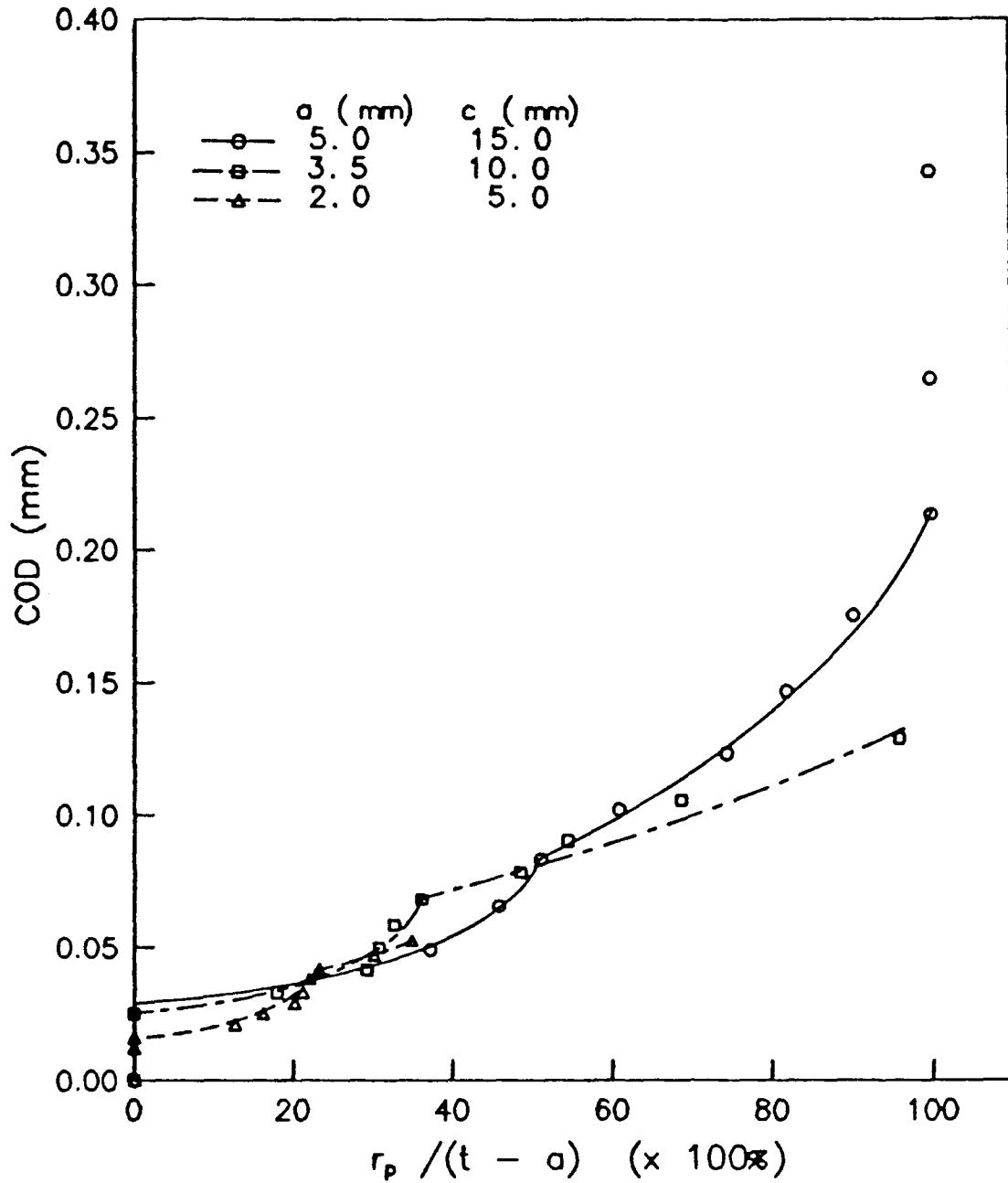
Figure 5.20: Development of plastic zone for exterior cracks.
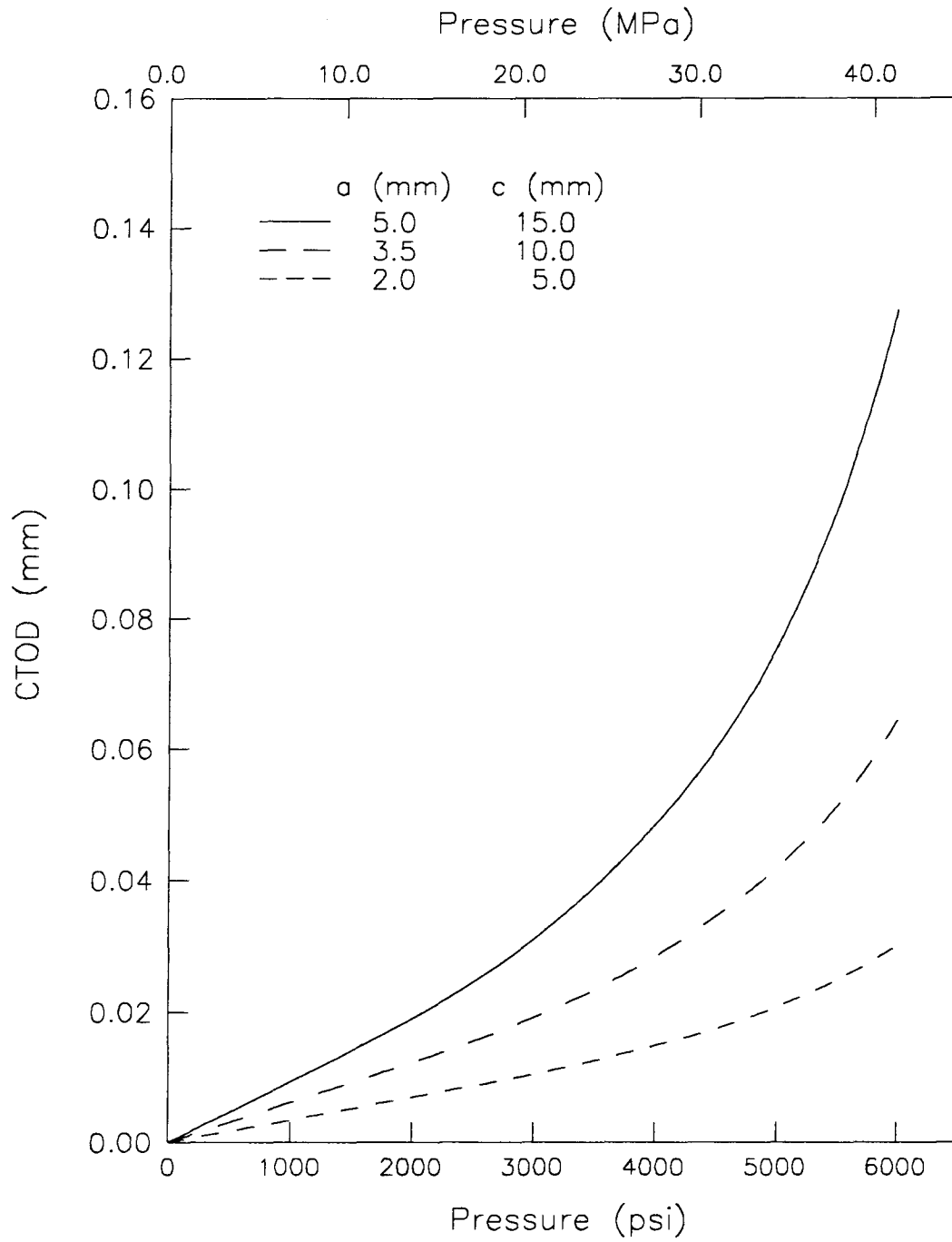
Figure 5.21: Crack tip opening displacement versus pressure for interior cracks.
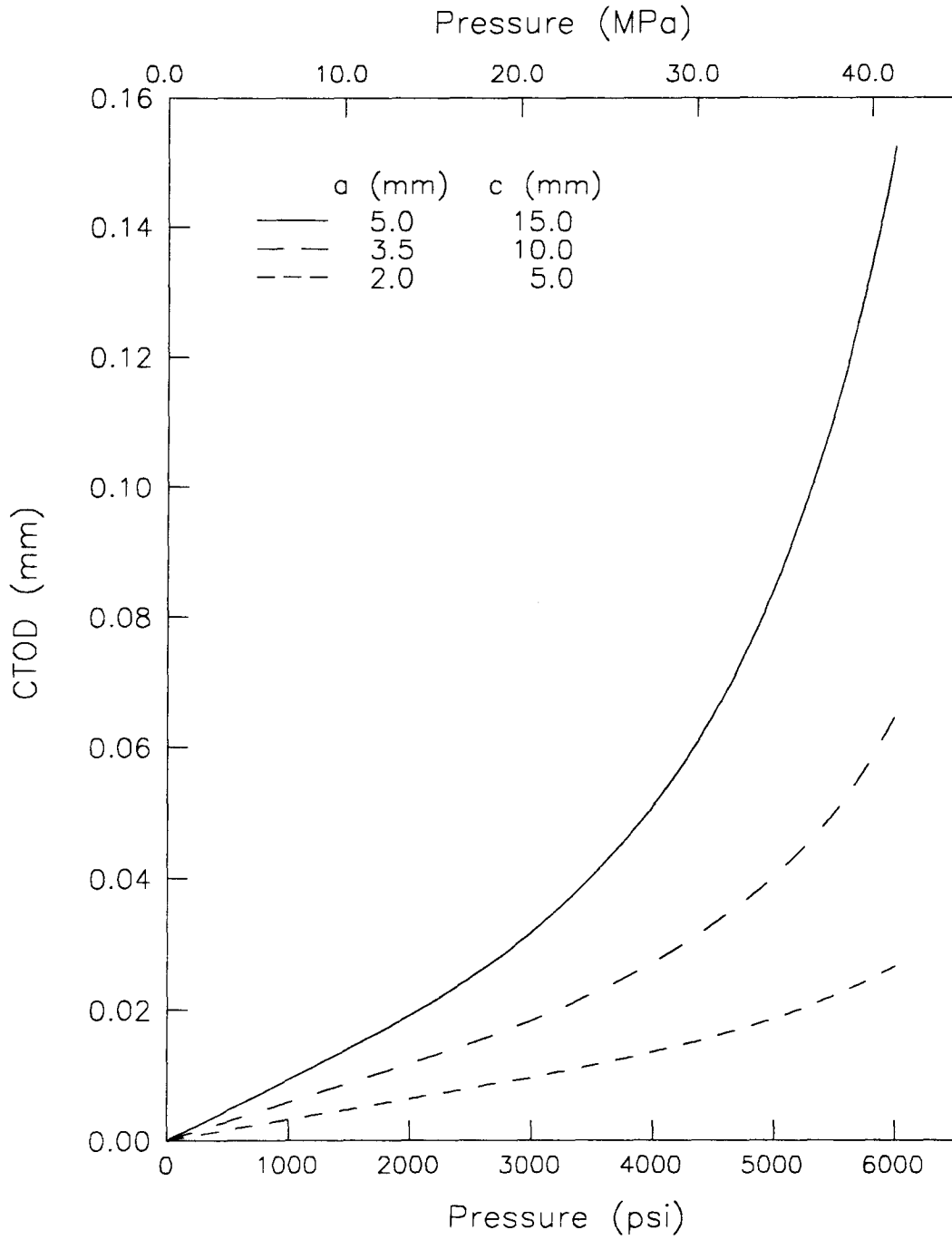
Figure 5.22: Crack tip opening displacement versus pressure for exterior cracks.
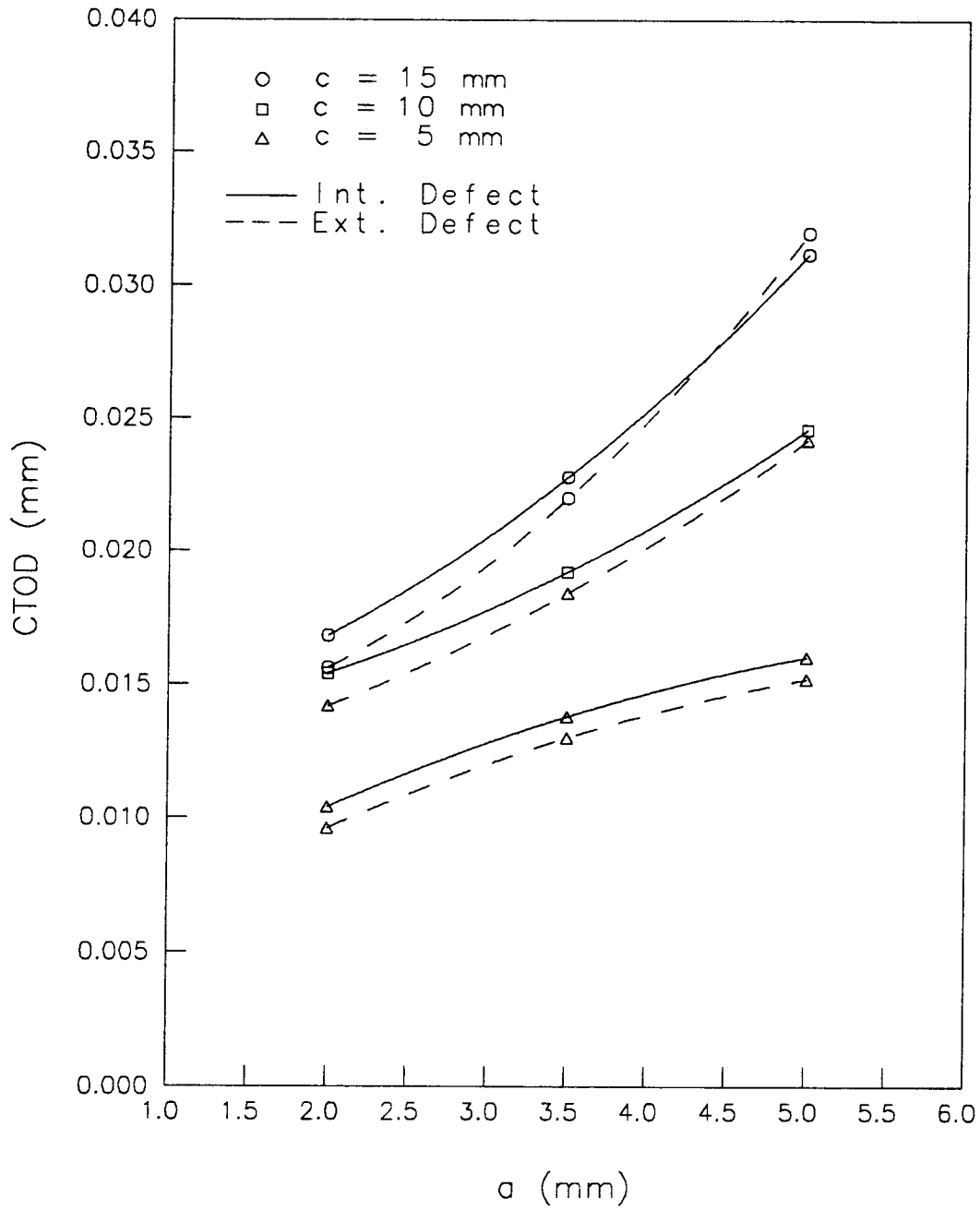
Figure 5.23: Crack tip opening displacement as a function of crack size at 20.69 MPa (3000 psi).
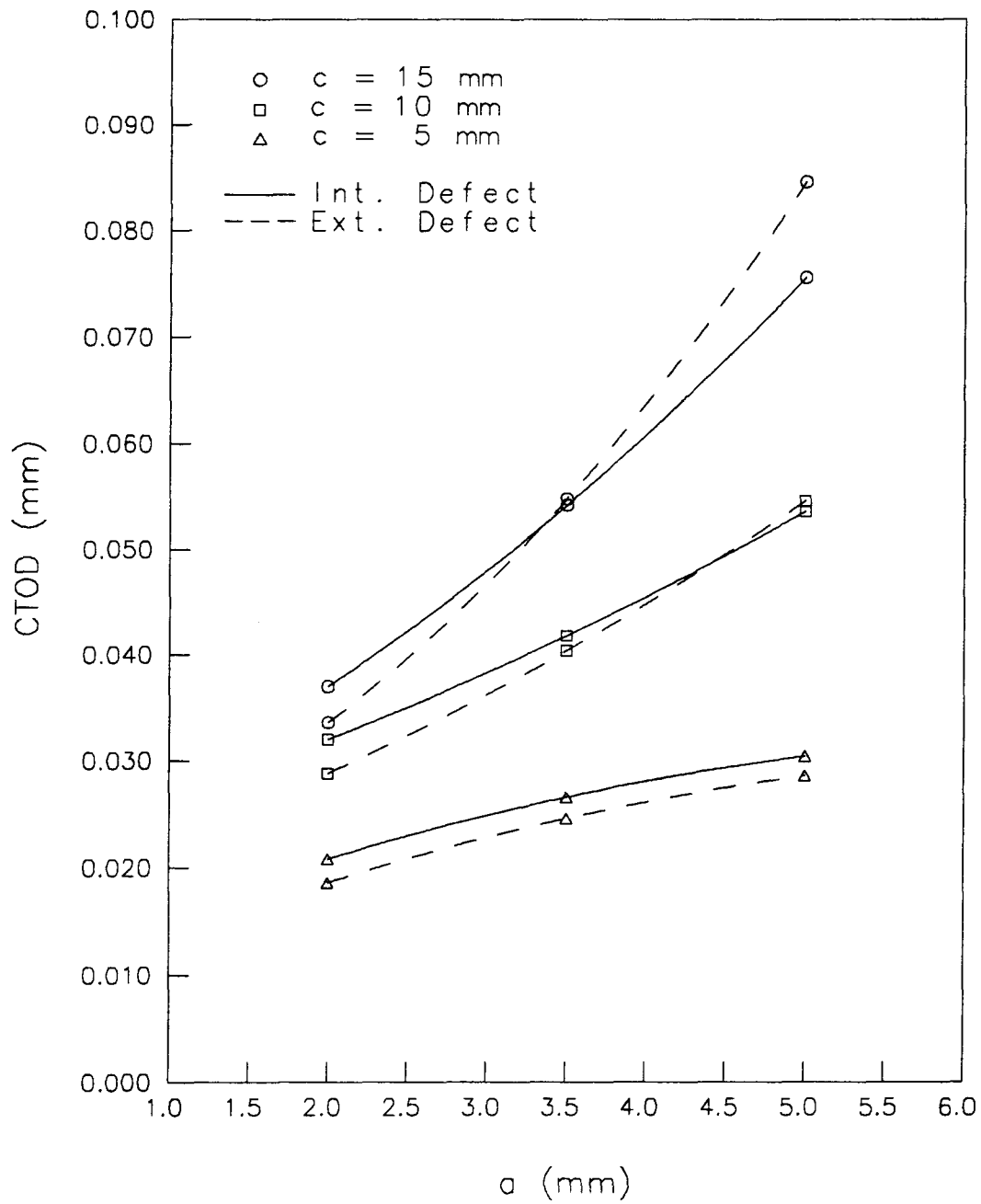
Figure 5.24: Crack tip opening displacement as a function of crack size at 34.48 MPa (5000 psi).
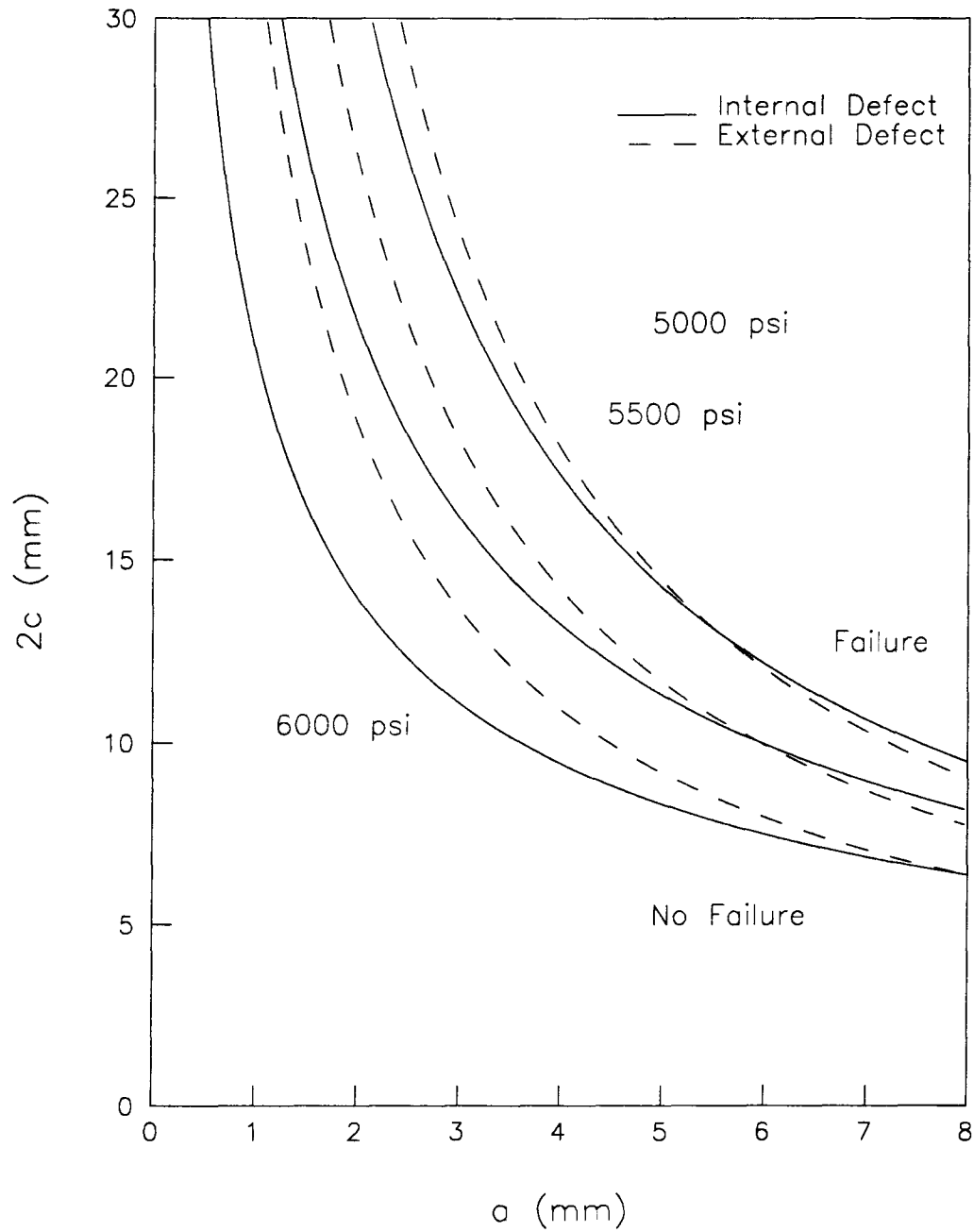
Figure 5.25: Limiting defect dimensions for failure at 34.48, 37.92 and 41.37 MPa (5000, 5500 and 6000 psi).
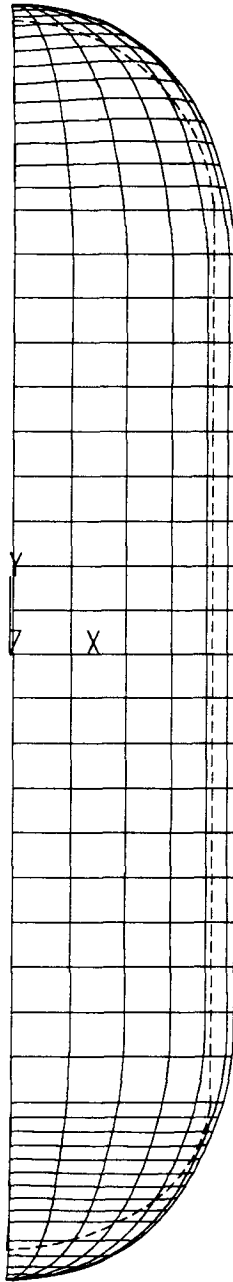
Figure 5.26: Finite element expansion of a NGV cylinder.
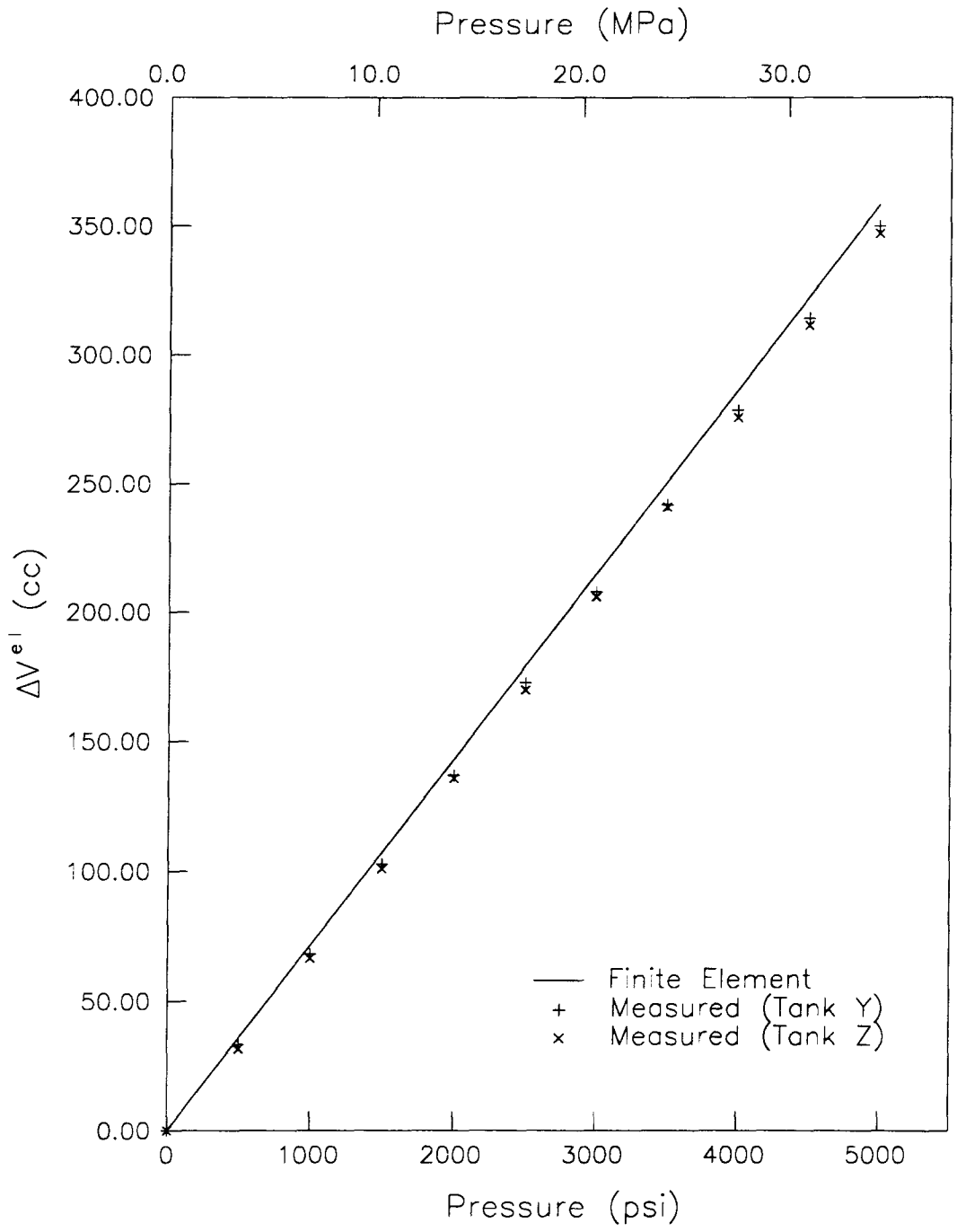
Figure 5.27: Predicted and measured elastic expansion.
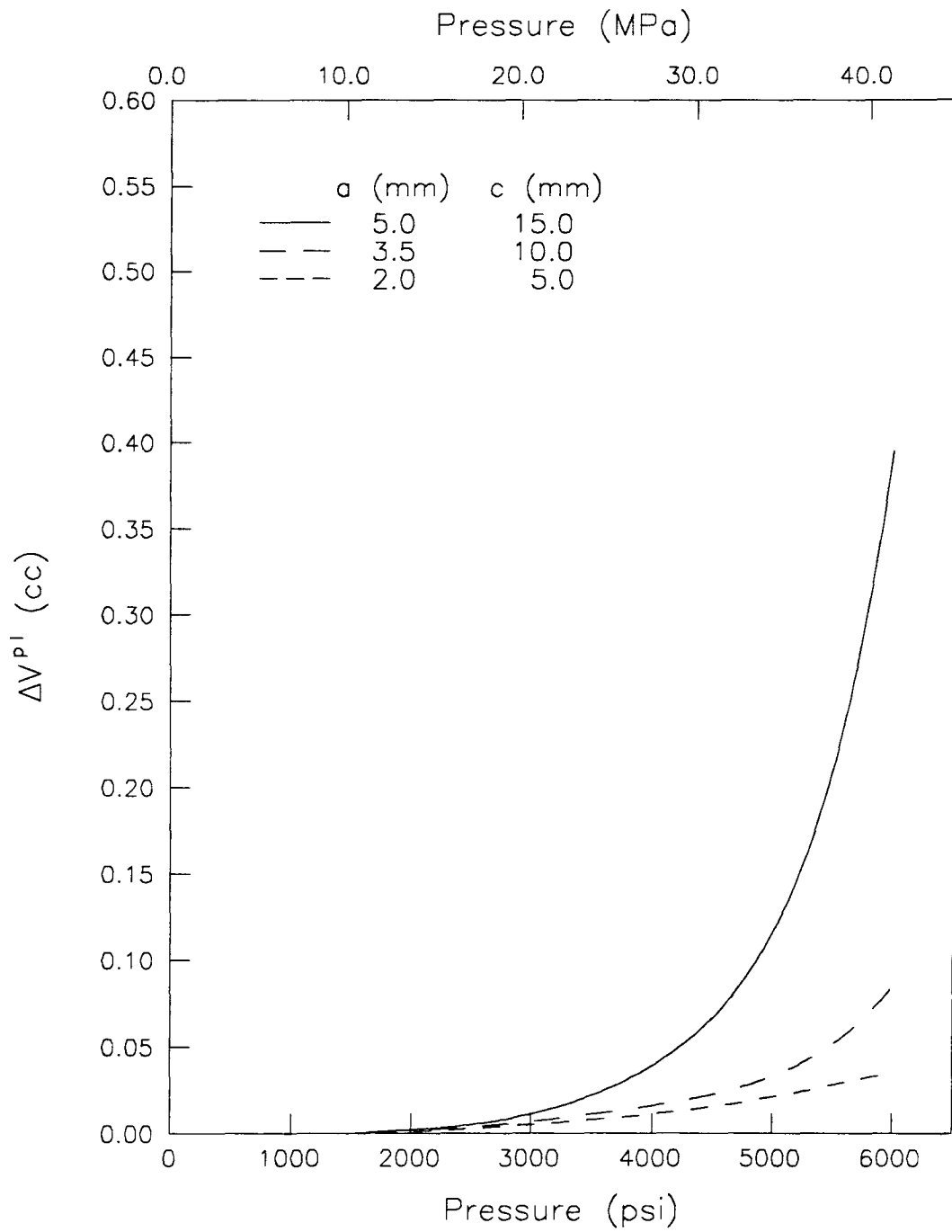
Figure 5.28: Plastic expansion as a function of pressure for interior cracks.
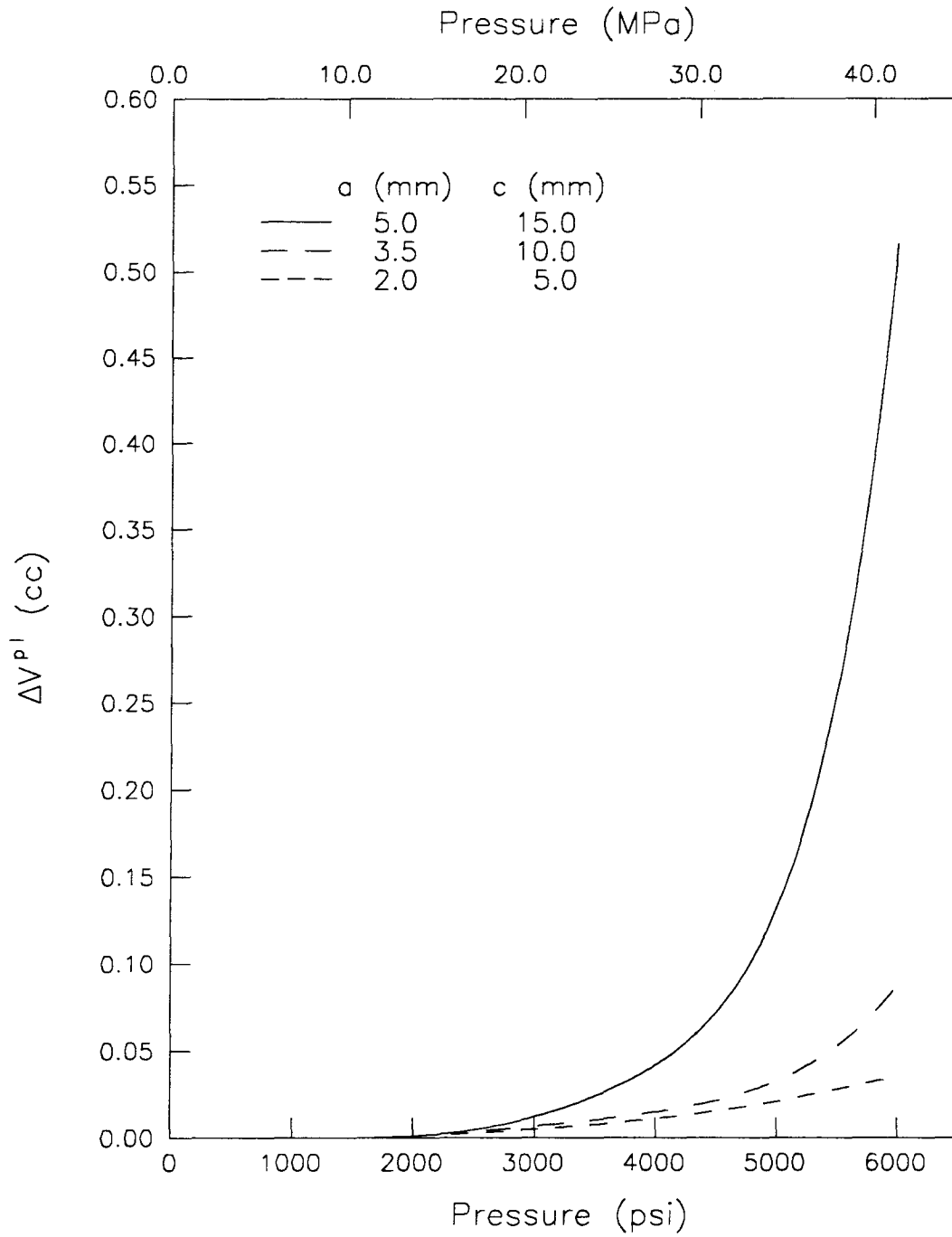
Figure 5.29: Plastic expansion as a function of pressure for exterior cracks.
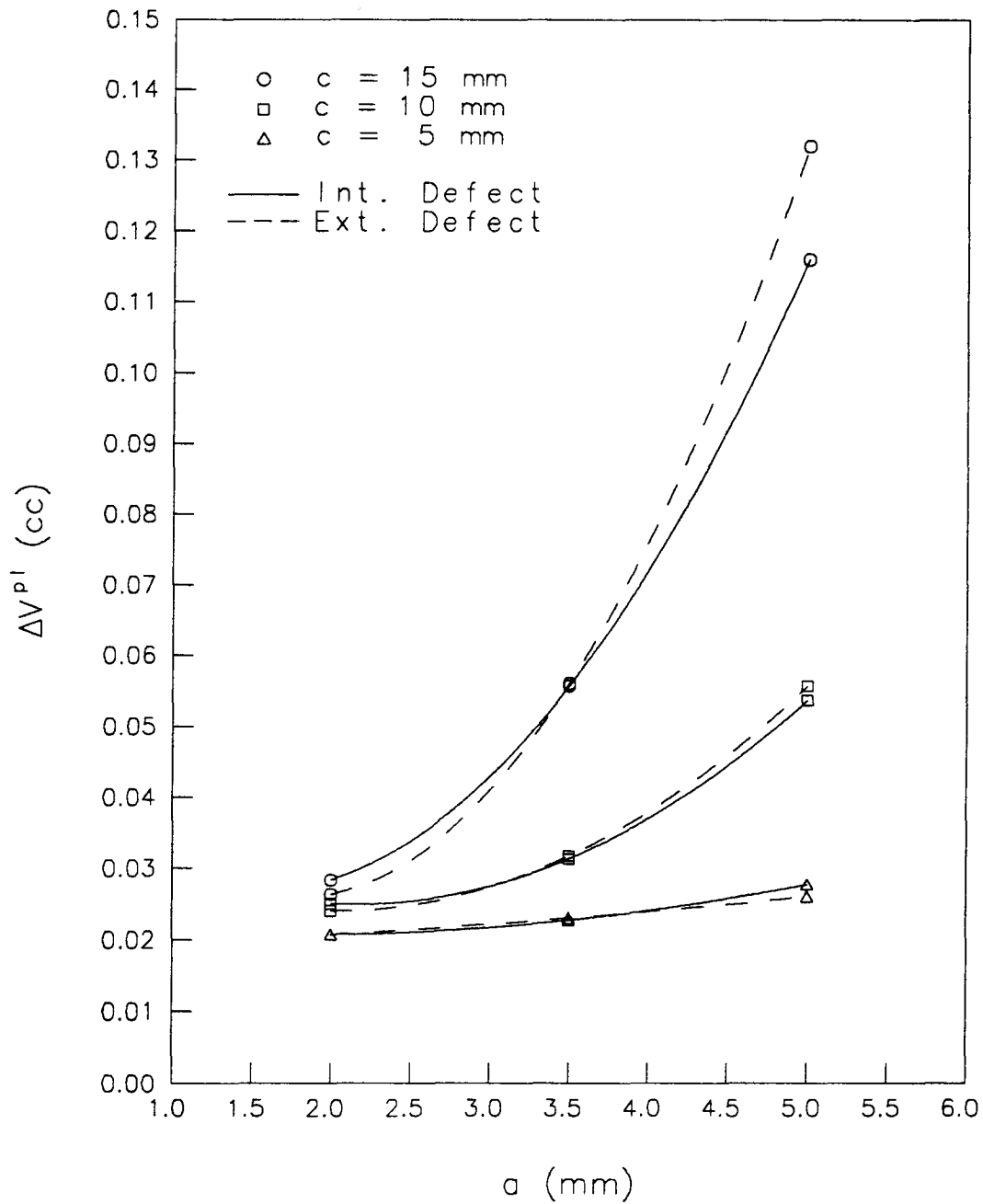
Figure 5.30: Plastic expansion as a function of crack size at 34.48 MPa (5000 psi) (hydrostatic test pressure).
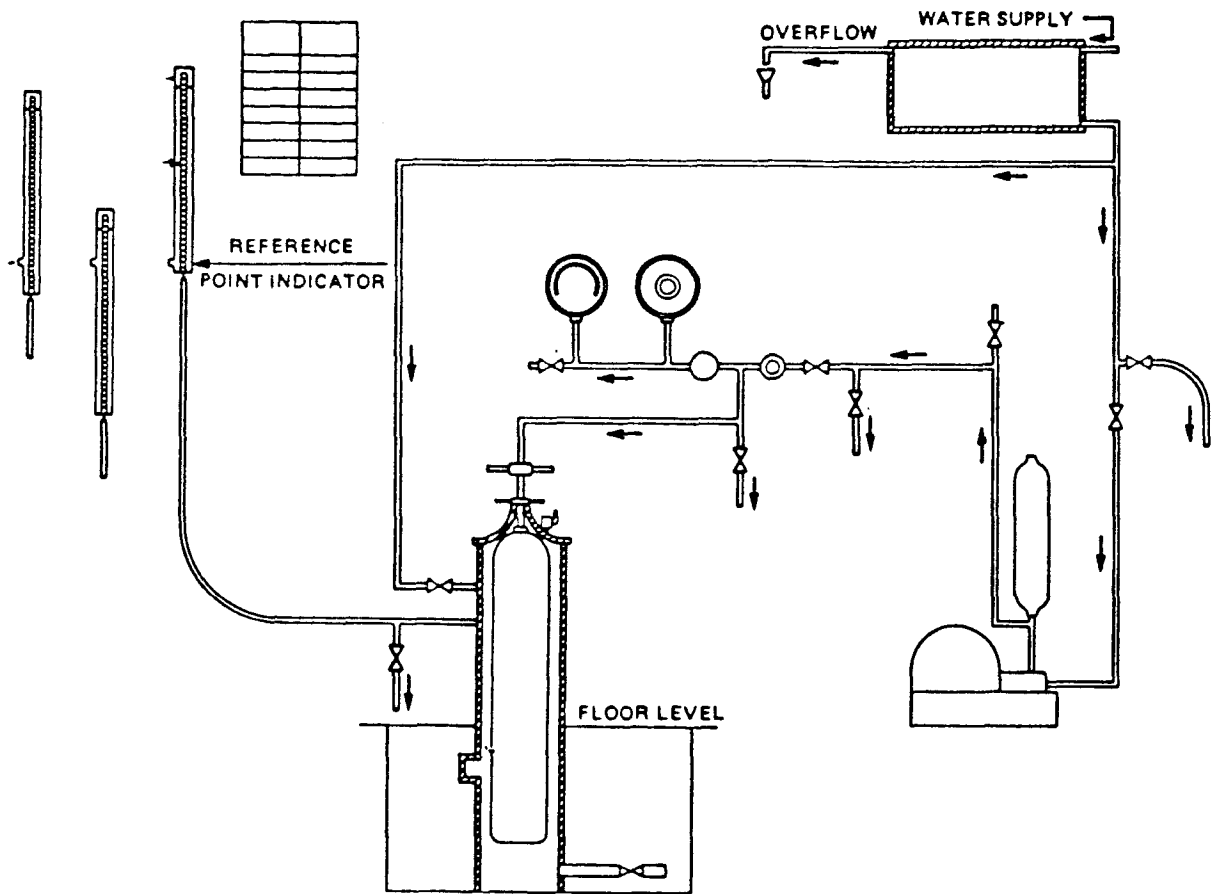
Figure 6.1: Schematic illustration of hydrostatic testing facility.
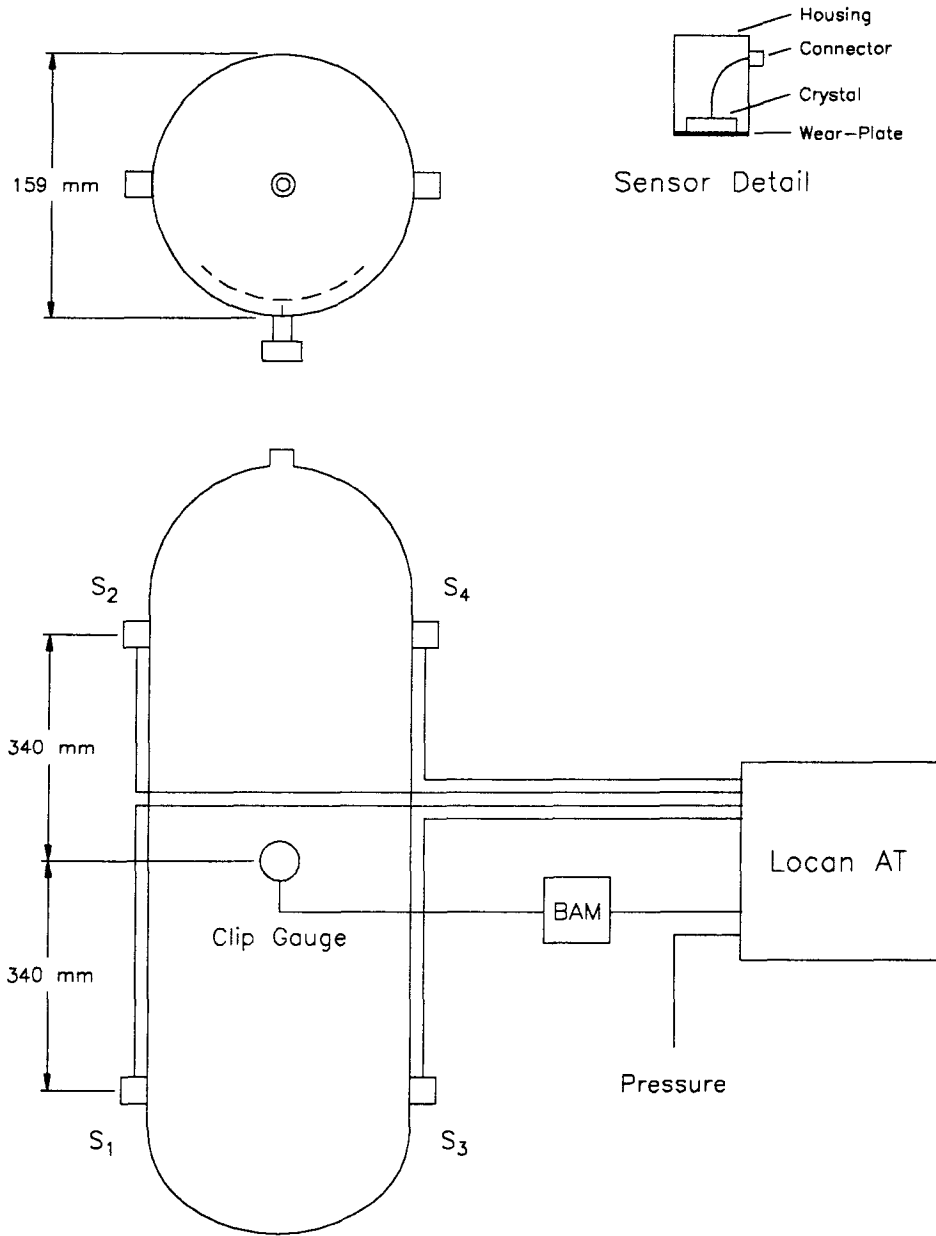
Figure 6.2: Schematic illustration of cylinder instrumentation.
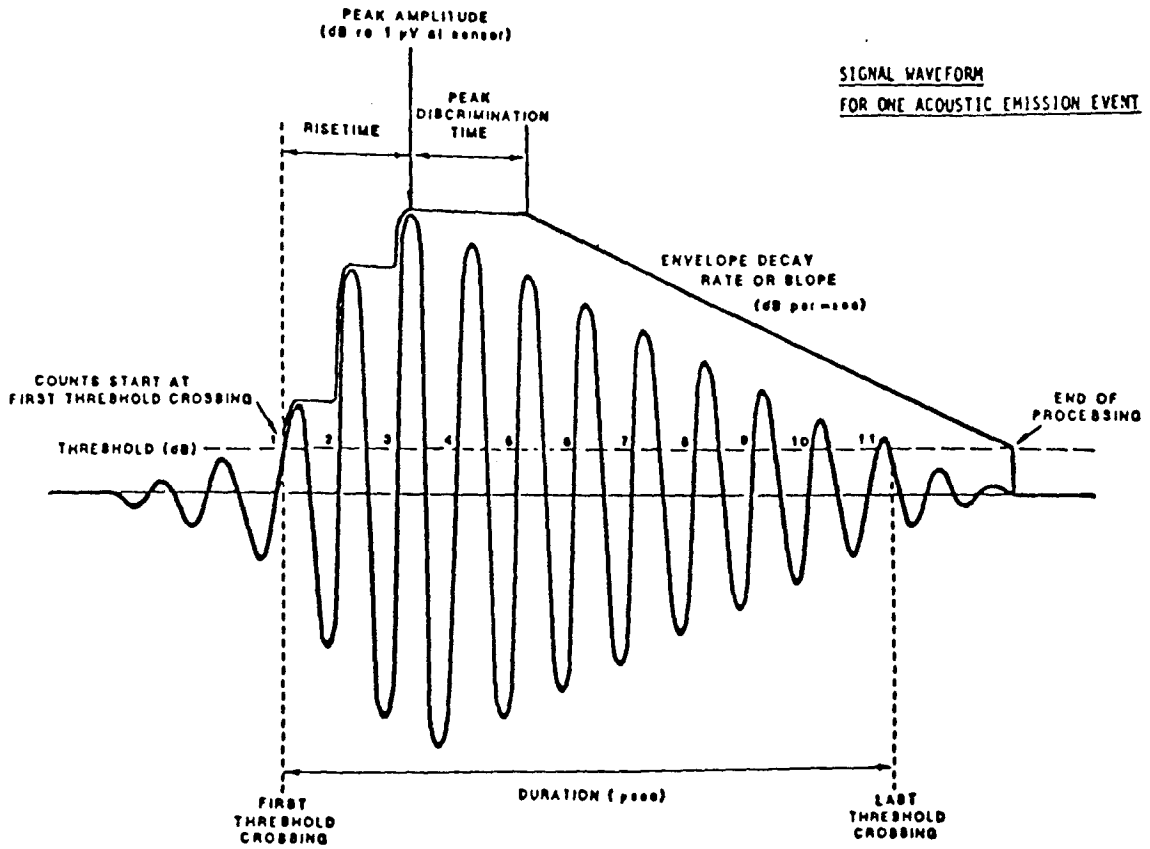
Figure 6.3: Characteristics of an acoustic emission hit.
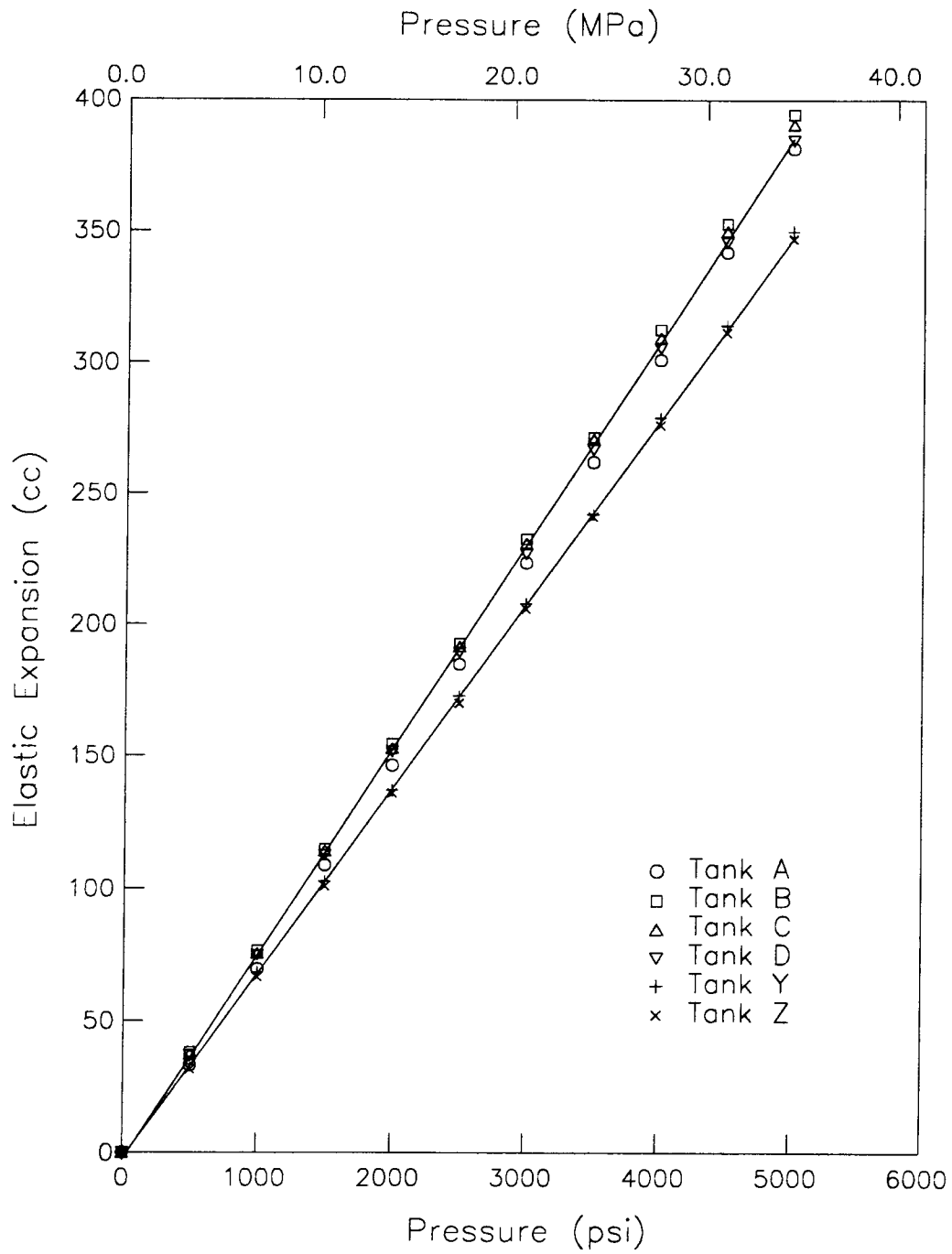
Figure 6.4: Measured elastic expansion (test and control cylinders).
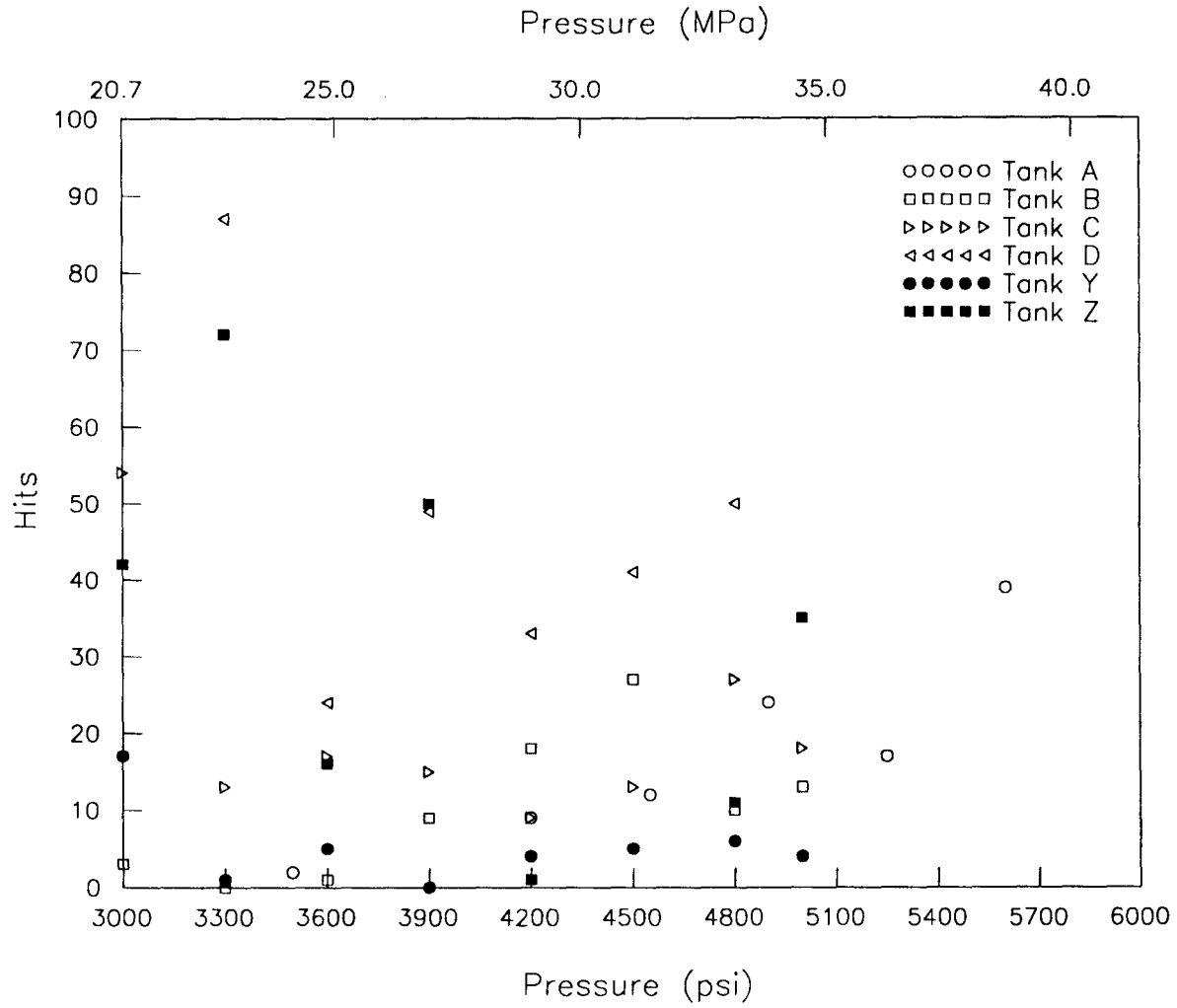
Figure 6.5: Hits past previous pressure during first cycle of cylinder tests (30 dB ≤ Amp ≤ 70 dB).
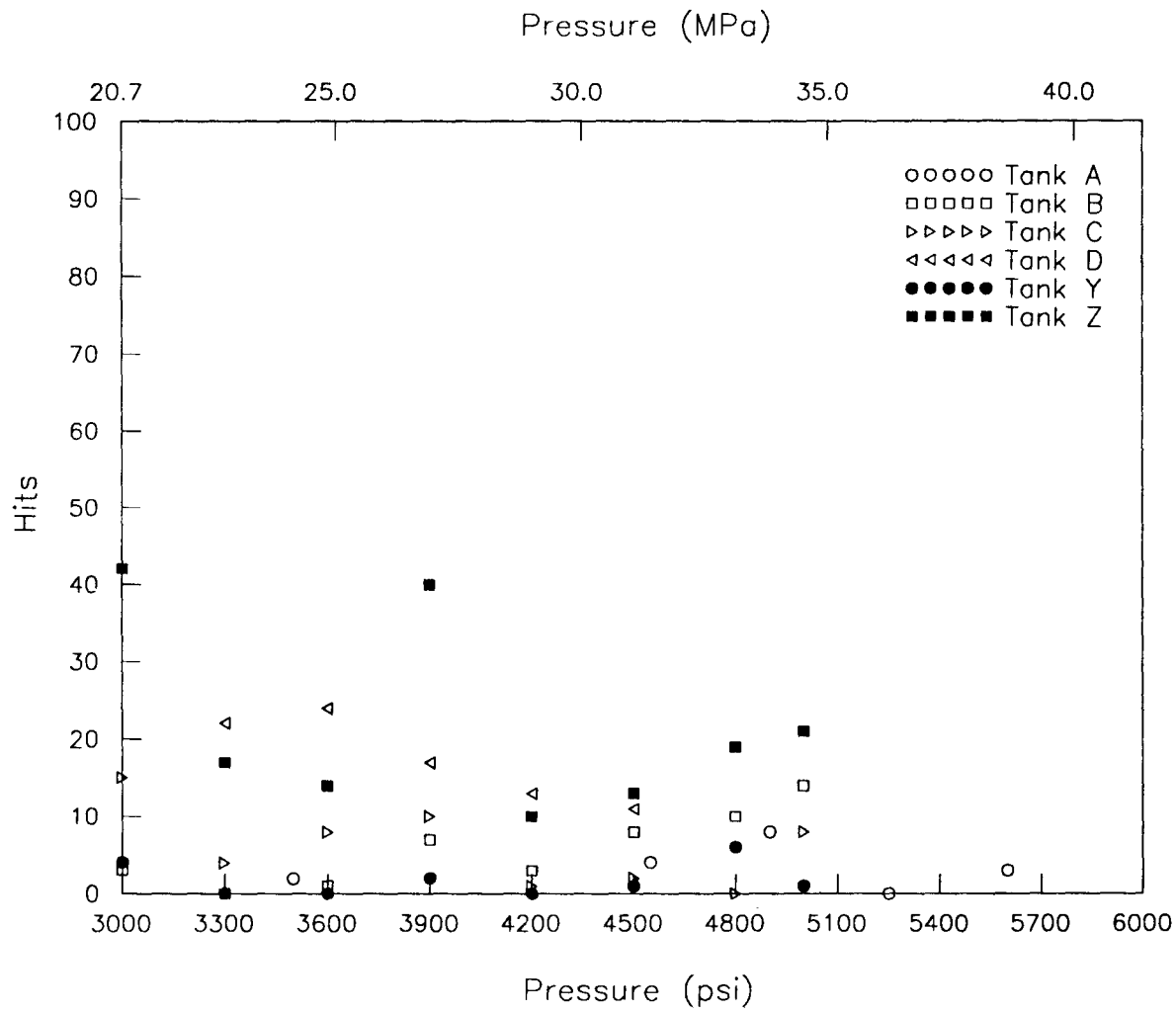
Figure 6.6: Hits past previous pressure during second cycle of cylinder tests (30 dB ≤ Amp ≤ 70 dB).
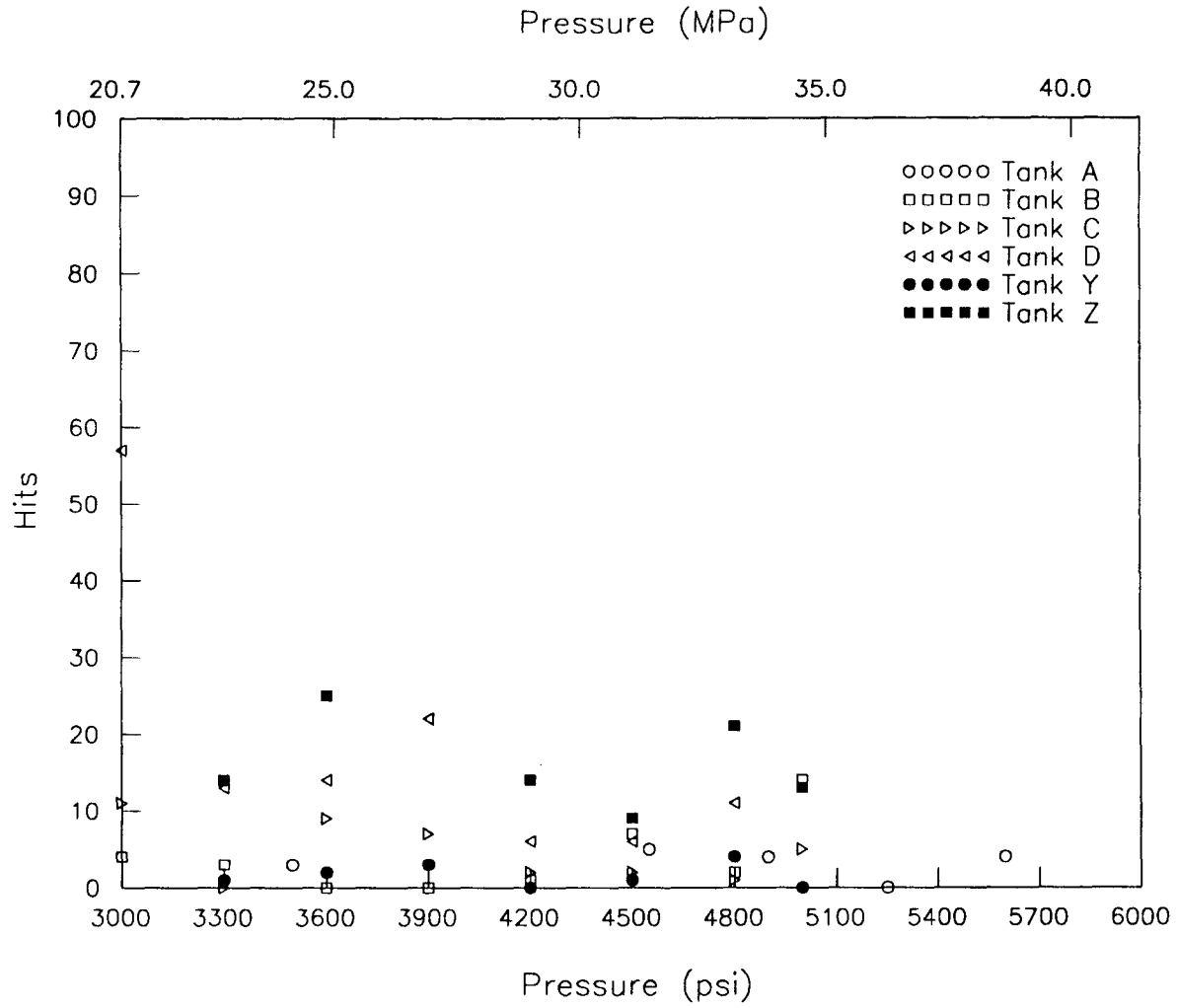
Figure 6.7: Hits past previous pressure during third cycle of cylinder tests (30 dB ≤ Amp ≤ 70 dB).
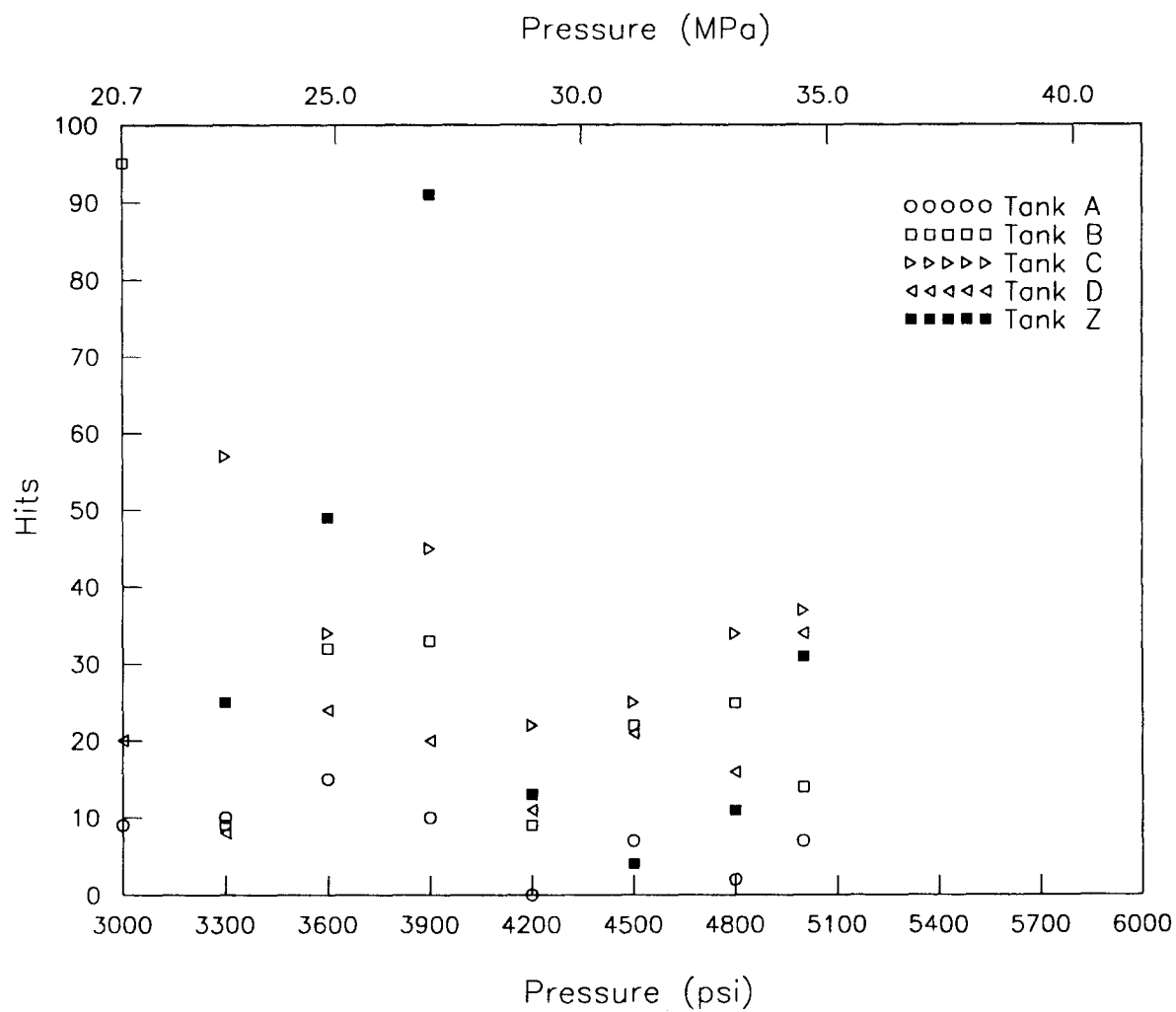
Figure 6.8: Hits past previous pressure during first cycle of cylinder retests (30 dB ≤ Amp ≤ 70 dB).
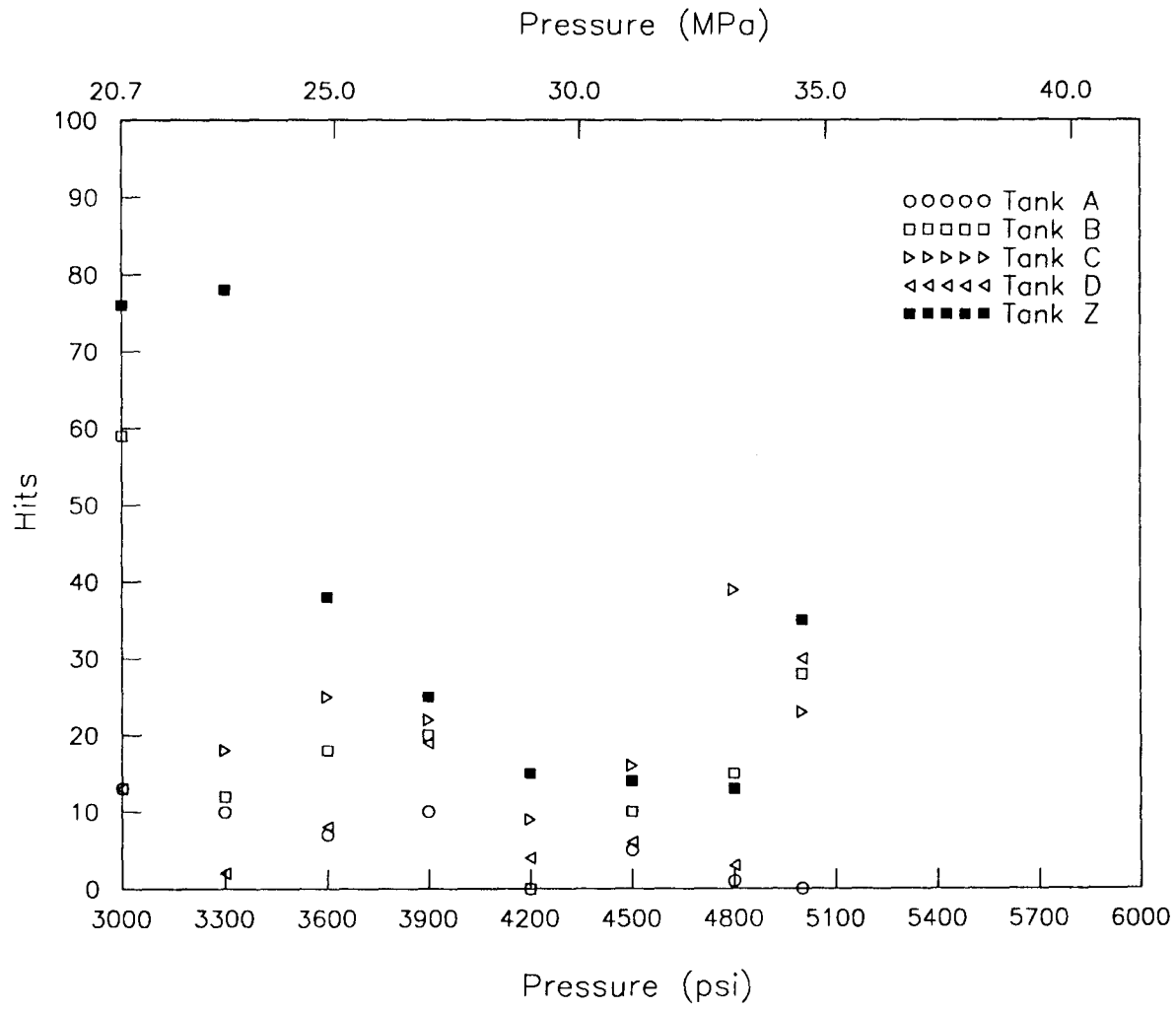
Figure 6.9: Hits past previous pressure during second cycle of cylinder retests (30 dB ≤ Amp ≤ 70 dB).
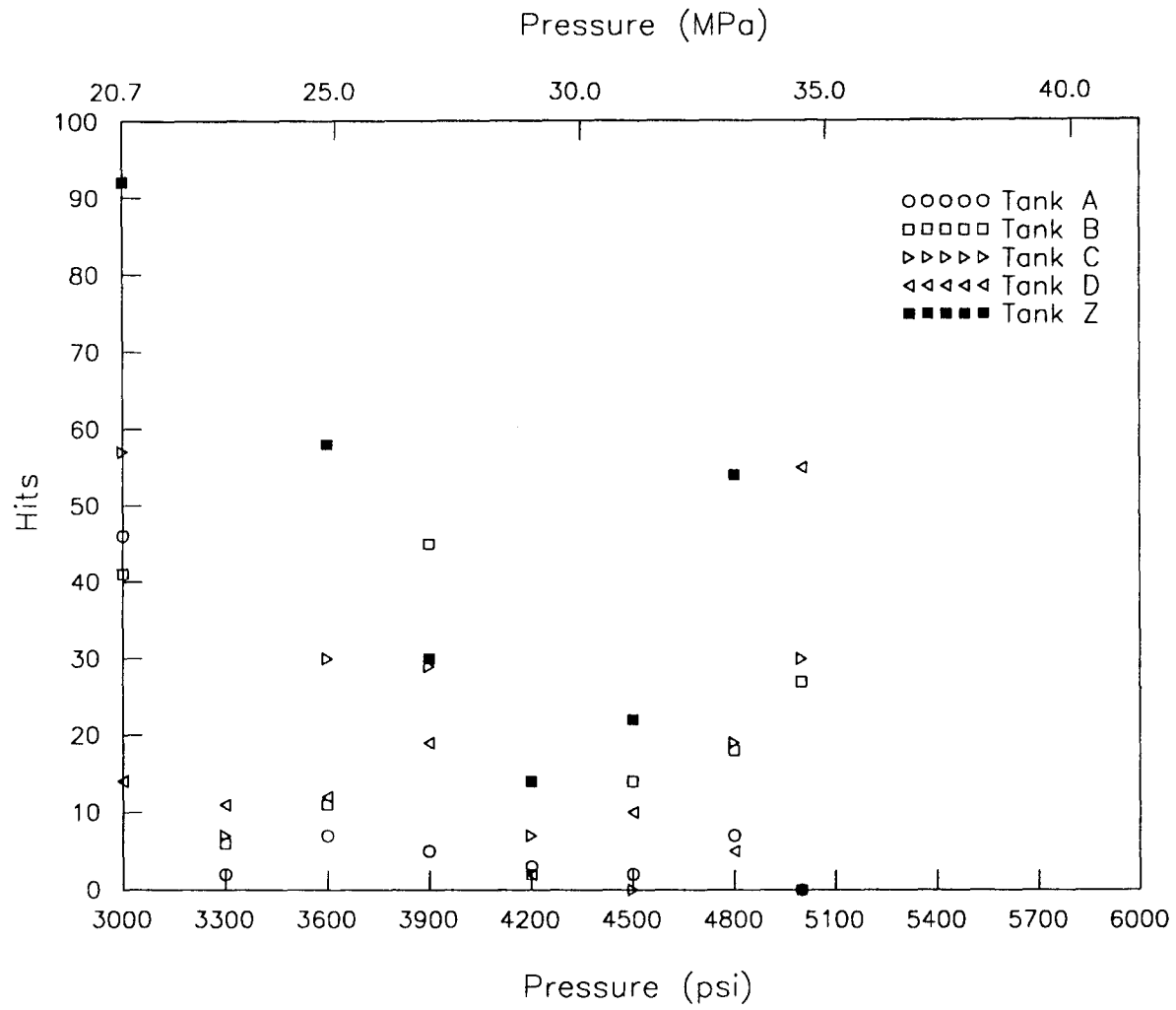
Figure 6.10: Hits past previous pressure during third cycle of cylinder retests (30 dB ≤ Amp ≤ 70 dB).
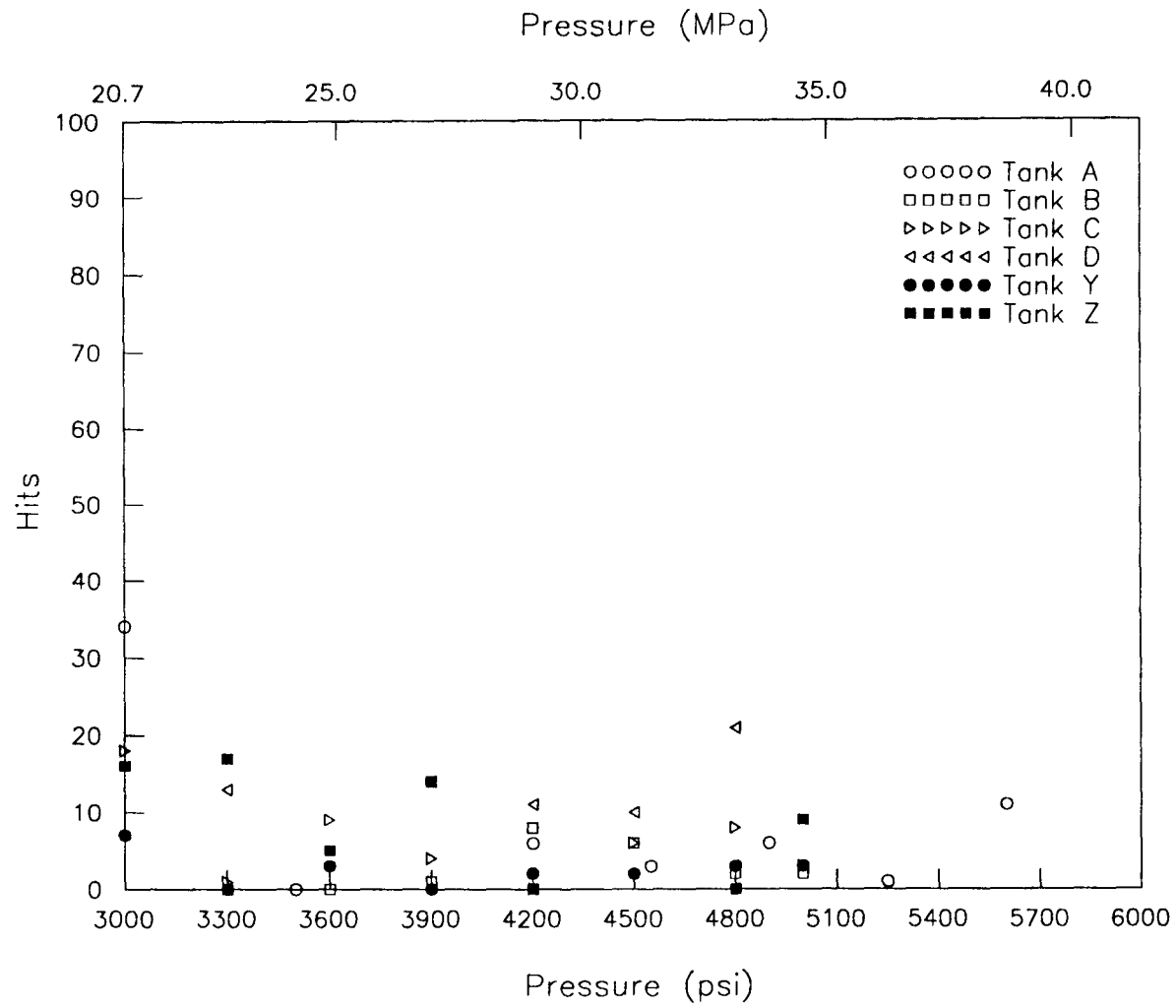
Figure 6.11: Hits past previous pressure during first cycle of cylinder tests (40 dB ≤ Amp ≤ 70 dB).
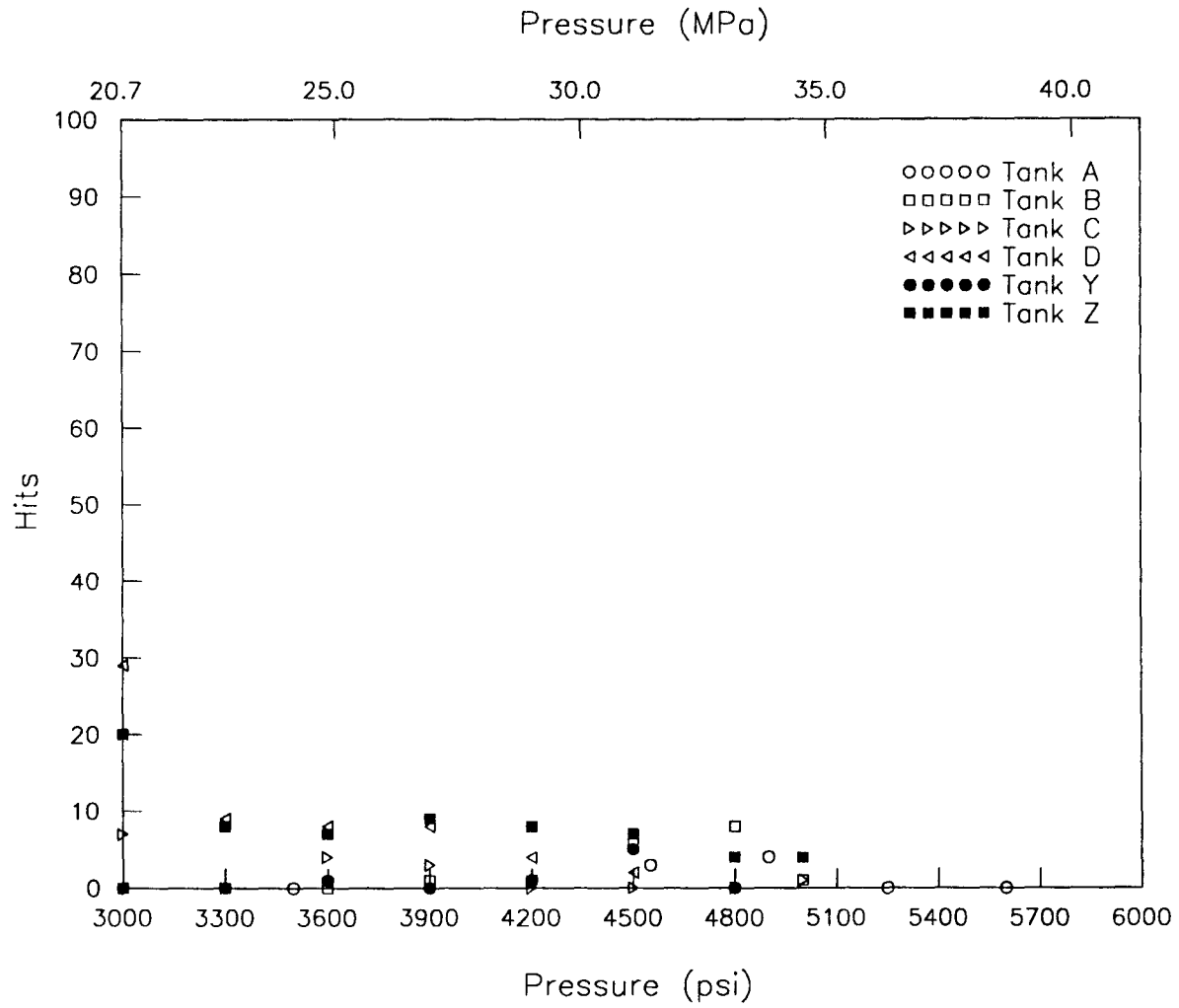
Figure 6.12: Hits past previous pressure during second cycle of cylinder tests (40 dB $\leq$ Amp $\leq$ 70 dB).
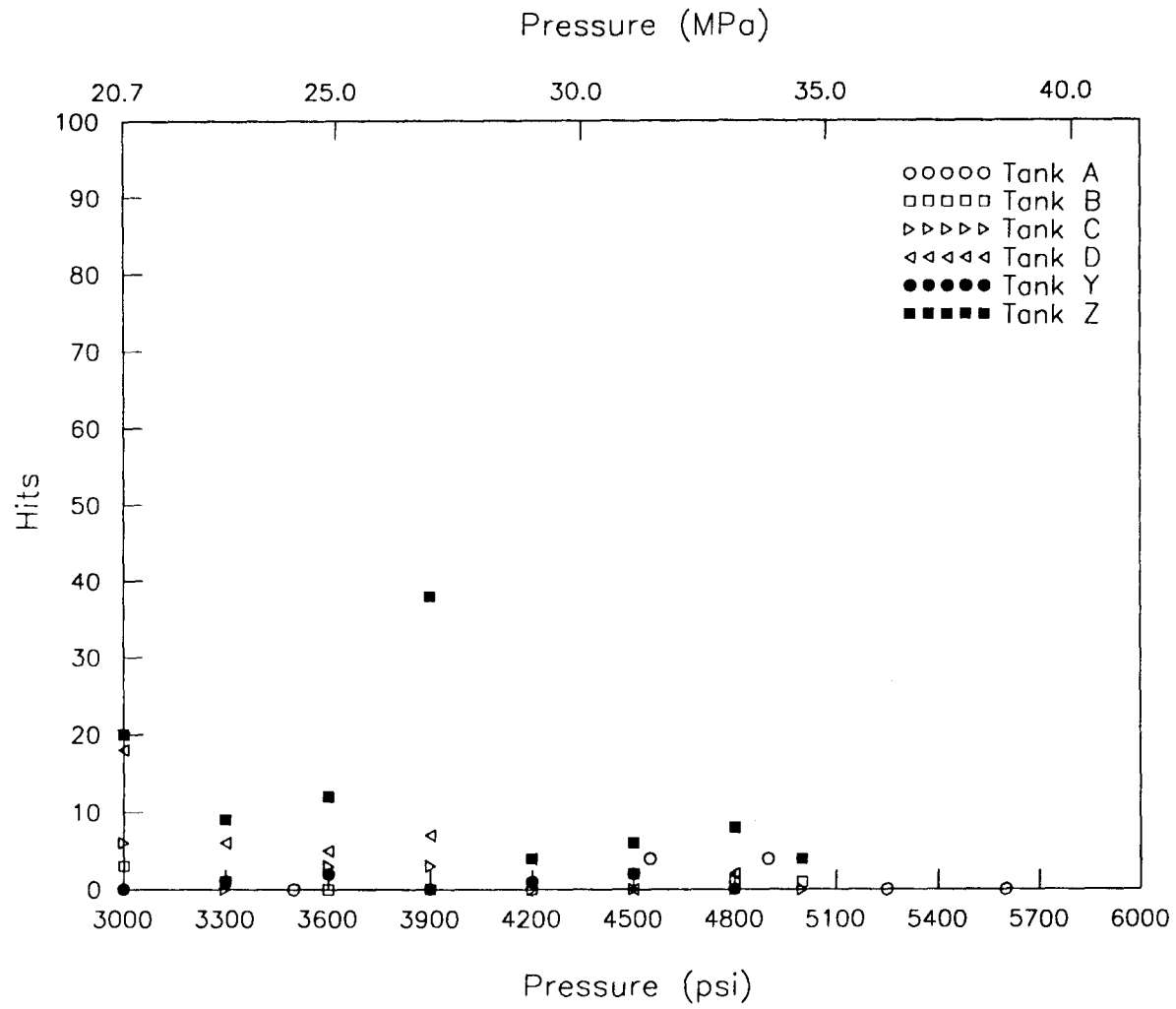
Figure 6.13: Hits past previous pressure during third cycle of cylinder tests (40 dB ≤ Amp ≤ 70 dB).
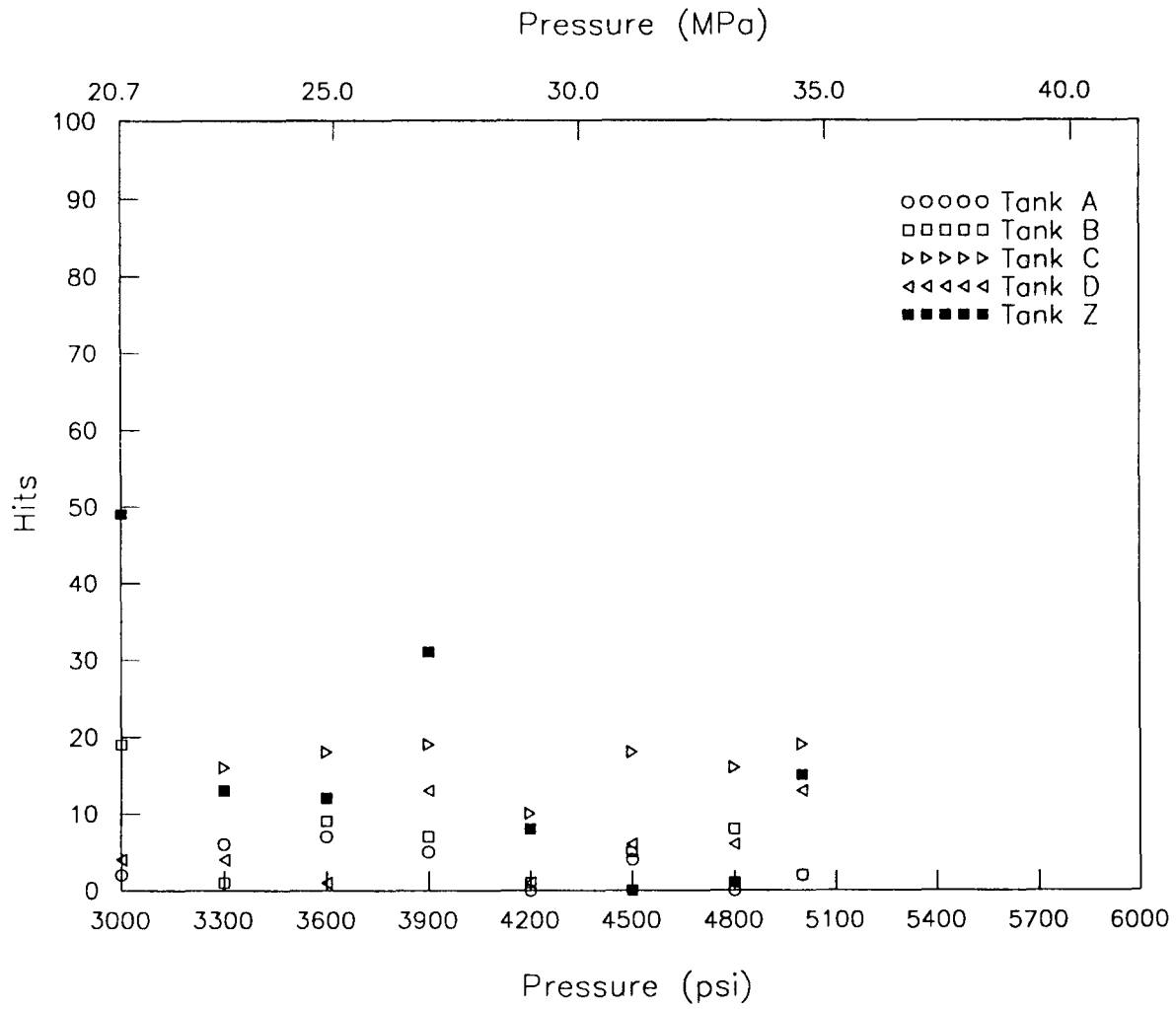
Figure 6.14: Hits past previous pressure during first cycle of cylinder retests (40 dB ≤ Amp ≤ 70 dB).
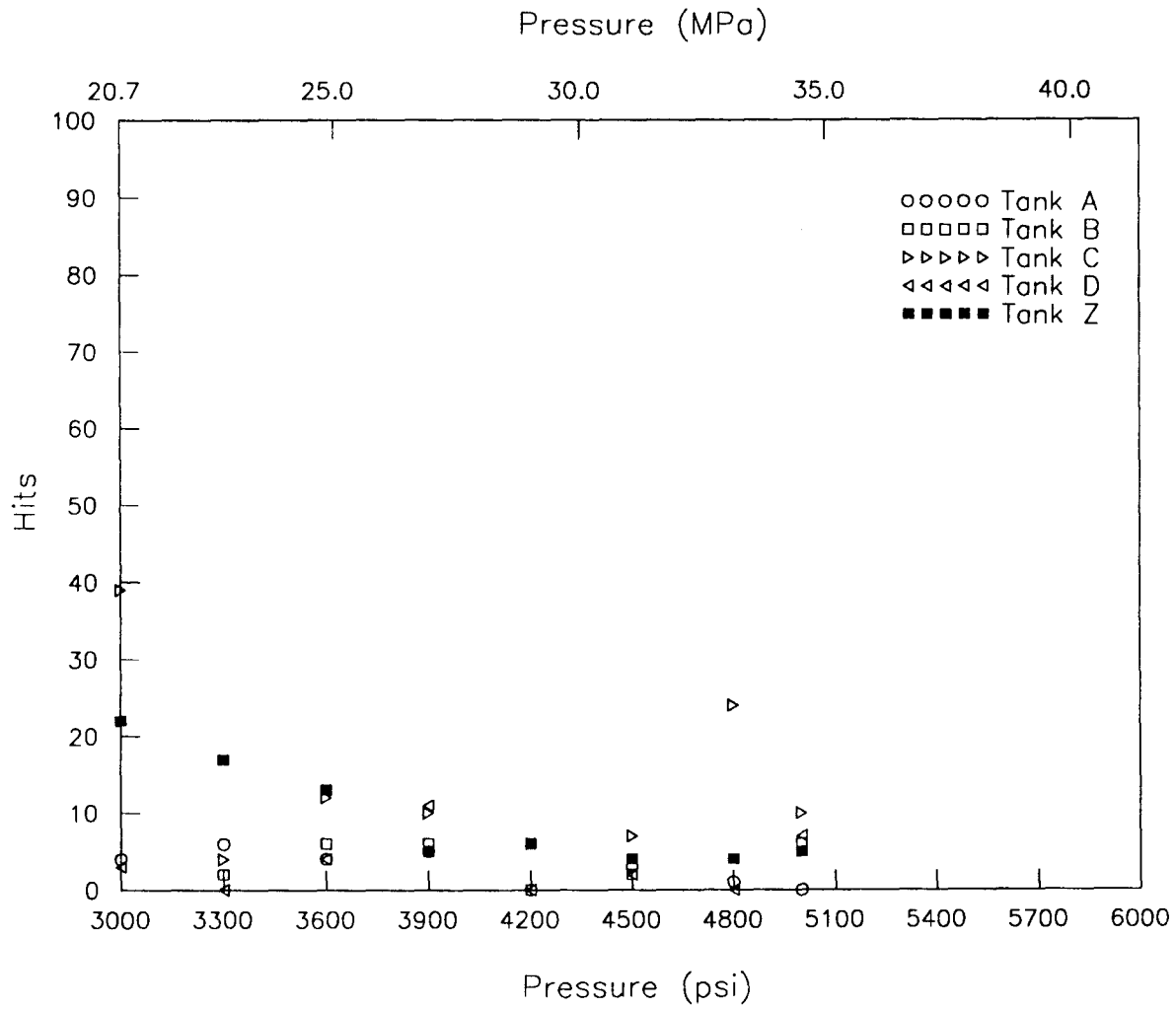
Figure 6.15: Hits past previous pressure during second cycle of cylinder retests (40 dB $\leq$ Amp $\leq$ 70 dB).
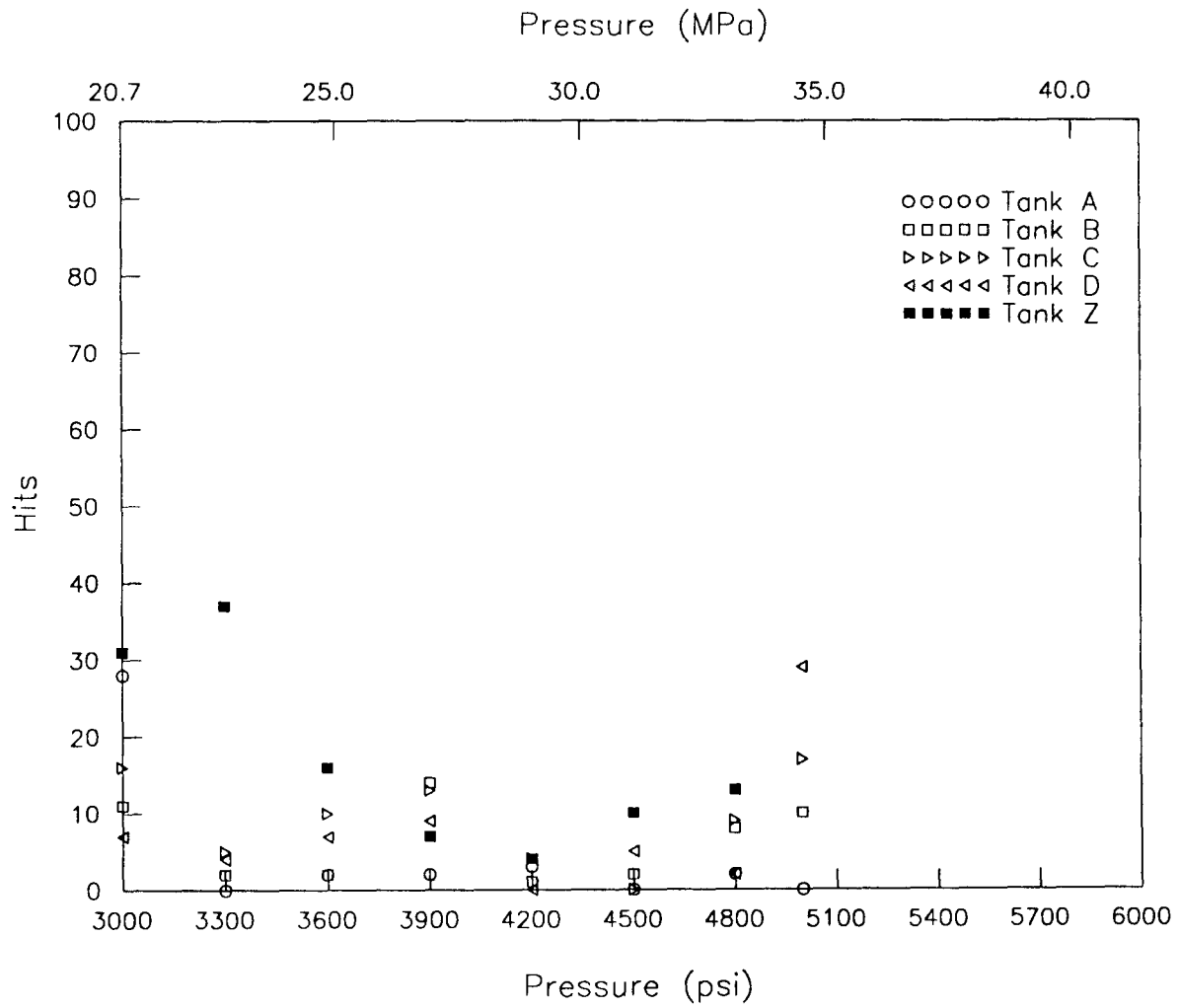
Figure 6.16: Hits past previous pressure during third cycle of cylinder retests (40 dB ≤ Amp ≤ 70 dB).
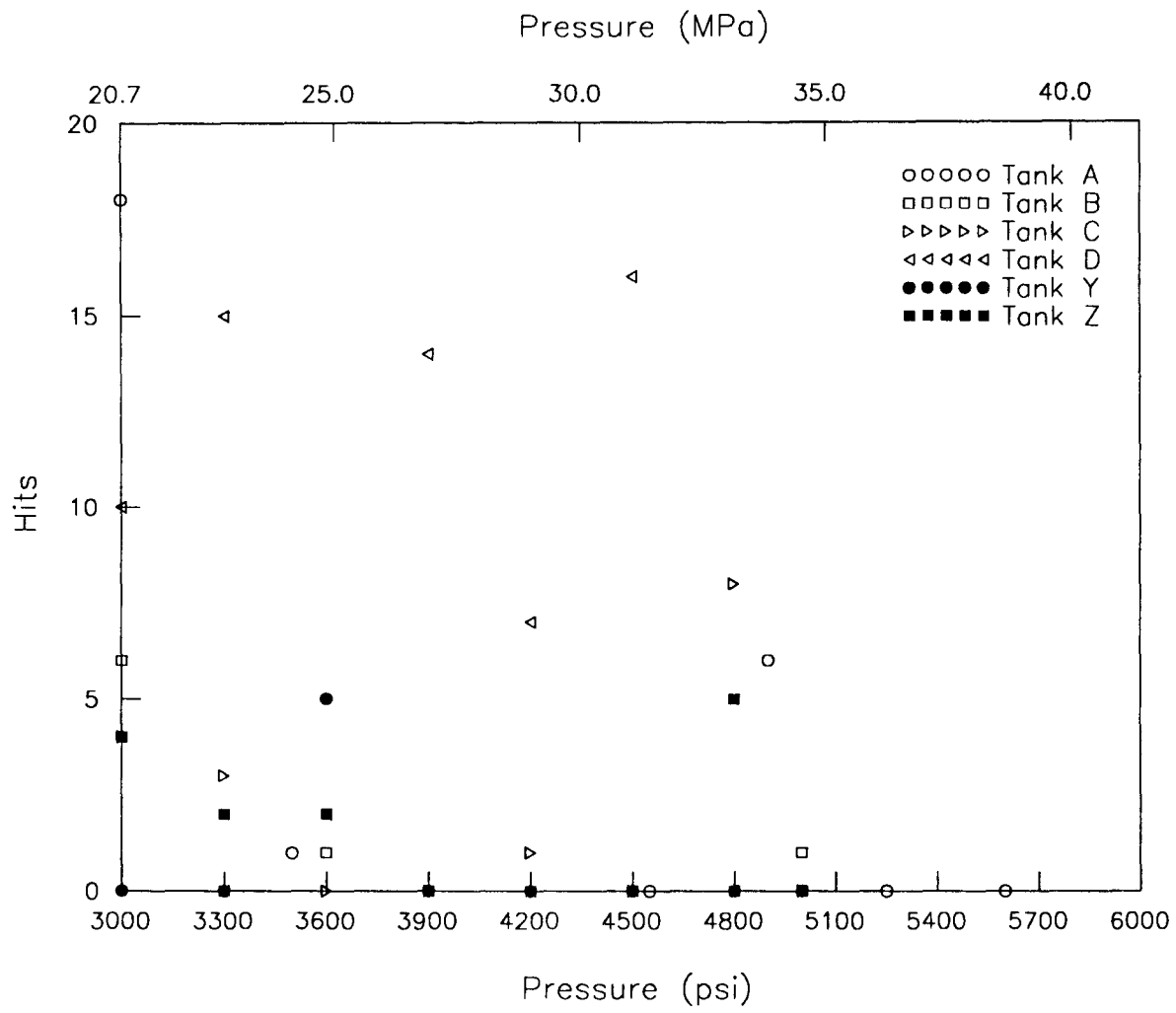
Figure 6.17: Hold time hits during first cycle of cylinder tests (30 dB ≤ Amp ≤ 70 dB).
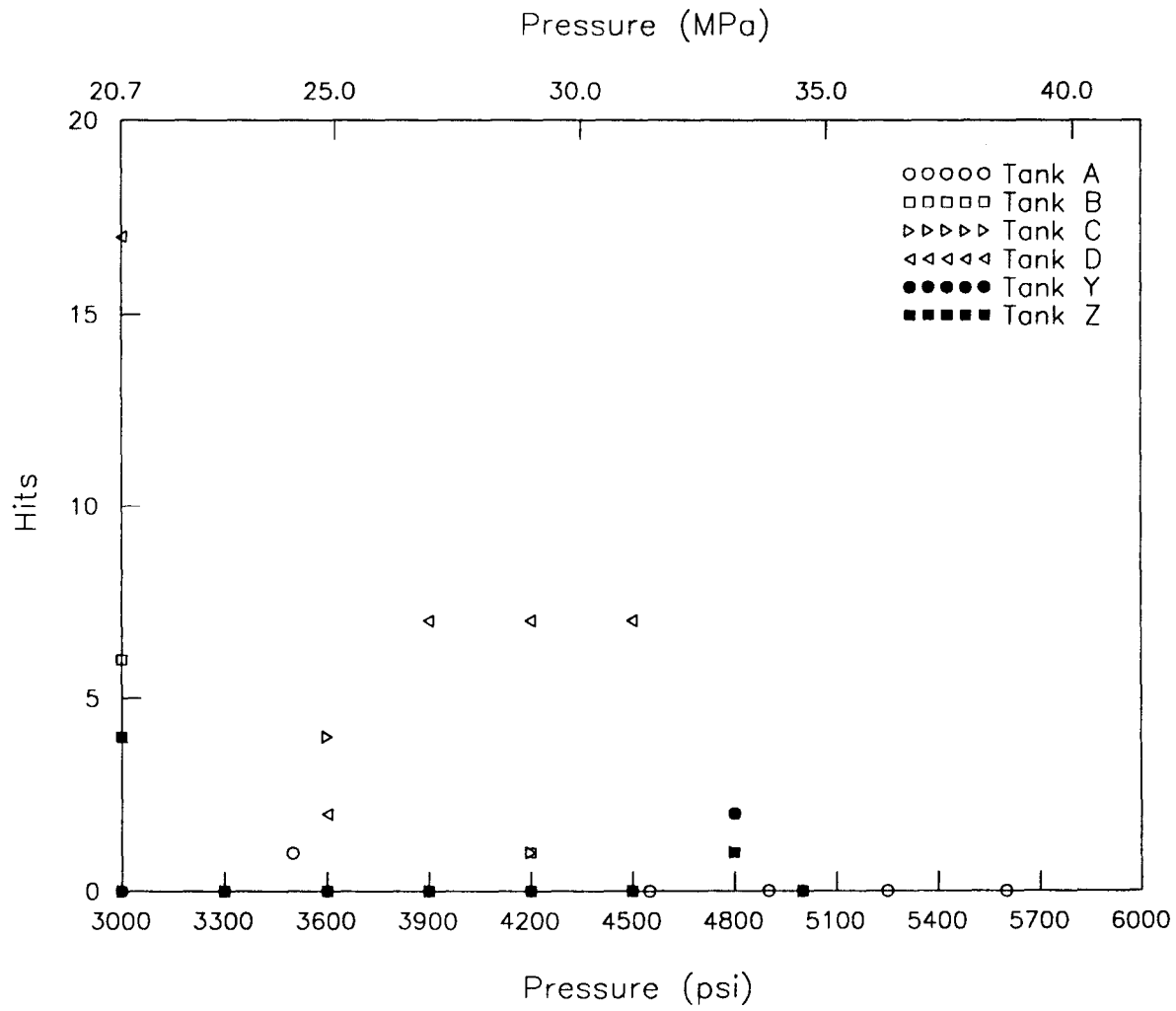
Figure 6.18: Hold time hits during second cycle of cylinder tests (30 dB ≤ Amp ≤ 70 dB).
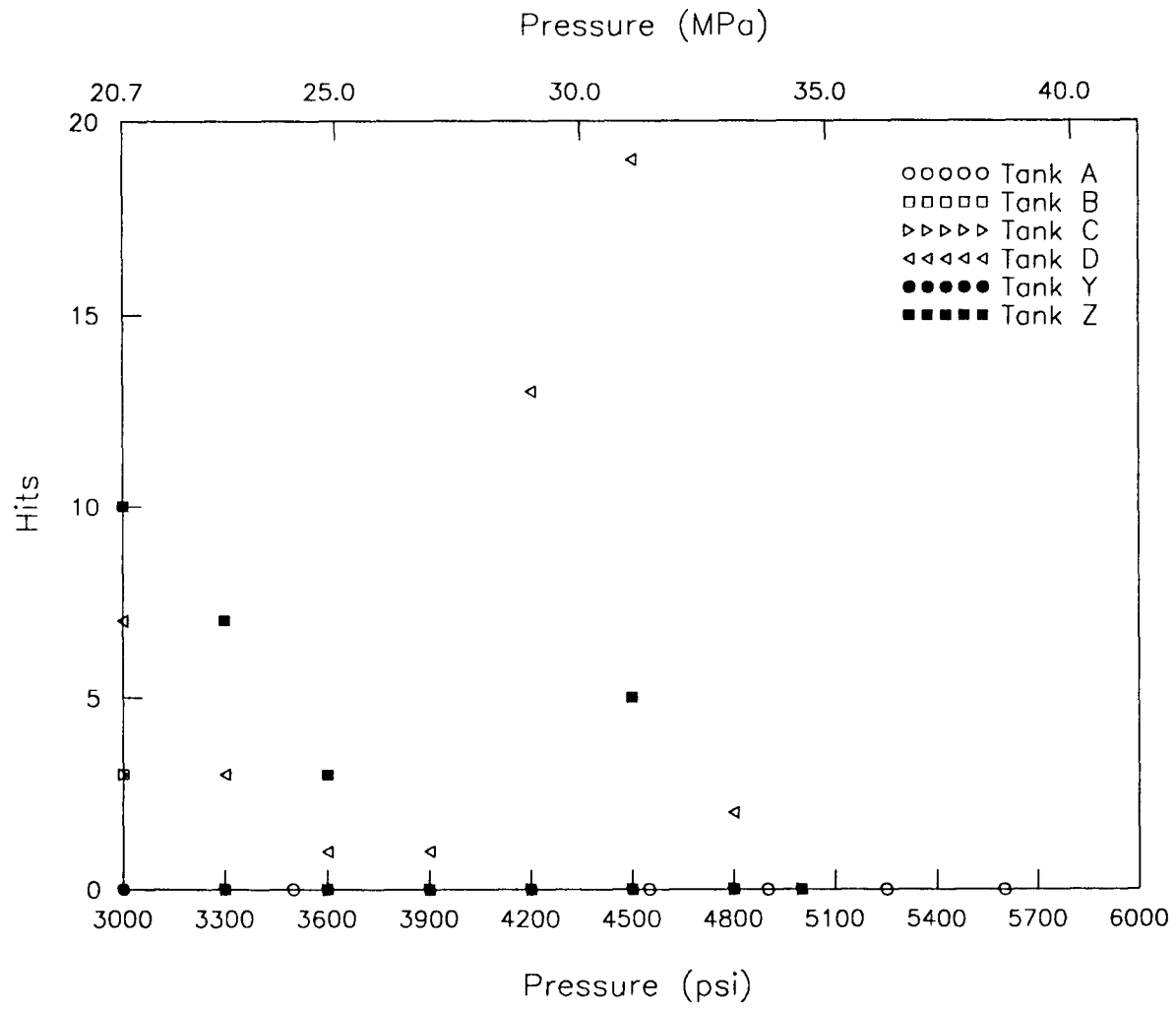
Figure 6.19: Hold time hits during third cycle of cylinder tests (30 dB ≤ Amp ≤ 70 dB).
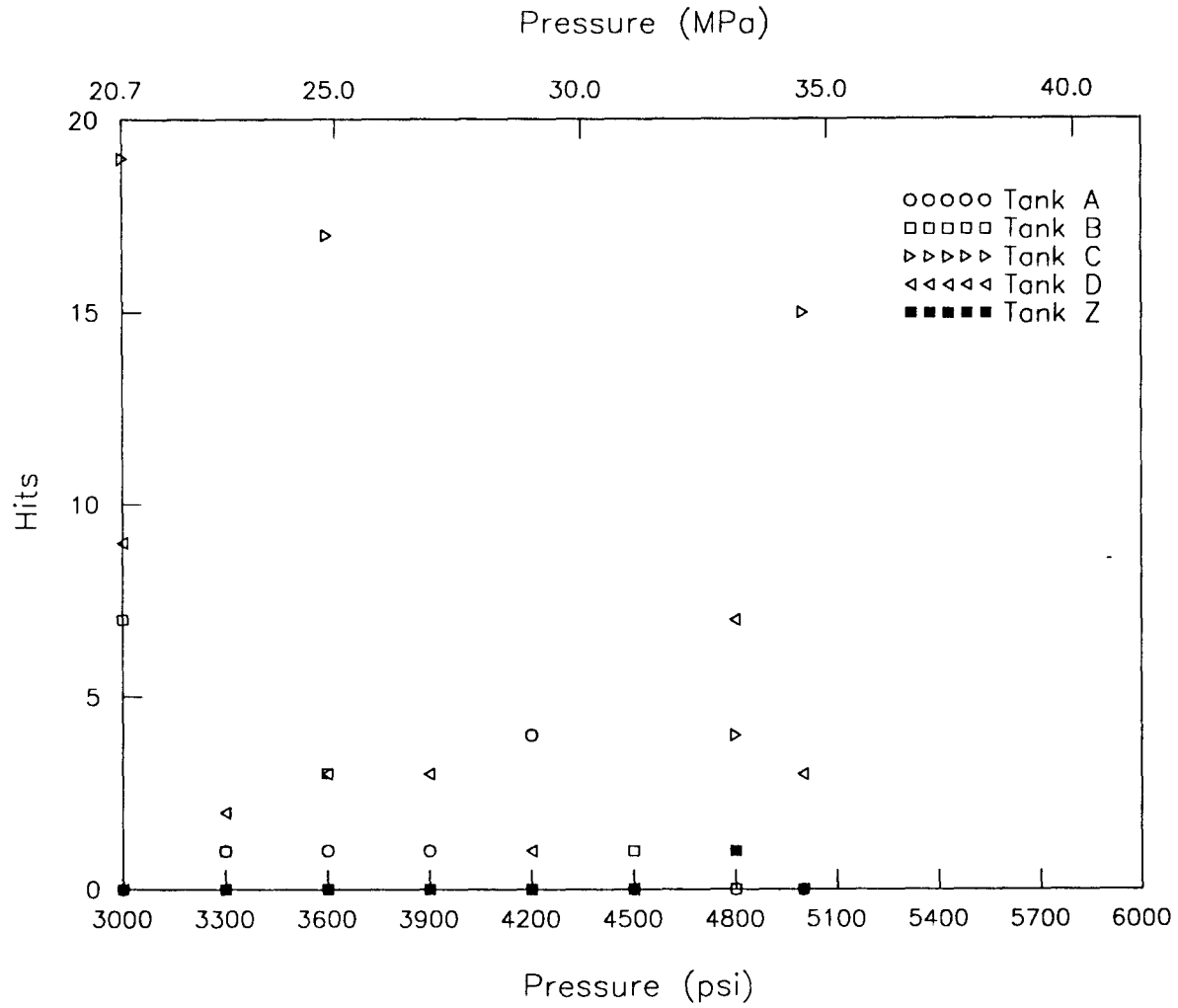
Figure 6.20: Hold time hits during first cycle of cylinder retests ($30 \text{ dB} \leq \text{Amp} \leq 70 \text{ dB}$).
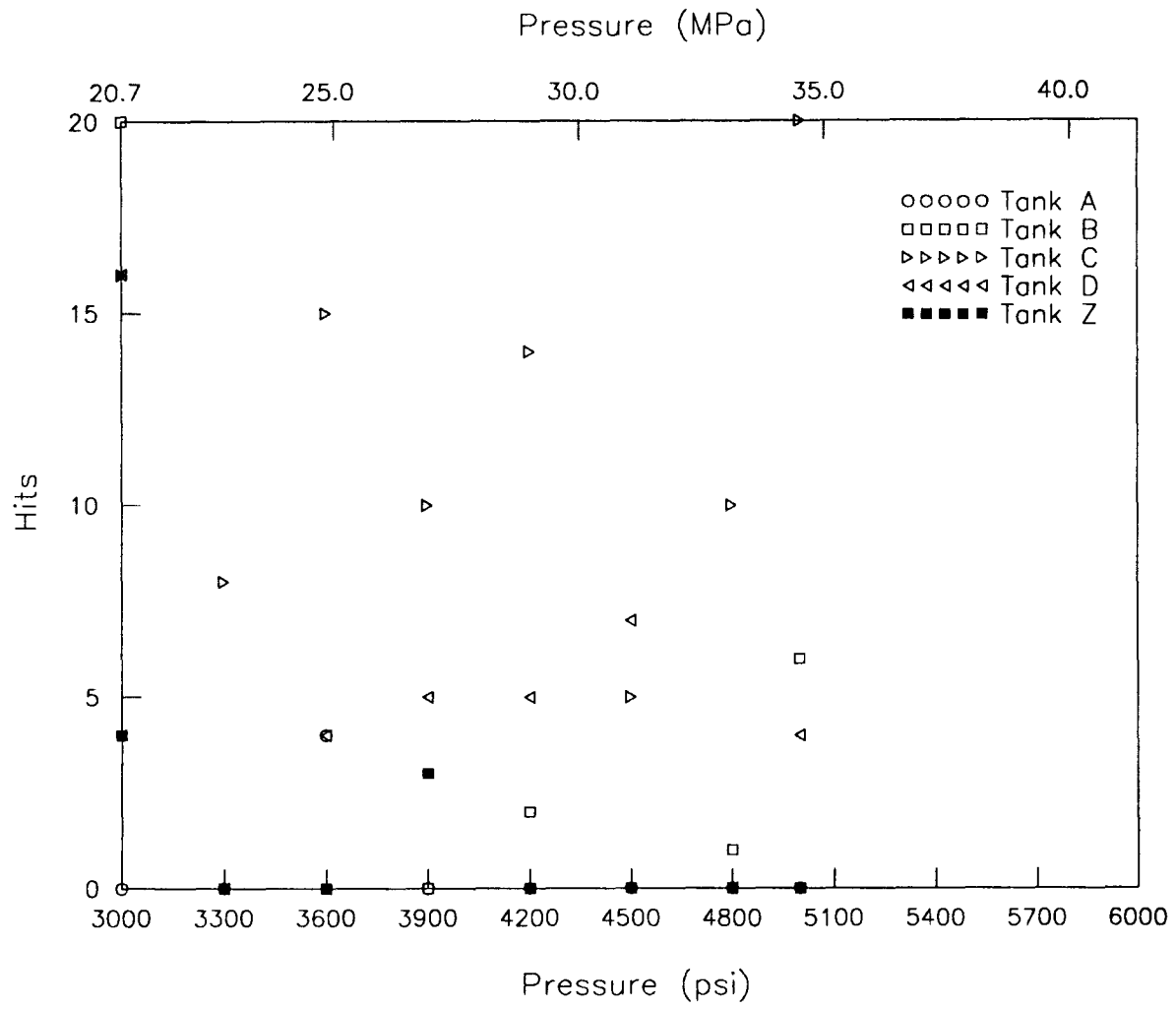
Figure 6.21: Hold time hits during second cycle of cylinder retests (30 dB $\leq$ Amp $\leq$ 70 dB).
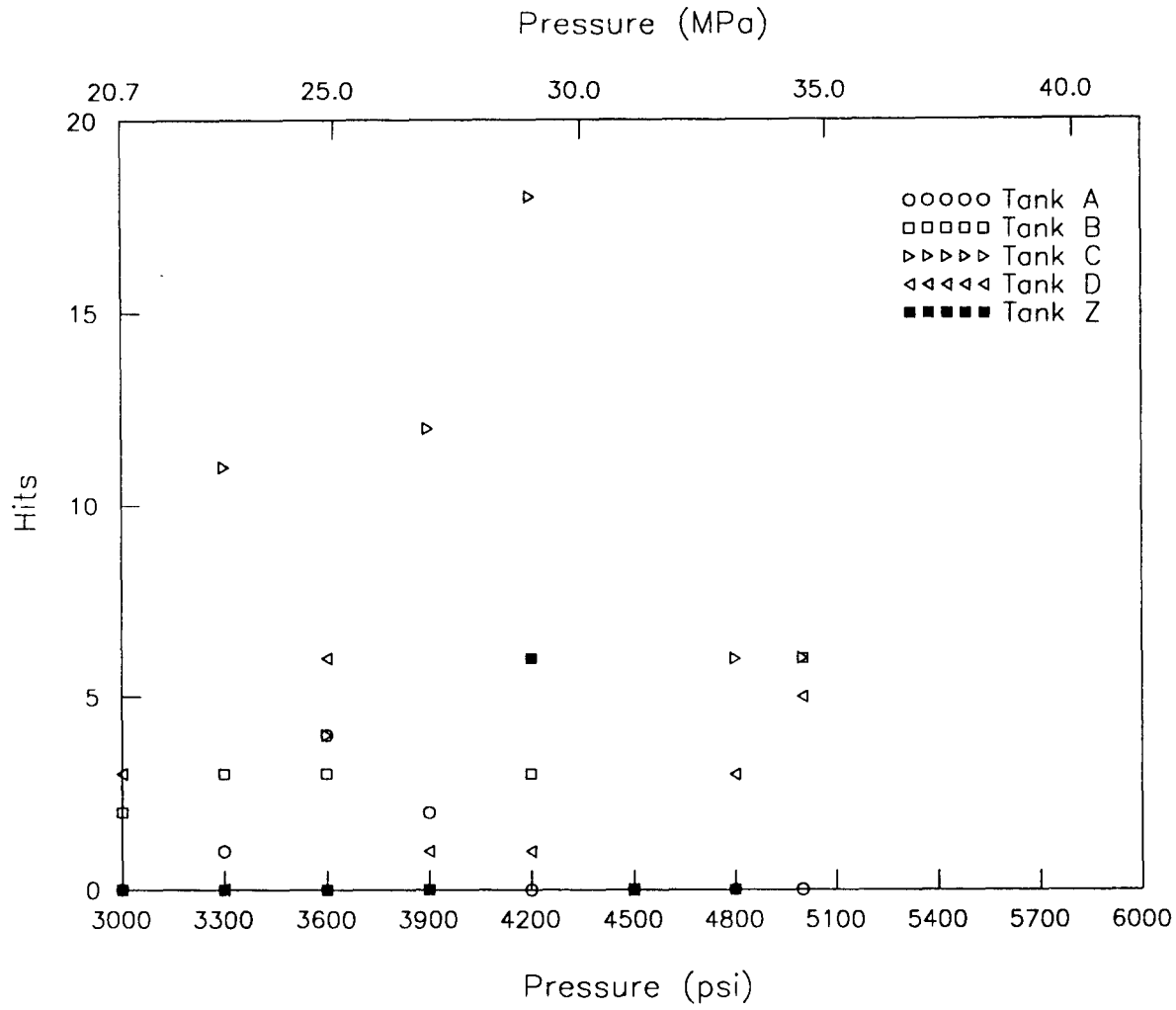
Figure 6.22: Hold time hits during third cycle of cylinder retests (30 dB $\leq$ Amp $\leq$ 70 dB).
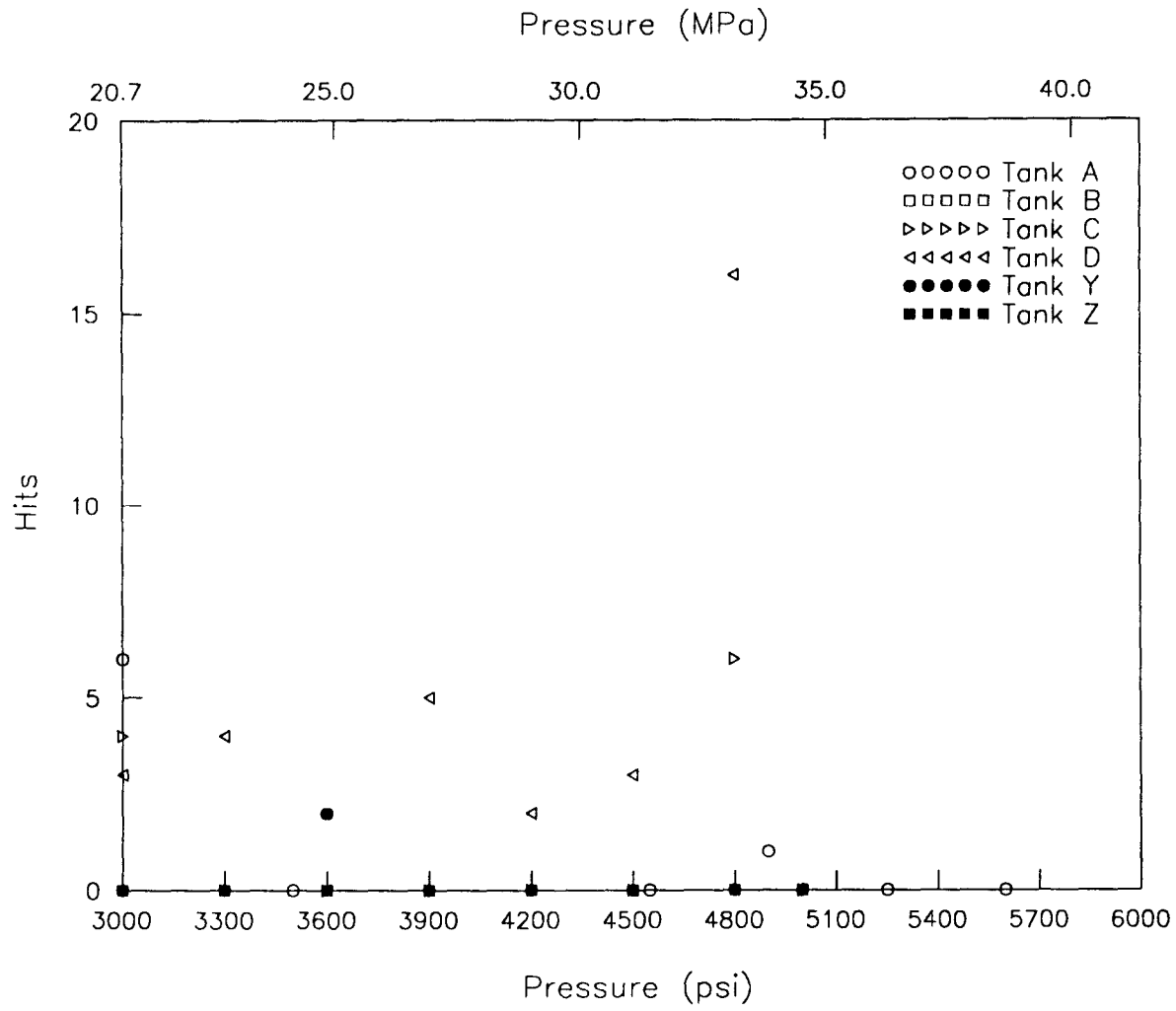
Figure 6.23: Hold time hits during first cycle of cylinder tests (40 dB ≤ Amp ≤ 70 dB).
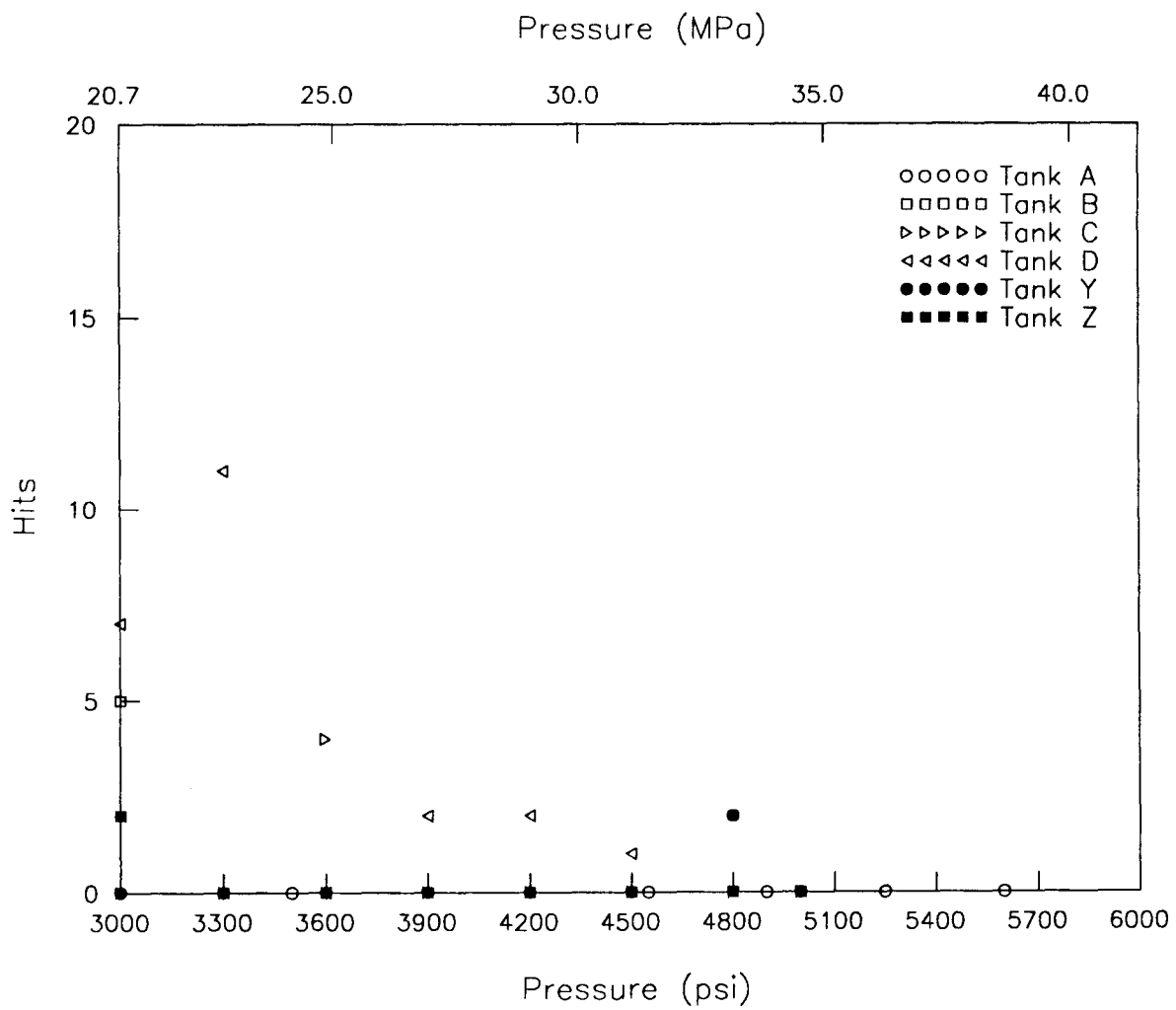
Figure 6.24: Hold time hits during second cycle of cylinder tests (40 dB $\leq$ Amp $\leq$ 70 dB).
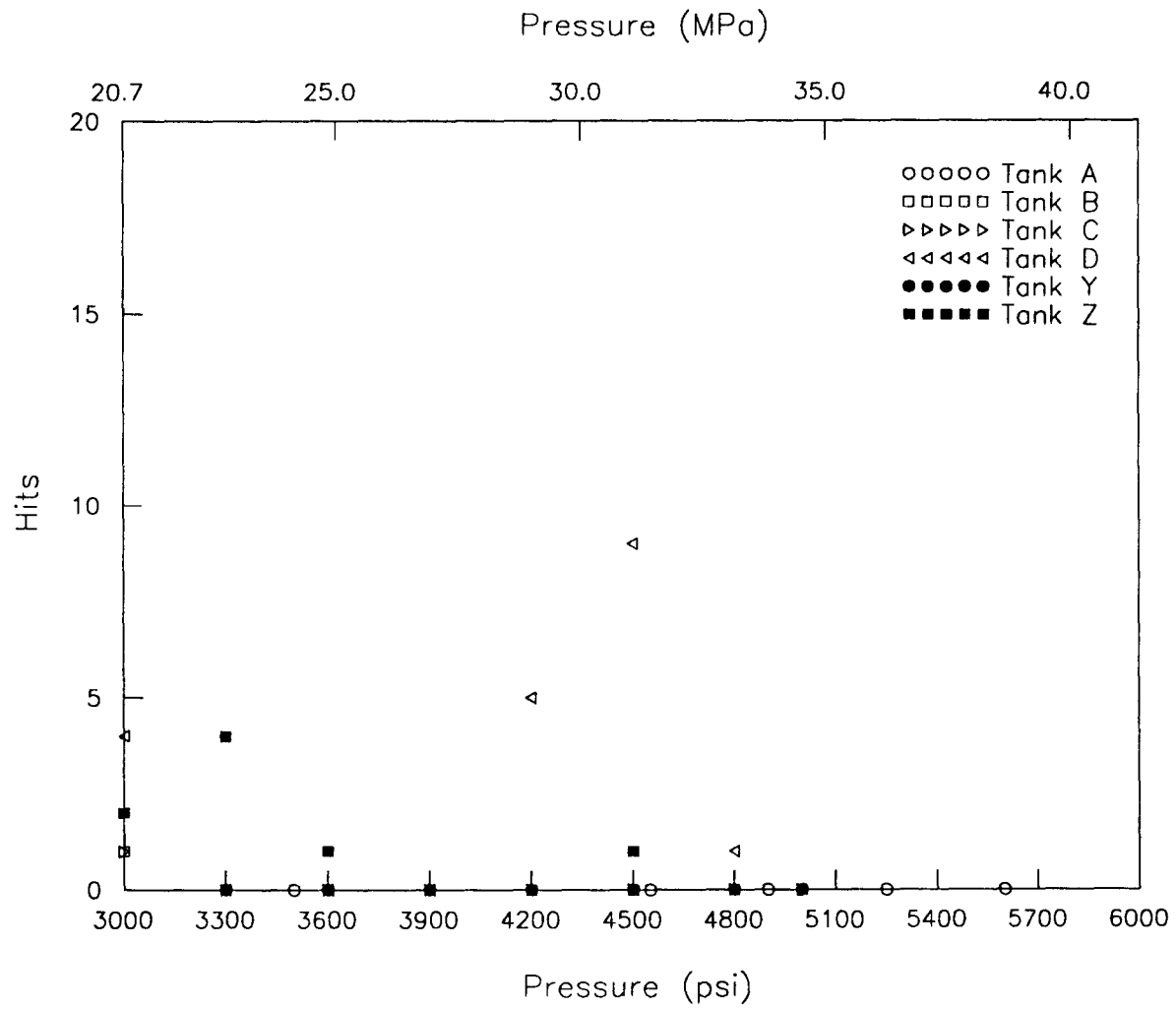
Figure 6.25: Hold time hits during third cycle of cylinder tests (40 dB $\leq$ Amp $\leq$ 70 dB).
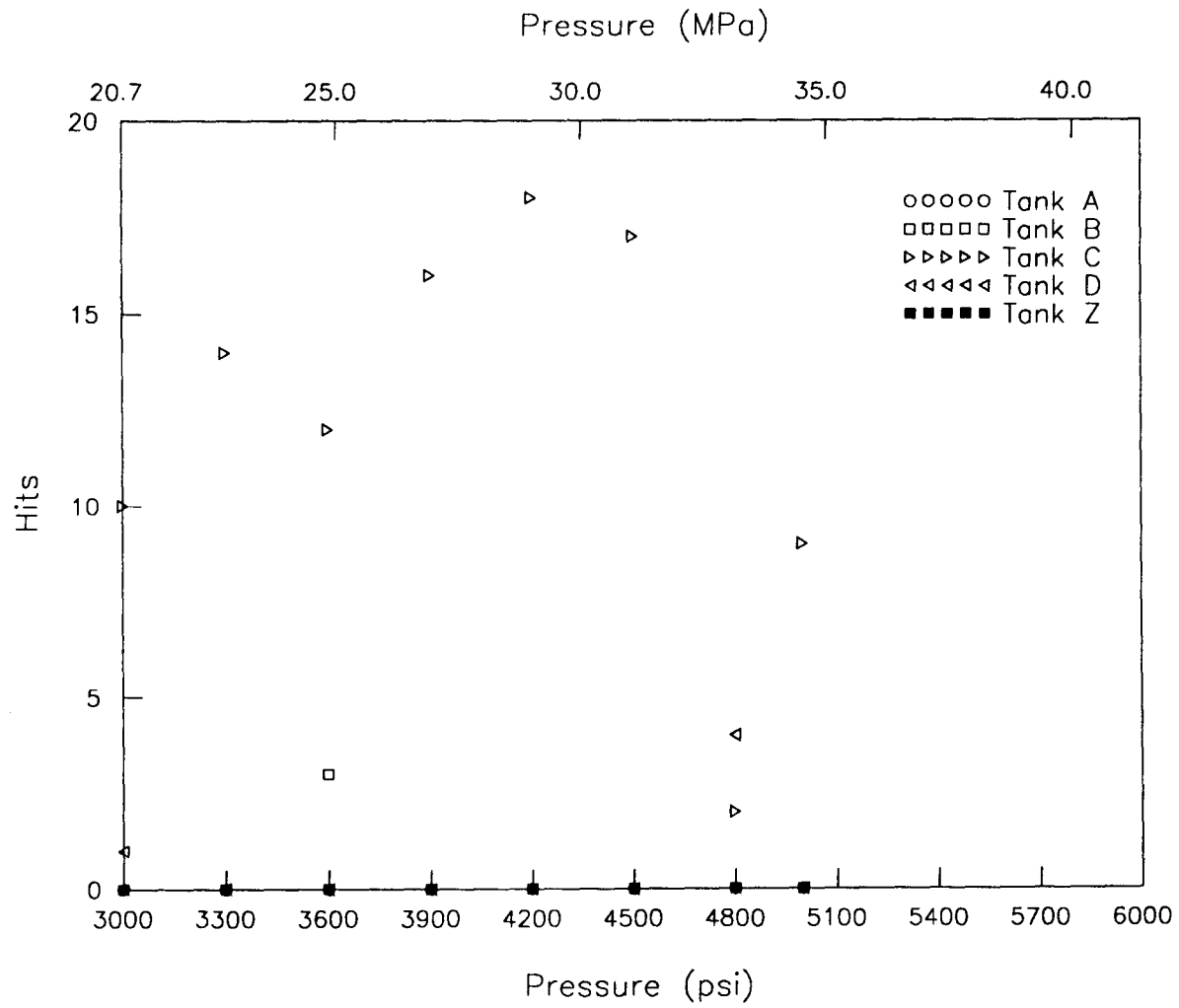
Figure 6.26: Hold time hits during first cycle of cylinder retests (40 dB ≤ Amp ≤ 70 dB).
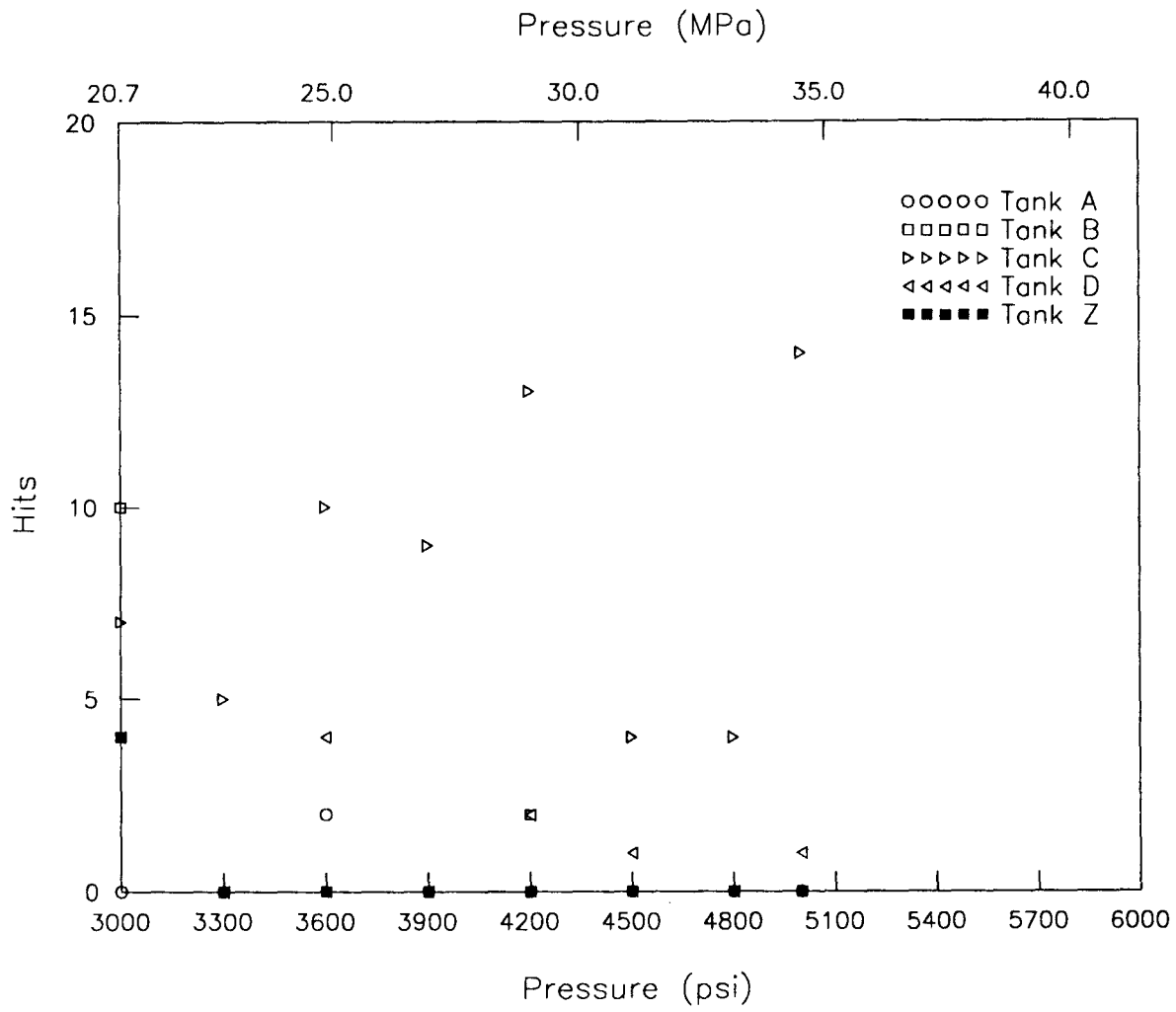
Figure 6.27: Hold time hits during second cycle of cylinder retests (40 dB ≤ Amp ≤ 70 dB).
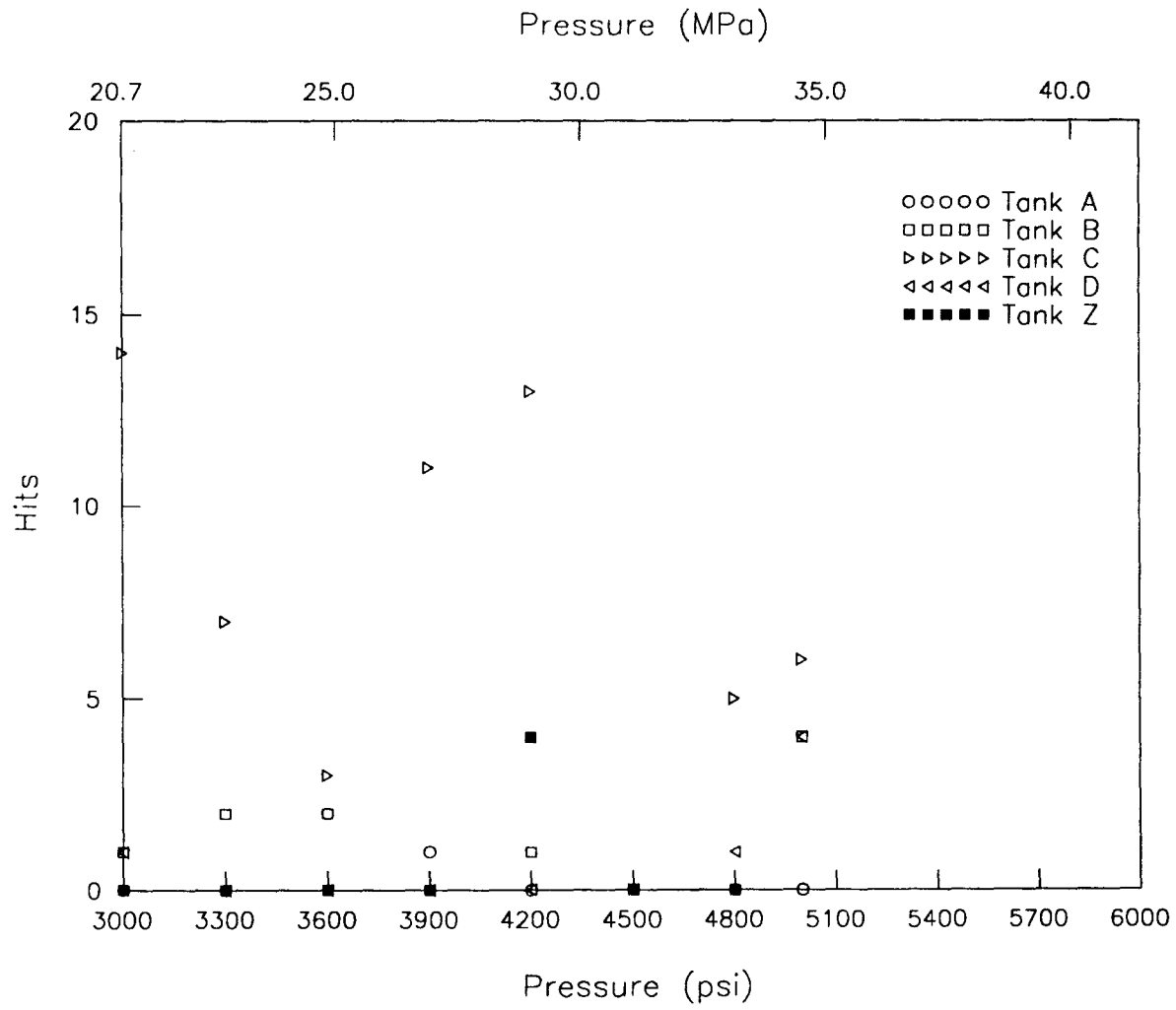
Figure 6.28: Hold time hits during third cycle of cylinder retests (40 dB ≤ Amp ≤ 70 dB).
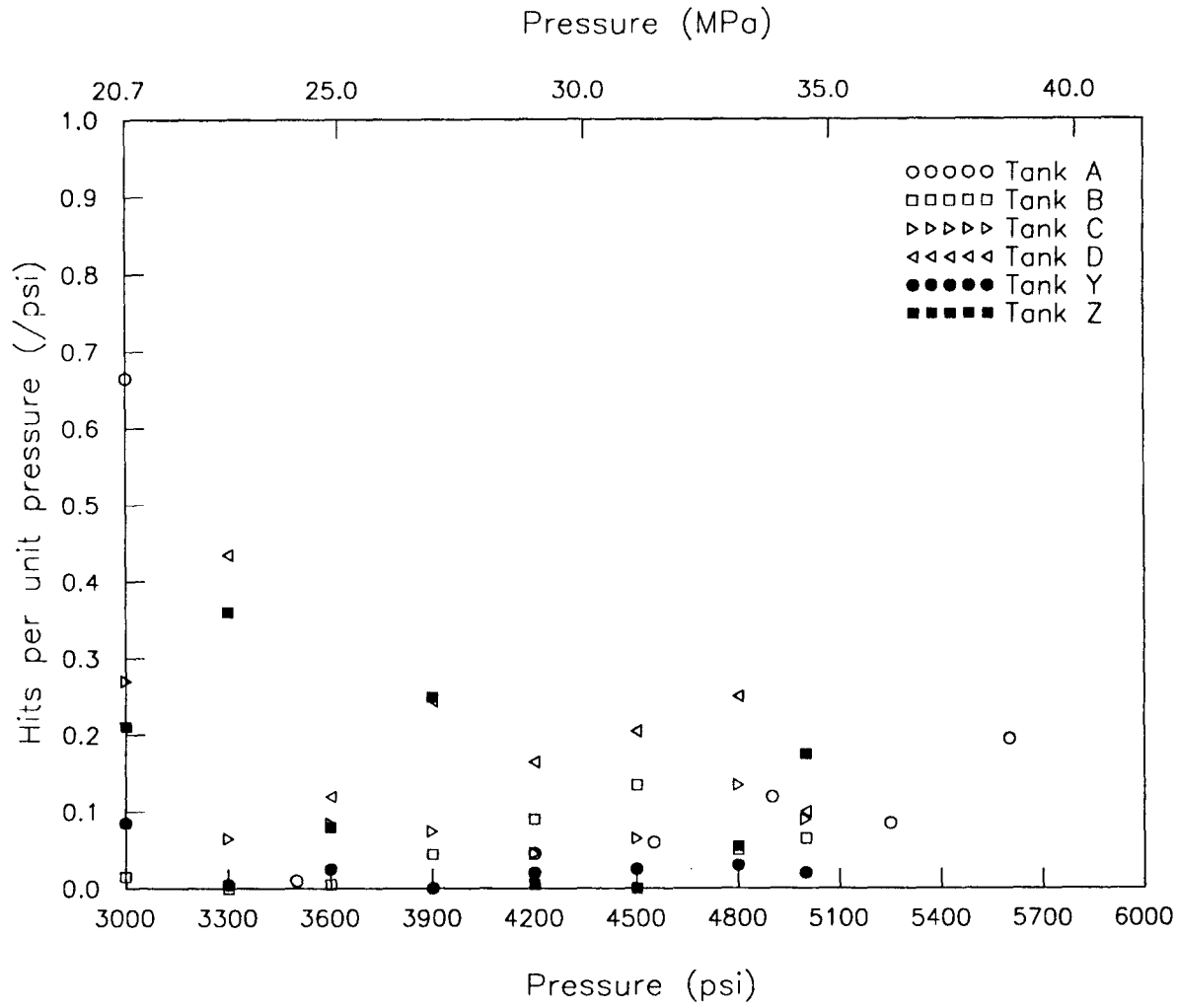
Figure 6.29: Hit rate (hits/MPa) during first cycle of cylinder tests (Amp ≥ 30 dB).
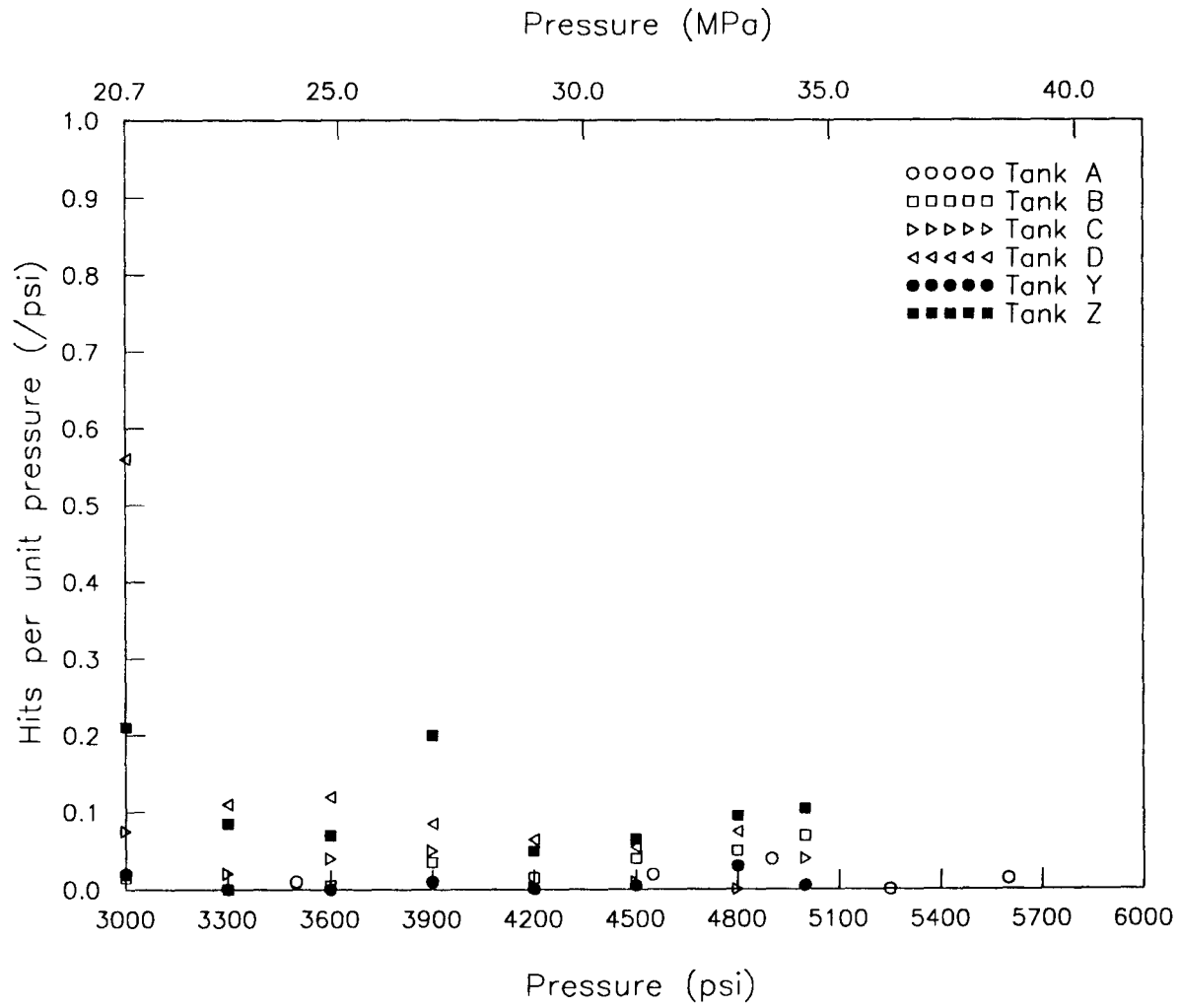
Figure 6.30: Hit rate (hits/MPa) during second cycle of cylinder tests (Amp $\geq$ 30 dB).
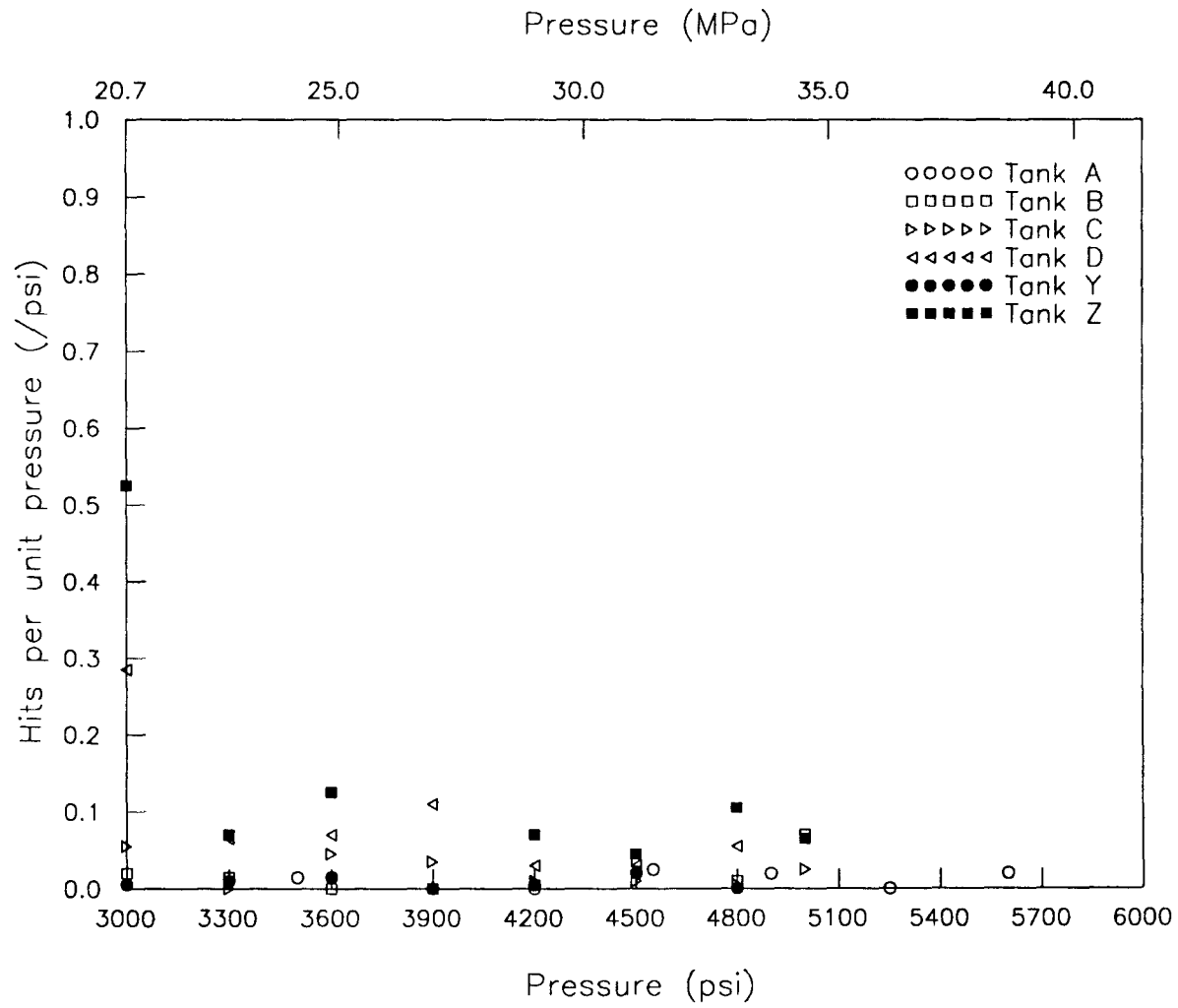
Figure 6.31: Hit rate (hits/MPa) during third cycle of cylinder tests (Amp ≥ 30 dB).
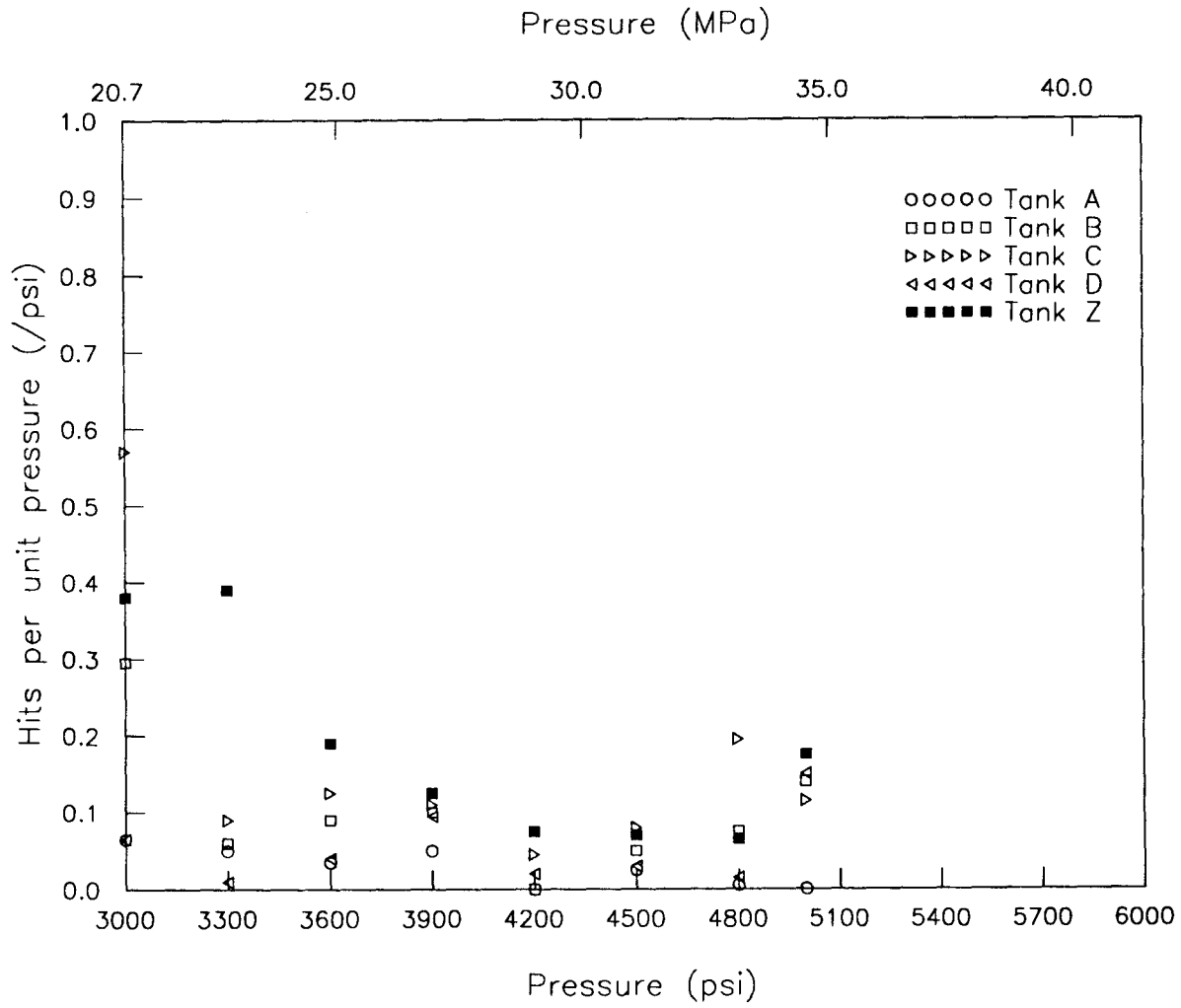
Figure 6.32: Hite rate (hits/MPa) during first cycle of cylinder retests (Amp $\geq$ 30 dB).
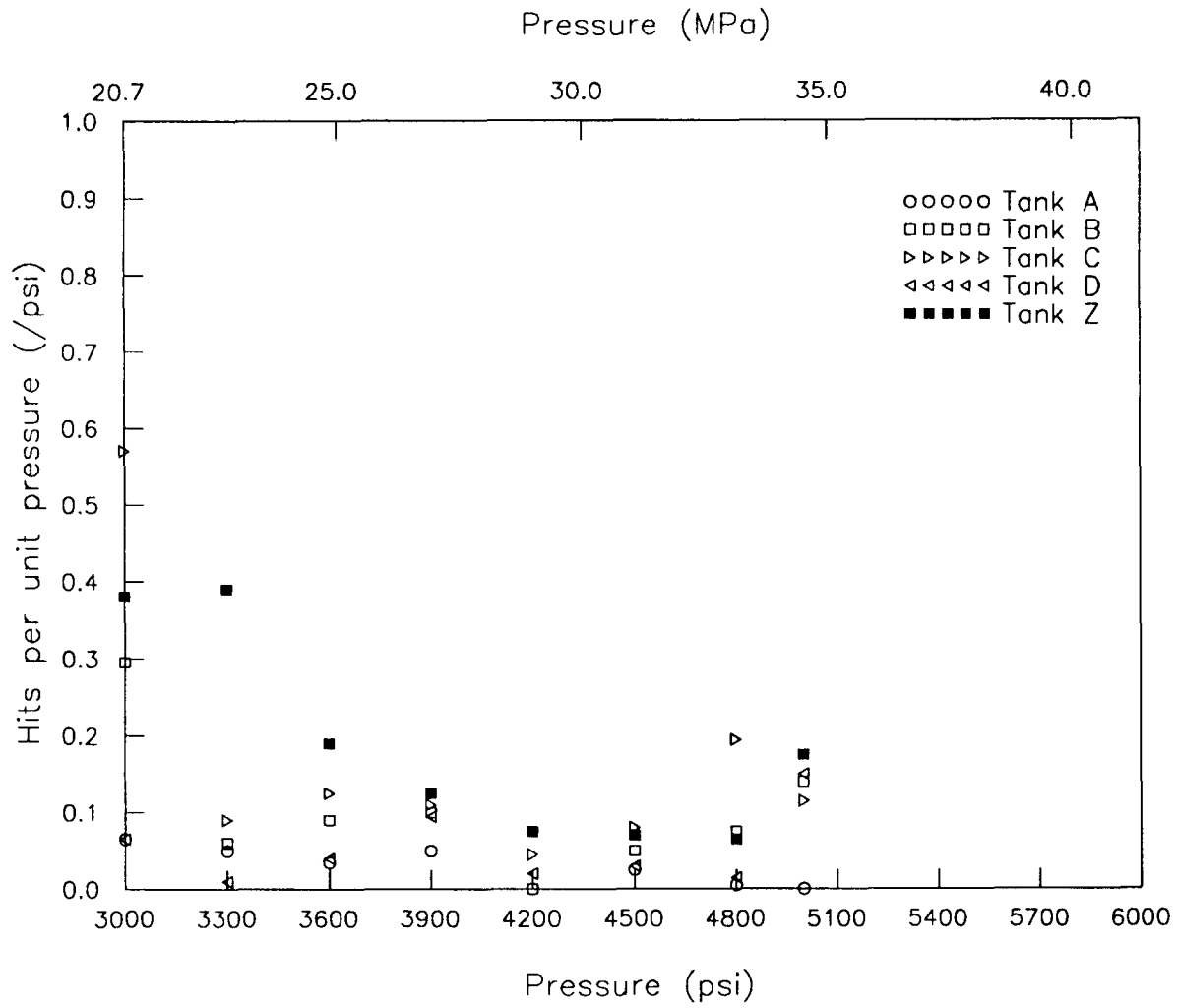
Figure 6.33: Hit rate (hits/MPa) during second cycle of cylinder retests (Amp $\geq$ 30 dB).
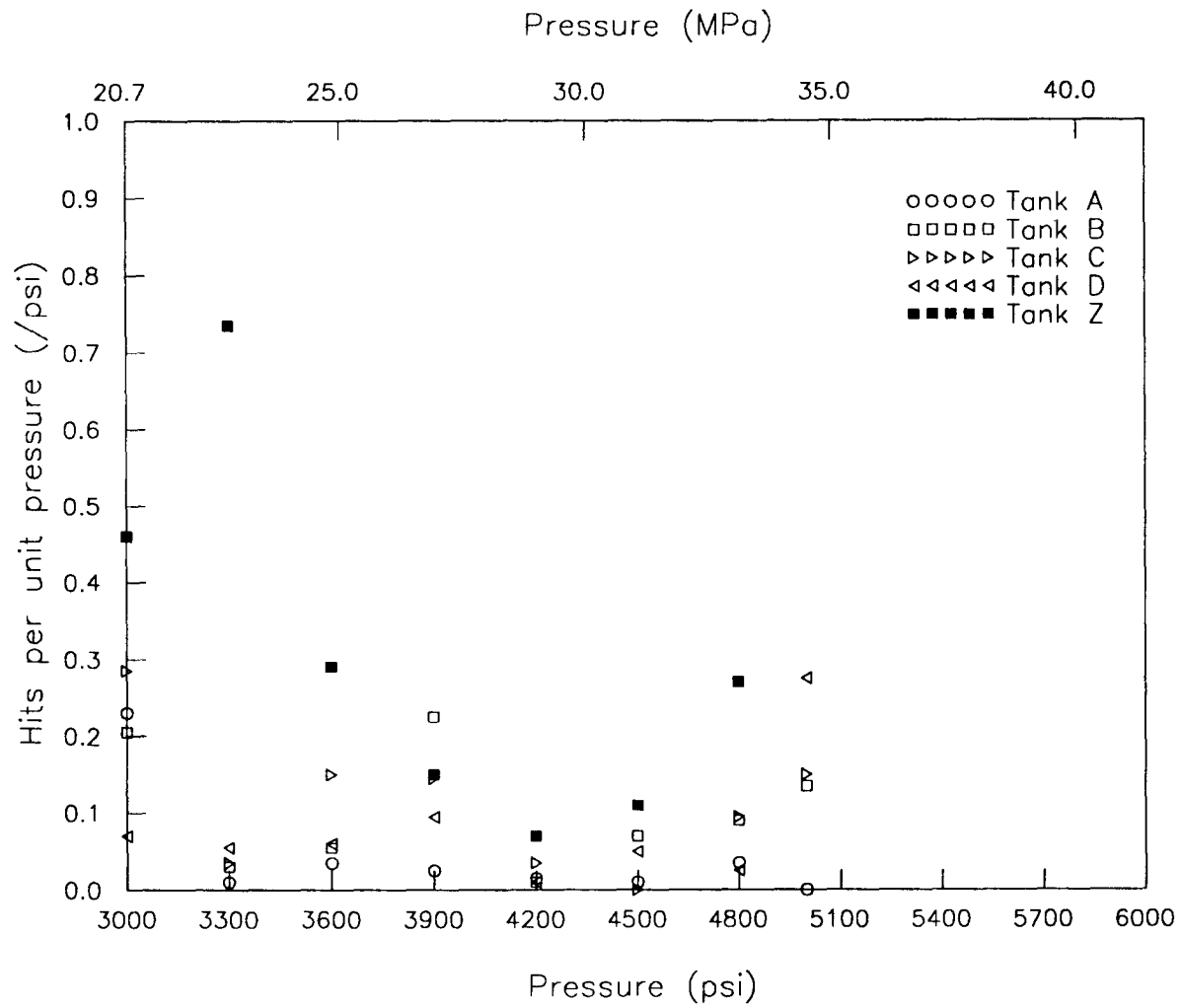
Figure 6.34: Hit rate (hits/MPa) during third cycle of cylinder retests (Amp $\geq$ 30 dB).
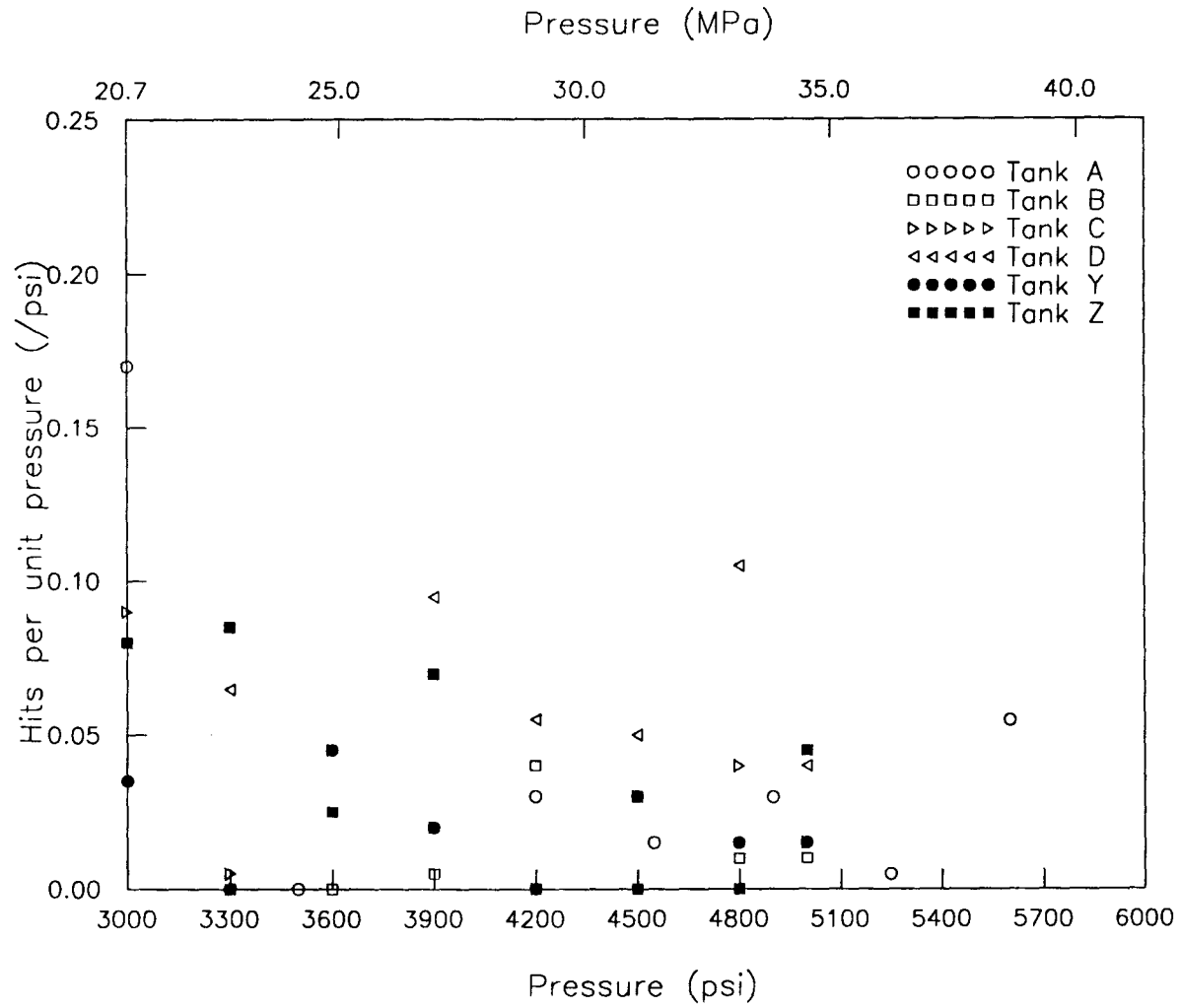
Figure 6.35: Hit rate (hits/MPa) during first cycle of cylinder tests (Amp $\geq$ 40 dB).
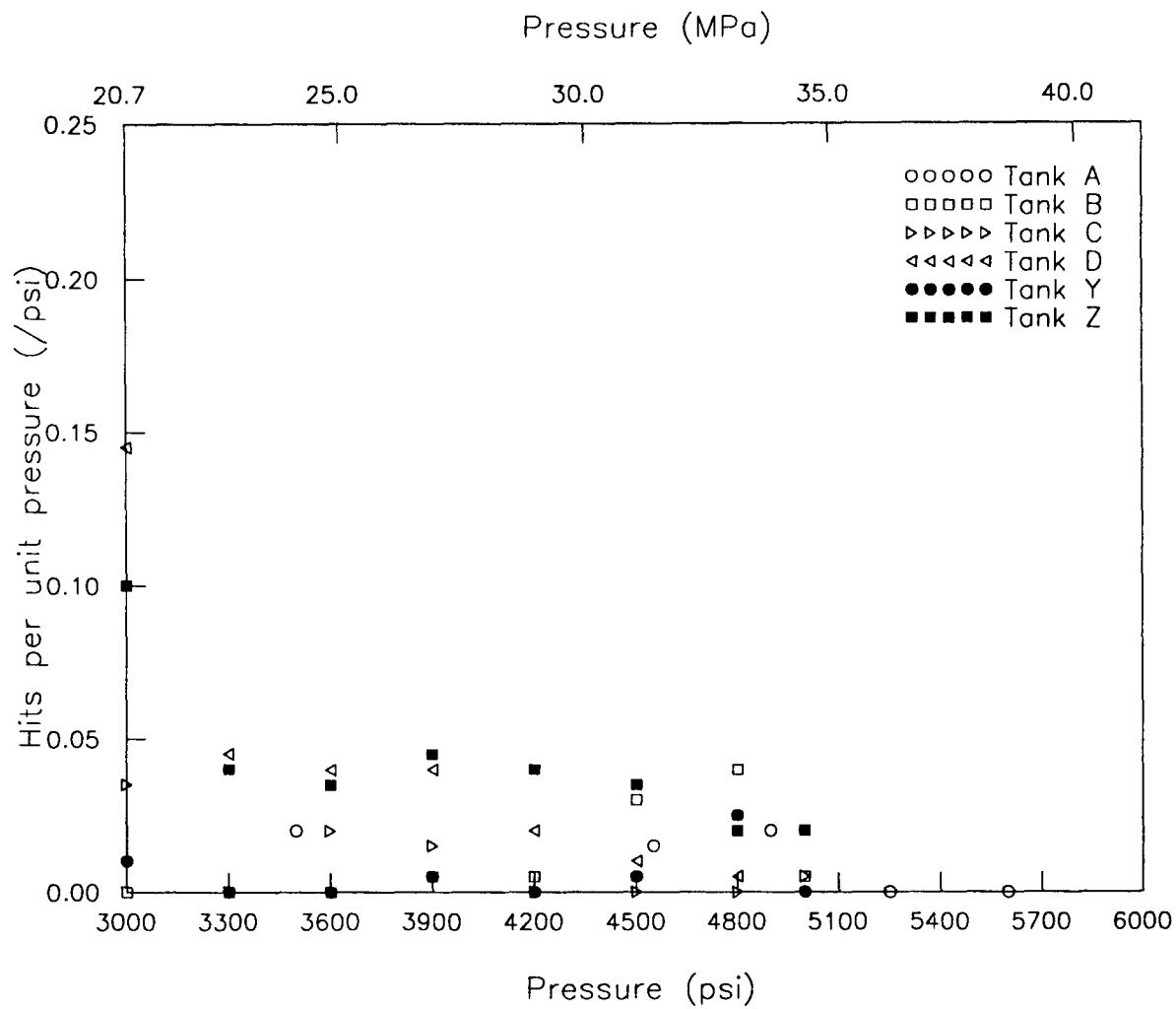
Figure 6.36: Hit rate (hits/MPa) during second cycle of cylinder tests (Amp ≥ 40 dB).
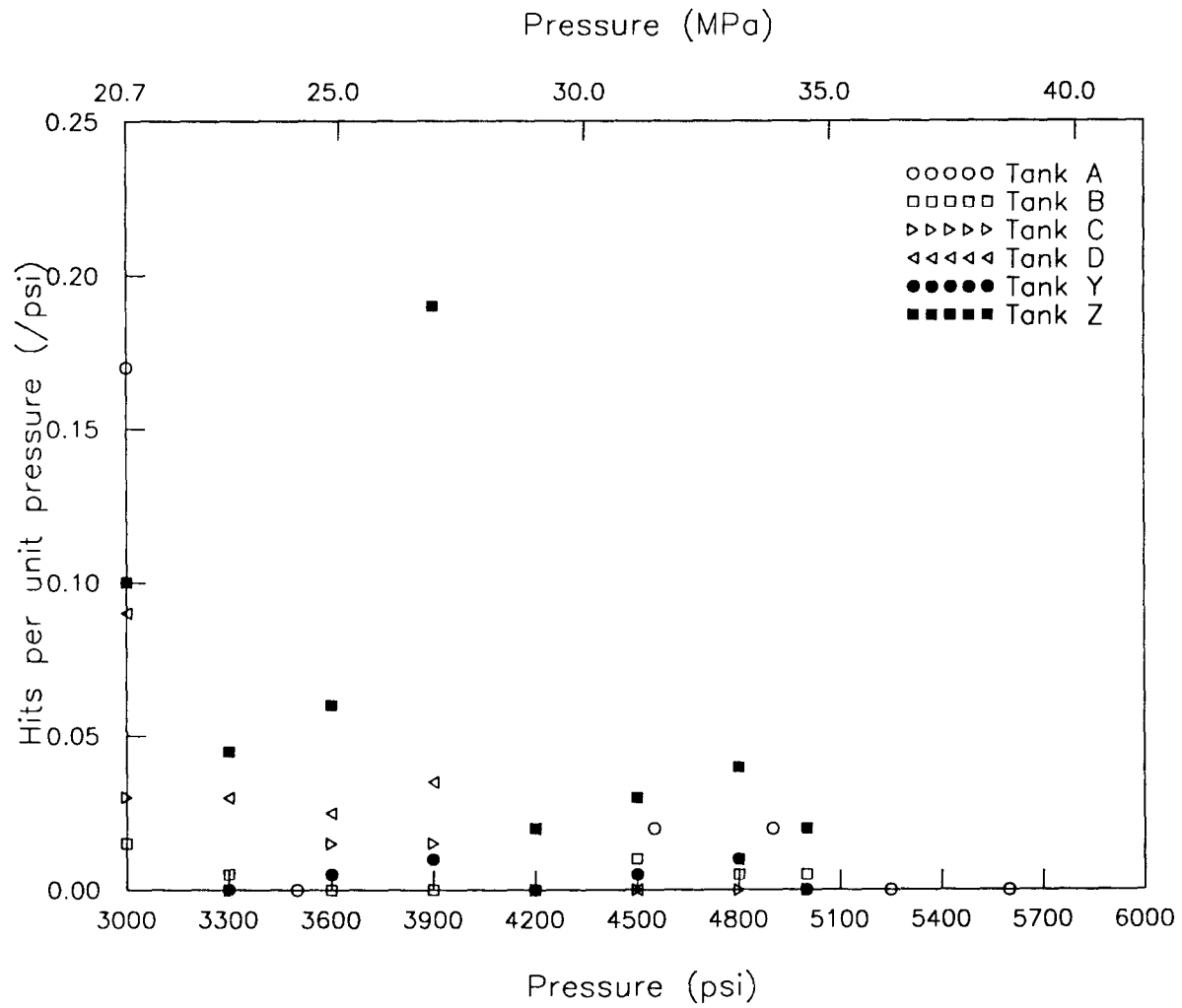
Figure 6.37: Hit rate (hits/MPa) during third cycle of cylinder tests (Amp $\geq$ 40 dB).

Pressure (MPa)
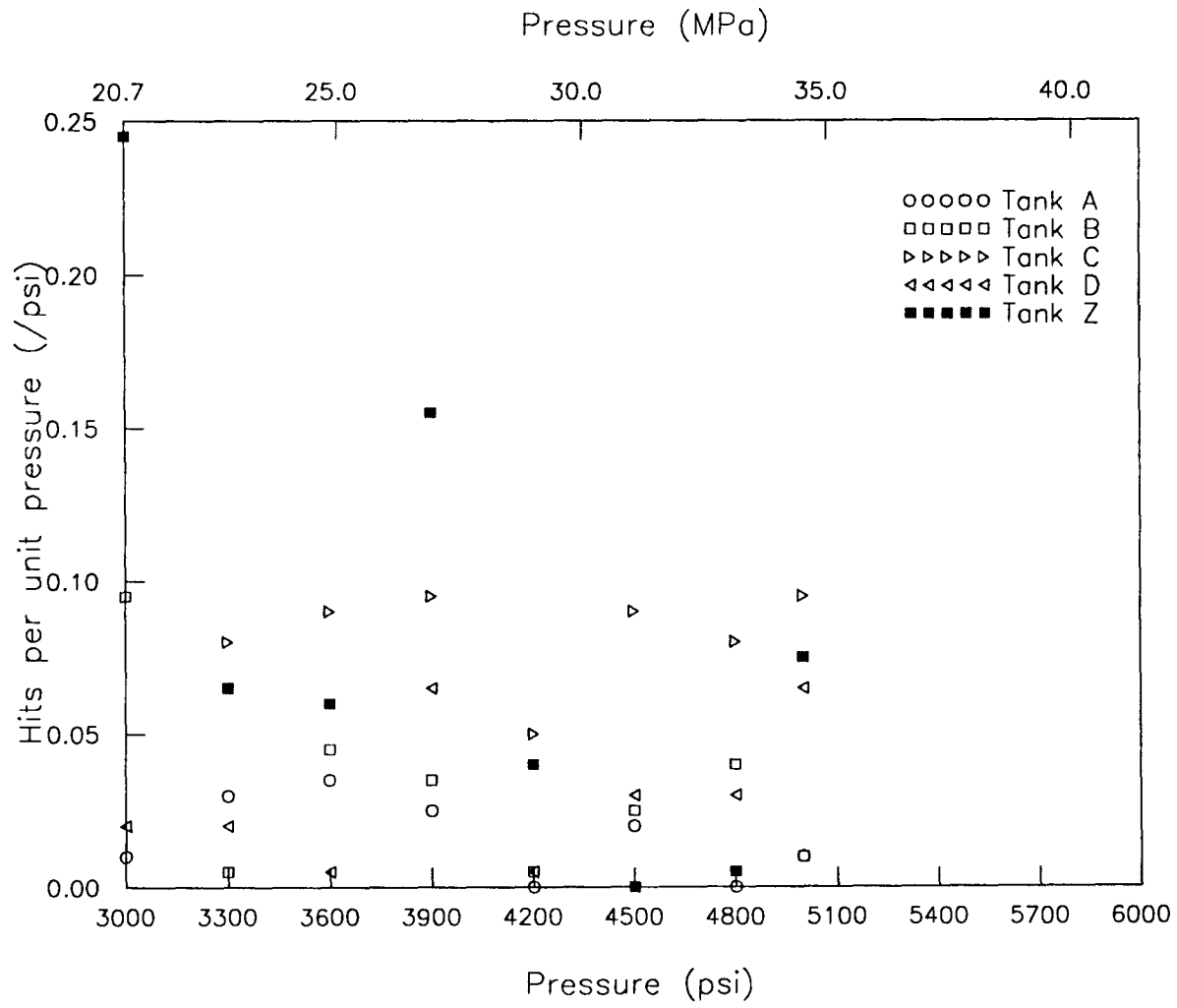
Figure 6.38: Hite rate (hits/MPa) during first cycle of cylinder retests (Amp ≥ 40 dB).
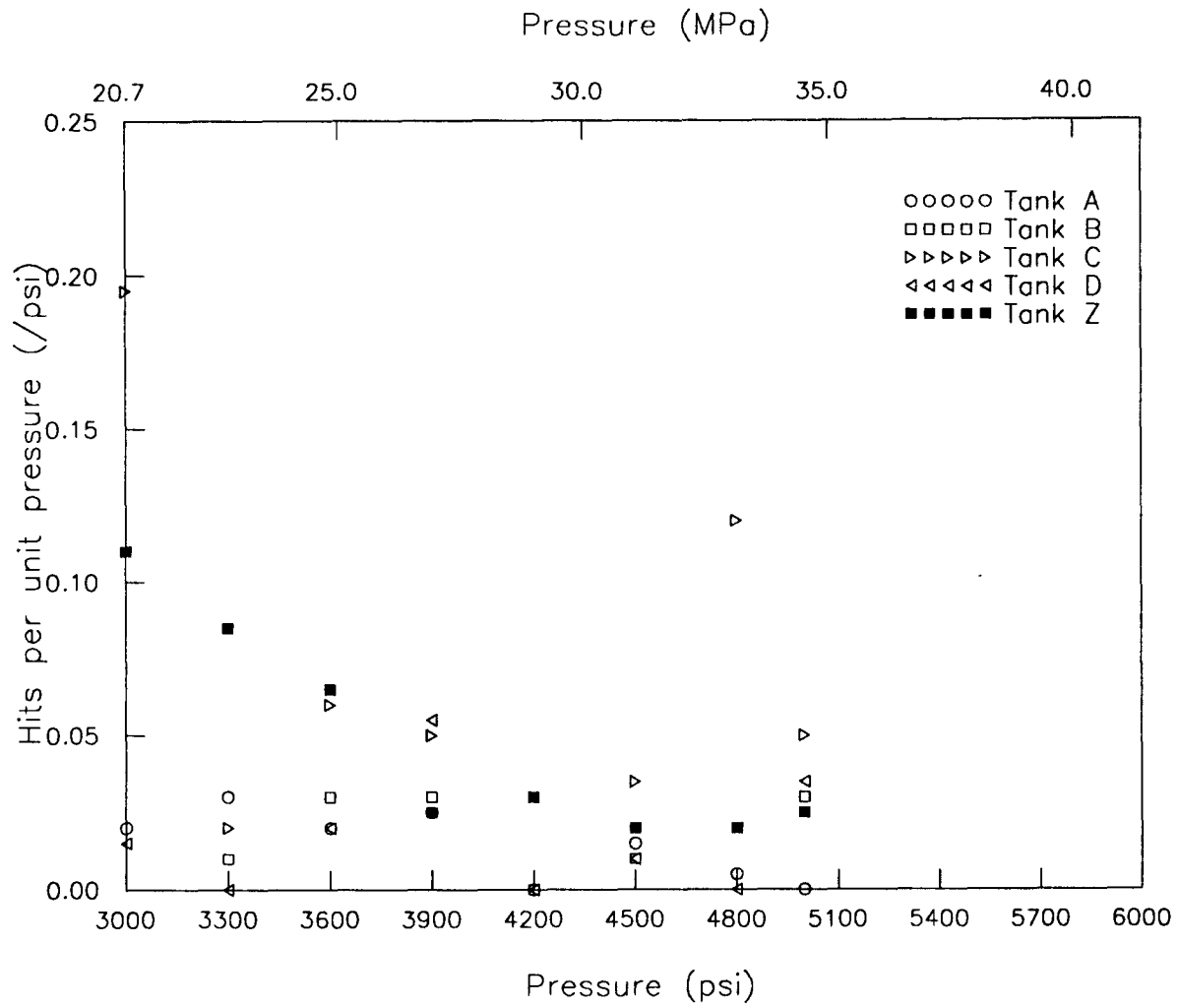
Figure 6.39: Hit rate (hits/MPa) during second cycle of cylinder retests (Amp ≥ 40 dB).
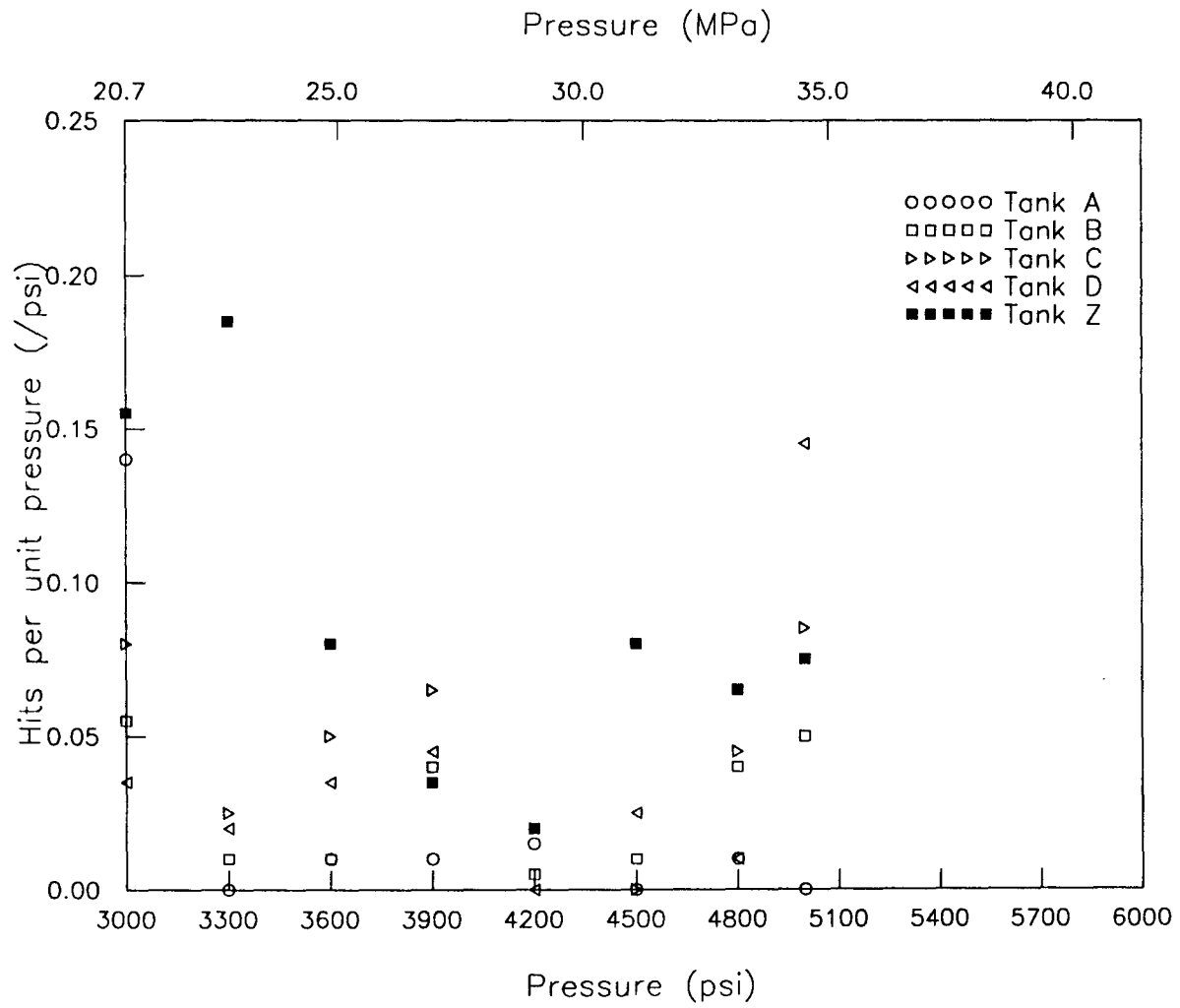
Figure 6.40: Hit rate (hits/MPa) during third cycle of cylinder retests (Amp $\geq$ 40 dB).
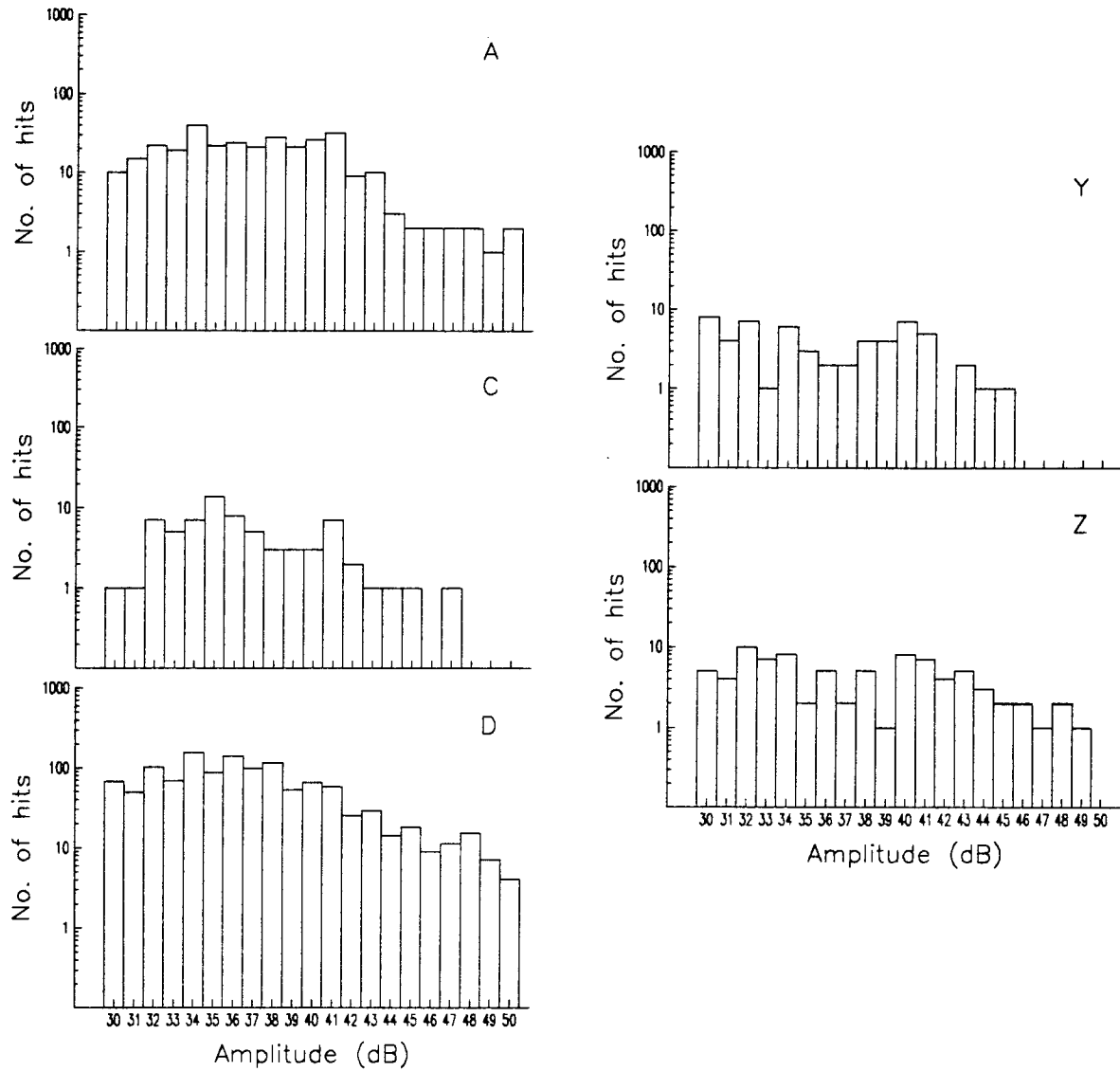
Figure 6.41: First cycle amplitude distributions (P = 20.69 MPa (3000 psi)).
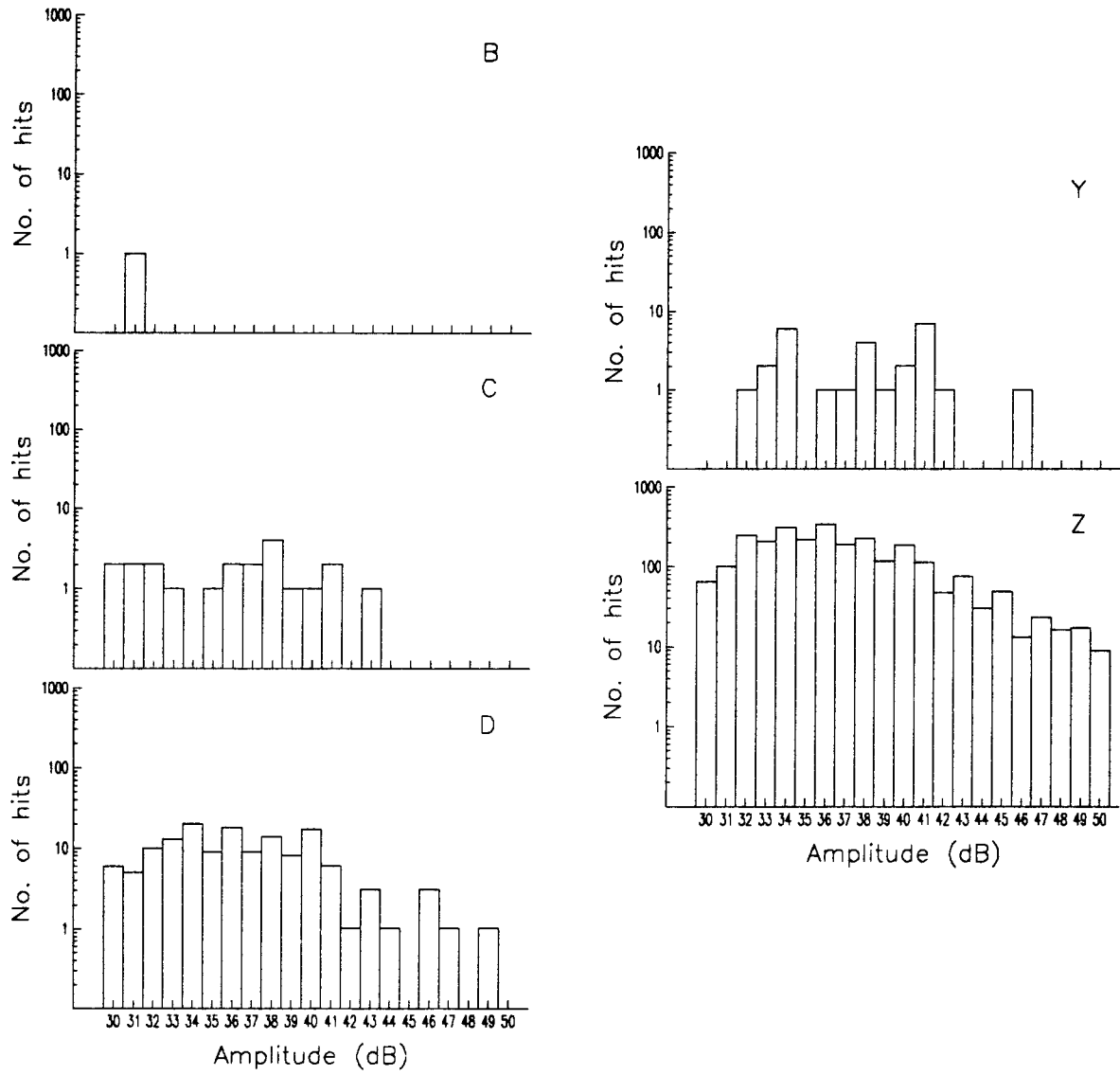
Figure 6.42: First cycle amplitude distributions ($P = 22.75$ MPa (3300 psi)).
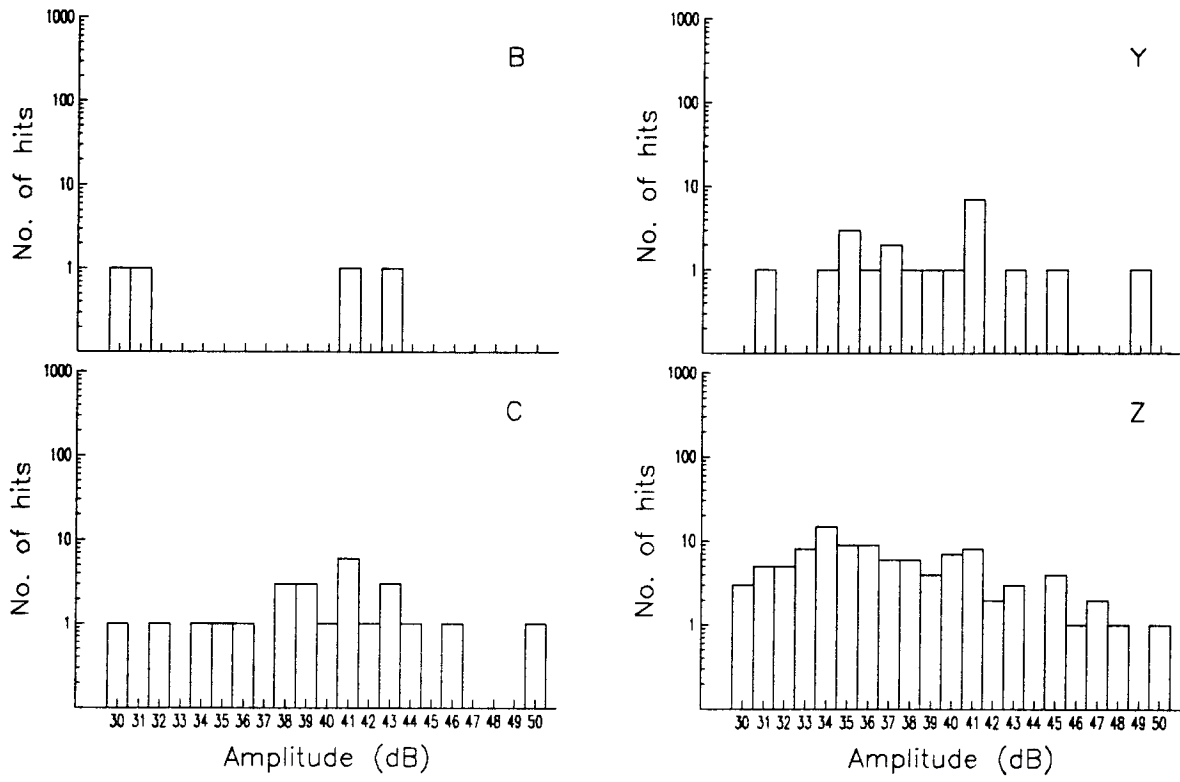
Figure 6.43: First cycle amplitude distributions ($P = 24.82$ MPa (3600 psi)).
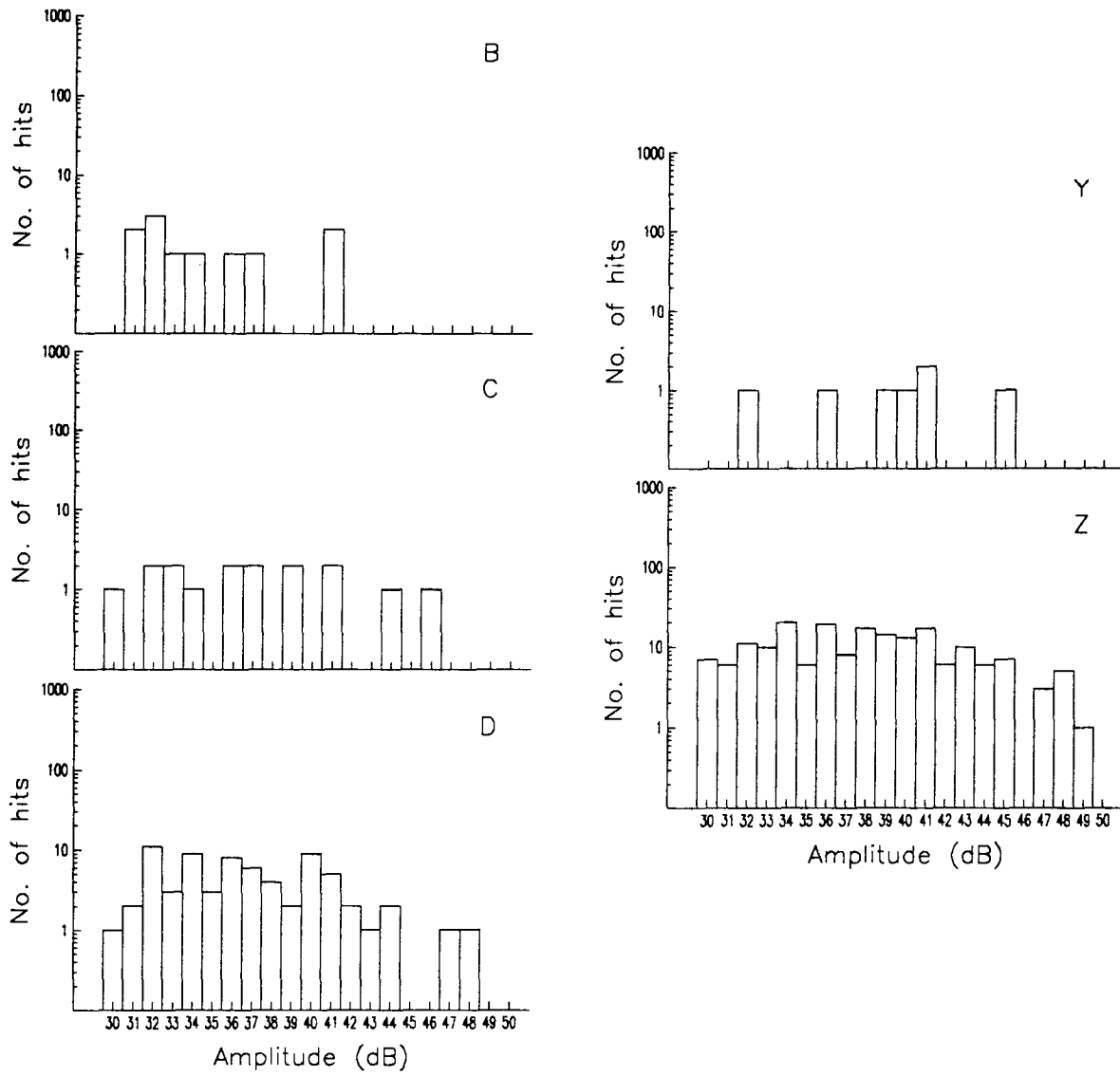
Figure 6.44: First cycle amplitude distributions ($P = 26.89$ MPa (3900 psi)).
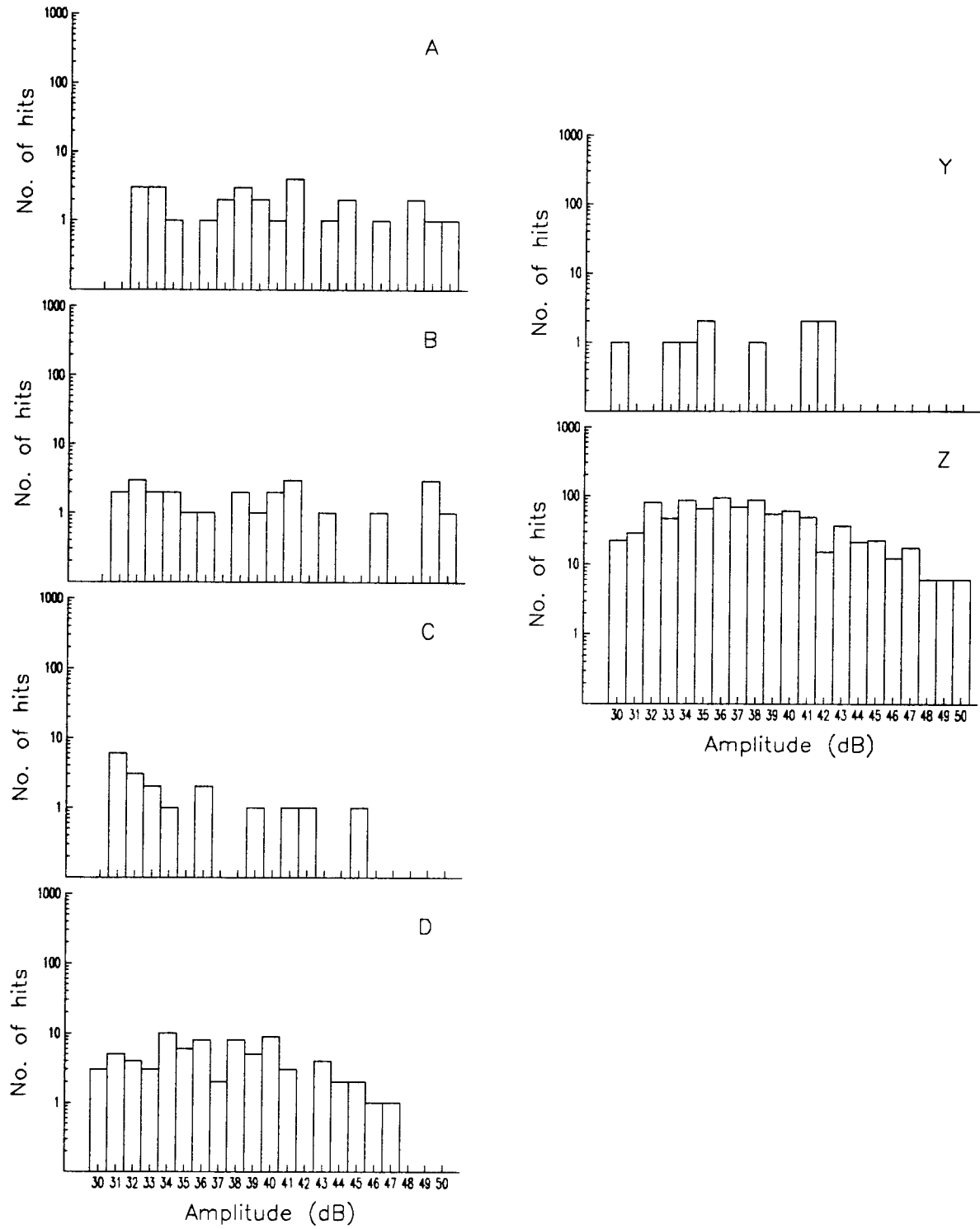
Figure 6.45: First cycle amplitude distributions ($P = 28.96$ MPa (4200 psi)).
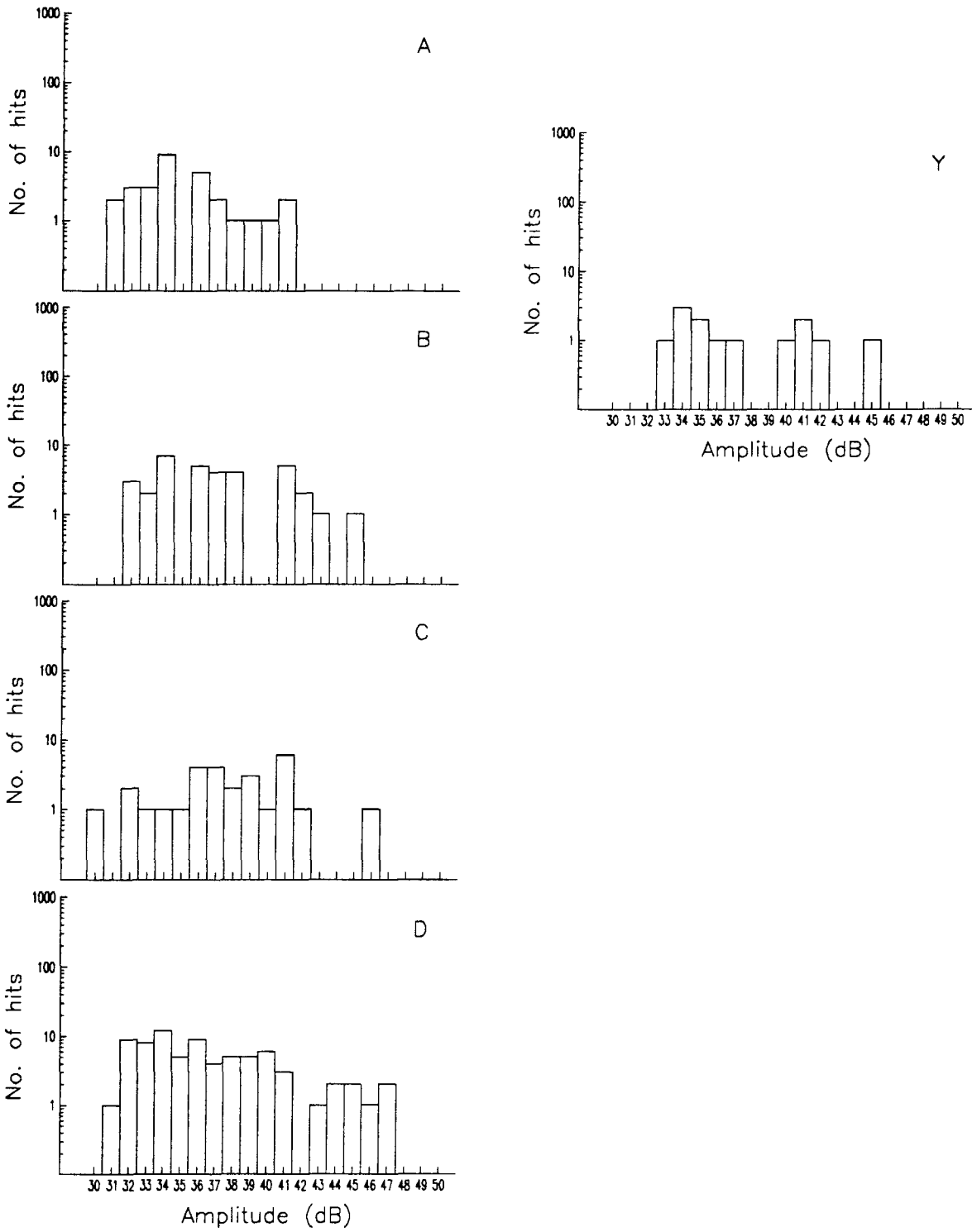
Figure 6.46: First cycle amplitude distributions ($P = 31.03$ MPa (4500 psi)).
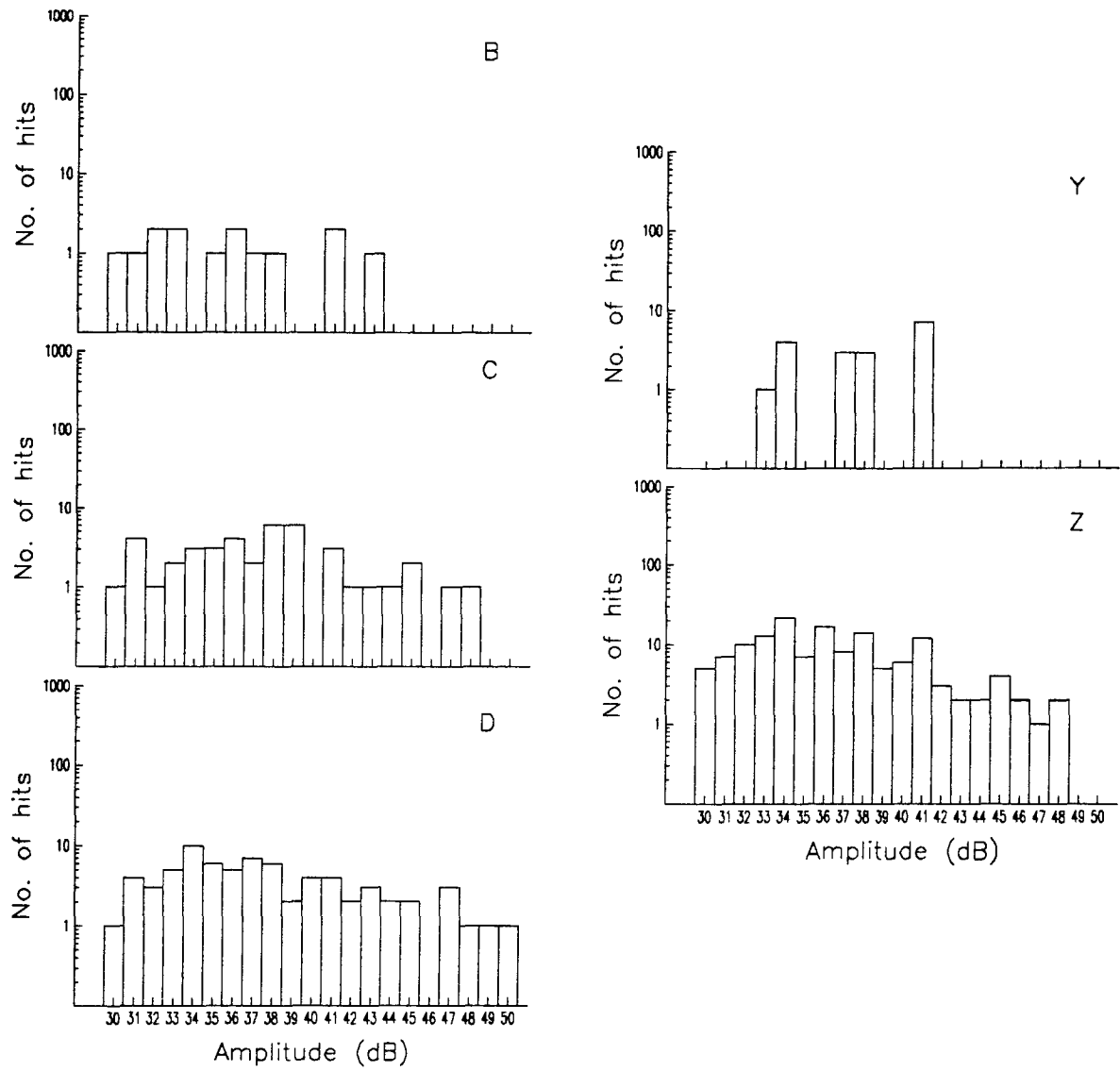
Figure 6.47: First cycle amplitude distributions ($P = 33.10$ MPa (4800 psi)).
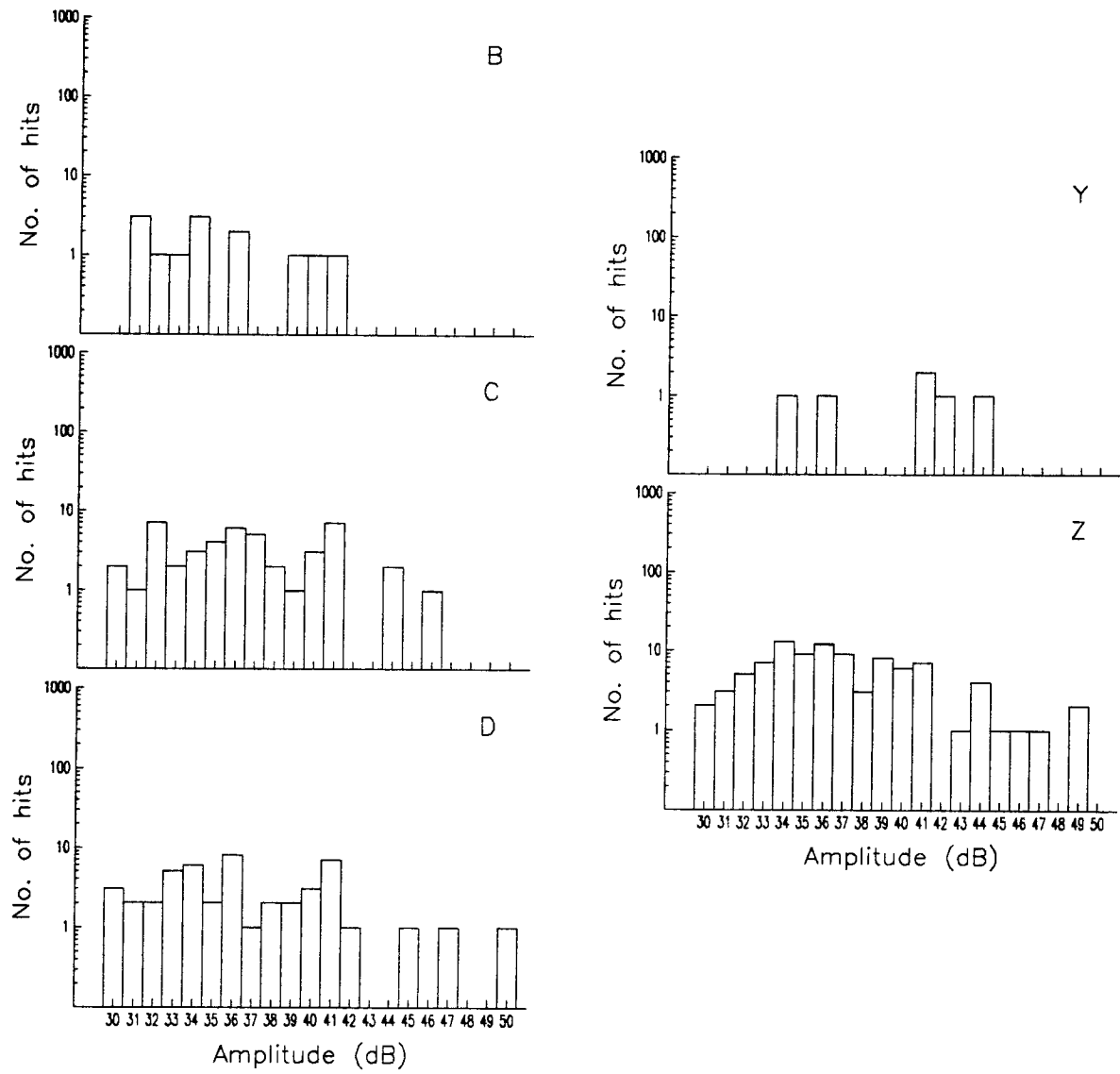
Figure 6.48: First cycle amplitude distributions ($P = 34.48$ MPa (5000 psi)).
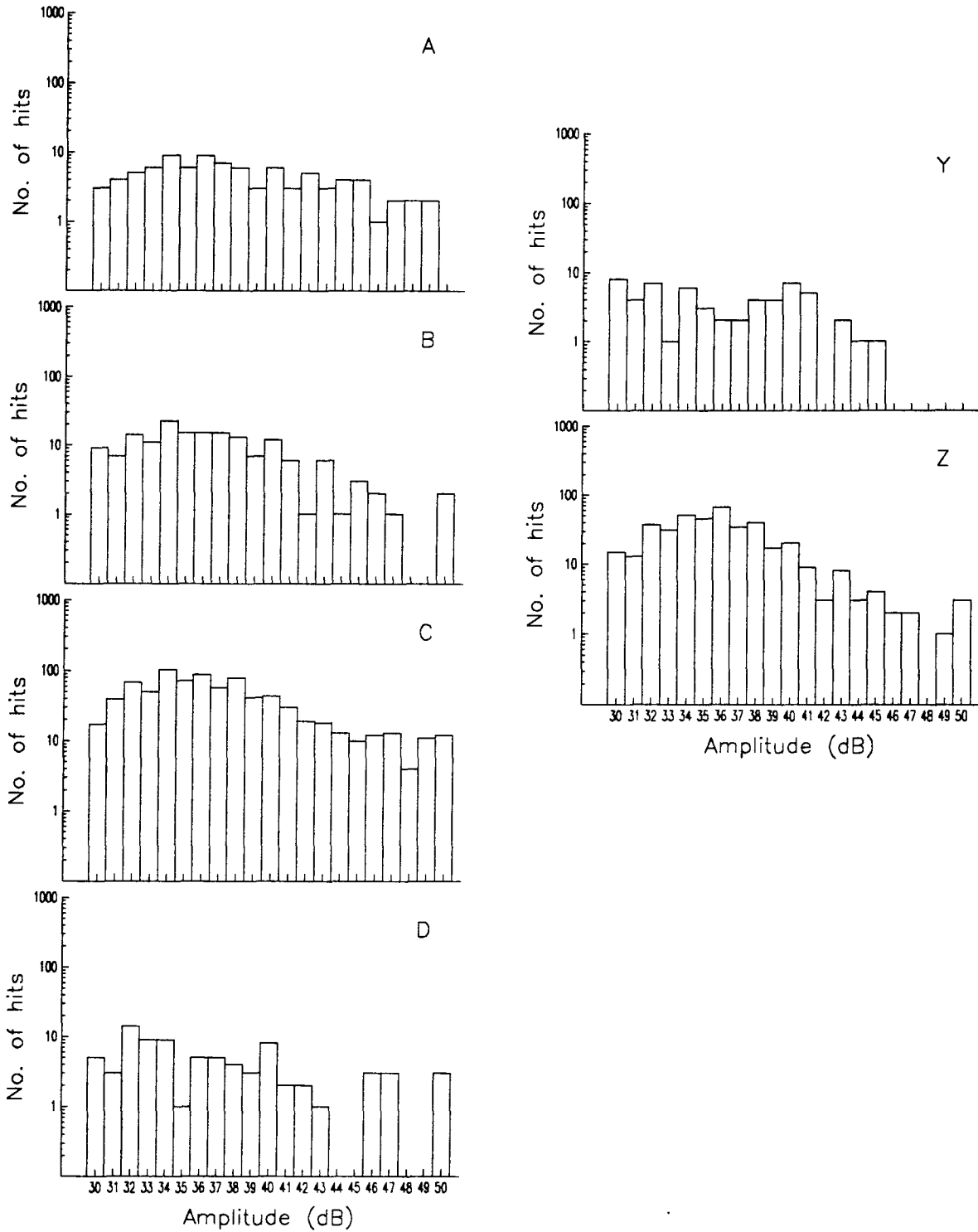
Figure 6.49: First cycle amplitude distributions (cylinder retests, $P = 20.69$ MPa (3000 psi)).
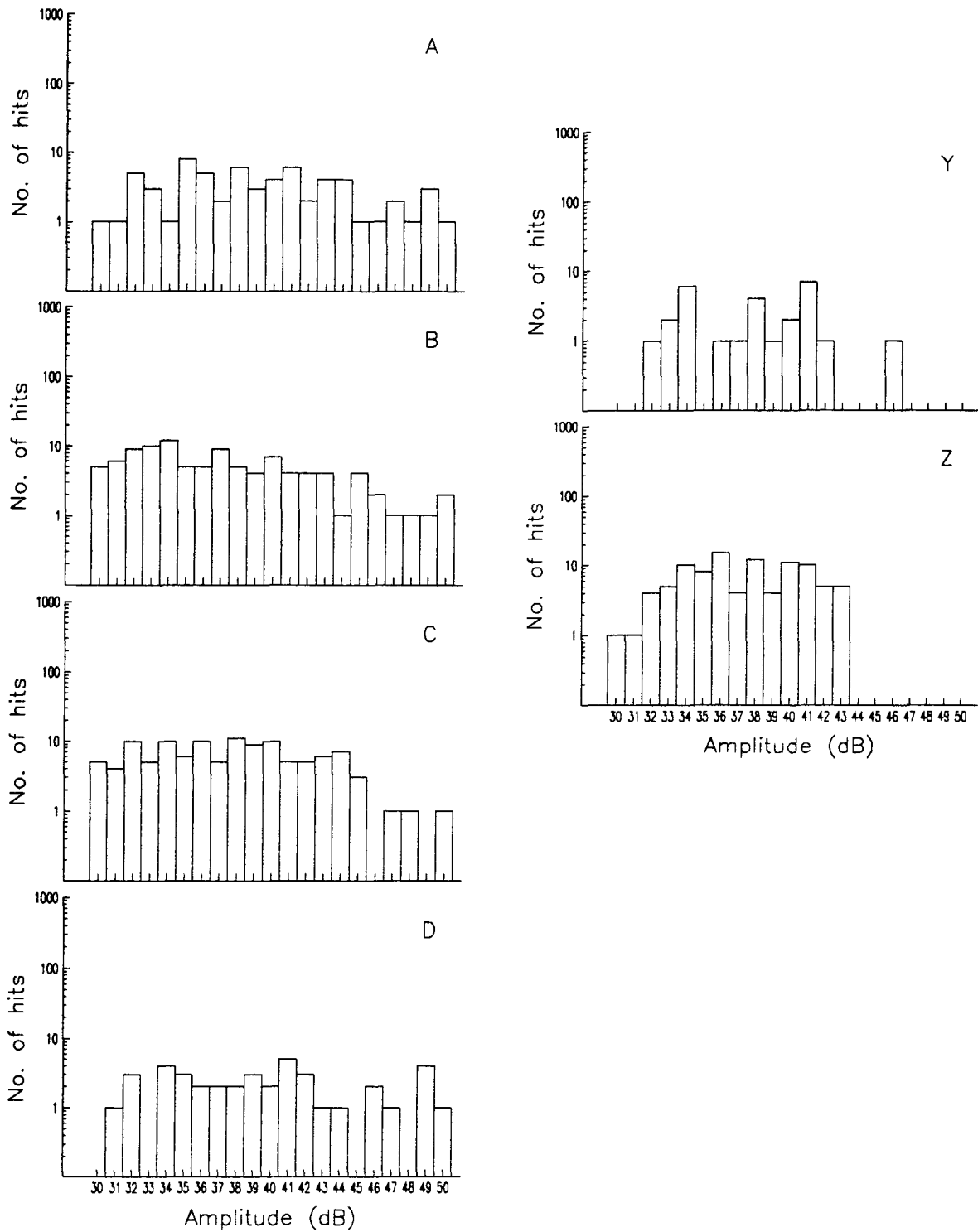
Figure 6.50: First cycle amplitude distributions (cylinder retests, $P = 22.75$ MPa (3300 psi)).
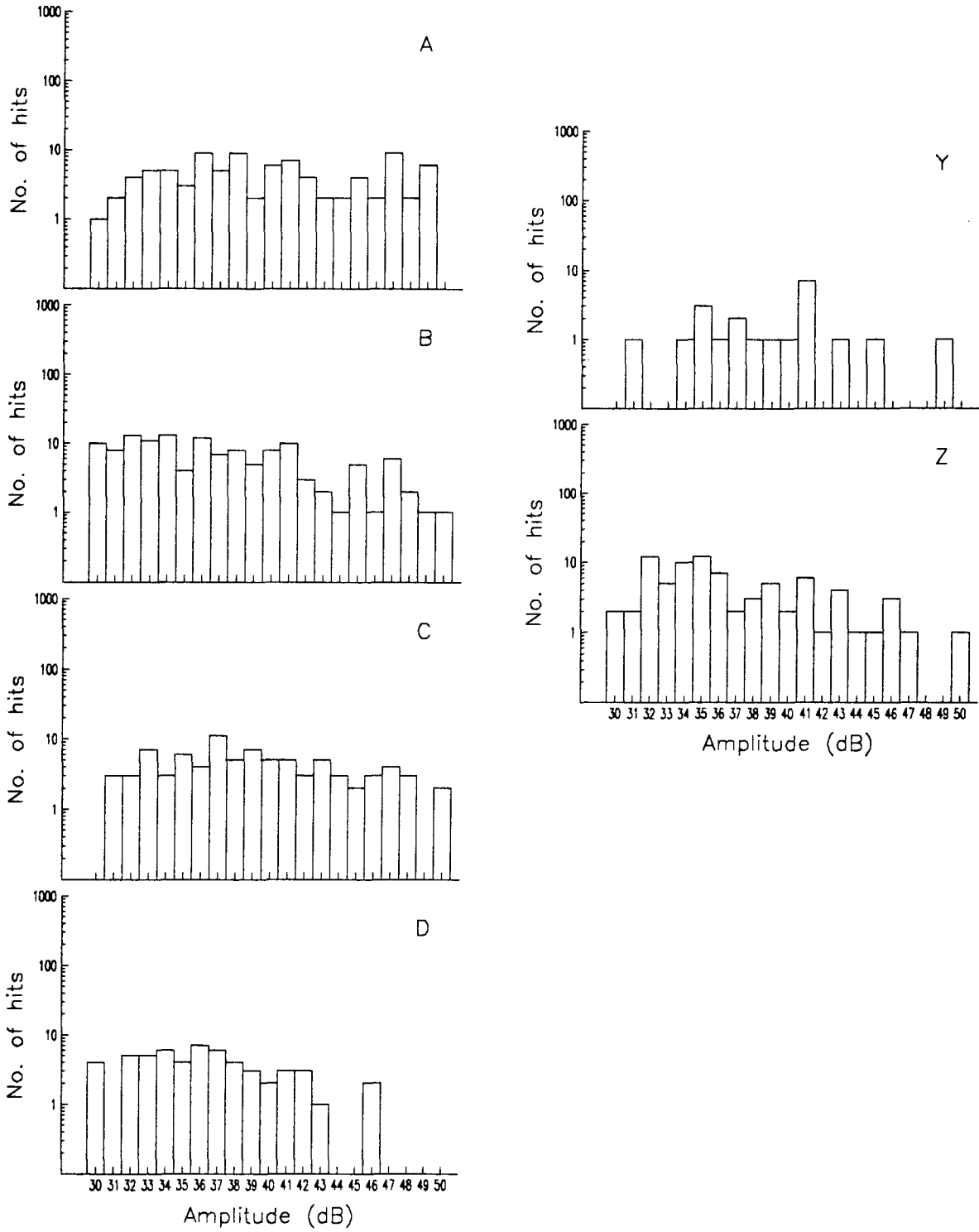
Figure 6.51: First cycle amplitude distributions (cylinder retests, $P = 24.82$ MPa (3600 psi)).
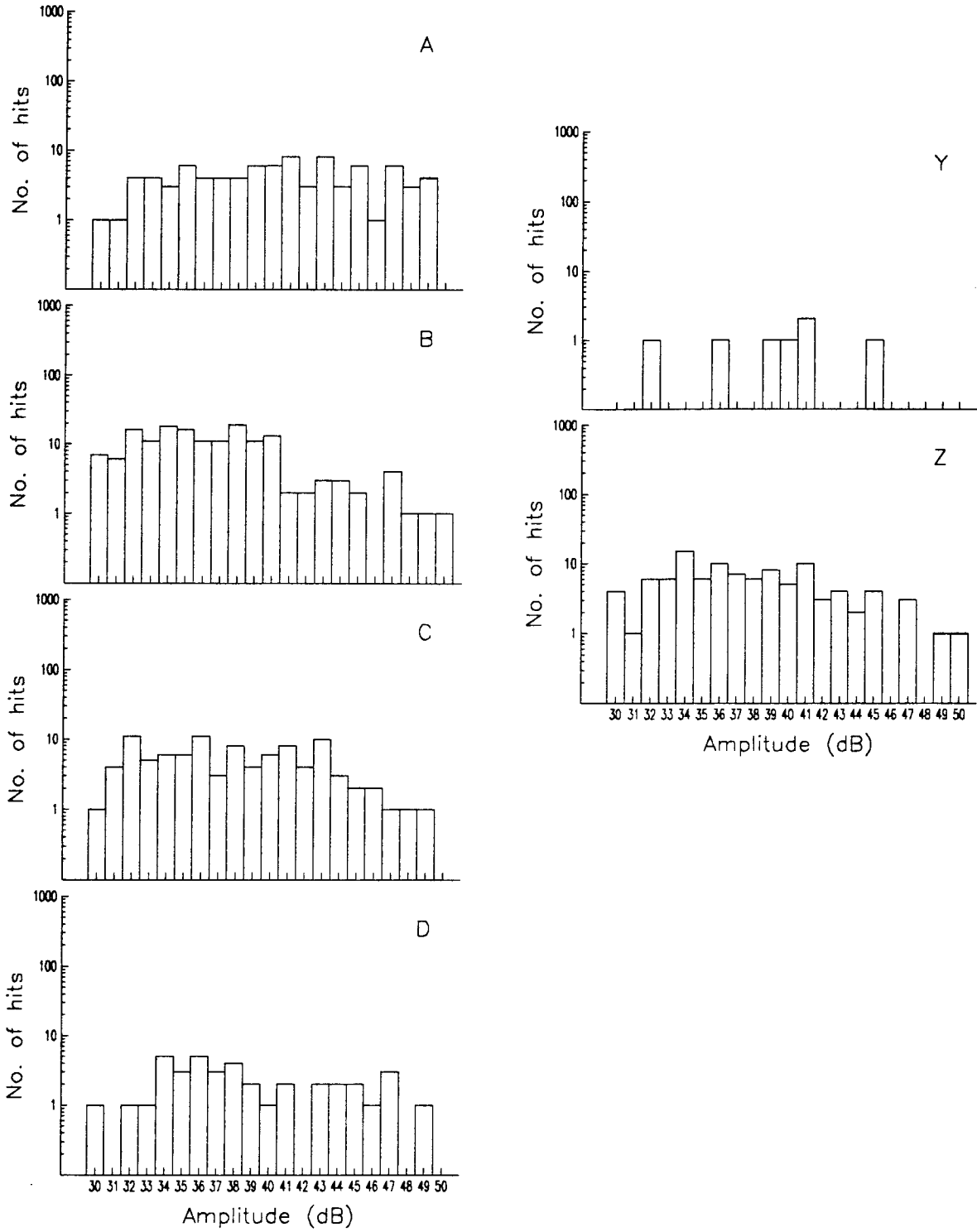
Figure 6.52: First cycle amplitude distributions (cylinder retests, $P = 26.89$ MPa (3900 psi)).
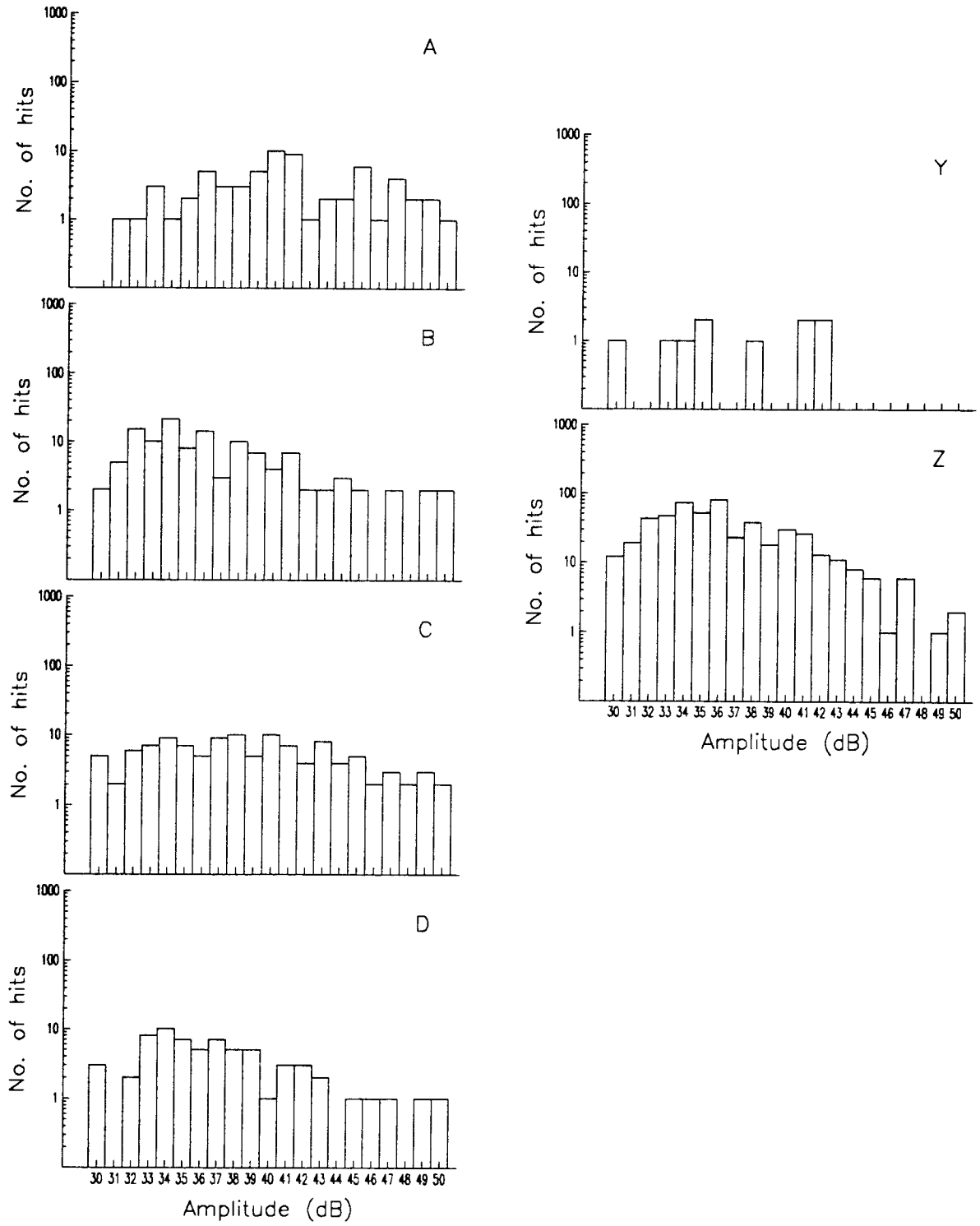
Figure 6.53: First cycle amplitude distributions (cylinder retests, $P = 28.96$ MPa (4200 psi)).
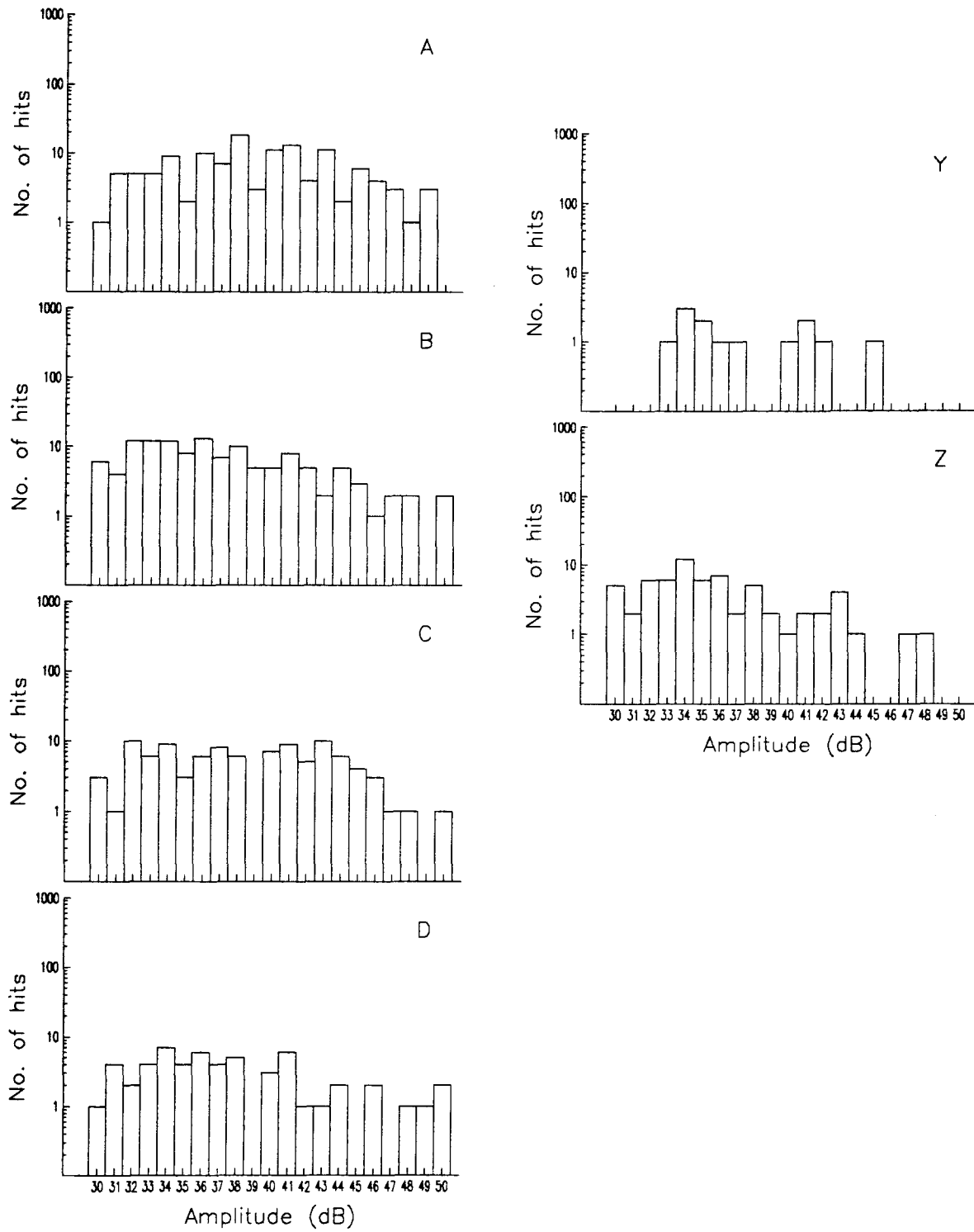
Figure 6.54: First cycle amplitude distributions (cylinder retests, $P = 31.03$ MPa (4500 psi)).
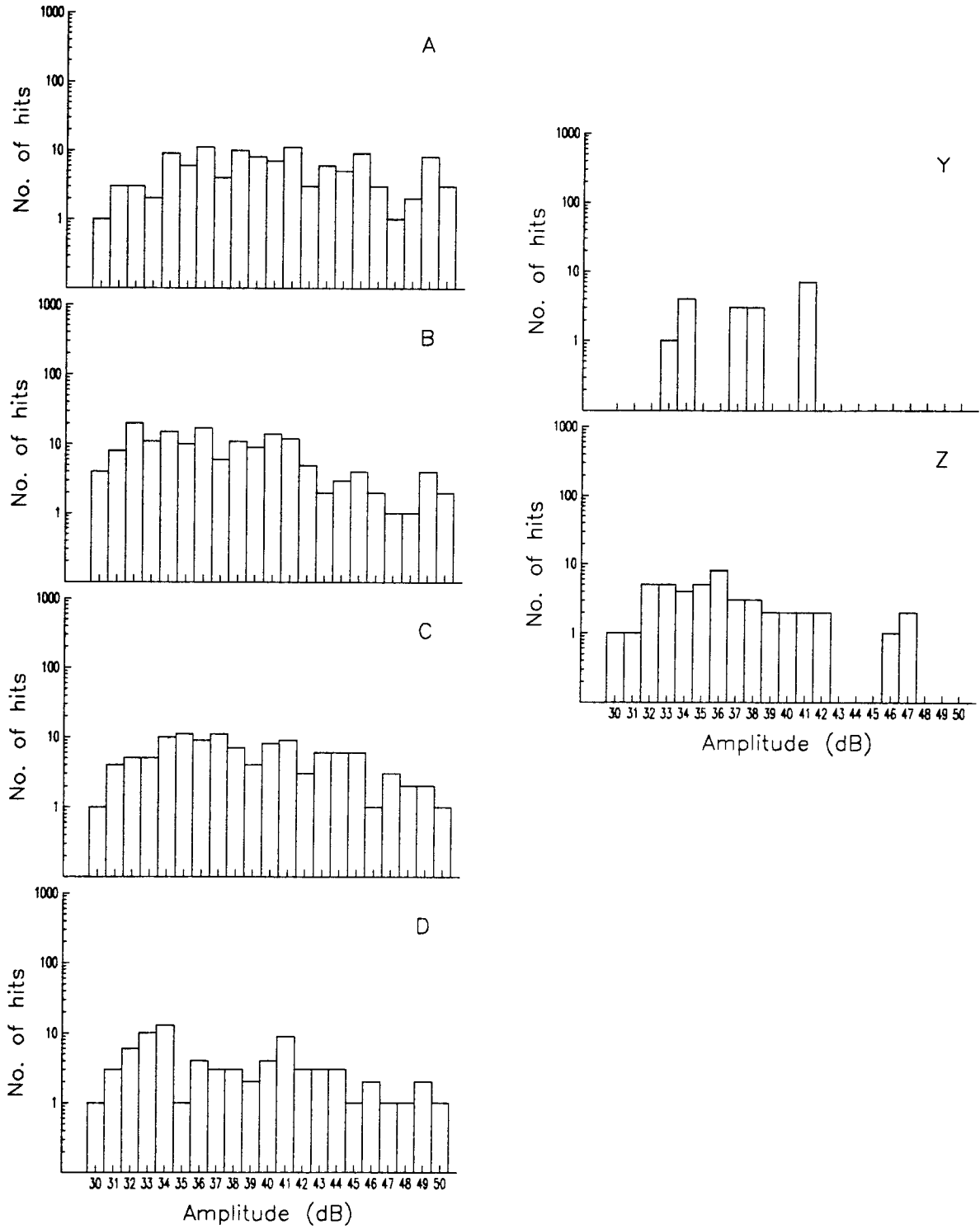
Figure 6.55: First cycle amplitude distributions (cylinder retests, $P = 33.10$ MPa (4800 psi)).
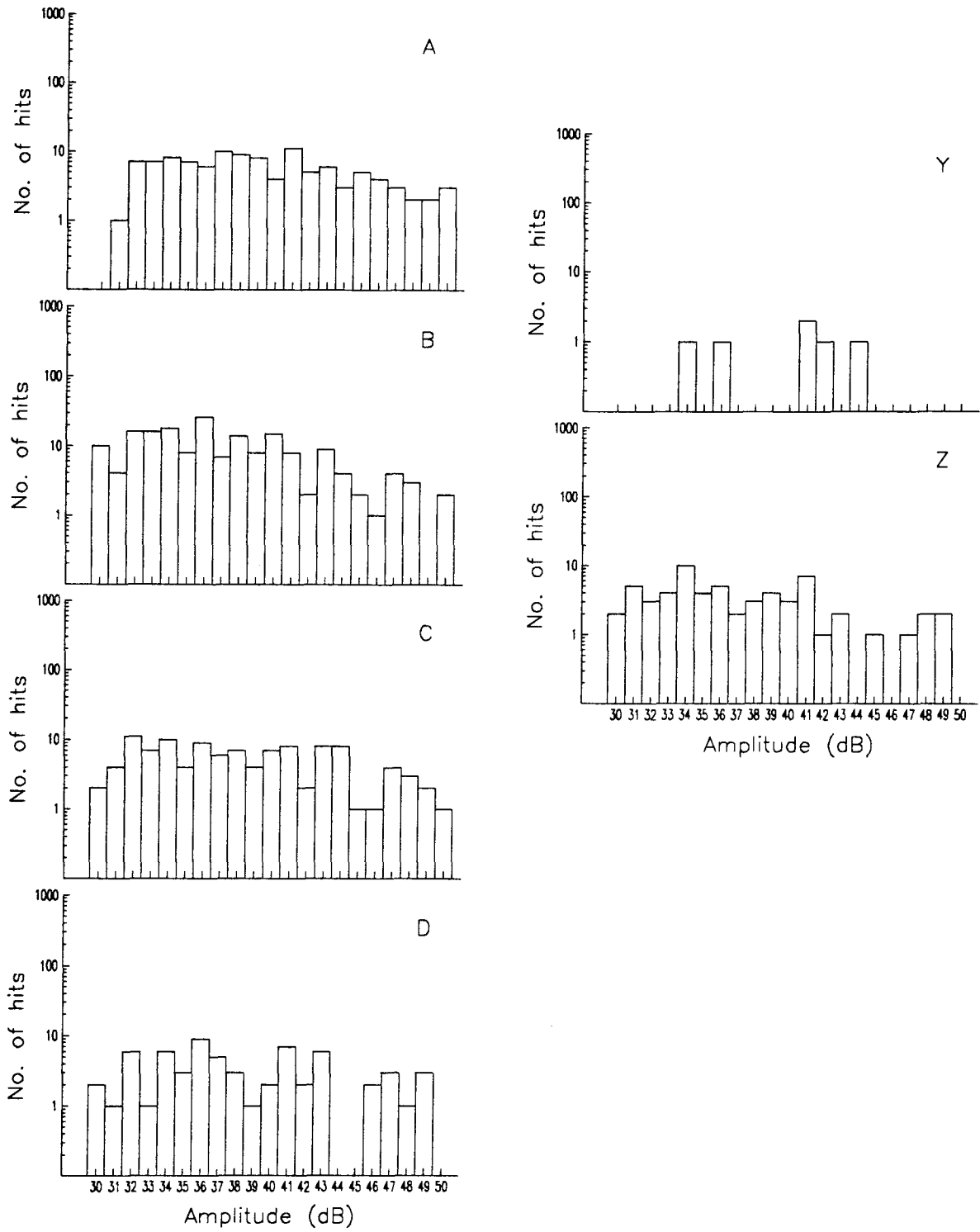
Figure 6.56: First cycle amplitude distributions (cylinder retests, $P = 34.48$ MPa (5000 psi)).
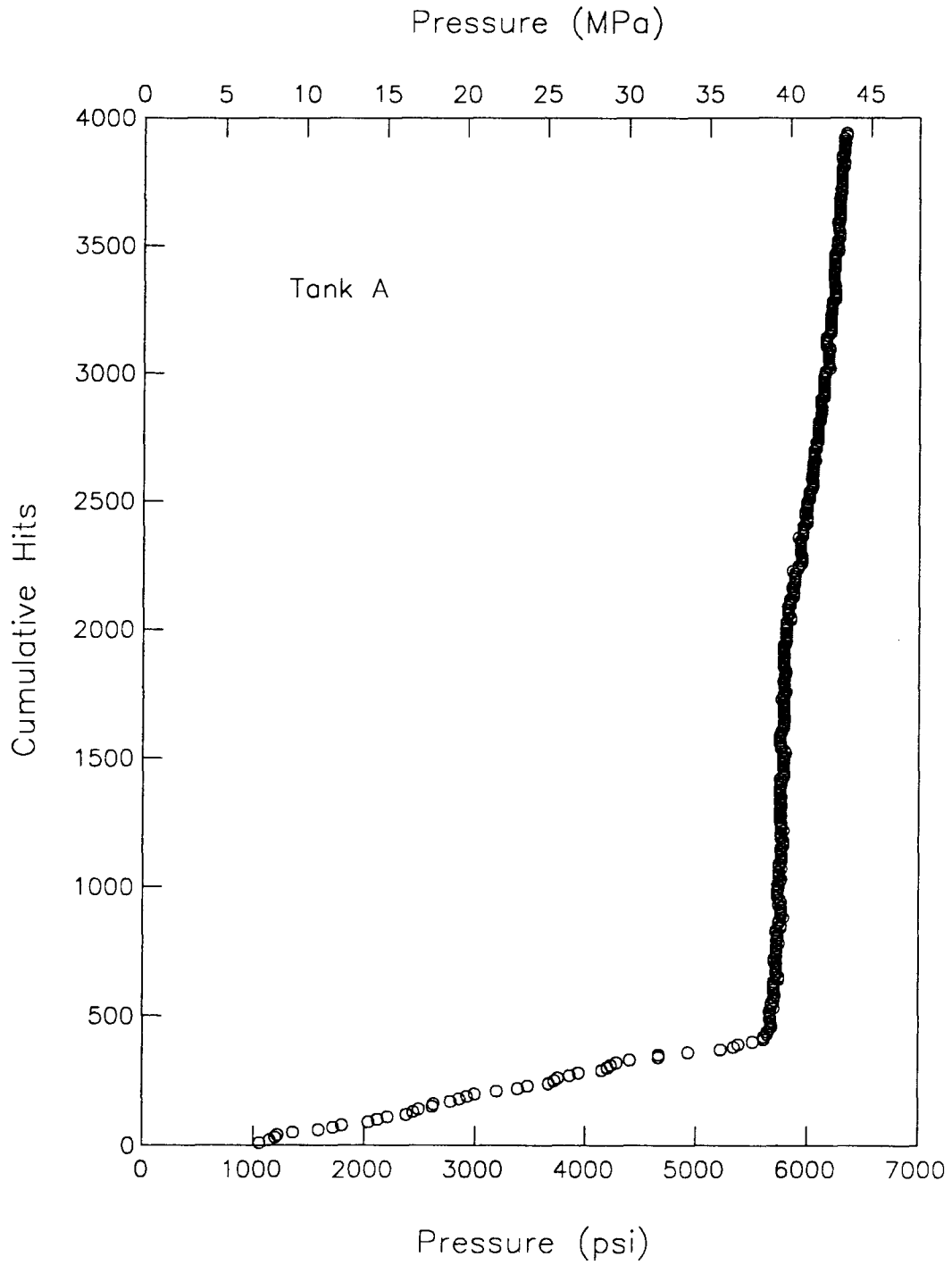
Figure 6.57: Cumulative hits versus pressure for burst test of Tank A.
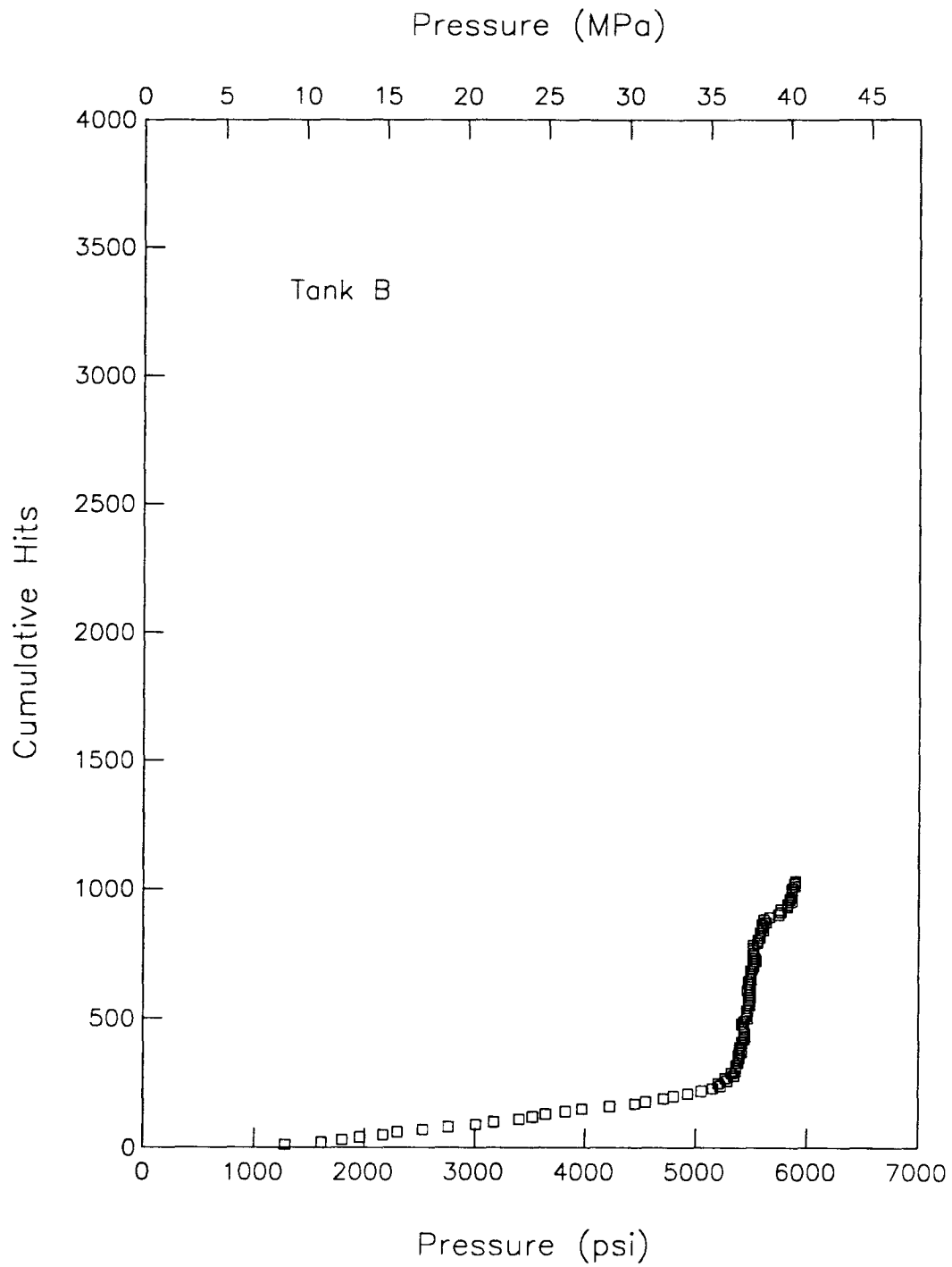
Figure 6.58: Cumulative hits versus pressure for burst test of Tank B.
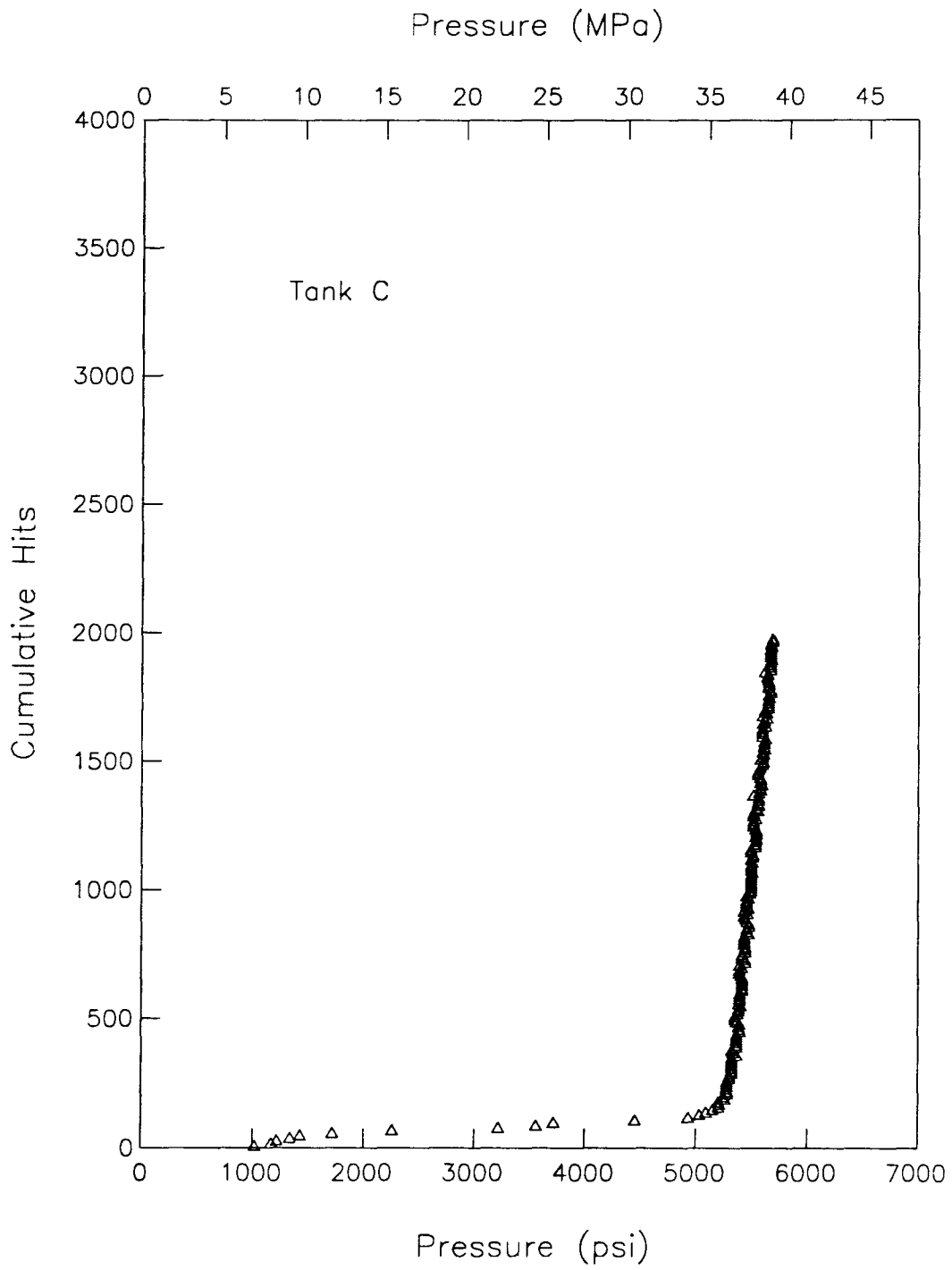
Figure 6.59: Cumulative hits versus pressure for burst test of Tank C.
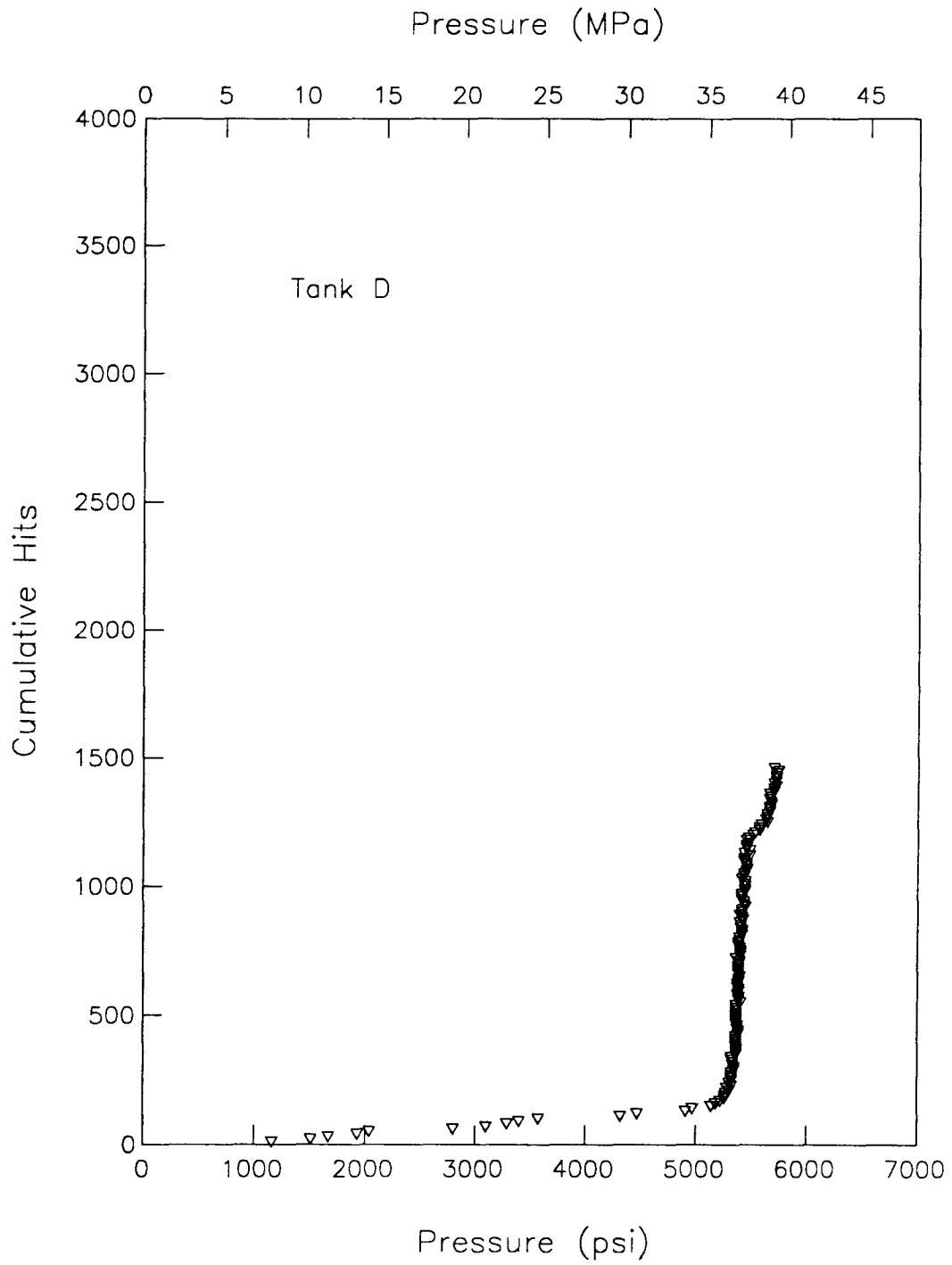
Figure 6.60: Cumulative hits versus pressure for burst test of Tank D.
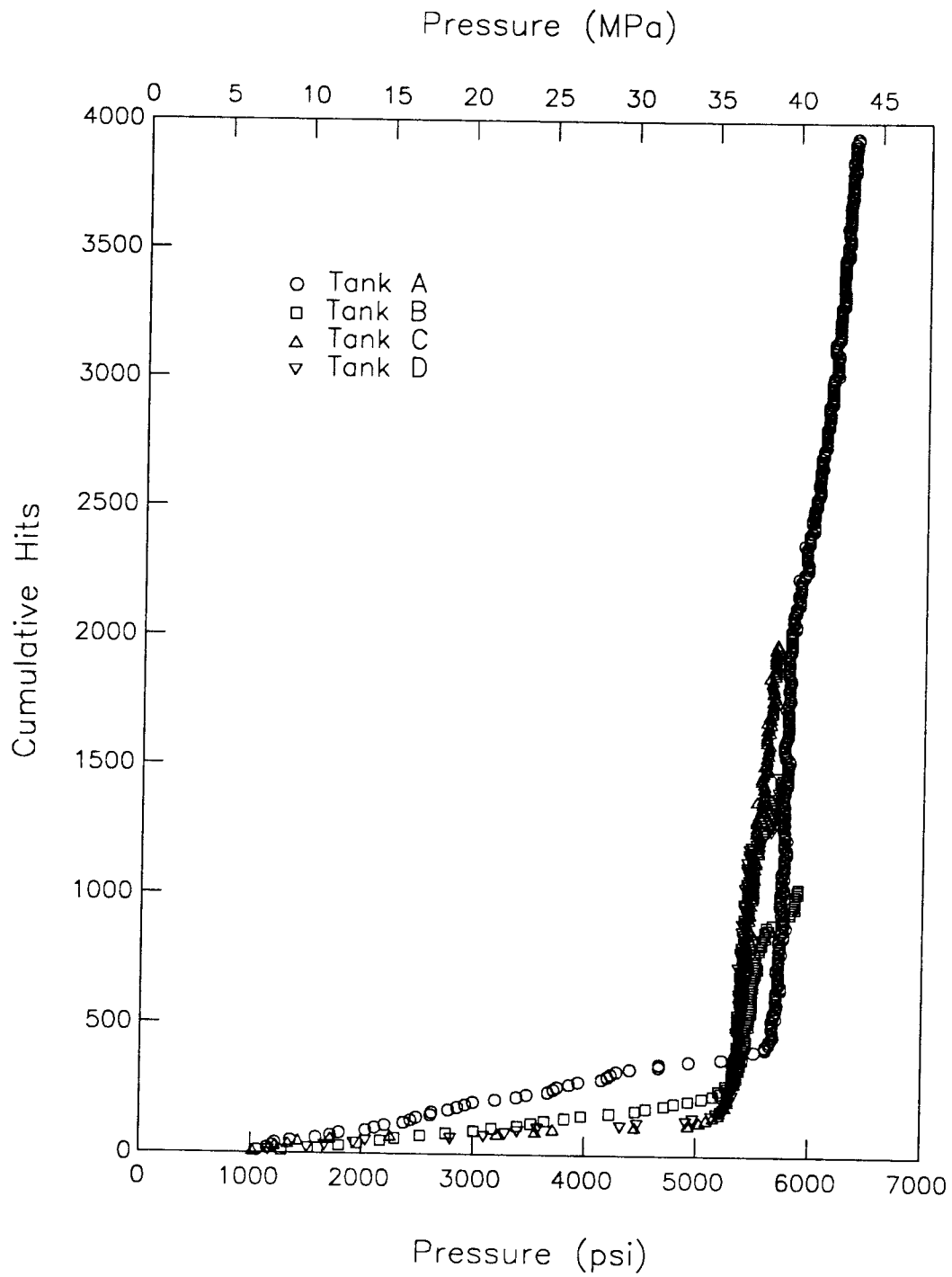
Figure 6.61: Cumulative hits versus pressure for burst tests.
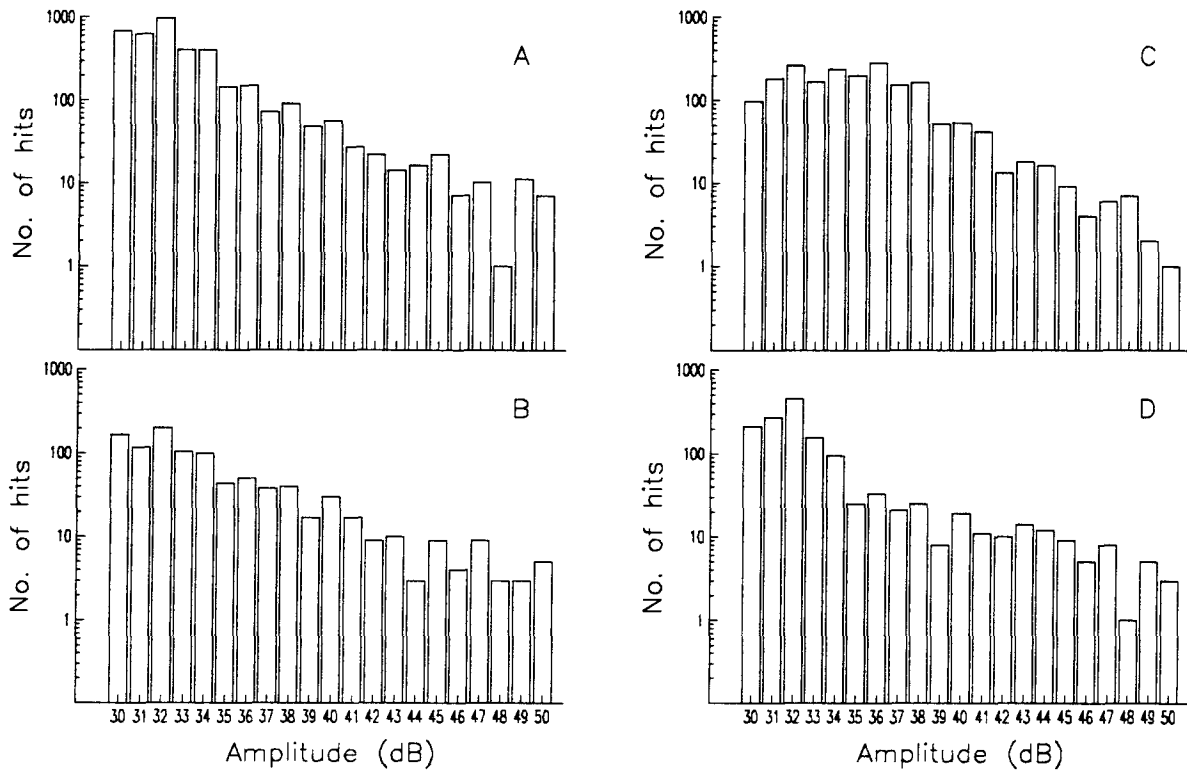
Figure 6.62: Amplitude distributions for cylinder burst tests.
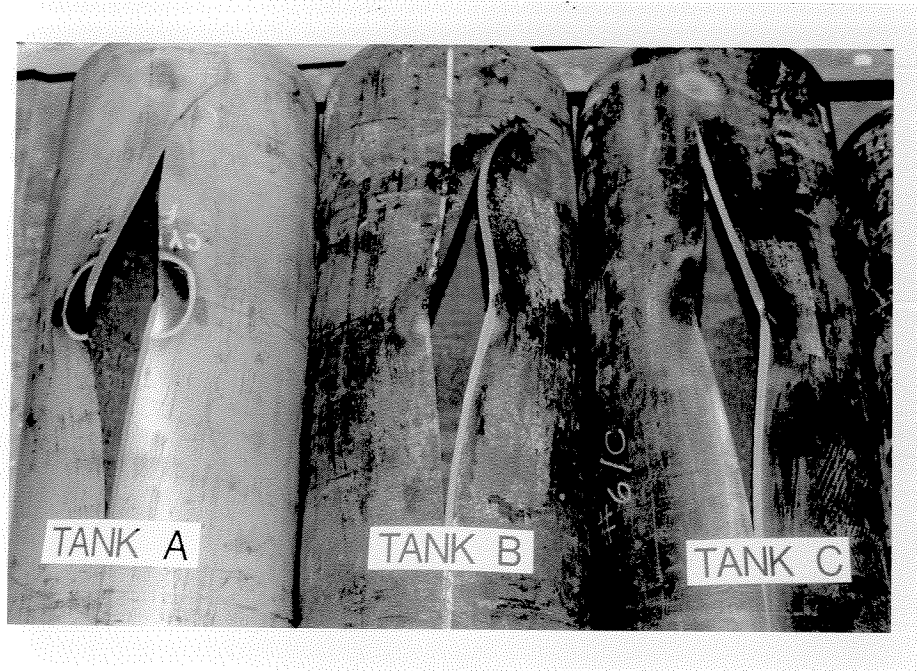
Figure 6.63: Tanks A, B and C following burst tests.
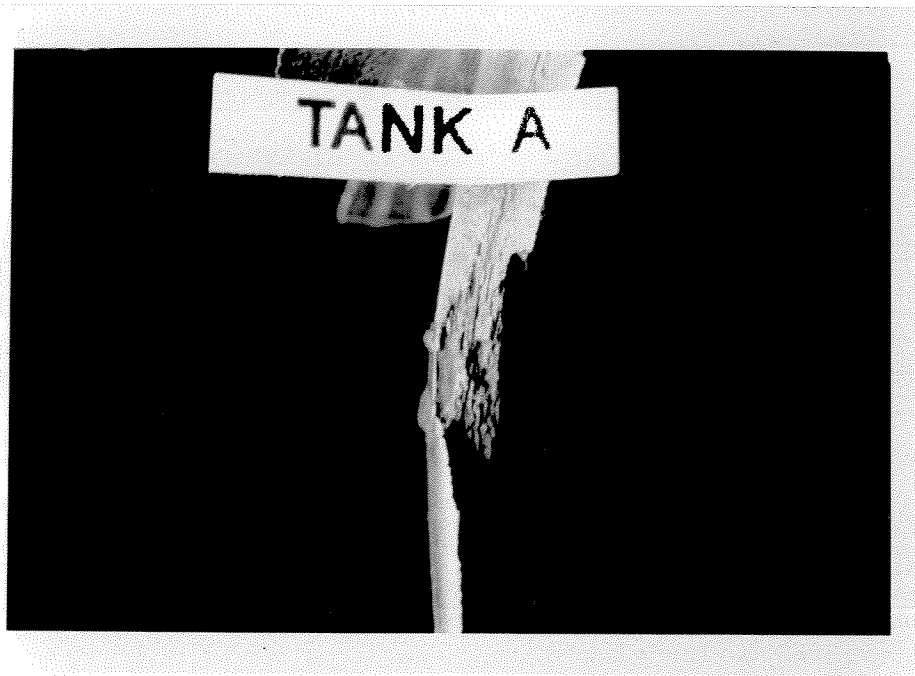
Figure 6.64: Fracture origin (Tank A).
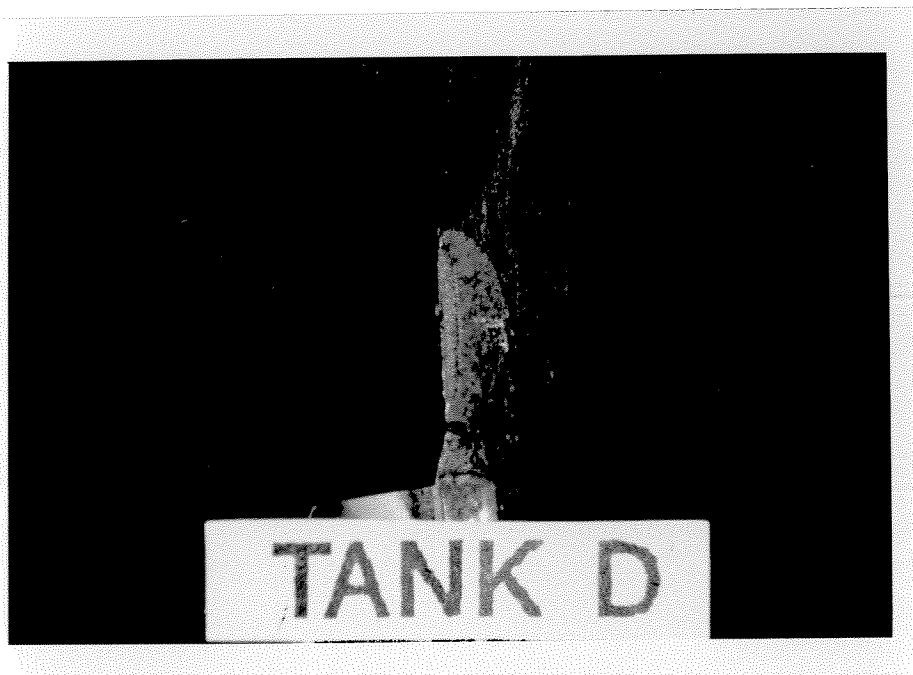
Figure 6.65: Fracture origin (Tank D).
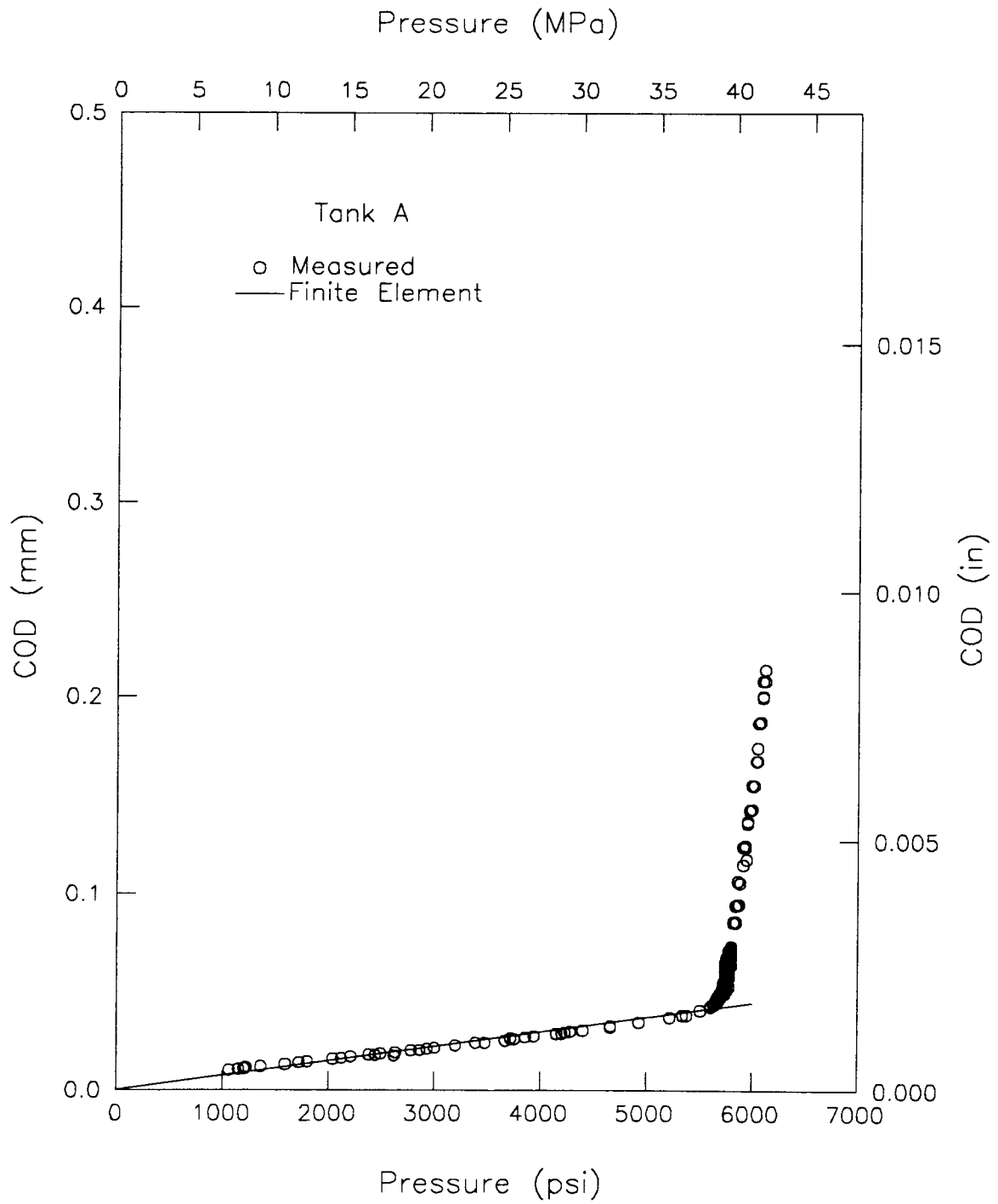
Figure 6.66: COD versus pressure for burst test of Tank A.
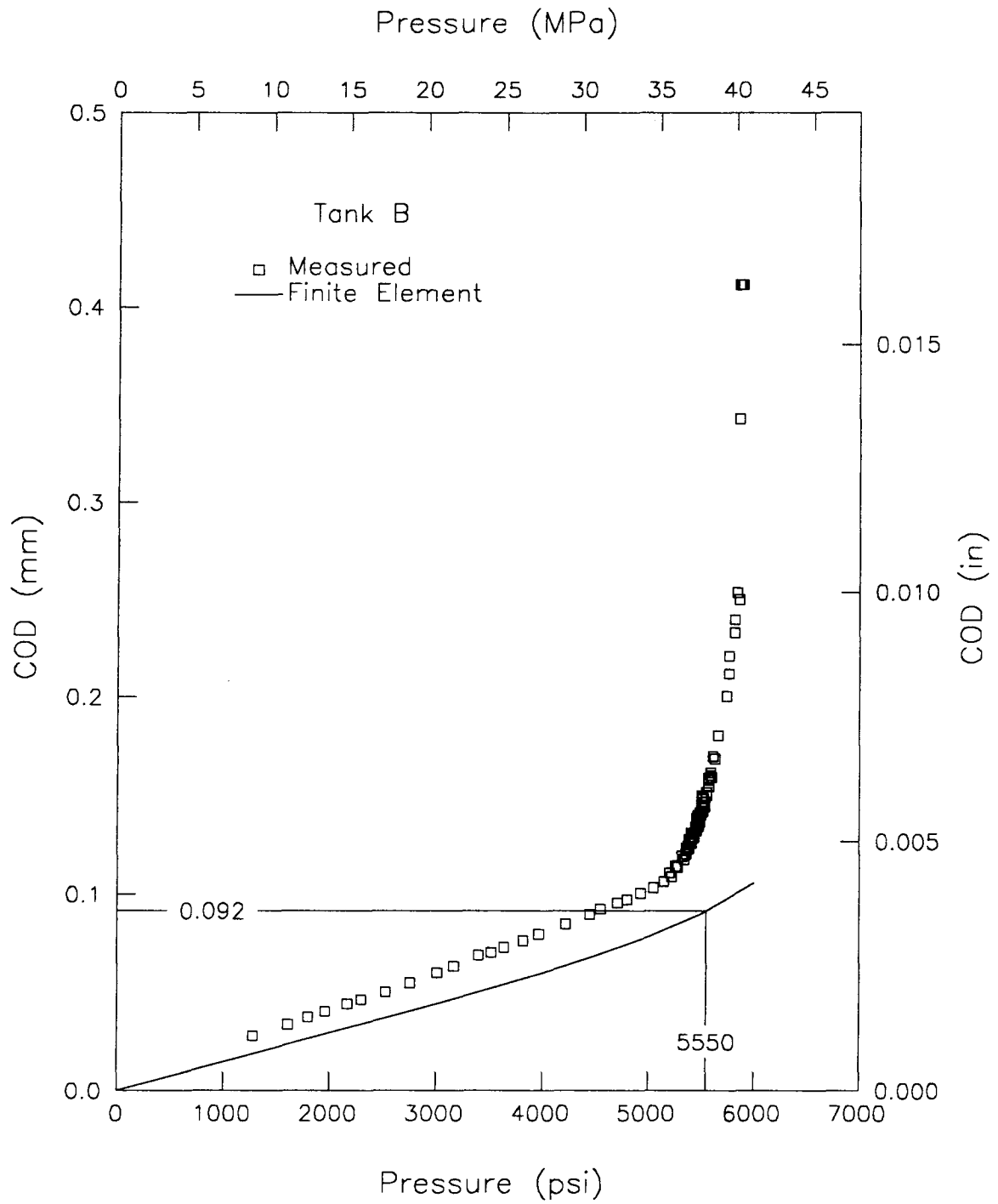
Figure 6.67: COD versus pressure for burst test of Tank B.
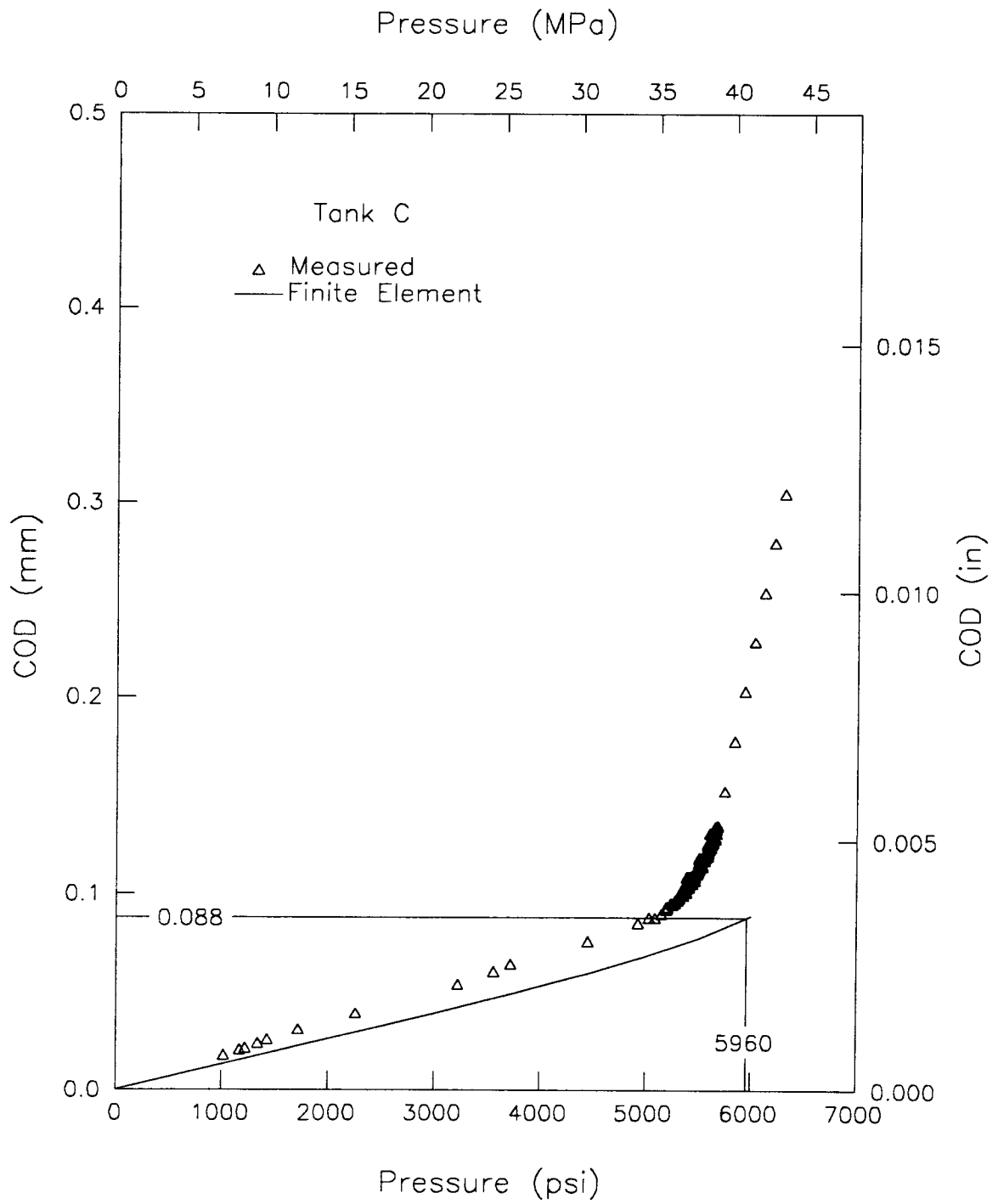
Figure 6.68: COD versus pressure for burst test of Tank C.
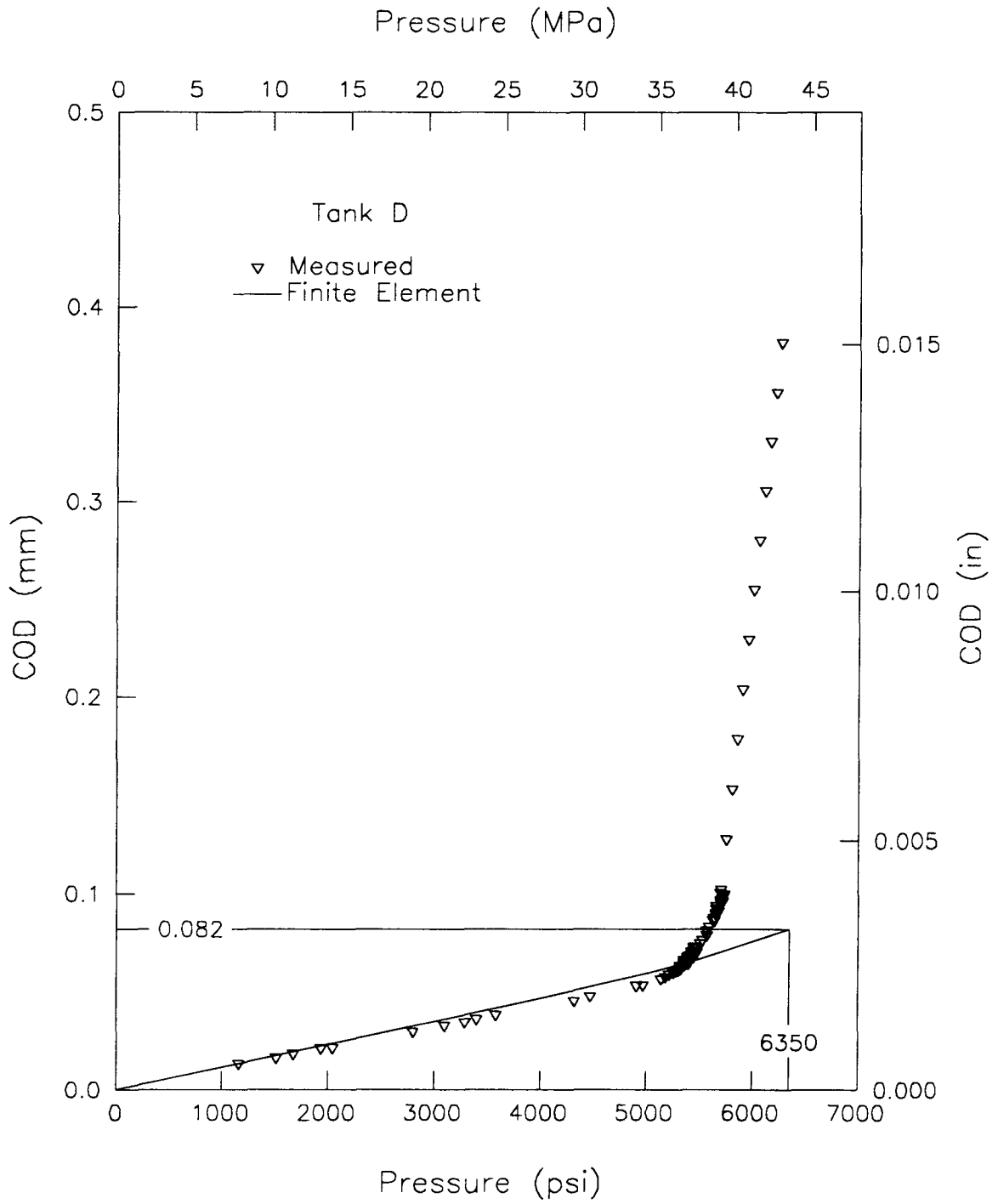
Figure 6.69: COD versus pressure for burst test of Tank D.
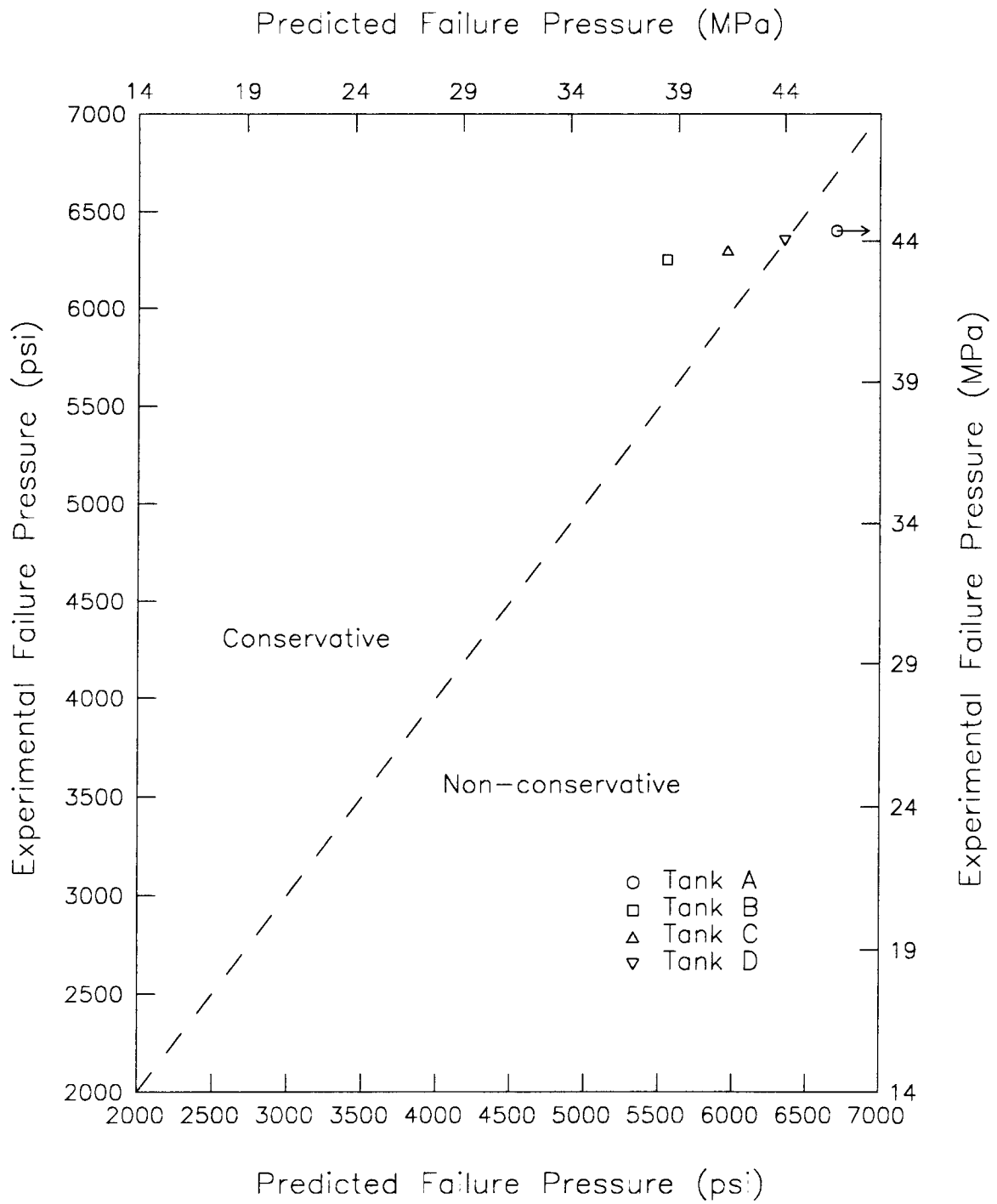
Figure 7.1: Actual versus predicted failure pressures (finite element/CTOD approach).
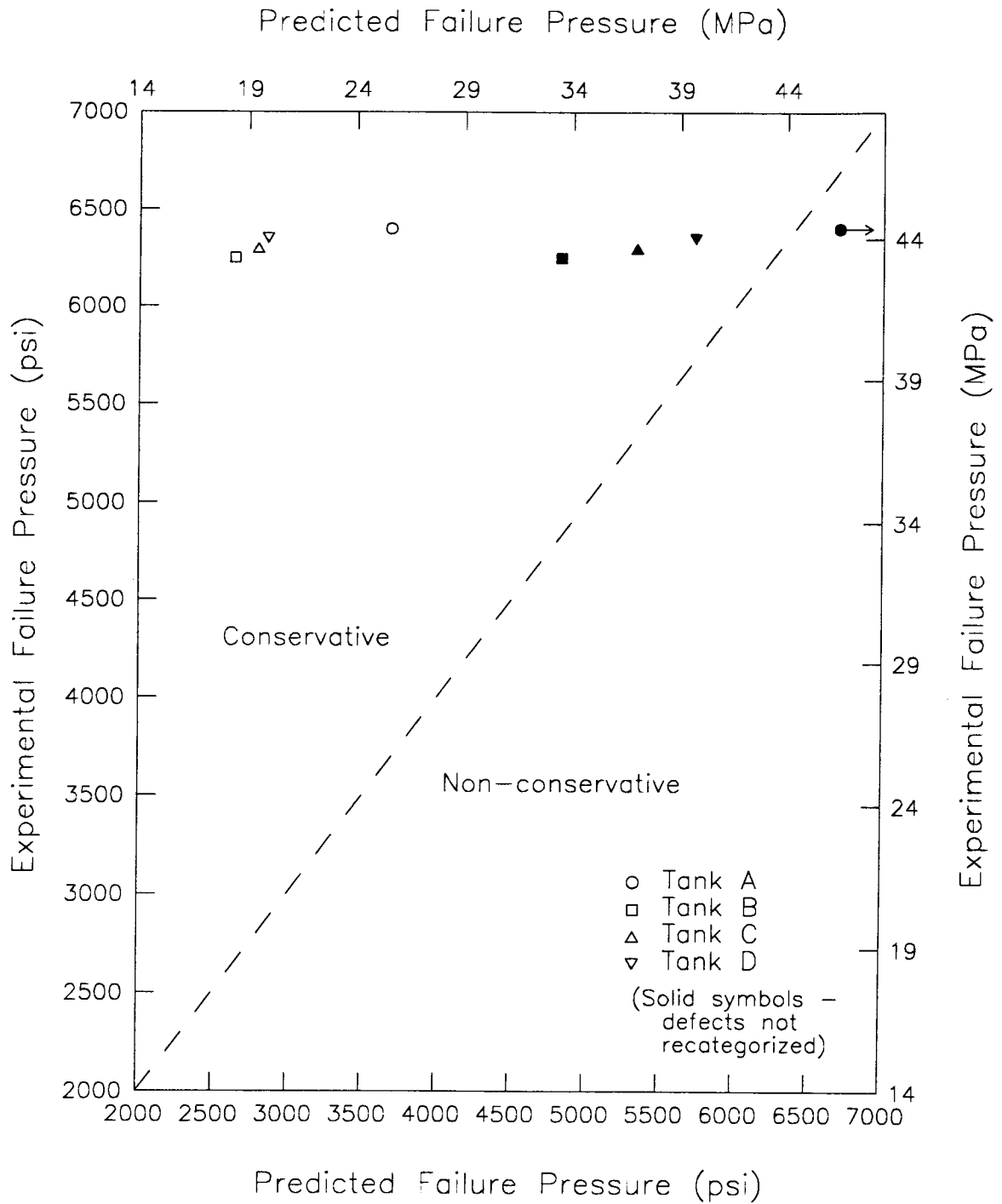
Figure 7.2: Actual versus predicted failure pressures (CTOD design curve).
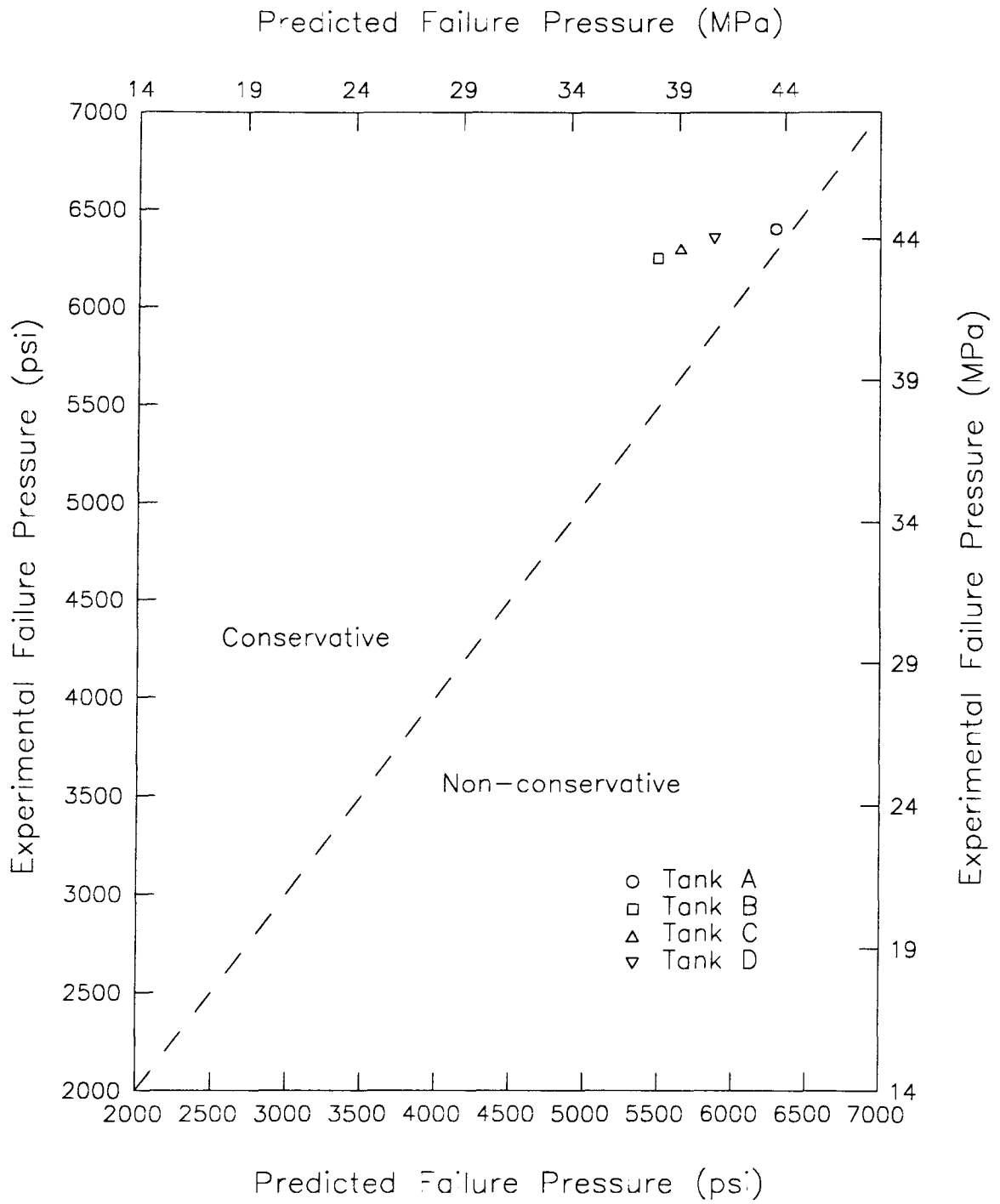
Figure 7.3: Actual versus predicted failure pressures (plastic collapse).
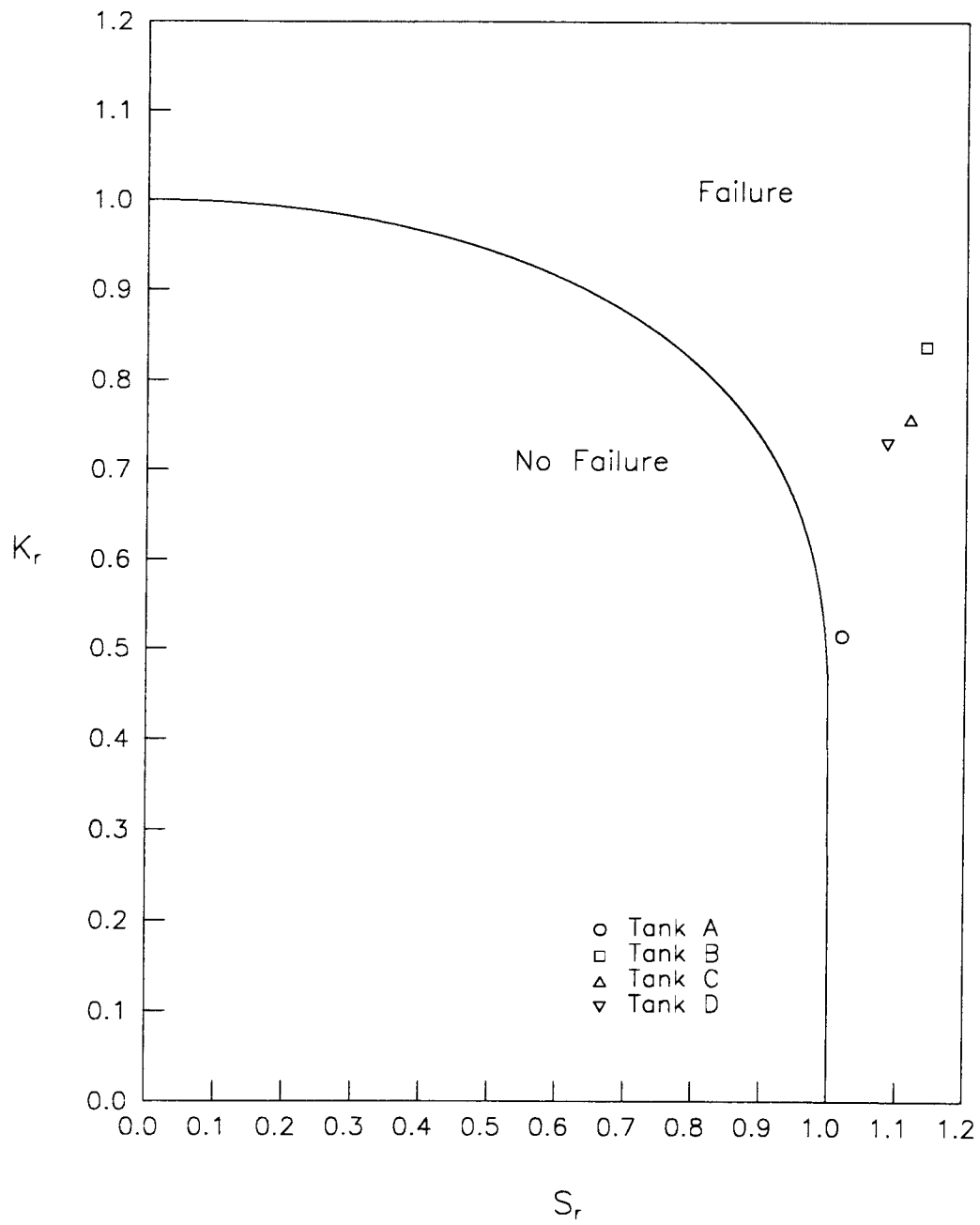
Figure 7.4: Actual versus predicted failure pressures (CEGB R6 Method).
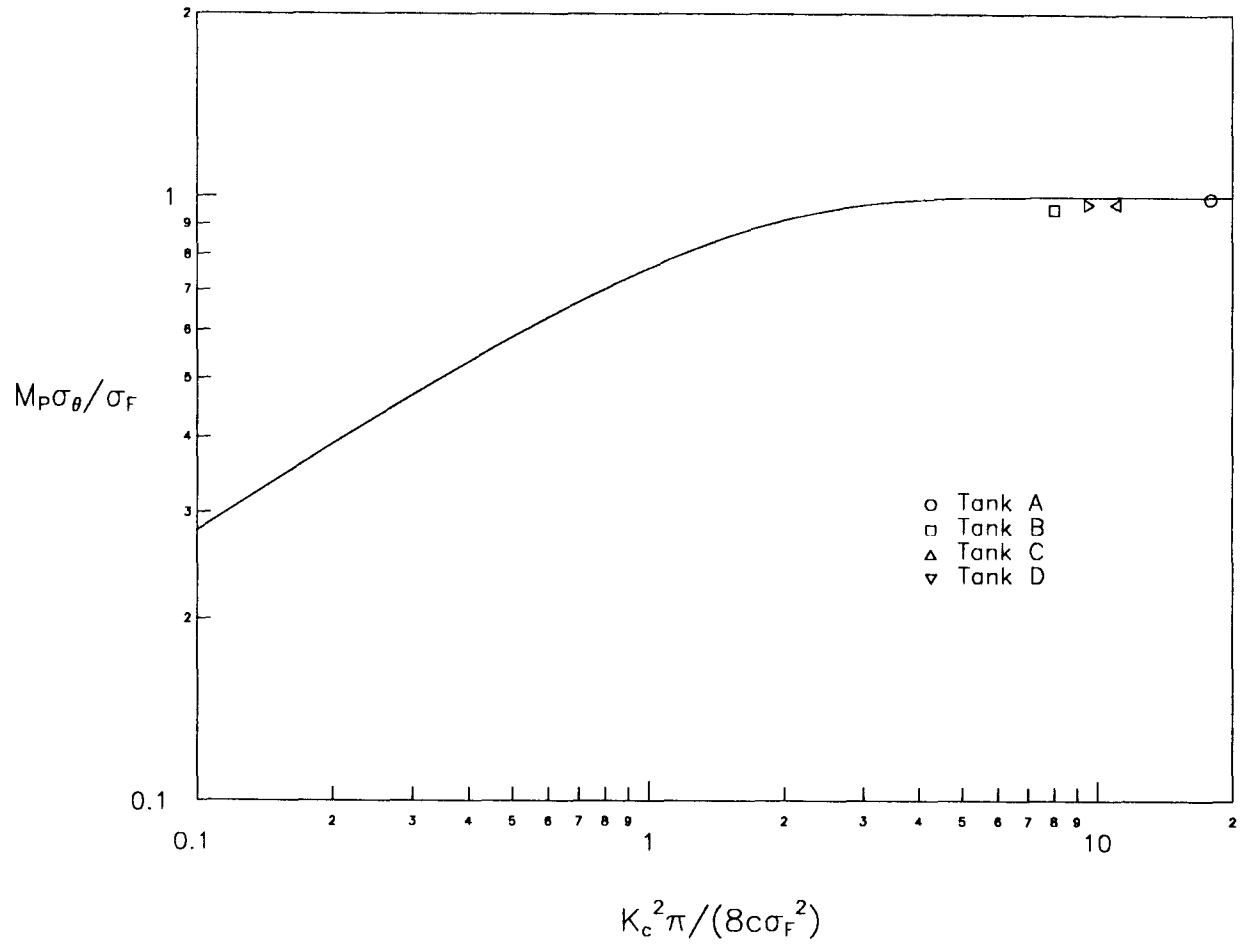
Figure 7.5: Actual versus predicted failure pressures (Battelle Empirical Analysis).
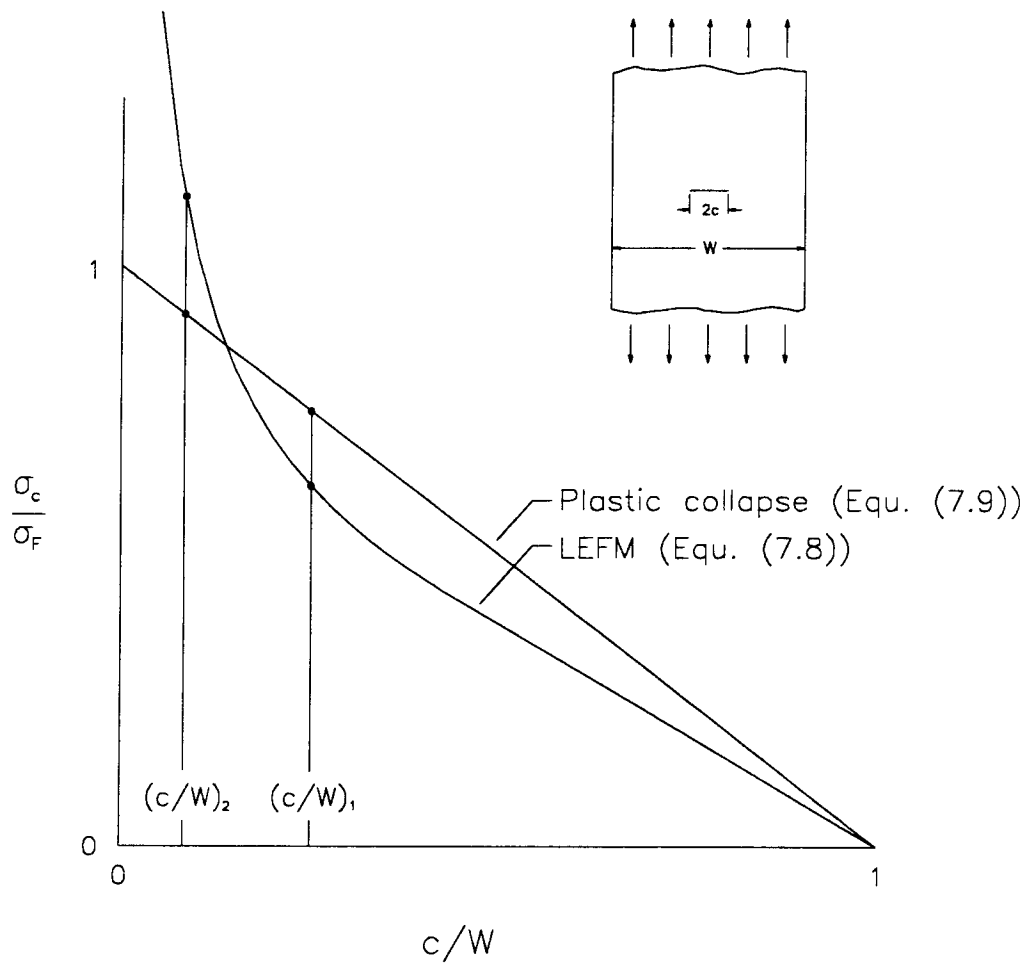
Figure 7.6: Comparison of LEFM and plastic collapse failure criteria.
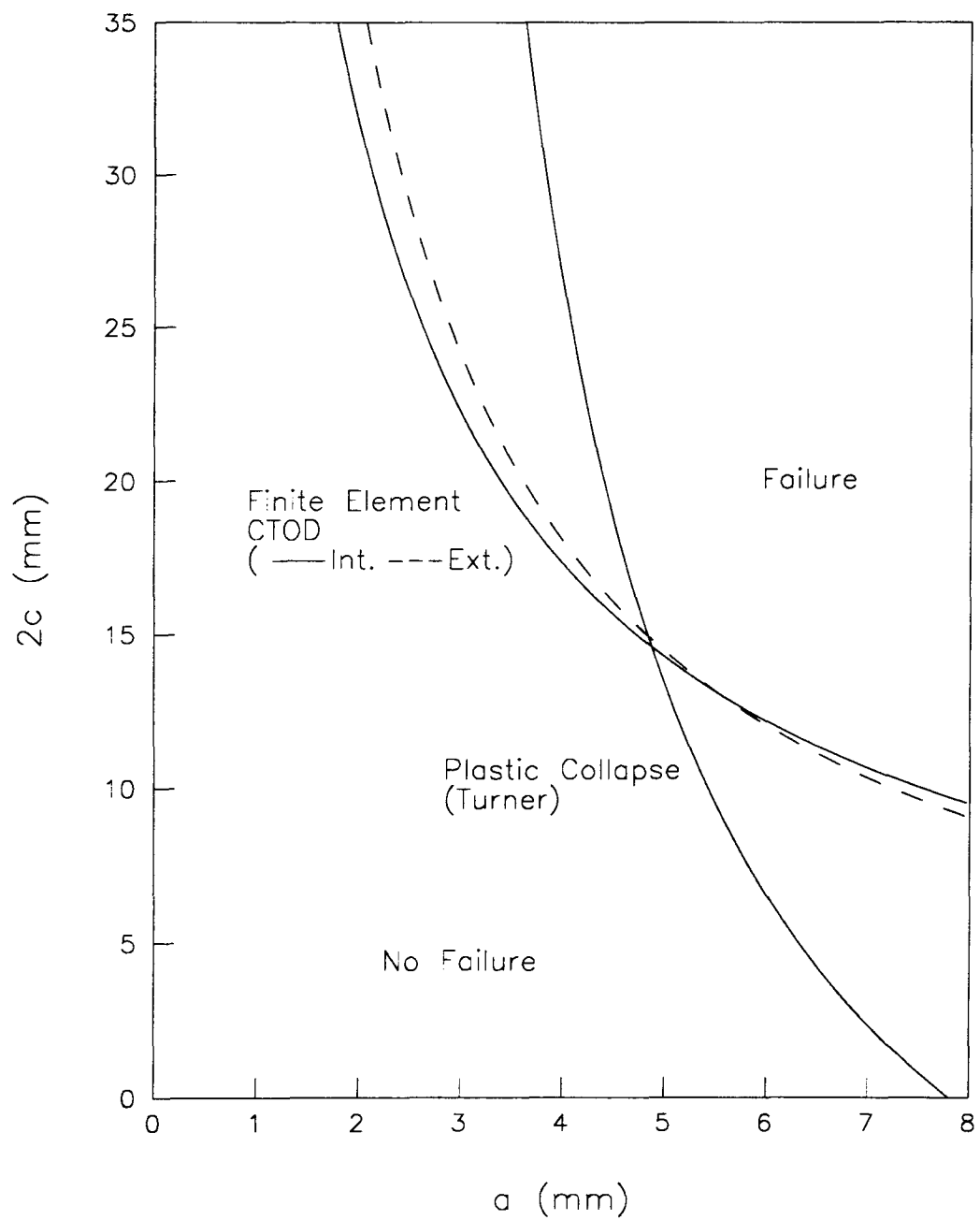
Figure 7.7: Comparison of numerical CTOD and plastic collapse limiting defect dimensions.
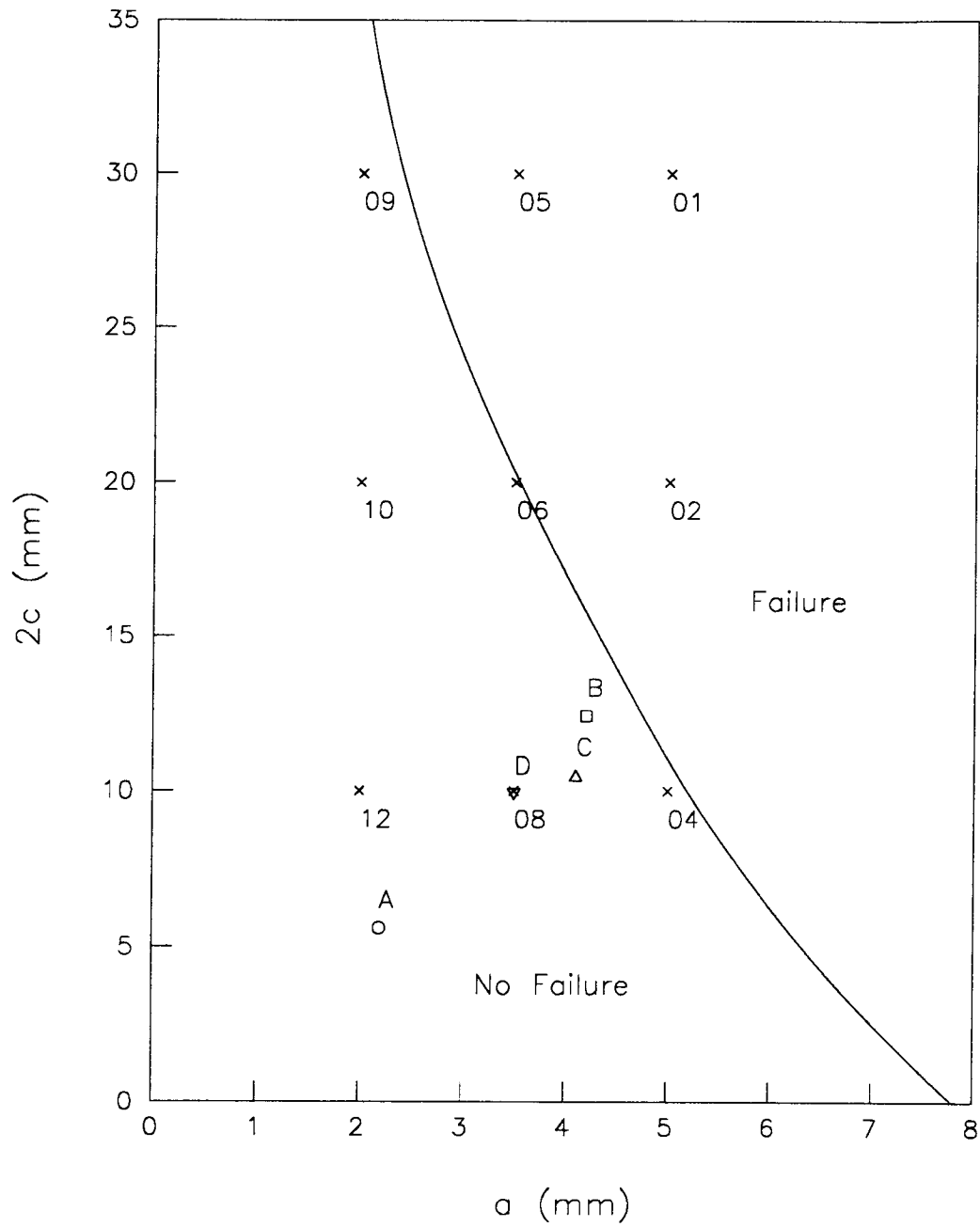
Figure 7.8: Limiting defect dimensions for failure during a hydrostatic test (numerical and experimental defect dimensions plotted).
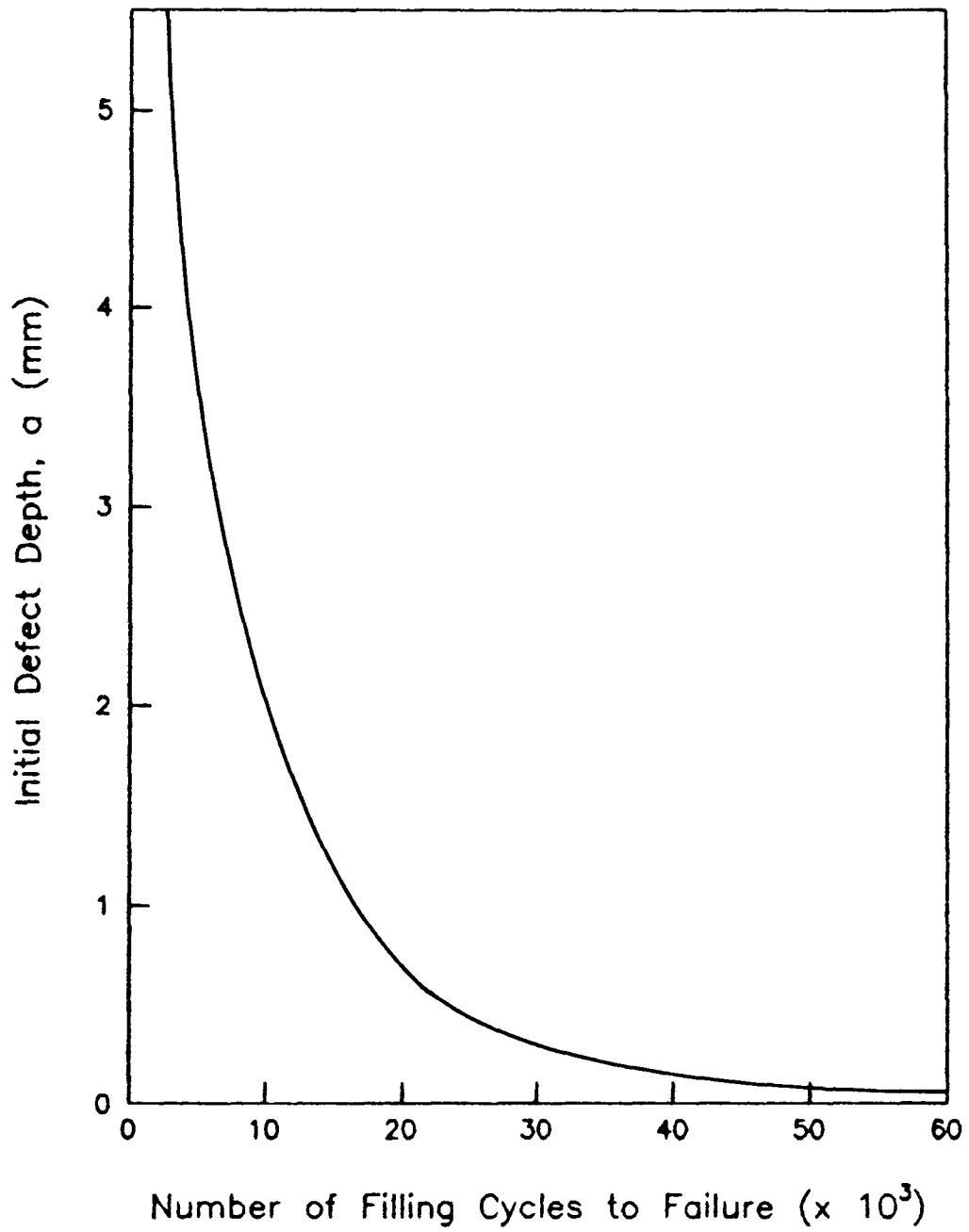
Figure 8.1: Number of fueling cycles to failure as a function of initial defect depth [13].
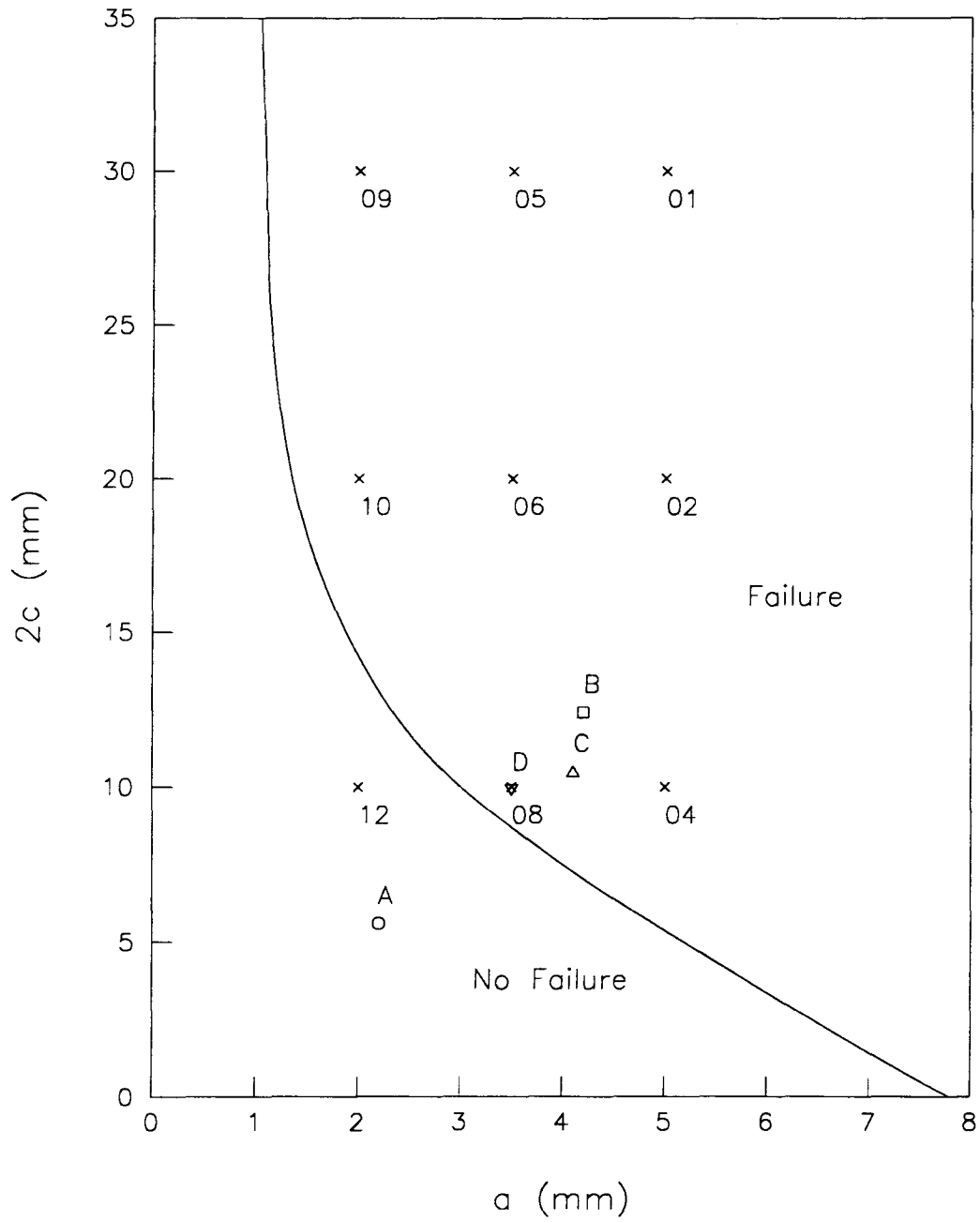
Figure 8.2: Limiting defect dimensions for in-service failure [13] (numerical and experimental defect dimensions plotted).
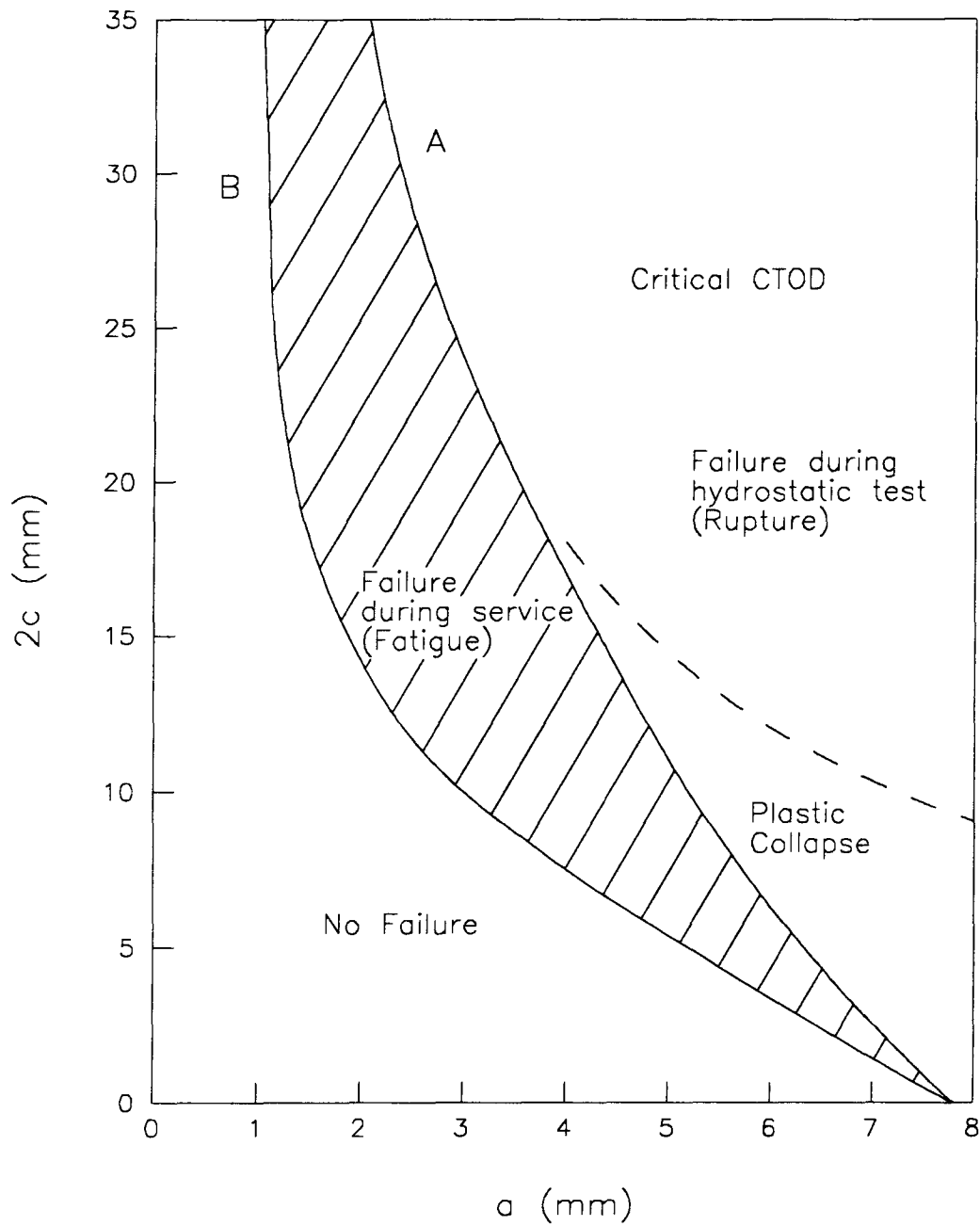
Figure 8.3: Limiting defect sizes for in-service and hydrostatic test failure.

Appendix A

ELEMENT DESCRIPTION

This appendix describes the various finite elements used in this study. (Notation is given at the end of Appendix B.)

A.1 Two-Dimensional Eight-Node Isoparametric Solid Element

Displacements within this element vary quadratically according to

$$\{u\} = \sum_{i=1}^{8} N_i(\xi, \eta)\{u_i\}$$

where

$$N_i(\xi, \eta) = \frac{1}{4}(1 + \xi\xi_i)(1 + \eta\eta_i)(-1 + \xi\xi_i + \eta\eta_i) \tag{A.1}$$

for corner nodes ($\xi = \pm 1, \eta = \pm 1$) and

$$N_i(\xi, \eta) = \frac{1}{2}(1 - \xi^2)(1 - \eta\eta_i) \tag{A.2}$$

$$N_i(\xi, \eta) = \frac{1}{2}(1 - \eta^2)(1 - \xi\xi_i) \tag{A.3}$$

for midside nodes ($\xi = 0$ and $\eta = 0$ respectively). This element in discussed further in Ref. [100].

A.2 Three-Dimensional 20-Node Isoparametric Solid Element

Displacements within this element vary quadratically according to

$$\{u\} = \sum_{i=1}^{20} N_i(\xi, \eta, \zeta)\{u_i\}$$

where

$$N_i(\xi, \eta, \zeta) = \frac{1}{8}(1 + \xi\xi_i)(1 + \eta\eta_i)(1 + \zeta\zeta_i)(-2 + \xi\xi_i + \eta\eta_i + \zeta\zeta_i) \qquad (A.4)$$

for corner nodes ($\xi = \pm 1, \eta = \pm 1, \zeta = \pm 1$) and

$$N_i(\xi, \eta, \zeta) = \frac{1}{4}(1 - \xi^2)(1 + \eta\eta_i)(1 + \zeta\zeta_i) \qquad (A.5)$$

$$N_i(\xi, \eta, \zeta) = \frac{1}{4}(1 - \eta^2)(1 + \zeta\zeta_i)(1 + \xi\xi_i) \qquad (A.6)$$

$$N_i(\xi, \eta, \zeta) = \frac{1}{4}(1 - \zeta^2)(1 + \xi\xi_i)(1 + \eta\eta_i) \qquad (A.7)$$

for midside nodes ($\xi = 0$, $\eta = 0$ and $\zeta = 0$ respectively). The pressure load vector is computed using

$$\{P\} = p \int_A \{N\} dA \qquad (A.8)$$

This element in discussed further in Ref. [99].

A.3   Eight-Node Isoparametric Thin Shell Element

Displacements within this element vary quadratically according to

$$\{u\} = \sum_{i=1}^{8} N_i(\xi, \eta)\{u_i\} + \sum_{i=1}^{8} N_i(\xi, \eta)\frac{\zeta t_i}{2}(\{a_i\}\{\theta_{xi}\} + \{b_i\}\theta_{yi})$$

The shape functions are given by equ.s (A.1) to (A.3). The element pressure load vector is determined from equ. (A.8). This element is discussed further in Ref. [35].

A.4   Element Stiffness Matrices

The stiffness matrices for all elements were computed in the standard way using

$$[K_e] = \int_V [B]^T [D][B] dV \qquad (A.9)$$

The integral was evaluated using a Gaussian quadrature scheme; 2×2 integration points are used for the two-dimensional isoparametric element and 3×3 integration points for the three-dimensional isoparametric element and the shell element.

Appendix B

ELEMENTARY ELASTIC-PLASTIC FINITE ELEMENT THEORY

This appendix provides a brief overview of elastic-plastic finite element theory related to the analysis discussed in Chapter 5. Solution methods are discussed first. General plasticity theory and some specializations of this theory for bilinear kinematically hardening materials follows.

B.1 Solution Methods

In finite element analysis, the equation of static equilibrium is

$$\int_V [B]^T \{\sigma\} dV = \{F^{nodal}\} \tag{B.1}$$

where $[B]$ is the strain-displacement matrix, $\{\sigma\}$ is the stress vector and $\{F^{nodal}\}$ is the nodal force vector. This equation follows directly from the principal of virtual work with no assumptions regarding material response. When behaviour is linear-elastic, stresses and strains are related by

$$\{\sigma\} = [D]\{\varepsilon\} \tag{B.2}$$

where $[D]$ is the elasticity matrix. Substituting this equation into Equ. (B.1), and noting that

$$\{\varepsilon\} = [B]\{u\}$$

gives the familiar result

$$[K]\{u\} = \{F^{nodal}\} \tag{B.3}$$

where the matrix $[K]$ is the stiffness matrix given by

$$[K] = \int_V [B]^T [D][B] dV \qquad (B.4)$$

Equ. (B.3) is linear and therefore readily solved for u. Once u is known, the other quantities of interest, i.e., stresses and strains can be determined using the stress-strain and strain-displacement relationships.

The relative simplicity with which solutions can be obtained in linear-elastic analysis is a consequence of the linear stress-strain relationship. In elastic-plastic analysis the situation is more complicated, as the stress-strain relationship is of the form

$$\{\sigma\} = \phi(\{\varepsilon\}) \qquad (B.5)$$

where ϕ is some non-linear function. Non-linearity of this relationship means that the equilibrium equation (Equ. (B.1) cannot be written explicitly in terms of nodal displacements. Solution of the equilibrium equation therefore, requires some iterative scheme. Two such schemes are the Newton-Raphson and initial stress methods.

In a manner analagous to that employed to find the roots of transcendental functions, the Newton-Raphson method is based on a Taylor series expansion of Equ. (B.5). Performing this expansion about ε_{n-1}, substituting into Equ. (B.1) and rearranging gives

$$[K_T]\{\Delta u\} = \{F^{nodal}\} - \int_V [B]^T \{\sigma_{n-1}\} dV \qquad (B.6)$$

where $[K_T]$, the *tangent* stiffness matrix, is given by

$$[K_T] = \int_V [B]^T \left[\frac{d\phi}{d\varepsilon}\right] [B] dV$$

and

$$\{\Delta u\} = \{u_n\} - \{u_{n-1}\}$$

Equation (B.6) is the equation of equilibrium in the Newton-Raphson method. Because the tangent stiffness matrix is a function of the current state of stress, it is reformed at

each iteration. While this process leads to rapid convergence, it is time consuming and hence, expensive. This drawback is overcome in the initial stress method.

In the initial stress method, the matrix $[d\phi/d\varepsilon]$ is taken to remain unchanged from iteration to iteration. This corresponds to taking

$$\left[\frac{d\phi}{d\varepsilon}\right] = [D]$$

in Equ. (B.6) and in turn, replacing the tangent stiffness matrix with the elastic stiffness matrix. Noting that total strain is the sum of elastic and plastic strains, i.e.,

$$\varepsilon = \varepsilon^{el} + \varepsilon^{pl}$$

the term $\{\sigma_{n-1}\}$ becomes $[D](\{\varepsilon_{n-1}\} - \{\varepsilon^{pl}_{n-1}\})$. Making these modifications, and rearranging gives

$$[K]\{u_n\} = \{F^{nodal}\} + \int_V [B]^T [D]\{\varepsilon^{pl}_{n-1}\}dV \tag{B.7}$$

which is the equation of equilibrium in the initial stress method. Hence, the equation of equilibrium in the initial stress method is one in which non-linearity is accounted for by an unbalanced load vector term. Because terms (other than ε^{pl}) are not updated from iteration to iteration, convergence in the initial stress method is typically slower (i.e., requires more iterations) than in the the Newton-Raphson method. However, because the stiffness matrix is formed only once, a solution can often be obtained in less time.

In elastic-plastic analysis, external loads are applied incrementally since there is the possibility of redistribution of internal loads. Typically, an initial load is applied that is just sufficient to cause yielding at one or more integration points. Successive load steps are set to some fraction of the initial load step. Iterative solution of the equilibrium equations (Equ. (B.6) or (B.7)) at the first load step begins with the elastic solution as an initial guess for $\{u\}$; successive load steps use the previous solution for $\{u\}$ as an

initial guess. Iteration within each load step continues until the change in plastic strain is some fraction of elastic strain, that is until

$$\frac{\Delta \varepsilon^{pl}}{\varepsilon^{el}} \leq R \tag{B.8}$$

where R is some constant. Ref. [88] recommends that $R \leq 0.05$.

B.2 Plasticity Theory

To proceed with an elastic-plastic analysis, an expression must be developed which quantifies plastic strain at each point in the load history. This is done utilizing the yield criteria, flow rules and hardening rules from the theory of plasticity.

Yield criteria define the state of stress which will cause plastic flow. These criteria are expressed in general terms by expressions of the form[88]

$$f(\{\sigma\}) - \sigma_Y = 0 \tag{B.9}$$

where $\{\sigma\}$ is the stress vector and σ_Y is the yield stress in uniaxial tension. An equation such as this describes a surface in the principal stress space. If the stress state is such that principal stresses lie on this surface, plastic flow will occur. The directions of the resulting plastic strains are determined by a flow rule; a flow has the form

$$\{d\varepsilon^{pl}\} = \lambda \left\{ \frac{\partial Q}{\partial \sigma} \right\} \tag{B.10}$$

where $\{d\varepsilon^{pl}\}$ is the incremental plastic strain vector, λ is a plastic multiplier, and Q is a plastic potential.

Material hardening rules are incorporated into yield criteria since, effectively, material hardening causes the yield criterion to change with increasing plastic strain. One material hardening rule is kinematic hardening. This rule states that the yield surface translates

in the principal stress space with progressive plastic straining. To account for this effect, the yield condition is written

$$F(\{\sigma\}, \{\alpha\}) = 0 \tag{B.11}$$

where $\{\alpha\}$ is the location of the center of the yield surface, given by

$$\{\alpha\} = \int C\{d\varepsilon^{pl}\} \tag{B.12}$$

and C is a constant which depends on the material stress-strain relationship.

B.3 Incremental Plastic Strain

A quantity of fundamental importance in elastic-plastic finite element analysis is the incremental plastic strain. An expression for this quantity can be obtained from the differential of Equ. (B.11),

$$\left\{\frac{\partial F}{\partial \sigma}\right\}^T \{d\sigma\} + \left\{\frac{\partial F}{\partial \alpha}\right\}^T \{d\alpha\} = 0 \tag{B.13}$$

and noting that

$$\{d\sigma\} = [D]\{d\varepsilon^{el}\} \tag{B.14}$$

$$= [D](\{d\varepsilon\} - \{d\varepsilon^{pl}\}) \tag{B.15}$$

$$\{d\alpha\} = C\{d\varepsilon^{pl}\} \tag{B.16}$$

Substituting Equ.s (B.15) and (B.16) into Equ. (B.13), and substituting Equ. (B.10) gives, after rearranging

$$\lambda = \frac{\left\{\frac{\partial F}{\partial \sigma}\right\}^T [D]\{d\varepsilon\}}{\left\{\frac{\partial F}{\partial \sigma}\right\}^T [D]\left\{\frac{\partial Q}{\partial \sigma}\right\} - C\left\{\frac{\partial F}{\partial \alpha}\right\}^T \left\{\frac{\partial Q}{\partial \sigma}\right\}}$$

Substituting this equation in Equ. (B.10) gives

$$\{d\varepsilon^{pl}\} = \frac{\left\{\frac{\partial F}{\partial \sigma}\right\}^T [D] \left\{\frac{\partial Q}{\partial \sigma}\right\}}{\left\{\frac{\partial F}{\partial \sigma}\right\}^T [D] \left\{\frac{\partial Q}{\partial \sigma}\right\} - C\left\{\frac{\partial F}{\partial \alpha}\right\}^T \left\{\frac{\partial Q}{\partial \sigma}\right\}} \{d\varepsilon\} \qquad (B.17)$$

From inspection, it can be seen that this equation gives incremental plastic strain in terms of total strain.

B.4 Specializations for Bilinear Kinematic Hardening Materials

Equation (B.17) is general in that in its derivation, no assumptions regarding the specific form of yield criterion F, flow rule Q or hardening rule are made. In the analysis performed in this study, the von Mises yield condition and associated flow rule, and kinematic hardening were assumed.

The von Mises yield criterion with kinematic hardening is written (c.f. Equ. (B.11))

$$F = \frac{3}{2}\left[(\{s\} - \{\alpha\})^T(\{s\} - \{\alpha\})\right]^{\frac{1}{2}} - \sigma_Y = 0 \qquad (B.18)$$

where $\{s\}$ is the deviatoric stress vector given by

$$\{s\} = \{\sigma\} - \sigma_m \left\{\begin{array}{c} 1 \\ 1 \\ 1 \\ 0 \\ 0 \\ 0 \end{array}\right\}$$

with $\sigma_m = \frac{1}{3}(\sigma_x + \sigma_y + \sigma_z)$. α is the yield surface translation vector (Equ. (B.12)).

An associated flow rule is one in which the plastic potential takes the same form as the yield condition (i.e., $Q = F$). This gives, for the terms $\{\partial Q/\partial \sigma\}$ and $\{\partial F/\partial \sigma\}$ in

Equ. (B.17)

$$\left\{\frac{\partial Q}{\partial \sigma}\right\} = \left\{\frac{\partial F}{\partial \sigma}\right\} = \frac{3}{2\sigma_e}\left(\{s\} - \{\alpha\}\right)$$

where σ_ϵ is an equivalent stress given by

$$\sigma_e = \left[\frac{3}{2}\left(\{s\} - \{\alpha\}\right)^T\left(\{s\} - \{\alpha\}\right)\right]^{\frac{1}{2}}$$

From Equ. (B.18) the terms $\{\partial F/\partial \alpha\}$ and $\{\partial F/\partial \kappa\}$ in Equ. (B.17) are

$$\left\{\frac{\partial F}{\partial \alpha}\right\} = -\frac{3}{2\sigma_e}[\{s\} - \{\alpha\}]$$

$$\left\{\frac{\partial F}{\partial \kappa}\right\} = 0$$

When bilinear kinematic hardening is assumed, the constant C in Equ. (B.12) is

$$C = \frac{2}{3}\frac{EE_T}{E - E_T}$$

where E is the elastic modulus and E_T is the tangent modulus (i.e., the slope of the hardening portion of the uniaxial stress-strain curve). The term $C\{\partial F/\partial \alpha\}^T\{\partial Q/\partial \sigma\}$ is therefore

$$C\left\{\frac{\partial F}{\partial \alpha}\right\}^T\left\{\frac{\partial Q}{\partial \sigma}\right\} = -\frac{EE_T}{E - E_T}$$

B.5 Notation

$\{u\}$ = displacement vector

N = shape function

ξ = element coordinate

η = element coordinate

ζ = element coordinate

t_i = element thickness

θ_x = rotation about local x-axis

θ_y = rotation about local y-axis

$\{a\}$ = unit vector in the ξ-direction

$\{b\}$ = unit vector normal in plane of element normal to $\{a\}$

$[B]$ = strain-displacement matrix

$[D]$ = elasticity matrix

$[K_e]$ = element stiffness matrix

A = element face area

V = element volume

Subscripts

i = nodal quantity

Appendix C

PROGRAM LISTINGS

```
C*************************************************************************
C***
C***    ANSYS input file for CTOD specimen.
C***    Written by S.G. Ribarits.
C***
C***        a = crack length
C***        s = span

/prep7

/title,COD SPECIMEN (a = 3.9 mm, s = 50.8 mm)

C*** Set model parameters

a=3.9               *crack length
s=25.4              *span

x1=2.1
x2=(a-2.8)*(x1/ (a-1.8))

y1=7.5
y2=((y1-a)*(x2/x1))
y3=((y1-a)*(.25/x1))

C*** Specify element type

et,1,82,,,2

C*** Specify material properties

ex,1,2e5

C*** Define local coordinate system

local,11,0,,-158.6

C*** Place keypoints

k, 1,(a+y3)
k, 2,          , (a+y2)
k, 3,          ,   y1
k, 4, .25  , (a+y3)
k, 5,  x2  , (a+y2)
k, 6,  x1  ,   y1
k, 7,  s   ,   y1
k, 9,  s   ,   y1
k,10,          ,(a-.25)
k,11,          ,   2.8
k,12,          ,   1.8
k,13, .075 ,(a-.25)
k,14, .075 ,   2.8
k,15, .075 ,   1.8
k,16, .25  ,(a-.25)
k,17, .25  ,   2.8
k,18, .25  ,   1.8
k,19, .25  ,(a-.25)
k,20,  x2  ,   2.8
k,21,  x1  ,   1.8
k,22,  s   ,   1.8
k,24,  s   ,   1.8
k,33,          ,   7.8
k,36,  x1  ,   7.8
k,39,  s   ,   7.8
k,42,
k,45, .075
k,48, .25
k,51,  x1
```

```
k,54,  s

kmove,36,0,   x1 ,999,,1,      150.8,999
kmove,51,0,   x1 ,999,,1,      158.6,999
kmove,48,0,   .25 ,999,,1      158.6,999
kmove, 7,0,   s  ,999,,1,(158.6-y1),999
kmove, 9,0,   s  ,999,,1,(158.6-y1),999
kmove,39,0,   s  ,999,,1,      150.8,999
kmove,22,0,   s  ,999,,1,      156.8,999
kmove,24,0,   s  ,999,,1,      156.8,999
kmove,54,0,   s  ,999,,1,      158.6,999
kmove,45,0,   .075 ,999,,1,    158.6,999


C*** Draw lines

csys,0

1, 1, 2,               $rp2, 3, 3
1,10,11,               $rp4, 3, 3

1, 2, 3,               $rp2, 3, 3
1,11,12,               $rp4, 3, 3

1, 1, 4, 2             $rp3, 1, 1
1,10,13, 1             $rp3, 1, 1
1,13,16, 1             $rp3, 1, 1
1,17,20, 2             $rp2, 1, 1
1, 4,19, 4             $rp3, 1, 1
1, 7,22, 2

1, 3,33, 1             $rp3, 3, 3
1,12,42,               $rp4, 3, 3
1,22,54, 1

csys,1

1,33,36, 2
1,42,45               $rp2, 3, 3
1,48,51, 2
1, 6, 9, 9, 5         $rp4,15,15

C*** Merge coincident keypoints

nummrg,kpoi

C*** Define areas

a, 1, 2, 5, 4
a, 4, 5,20,16
a,16,20,17,17
a,13,16,17,14
a,10,13,14,11
a, 2, 3, 6, 5
a, 5, 6,21,20
a,17,20,21,18
a,14,17,18,15
a, 3,33,36, 6
a, 6,36,39, 7
a, 6, 7,22,21
a,21,22,54,51
a,18,21,51,48
a,11,14,15,12
a,12,15,45,42
a,15,18,48,45

C*** Mesh areas
```

```
numstr,node,44
numstr,elem,9
elsize,1,,1
amesh,1,14

C*** Generate crack tip elements

csys,11

*create,nplace
node=arg1
kpoi=arg2
*get,x,kx,kpoi
*get,y,ky,kpoi
n,node,x,y
*end
*use,nplace,27,1
*use,nplace,31,4
*use,nplace,39,16
*use,nplace,41,13
*use,nplace,43,10

n,1,,a          $rp17,1
fill,27,31,3
fill,31,39,7
fill,39,41,1
fill,41,43,1

en,  1,27,29, 3, 1,28,19, 2,18
rp8, 1, 2, 2, 2, 2, 2, 1, 2, 1

C*** Reorder model

csys
wsort,x

C*** Modify crack tip elements

*create,nmove
nod1=arg1
nod2=arg2
nmid=arg3
csys
*get,x1,nx,nod1
*get,x2,nx,nod2
*get,y1,ny,nod1
*get,y2,ny,nod2
xmid=((.75*x1)+(.25*x2))
ymid=((.75*y1)+(.25*y2))
nmodif,nmid,xmid,ymid
*end
*use,nmove, 1,27,18
*use,nmove, 3,29,19
*use,nmove, 5,31,20
*use,nmove, 7,33,21
*use,nmove, 9,35,22
*use,nmove,11,37,23
*use,nmove,13,39,24
*use,nmove,15,41,25
*use,nmove,17,43,26

C*** Merge coincident nodes

nummrg,nodes

C*** Apply boundary conditions
```

```
lsrsel,, 1
lsasel,, 7
lsasel,,28
nline,1
nasel,, 1
nasel,,18
symbc,,1,all
nall
lsall
kd,54,uy

C*** Apply load

kf,33,fy,(-100)

afwrite
finish

C*** Run model

/exe
/input,27
finish

C*** Postprocess

/post1
/output,cod,09
set
/nopr
csys
nrsel,x,.249,.251
csys,1
nrsel,x,158.59,158.61
csys
/gopr
prdisp
/nopr
nall
nrsel,x,-.001,.001
csys,1
nrsel,x,150.79,150.81
csys
/gopr
prdisp

/nopr
nall
cs,12,,1,27,31
lpath,1,26,43
/gopr
kcalc,,,,1
finish
/output,6
```

```
PROGRAM CODREAD
C**********************************************************************
C
C      PROGRAM TO ANALYSE RESULTS FROM COD TESTS.  A BINARY DAS20 FILE IS
C      READ AND PULSES RECORDED ON CHANNEL PCHAN ARE COUNTED AND MATCHED
C      TO POTENTIAL DROP DATA FROM AN ASCII MDT FILE.  DATA FROM ALL
C      CHANNELS IS THEN CONVERTED TO PHYSICAL QUANTITIES AND REWRITTEN TO
C      AN ASCII FILE FOR FURTHER ANALYSIS.
C      WRITTEN BY S.G. RIBARITS.
C
C           VARIABLES
C      A      = CRACK LENGTH
C      AO     = INITIAL CRACK LENGTH
C      A1, B1 = CALIBRATION CONSTANTS FOR COD DATA
C      A2, B2 = CALIBRATION CONSTANTS FOR LOAD DATA
C      A3, B3, C3
C             = CONSTANTS IN JOHNSONS EQUATION
C      COD    = CRACK OPENING DISPLACEMENT
C      CODMN  = OFFSET IN COD DATA
C      COUNT  = NUMBER OF PULSES COUNTED ON CHANNEL PCHAN
C      FSIZE  = NUMBER OF RECORDS TO WRITE TO OUTPUT FILE
C      G1     = GAIN FOR COD DATA
C      G2     = GAIN FOR LOAD DATA
C      G3     = GAIN FOR PD DATA
C      LOAD   = LOAD
C      LOADMN = OFFSET IN LOAD DATA
C      MIN1   = MINIMUM COD DATA
C      MIN2   = MINUMUM LOAD DATA
C      NCHAN  = NUMBER OF CHANNELS
C      NPOINT = NUMBER OF DATA POINTS PER CHANNEL
C      NWRITE = NUMBER OF RECORDS IN ORIGINAL DATA FILE TO SKIP
C      PCHAN  = CHANNEL CONTAINING PULSES
C      UNIT1  = UNIT CONNECTED TO DAS20 BINARY DATA FILE
C      UNIT2  = UNIT CONNECTED TO MDT ASCII FILE
C      UNIT3  = UNIT CONNECTED TO GAIN INPUT FILE
C      UNIT4  = UNIT CONNECTED TO LOAD AND COD CALIBRATION INPUT FILE
C      UNIT7  = UNIT CONNECTED TO PD CALIBRATION INPUT FILE
C      UNIT8  = UNIT CONTECTED TO OUTPUT FILE
C      RANGE  = RANGE USED TO SCALE PD DATA
C      THRHLD = TRESHOLD SET TO DETECT PULSES ON PCHAN
C      UO     = VOLTAGE CORRESPONDING AO
C      W      = SPECIMEN WIDTH
C      Y      = HALF DISTANCE BETWEEN PD PROBES
C
C           ARRAYS
C      X      = DATA
C
C
      INTEGER*1 UNIT1, UNIT2, UNIT3, UNIT4, UNIT7, UNIT8,
     +          PCHAN, NCHAN
      INTEGER*2 X(35000,3), THRHLD, MIN1, MIN2
      INTEGER COUNT, FSIZE
      REAL LOAD
      PARAMETER(PI=3.141592654)
C
C      INITIALIZE VARIABLES
C
      NCHAN = 3
      NPOINT = 12000
      THRHLD = 1024
      PCHAN = 3
      RANGE = 5.0
C
C      READ BINARY DAS20 FILE
C
      UNIT1 = 1
      OPEN(UNIT=UNIT1,FILE='TEST1DAS.DAT',
```

```fortran
     +     STATUS='OLD',ACCESS='DIRECT',FORM='UNFORMATTED',RECL=2)
      CALL READER(UNIT1,NCHAN,NPOINT,X)
      CLOSE(UNIT=UNIT1)
C
C     COUNT PULSES ON CHANNEL PCHAN
C
      CALL PULSE(PCHAN,X,NPOINT,THRHLD,COUNT)
C
C     READ POTENTAL DROP DATA CORRESPONDING TO PCHAN PULSE NUMBER
C
      UNIT2 = 2
      OPEN(UNIT=UNIT2,FILE='TEST1PD.DAT',
     +     STATUS='OLD',ACCESS='SEQUENTIAL',FORM='FORMATTED',
     +     BLANK='ZERO')
      CALL PDREAD(UNIT2,X,PCHAN,COUNT,NPOINT,RANGE)
      CLOSE(UNIT=UNIT2)
C
C     READ GAINS, CALIBRATION FACTORS, AND POTENTIAL DROP CONSTANTS
C
      UNIT3 = 3
      UNIT4 = 4
      UNIT7 = 7
      OPEN(UNIT=UNIT3,FILE='GAINS1.DAT',
     +     STATUS='OLD',ACCESS='SEQUENTIAL',FORM='FORMATTED',
     +     BLANK='ZERO')
      OPEN(UNIT=UNIT4,FILE='CFACTS1.DAT',
     +     STATUS='OLD',ACCESS='SEQUENTIAL',FORM='FORMATTED',
     +     BLANK='ZERO')
      OPEN(UNIT=UNIT7,FILE='PDCONST1.DAT',
     +     STATUS='OLD',ACCESS='SEQUENTIAL',FORM='FORMATTED',
     +     BLANK='ZERO')
C
      READ(3,*) G1, G2, G3
      READ(4,*) A1, B1, A2, B2
      READ(7,*) W, Y, AO, UO
C
      CLOSE(UNIT=UNIT3)
      CLOSE(UNIT=UNIT4)
      CLOSE(UNIT=UNIT7)
C
C     CALCULATE CONSTANTS IN JOHNSON'S EQUATION
C
      A3 = (2*W)/PI
      B3 = COSH((PI*Y)/(2*W))
      C3 = ACOSH(B3/COS((PI*AO)/(2*W)))
C
C     CONVERT INTEGER VALUES TO PHYSICAL QUANTITIES AND WRITE EVERY
C     NWRITE DATA SET TO OUTPUT FILE
C
      FSIZE = 1000
      NWRITE = INT(NPOINT/FSIZE)
      UNIT8 = 8
      OPEN(UNIT=UNIT8,FILE='TEST1OUT.PRN',
     +     STATUS='UNKNOWN',ACCESS='SEQUENTIAL',FORM='FORMATTED',
     +     BLANK='ZERO')
      MIN1 = 4096
      MIN2 = 4096
      DO 4 I = 1, NPOINT, NWRITE
         IF(X(I,1).LT.MIN1) MIN1 = X(I,1)
         IF(X(I,2).LT.MIN2) MIN2 = X(I,2)
    4 CONTINUE
C
      CODMN = (MIN1/4096.)*G1
      CODMN = A1*CODMN + B1
      LOADMN = (MIN2/4096.)*G2
      LOADMN = A2*LOADMN + B2
C
```

```fortran
      PRINT*,'CODMN =',CODMN,'LOADMN =',LOADMN
C
      DO 2 I = 1, NPOINT, NWRITE
         COD = (X(I,1)/4096.)*G1
         COD = A1*COD + B1
         COD = COD - CODMN
         LOAD = (X(I,2)/4096.)*G2
         LOAD = A2*LOAD + B2
         LOAD = LOAD - LOADMN
         A = (X(I,3)/4096.)*G3
         A = A3*ACOS(B3/COSH((A/U0)*C3))
         WRITE(UNIT8,1) COD, LOAD, A
    1    FORMAT(3(G12.5,1X))
    2 CONTINUE
C
C     CLOSE FILES AND TERMINATE PROGRAM
C
      CLOSE(UNIT=UNIT8)
C
      STOP
      END
C
C*********************************************************************
C
      SUBROUTINE READER(IUNIT,NCHAN,NPOINT,X)
C
C     SUBROUTINE TO READ BINARY DAS20 DATA FILES.
C     WRITTEN BY S.G. RIBARITS
C
C        DATA   = DATA
C        ICHAN  = CHANNEL
C        IUNIT  = UNIT CONNECTED TO DAS20 BINARY DATA FILE
C        IROW   = ROW IN ARRAY X CORRESPONDING TO NREC AND ICHAN
C        NCHAN  = NUMBER OF CHANNELS
C        NPOINT = NUMBER OF DATA POINTS PER CHANNEL
C        NUM    = 16 BIT VALUE ENCODED WITH DATA AND CHANNEL
C        NREC   = NUMBER OF RECORDS TO READ
C        VAL    = TEMPORARY VARIABLE
C        X      = ARRAY CONTAINING DATA
C
      INTEGER*1 IUNIT, ICHAN, NCHAN
      INTEGER*2 NUM, DATA
      INTEGER*2 X(35000,3)
C
      NREC = NPOINT*NCHAN
C
      DO 1000 IREC = 1, NREC
      READ(IUNIT,REC=IREC) NUM
      IF (NUM.GE.0) THEN
         VAL = NUM/16.0
         DATA = IFIX(VAL)
      ELSE
         VAL = (65536.0 + NUM)/16.0
         DATA = IFIX(VAL)
      END IF
      ICHAN = INT((VAL - DATA)*16.0)
      ICHAN = ICHAN + 1
      IROW = (IREC - ICHAN)/NCHAN + 1
      X(IROW,ICHAN) = DATA
 1000 CONTINUE
C
      RETURN
      END
C
C*********************************************************************
C
      SUBROUTINE PULSE(PCHAN,X,NPOINT,THRHLD,COUNT)
```

```
C
C     SUBROUTINE TO COUNT CHANNEL PCHAN PULSES.
C     WRITTEN BY S.G. RIBARITS
C
C        COUNT  = NUMBER OF PULSES COUNTED
C        NPOINT = NUMBER OF DATA POINTS PER CHANNEL
C        OFF,ON = LOGICAL VARIABLES USED TO FLAG PULSES
C        PCHAN  = CHANNEL CONTAINING PULSES
C        THRHLD = THRESHOLD SET TO DETECT PULSES
C        X      = ARRAY CONTAINING DATA
C
      INTEGER*1 PCHAN
      INTEGER*2 X(35000,3),THRHLD
      INTEGER COUNT
      LOGICAL ON,OFF
C
      OFF= .FALSE.
      ON= .FALSE.
      COUNT = 1
C
      DO 1000 I = 1, NPOINT
         IF (X(I,PCHAN).GT.THRHLD) THEN
            ON = .TRUE.
         END IF
         IF (X(I,PCHAN).LT.THRHLD.AND.ON) THEN
            OFF = .TRUE.
            ON = .FALSE.
         END IF
         IF (OFF.AND..NOT.ON) THEN
            COUNT = COUNT + 1
            OFF = .FALSE.
            ON = .FALSE.
         END IF
         X(I,PCHAN) = COUNT
 1000 CONTINUE
      RETURN
      END
C
C**********************************************************************
C
      SUBROUTINE PDREAD(IUNIT,X,PCHAN,COUNT,NPOINT,RANGE)
C
C     SUBROUTINE TO READ MDT ACSII FILE AND MATCH DATA WITH
C     PULSES COUNTED ON PCHAN.
C     WRITTEN BY S.G. RIBARITS
C
C        COUNT  = NUMBER OF PULSES COUNTED
C        DATA   = SCALED POTENTIAL DROP DATA
C        IUNIT  = UNIT CONNECTED TO MDT ASCII FILE
C        NPOINT = NUMBER OF DATA POINTS PER CHANNEL
C        PCHAN  = CHANNAL CONTAINING PULSES
C        PDCHAN = POTENTIAL DROP CHANNEL
C        PDDATA = POTENTIAL DROP DATA
C        RANGE  = RANGE USED TO SCALE POTENTIAL DROP DATA
C        X      = ARRAY CONTAINING DATA
C
      INTEGER*1 IUNIT, PCHAN, PDCHAN
      INTEGER*2 X(35000,3), DATA
      INTEGER COUNT
C
      ICOUNT = 1
      IPOINT = 1
    1 IF (.NOT.(ICOUNT.LE.COUNT.AND.IPOINT.LE.NPOINT)) GOTO 4
      READ(IUNIT,*) PDCHAN, PDDATA
      DATA = NINT((PDDATA/RANGE)*4096.)
    2    IF (.NOT.(X(IPOINT,PCHAN).EQ.ICOUNT)) GOTO 3
         X(IPOINT,PCHAN) = DATA
```

```fortran
              IPOINT = IPOINT + 1
              IF (.NOT.(IPOINT.LE.NPOINT)) GOTO 3
              GOTO 2
      3     CONTINUE
              ICOUNT = ICOUNT + 1
              GOTO 1
      4 CONTINUE
C
        RETURN
        END
C
C*************************************************************************
C
        REAL FUNCTION ACOSH(X)
C
C       CALCULATES THE INVERSE HYPERBOLIC COSINE OF ARGUMENT X
C
        IF (X.LT.1) THEN
           WRITE(*,1)
      1     FORMAT('*ERROR*  AN ARGUMENT THAT WAS LESS THAN 1',
        +            ' WAS PASSED TO FUNCTION ACOSH')
           RETURN
        END IF
C
        ACOSH = LOG(X + SQRT(X*X - 1))
C
        RETURN
        END
```

```
C**********************************************************************
C***
C***    ANSYS input file for NGV cylinder coarse model.
C***    Written by S.G. Ribarits.
C***
C***        p = pressure
C***

/prep7

/title, NGV Cylinder, Coarse model (P = 1500 psi)

C*** Set model parameters

*set,p,1500

C*** Specify element types

et,1,93
et,2,93

C*** Define material properties/real constants

ex,1,2e5
r,1,7.8

C*** Define local coordinate systems

local,11,1,,334
local,12,1,49.8,-334
local,13,1,,-266.354
local,14,1,,,,,,-90

C*** Generate areas

k,1,9.771,,488.391
k,2,154.7,,334
k,3,154.7,,-334
k,4,111.991,,-418.477
k,5,19.9421,,-454.198
k,6,,,-455.254
csys,11
l,1,2,14
csys,14
l,2,3,20
csys,12
l,3,4,9
csys,13
l,4,5,5
l,5,6,1
csys,14
k,100,,,-100
k,200,,,100
arotat,1,2,3,4,5,,100,200,90
lsrsel,,6,10
ldvs,all,,6
lsall

C*** Mesh areas

type,1
elsize,35,,2
amesh,1,4
elsize,35,,1
amesh,5

C*** Specify elements for print controls
```

```
nrsel,y,-1,61
nrsel,z,-1,201
enode,1
type,2
emodif,all,0
eall
nall
```

C*** Reorder elements

```
nsrsel,,6
nline,1
lsall
wstart,all
nall
waves
```

C*** Apply boundary conditions

```
symbc,,1,,.5
symbc,,3,,.5
nrsel,z,-.5,.5
d,all,uy
nall
lsrsel,,6
nline,1
lsall
ddele,all
nrotat,all
d,all,ux,,,,,uy,rotx,roty,rotz
nall
```

C*** Apply load

```
*p = 1500
ep,all,2,.006895*arg1
podisp,-1
postr,-1,1
postr,,2
porf,-1
afwrit
finish
```

C*** Assign output to FILE12.CRS and run model

```
/get,12,file12,crs
/input,27
finish
```

```
C**********************************************************************
C***
C***    ANSYS input file for NGV cylinder defect submodel.
C***    Written by S.G. Ribarits.
C***
C***       a    = crack depth
C***       arc  = submodel arc length
C***       c    = half crack length
C***       ht   = submodel height
C***       fact = ratio of pressure in current load step
C***              to pressure in previous load step
C***       ksqu = c**2 - a**2
C***       loc  = flag set to 1 for interior defect,
C***              2 for exterior defect
C***       p0   = initial pressure
C***       p1   = pressure in previous load step
C***       p2   = pressure in current load step
C***       pinc = incremental pressure
C***       post = flag set to 1 to print results for current load
C***              step, 1 suppress to results for current load step
C***       rsqu = x**2 + y**2
C***       s    = geometry parameter
C***       x,y  = nodal coordinates in csys 12
C***

/prep7

/title, Interior Crack Submodel, (a = 5, c = 15)

C*** Set model parameters

*set,ht,100
*set,arc,30
*set,loc,1
*set,a,5.0
*set,c,15.0
*set,s,(180.0*((2.0/154.7)/3.14159))
*set,post,1
*set,p0,1500
*set,pinc,250

C*** Define material properties

ex,1,2e5
knl,1
nl,1,13, 10
nl,1,19, 20,    25
nl,1,25, 822, 822
nl,1,31,5050,5050

C*** Specify element types

et,1,45
et,2,45
et,3,45

C*** Define local coordinate systems

*if,loc,eq,2,:lb3
dist = 150.8
ang = 0
*go,:lb4
:lb3
dist = 158.6
ang = 180
:lb4
local,21,,,,,,,,-90
```

```
local,11,1,,,,,,-90
local,12,0,dist,,,90,,ang
local,13,1,dist,,,90,,ang

C*** Generate solid model

csys,13

k, 1,  0.05
k, 8,a-2.0
k,15,a+2.0
kgen,3,1,15,7,,17.5,,1
kgen,5,3,17,7,,13.75,,1

csys,12

k,22,11.140
k,23,11.140,3.512
k,24,11.140,7.8
kgen,2,22,24,1,(ht-11.140),,,7
k,24,11.140,7.8
k,25,6.840,7.8
k,26,4.060,7.8
k,27,1.909,7.8
k,28,,7.8

csys,13

kgen,2,1,31,1,,,s,31
kgen,2,32,62,1,,,(arc-s),31

l,1,8,2                    $rp7,1,1
l,32,39,2                  $rp7,1,1
l,63,70,2                  $rp7,1,1
l,39,46,2                  $rp7,1,1
l,70,77,2                  $rp7,1,1
l,15,22,2                  $rp7,1,1
l,46,53,2                  $rp7,1,1
l,77,84,2                  $rp7,1,1

csys,12

l,22,23,1                  $rp6,1,1
l,53,54,1                  $rp6,1,1
l,84,85,1                  $rp6,1,1
l,22,29,5,10               $rp3,1,1
l,53,60,5,10               $rp3,1,1
l,84,91,5,10               $rp3,1,1
l,32,63,9,10               $rp31,1,1

csys,13

v,1,2,9,8,32,33,40,39      $rp6,1,1,1,1,1,1,1,1
v,15,16,23,22,46,47,54,53  $rp6,1,1,1,1,1,1,1,1
v,32,33,40,39,63,64,71,70  $rp6,1,1,1,1,1,1,1,1
v,39,40,47,46,70,71,78,77  $rp6,1,1,1,1,1,1,1,1
v,46,47,54,53,77,78,85,84  $rp6,1,1,1,1,1,1,1,1

csys,12

v,22,23,30,29,53,54,61,60  $rp2,1,1,1,1,1,1,1,1
v,53,54,61,60,84,85,92,91  $rp2,1,1,1,1,1,1,1,1

C*** Place nodes at keypoints

*create,nplace
*set,kpoi,arg1
```

```
*set,node,arg2
*get,nx,kx,kpoi
*get,ny,ky,kpoi
*get,nz,kz,kpoi
n,node,nx,ny,nz
*end
*use,nplace,8,16
rp7,,1,20
*use,nplace,39,17
rp7,,1,20
*use,nplace,46,19
rp7,,1,20
*use,nplace,15,20
rp7,,1,20
fill,16,20,1,1,,7,20          $rp5,,,,1
fill,17,19,1,18,7,20
fill,1,16,2,6,5,5,1           $rp7,20,20,,20

C*** Generate crack tip elements

type,1
e,6,7,2,1,26,27,22,21
egen,4,1,-1
egen,3,5,-4
egen,6,20,-12

C*** Mesh volumes

elsize,35,,2
vmesh,all

C*** Connect crack tip elements to solid model

nrsel,,1,5,1
nasel,,21,25,1               $rp6,,20,20
ninv
merge
nall
numcmp,node

C*** Modify element types

vlrsel,,7,12,1
vlasel,,31,32,1
evolu
easel,,4,12,4               $rp6,,12,12
type,2
emodif,all,0
eall
vlall
vlrsel,,1,6,1
evolu
easel,,1,9,4               $rp6,,12,12
type,3
emodif,all,0
eall
vlall

C*** Detach elements from solid model

modmsh,nocheck
modmsh,detach

C*** Transform nodal coordinates to elliptical

csys,12
*set,ksqu,(c**2)-(a**2)
```

```
*create,modfy1
*get,x,nx,arg1
*get,y,ny,arg1
*set,rsqu,(x**2)+(y**2)
*set,x,x*sqrt(1+(ksqu/rsqu))
nmodif,arg1,x
*end
*use,modfy1,1
rp802,,1
```

C*** Fix badly formed elements

```
nrsel,y,-.01,.06
nmodif,all,,1e-10
nall
```

```
*create,efix
*get,n1,en1,arg1
*get,n2,en2,arg1
*get,n3,en3,arg1
*get,n4,en4,arg1
*get,n5,en5,arg1
*get,n6,en6,arg1
*get,n7,en7,arg1
*get,n8,en8,arg1
emodif,arg1,1,n2,n4,n3,n3,n6,n8,n7,n7
ndele,n1
ndele,n5
*end
type,3
*use,efix,73
type,1
*use,efix,97
rp9,,1
```

```
numcmp,nodes
```

C*** Change element type to 20 node isoparametric

```
et,1,95
et,2,95
et,3,95
emid
```

C*** Transform nodal coordinates to cylindrical

```
csys,21
trans,11,,all
```

C*** Reorder elements

```
csys,0
wsort,z
nrsel,z,-.01,.01
wstart,all
nall
waves
merge
numcmp,nodes
```

C*** Write boundary nodes to file26.dat

```
csys,11
nfile,,26
nrsel,z,(ht-1.0),(ht+5.0)
nasel,y,(arc-1.0),(arc+1.0)
nwrite
```

```
nall
finish

C*** Perform cut boundary displacement conversion

/get,12,file12,crs
/aux1
cbdsp,,,,1
finish

C*** Reassign output to file12.dat

/get,12,file12,dat
/prep7
resume

C*** Apply boundary conditions

ersel,type,2
nelem
csys,11
nrsel,y,-.001,.001
nusel,z,(ht-1.0),(ht+5.0)
symbc,11,2,,.001
nall
eall
nrsel,z,-.001,.001
nusel,y,(arc-1.0),(arc+1.0)
symbc,11,3,,.001
nall

C*** Set solution option and convergence criteria

kay,9,2
iter,-25,,25
kuse,0
cnvr,.05

C*** Apply 1500 psi pressure

*set,p0,(p0*.006895)
*set,pinc,(pinc*.006895)
podisp
postr,,,5
porf,-1
/input,24
psf,11,1,150.8,p0,,.001
ersel,type,3
nelem
nrsel,y,-.001,.001
psf,11,2,,p0,,.001
nall
eall
lwrite

C*** Apply 6000 psi pressure in 250 psi increments

post=0
*create, loads
*set,p2,(p0+(pinc*arge1))
*set,p1,(p0+(pinc*(arg1-1)))
*set,fact,p2/p1
lscale,fact,,fact
*if,post,eq,0,:lb3
podisp
postr,,,5
porf,-1
```

```
post=0
*go,:lb4
:lb3
podisp,-1
postr,-1
porf,-1
post=1
:lb4
lwrite
*end
*use,loads,1
rp18,,1
afwrit
finish

C*** Assign output and run submodel

\get,12,file12,01i
\input,27
finish
```

```
C***********************************************************************
C***
C***    Routine to calculate and plot membrane and bending stresses
C***    at boundary of IGV cylinder submodel.
C***    Written by S.G. Ribarits
C***
C***

/post1

C*** Define local coordinate system

local,11,,,,,-90
csys,11
dsys,11

C*** Create macro STRPLT

/show,file33,dat,1
*create,strplt
set,arg1
lpath,604,674
pdef,intr,szi,sz
pdef,save
lpath,619,719
pdef,intr,szo,sz
pcalc,add,szb,szi,szo,+.5,-.5
pcalc,add,szm,szi,szo,+.5,+.5
pcalc,div,sigz,szb,szm
/graph,labx,Y
/graph,laby,SIG
frame,-.95,.+95
pview,plot,sigz
lpath,674,320
pdef,intr,syi,sy
pdef,save
lpath,719,581
pdef,intr,syosy
calc,add,syb,syi,syo,+.5,-.5
calc,add,syb,syi,syo,+.5,+.5
pcalc,div,sigy,syb,sbm
/graph,labx,Z
/graph,laby,SIG
frame,-.95,+.95
pview,plot,sigy
*end

C*** Execute STRPLT for 1500 psi, 2000 psi, 2500 psi...6000psi

*use,strplt,1
rp10,,2

finish
```

```
C**********************************************************************
C***
C***    Routine to calculate stress intensity factor as
C***    a function of angle around an elliptical defect.
C***    Written by S.G. Ribarits
C***
C***

/post1
set,1

C*** Create macro CSCALC

*create,cscalc
csys
*get,x1,nx,arg1
*get,x2,nx,arg2
*get,y1,ny,arg1
*get,y2,ny,arg2
*get,z1,nz,arg1
*set,delx,x1-x2
*set,dely,y1-y2
*if,delx,eq,0,:lb1
*set,ang,atan(dely/delx)
*set,ang,(180*ang)/3.14159
*go,:lb2
:lb1
*set,ang,90
:lb2
local,21,0,x1,y1,z1,ang,,90
csys
*set,delx,x1-150.8
*set,dely,y1
*if,dely,le,0,:lb3
*set,phi,atan(delx/dely)
*set,phi,(180*phi)/3.14159
*go,:lb4
:lb3
*set,phi,90
:lb4
csys,21
*end

C*** Calculate stress intensity factors

*use,cscalc,1,2
lpath,1,689,2
kcalc,1
*set,phi1,phi
*get,ki1,kcalc,ki

*use,cscalc,17,18
lpath,17,739,18
kcalc
*set,phi2,phi
*get,ki2,kcalc,ki
    .
    .
    .

*use,cscalc,113,114
lpath,113,1039,114
kcalc
*set,phi8,phi
*get,ki8,kcalc,ki

C*** Print results
```

```
/output,kfactors,01i
*stat
/output,6

finish


C************************************************************************
C***
C***    Macro to calculate COD, CTOD and point of rotation r.
C***    Written by S.G. Ribarits
C***
C***

/post1

C*** Set parameters

*set,a,5.0
*set,loc,1

C*** Define local coordinate system

*if,loc,eq,2,:lb3
dist = 150.8
ang = 0
*go,:lb4
:lb3
dist = 158.6
ang = 180
:lb4
local,22,,dist,,,ang,,-90

C*** Create macro to calculate COD, CTOD and r

*create, ctod
p = (250*(arg1-1)) + 1500
setg
csys,22
nrsel,z,-.001,.001
nrsel,y,-.001,.001
nrsel,x,-.001,(.65*a)
ninv
ndele,all
ninv
set,arg1
sum1 = 0
sum2 = 0
sum3 = 0
sum4 = 0
n = 0
*get,max,ndmx
:lb1
*get,node,ndmn
*get,xloc,x,node
*get,disp,uy,node
xloc = xloc/a
sum1 = xloc + sum1
sum2 = disp + sum2
sum3 = (xloc*disp) + sum3
sum4 = (xloc**2) + sum4
n = n + 1
nusel,,node
*if,node,eq,max,:lb2
*go,:lb1
:lb2
val1 = (sum1*sum2)/n
```

```
val2 = (sum1**2)/n
c1 = (sum3 - val1)/(sum4 - val2)
c2 = (sum2 - (c1*sum1))/n
cod = c2
ctod = c1 + c2
r = -c2/c1
nall
*stat
*end
```

C*** Execute CTOD for 1500 psi, 2000 psi, 2500 psi...6000psi

```
/output,CTOD,01i
*use,ctod,1
rp10,,2
/output,6
finish
```

C**
C***
C***   Macro to read displacements of nodes on exterior
C***   of submodel.
C***   Written by S.G. Ribarits
C***
C***

/post1

C*** Define local coordinate system and select nodes

```
local,11,1,,,,,,-90
```

C*** Create macro to read displacements

```
nlines,1000
/nopr
```

```
*create dspread
set,arg1
csys,11
nrsel,x,158.59,158.61
csys,0
prdisp,all
*end
```

C*** Execute DSPREAD for 1500 psi, 2000 psi, 2500 psi...6000psi

```
/output,disp,01i
*use,dspread,1
rp10,,2
/output,6
finish
```

```
      PROGRAM ARRANGE
C************************************************************************
C
C         PROGRAM TO ORDER NODE NUMBERS ON FACES OF ELEMENTS FOR VOLUME
C         CALCULATIONS. NODE NUMBERS OF NODES ON THE EXTERIOR OF THE MODEL
C         (FILE26.RUN) ARE COMPARED WITH THE NODE NUMBERS DEFINING EACH
C         ELEMENT (FILE14.RUN) TO DETERMINE WHICH ELEMENT FACES LIE ON THE
C         EXTERIOR OF THE MODEL. THE NODE NUMBERS DEFINING THESE FACES ARE
C         THEN PLACED IN ARRAY IFACE IN AN ORDER WHICH DEPENDS ON ELEMENT
C         CONNECTIVITY.
C         WRITTEN BY S.G. RIBARITS
C
C              VARIABLES
C           NELEM  = NO. OF ELEMENTS
C           NNODES = NO. OF NODES
C           RUN    = RUN CODE
C
C              ARRAYS
C           IEL    = ANSYS ELEMENT NUMBER
C           IELEM  = NODES ON ELEMENT
C           IFACE  = NODES ON ELEMENT FACE
C           IREAL  = ELEMENT REAL CONSTANT (ANSYS VARIABLE)
C           ITYPE  = ELEMENT TYPE (ANSYS VARIABLE)
C           MAT    = ELEMENT MATERIAL CODE (ANSYS VARIABLE)
C           NNUM   = NODE NUMBERS OF NODES ON EXTERIOR OF MODEL
C           X,Y,Z  = GLOBAL COORDINATES OF NODES
C
C
      INTEGER COUNT
      IMPLICIT DOUBLE PRECISION (A-H,O-Z)
      CHARACTER RUN*3
      DIMENSION NNUM(1000),X(1000),Y(1000),Z(1000),
     +          IELEM(500,20),IFACE(500,8),MAT(500),ITYPE(500),
     +          IREAL(500),IEL(500)
C
C   INITIALIZE RUN
C
      RUN = '01I'
C
C   OPEN INPUT/OUTPUT FILES
C
      OPEN(UNIT=1,FILE='FILE26.'//RUN,STATUS='OLD',
     +    ACCESS='SEQUENTIAL',FORM='FORMATTED',BLANK='ZERO')
      OPEN(UNIT=2,FILE='FILE14.'//RUN,STATUS='OLD',
     +    ACCESS='SEQUENTIAL',FORM='FORMATTED',BLANK='ZERO')
      OPEN(UNIT=3,FILE='FNODES.'//RUN,STATUS='UNKNOWN',
     +    ACCESS='SEQUENTIAL',FORM='FORMATTED',BLANK='ZERO')
C
      COUNT = 1
   10 READ(1,20,END=30) NNUM(COUNT), X(COUNT), Y(COUNT), Z(COUNT)
   20 FORMAT(I5,3G16.9)
      COUNT = COUNT + 1
      GOTO 10
   30 REWIND(UNIT=1)
      NNODES = COUNT - 1
C
      COUNT = 1
   40 READ(2,50,END=60) (IELEM(COUNT,I),I=1,8), MAT(COUNT),
     +                   ITYPE(COUNT), IREAL(COUNT), IEL(COUNT)
      READ(2,50) (IELEM(COUNT,I),I=9,20)
   50 FORMAT(12I6,8X)
      COUNT = COUNT + 1
      GOTO 40
   60 REWIND(UNIT=2)
      NELEM = COUNT - 1
C
      WRITE(3,70) NNODES, NELEM
```

```
   70 FORMAT(2I6)
C
      DO 140 I = 1, NELEM
         DO 80 J = 1, 8
            IFACE(I,J) = 0
   80    CONTINUE
         FLAG = 0
         K = 1
         J = 0
   90    IF (FLAG.EQ.1) GOTO 110
            DO 100 L = 1, 8
               IF(NNUM(K).EQ.IELEM(I,L)) THEN
                  IFACE(I,L) = 1
                  J = J + 1
               END IF
  100       CONTINUE
            IF (K.EQ.NNODES.OR.J.EQ.4) FLAG = 1
            K = K + 1
            GOTO 90
  110    CONTINUE
         IF (J.EQ.4) THEN
            IF ((IFACE(I,1).EQ.1).AND.(IFACE(I,2).EQ.1).AND.
     +          (IFACE(I,3).EQ.1).AND.(IFACE(I,4).EQ.1)) THEN
               IFACE(I,1) = IELEM(I,1)
               IFACE(I,2) = IELEM(I,9)
               IFACE(I,3) = IELEM(I,2)
               IFACE(I,4) = IELEM(I,10)
               IFACE(I,5) = IELEM(I,3)
               IFACE(I,6) = IELEM(I,11)
               IFACE(I,7) = IELEM(I,4)
               IFACE(I,8) = IELEM(I,12)
            END IF
            IF ((IFACE(I,5).EQ.1).AND.(IFACE(I,6).EQ.1).AND.
     +          (IFACE(I,7).EQ.1).AND.(IFACE(I,8).EQ.1)) THEN
               IFACE(I,1) = IELEM(I,5)
               IFACE(I,2) = IELEM(I,16)
               IFACE(I,3) = IELEM(I,8)
               IFACE(I,4) = IELEM(I,15)
               IFACE(I,5) = IELEM(I,7)
               IFACE(I,6) = IELEM(I,14)
               IFACE(I,7) = IELEM(I,6)
               IFACE(I,8) = IELEM(I,13)
            END IF
            IF ((IFACE(I,3).EQ.1).AND.(IFACE(I,4).EQ.1).AND.
     +          (IFACE(I,7).EQ.1).AND.(IFACE(I,8).EQ.1)) THEN
               IFACE(I,1) = IELEM(I,3)
               IFACE(I,2) = IELEM(I,19)
               IFACE(I,3) = IELEM(I,7)
               IFACE(I,4) = IELEM(I,15)
               IFACE(I,5) = IELEM(I,8)
               IFACE(I,6) = IELEM(I,20)
               IFACE(I,7) = IELEM(I,4)
               IFACE(I,8) = IELEM(I,11)
            END IF
            IF ((IFACE(I,1).EQ.1).AND.(IFACE(I,2).EQ.1).AND.
     +          (IFACE(I,5).EQ.1).AND.(IFACE(I,6).EQ.1)) THEN
               IFACE(I,1) = IELEM(I,1)
               IFACE(I,2) = IELEM(I,17)
               IFACE(I,3) = IELEM(I,5)
               IFACE(I,4) = IELEM(I,13)
               IFACE(I,5) = IELEM(I,6)
               IFACE(I,6) = IELEM(I,18)
               IFACE(I,7) = IELEM(I,2)
               IFACE(I,8) = IELEM(I,9)
            END IF
            IF ((IFACE(I,2).EQ.1).AND.(IFACE(I,3).EQ.1).AND.
     +          (IFACE(I,6).EQ.1).AND.(IFACE(I,7).EQ.1)) THEN
```

```
                 IFACE(I,1) = IELEM(I,2)
                 IFACE(I,2) = IELEM(I,18)
                 IFACE(I,3) = IELEM(I,6)
                 IFACE(I,4) = IELEM(I,14)
                 IFACE(I,5) = IELEM(I,7)
                 IFACE(I,6) = IELEM(I,19)
                 IFACE(I,7) = IELEM(I,3)
                 IFACE(I,8) = IELEM(I,10)
            END IF
            IF ((IFACE(I,1).EQ.1).AND.(IFACE(I,4).EQ.1).AND.
     +          (IFACE(I,5).EQ.1).AND.(IFACE(I,8).EQ.1)) THEN
                 IFACE(I,1) = IELEM(I,1)
                 IFACE(I,2) = IELEM(I,12)
                 IFACE(I,3) = IELEM(I,4)
                 IFACE(I,4) = IELEM(I,20)
                 IFACE(I,5) = IELEM(I,8)
                 IFACE(I,6) = IELEM(I,16)
                 IFACE(I,7) = IELEM(I,5)
                 IFACE(I,8) = IELEM(I,17)
            END IF
            WRITE(3,120) (IFACE(I,M),M=1,8)
 120        FORMAT(8(3X,I4))
          END IF
          IF (J.NE.4) THEN
            WRITE(6,130) IEL(I)
 130        FORMAT('*WARNING*  LESS THAN 4 CORNER NODES WERE FOUND ON',
     +             ' ELEMENT',I5)
          END IF
 140    CONTINUE
C
        CLOSE(UNIT=1)
        CLOSE(UNIT=2)
        CLOSE(UNIT=3)
C
        STOP
        END
```

```
      PROGRAM VOLCALC
C*********************************************************************
C
C        PROGRAM TO CALCULATE THE VOLUME OF A CNG CYLINDER FROM FINITE
C        ELEMENT RESULTS.  THE INCREMENTAL VOLUME BOUNDED BY AN ELEMENT
C        FACE AND THE ORIGIN IS CALCULATED AND SUMMED.
C        WRITTEN BY S.G. RIBARITS
C
C            VARIABLES
C        ILOAD    = COUNTER
C        INODE    = NODE NUMBER
C        LSTEP    = LOAD STEP
C        NELEM    = NO. OF ELEMENTS
C        IFACE    = NO. OF NODES ON ELEMENT FACE
C        NNODES   = NO. OF NODES
C        PRESS    = PRESSURE
C        V        = TOTAL VOLUME
C        VINC     = INCREMENTAL VOLUME
C
C            ARRAYS
C        IFACE    = NODES ON FACE OF ELEMENT
C        LOAD     = PRESSURE CORRESPONDING TO ILOAD
C        UX,UY,UZ = NODAL DISPLACEMENTS
C        X,Y,Z    = GLOBAL COORDINATES OF NODES
C        XX,YY,ZZ = LOCAL COORDINATES OF NODES
C
C
      INTEGER PRESS
      IMPLICIT DOUBLE PRECISION (A-H,O-Z)
      CHARACTER RUN*3
      DIMENSION X(5000),Y(5000),Z(5000),IFACE(500,8),
     +          UX(5000),UY(5000),UZ(5000),XX(8),YY(8),ZZ(8),
     +          LOAD(6)
      DATA LOAD/1500,2000,3000,4000,5000,6000/
C
C     INITIALIZE RUN
C
      RUN = '01I'
C
C     OPEN INPUT/OUTPUT FILES
C
      OPEN(UNIT=1,FILE='FILE26.'//RUN,STATUS='OLD',
     +     ACCESS='SEQUENTIAL',FORM='FORMATTED',BLANK='ZERO')
      OPEN(UNIT=2,FILE='FNODES.'//RUN,STATUS='OLD',
     +     ACCESS='SEQUENTIAL',FORM='FORMATTED',BLANK='ZERO')
      OPEN(UNIT=3,FILE='DISP.'//RUN,STATUS='OLD',
     +     ACCESS='SEQUENTIAL',FORM='FORMATTED',BLANK='ZERO')
      OPEN(UNIT=4,FILE='VOLU'//RUN//'.PRN',STATUS='UNKNOWN',
     +     ACCESS='SEQUENTIAL',FORM='FORMATTED',BLANK='ZERO')
C
C     READ NODES AND ELEMENTS
C
      READ(2,5) NNODES,NELEM
    5 FORMAT(2I6)
C
      DO 20 I = 1, NNODES
         READ(1,10) INODE, X(INODE), Y(INODE), Z(INODE)
   10    FORMAT(I5,3G16.9)
   20 CONTINUE
      DO 40 IELEM = 1, NELEM
         READ(2,30) (IFACE(IELEM,I),I =1,8)
   30    FORMAT(8(3X,I4))
   40 CONTINUE
C
C     WRITE HEADER TO OUTPUT FILE
C
      WRITE(4,45) RUN
```

```
   45 FORMAT('RUN',1X,A3//'LOAD STEP',3X,'PRESSURE (psi)',3X,
      +        'VOLUME (cc)')
C
C     LOOP THROUGH LOAD STEPS; READ LOAD STEP DATA AND DISPLACEMENTS
C
      DO 130 ILOAD = 0, 6
         IF (ILOAD.GT.0) THEN
            READ(3,50) LSTEP
   50       FORMAT(//////////14X,I3/////)
            ASSIGN 60 TO NN
            DO 80 J = 1, NNODES
               IF (J.EQ.NNODES.AND.ILOAD.LT.6) ASSIGN 70 TO NN
               READ(3,NN) INODE, UX(INODE), UY(INODE), UZ(INODE)
   60          FORMAT(2X,I5,1X,3(1X,G15.8))
   70          FORMAT(2X,I5,1X,3(1X,G15.8)////)
   80       CONTINUE
         END IF
C
C     CALCULATE INCREMENTAL VOLUMES AND ADD TO TOTAL VOLUME
C
         V = 0.D0
         DO 110 IELEM = 1, NELEM
            DO 90 INODE = 1, 8
               XX(INODE) = X(IFACE(IELEM,INODE))
               YY(INODE) = Y(IFACE(IELEM,INODE))
               ZZ(INODE) = Z(IFACE(IELEM,INODE))
               IF (ILOAD.GT.0) THEN
                  XX(INODE) = XX(INODE) + UX(IFACE(IELEM,INODE))
                  YY(INODE) = YY(INODE) + UY(IFACE(IELEM,INODE))
                  ZZ(INODE) = ZZ(INODE) + UZ(IFACE(IELEM,INODE))
               END IF
   90       CONTINUE
            XK = -(XX(1) + XX(3) + XX(5) + XX(7))/4.D0
      +           +(XX(2) + XX(4) + XX(6) + XX(8))/2.D0
            YK = -(YY(1) + YY(3) + YY(5) + YY(7))/4.D0
      +           +(YY(2) + YY(4) + YY(6) + YY(8))/2.D0
            ZK = -(ZZ(1) + ZZ(3) + ZZ(5) + ZZ(7))/4.D0
      +           +(ZZ(2) + ZZ(4) + ZZ(6) + ZZ(8))/2.D0
            DO 100 INODE = 1, 8
               NI = INODE
               NJ = INODE + 1
               IF (NJ.EQ.9) NJ = 1
               XI = XX(NI)
               YI = YY(NI)
               ZI = ZZ(NI)
               XJ = XX(NJ)
               YJ = YY(NJ)
               ZJ = ZZ(NJ)
               VINC = DABS((XI*(YJ*ZK - ZJ*YK) - YI*(XJ*ZK - ZJ*XK)
      +                                   + ZI*(XJ*YK - YJ*XK))/6.D0)
               V = V + VINC
  100       CONTINUE
  110    CONTINUE
C
C     PRINT RESULTS FOR LOAD STEP
C
         IF (ILOAD.EQ.0) THEN
            LSTEP = 0
            PRESS = 0
         ELSE
            PRESS = LOAD(ILOAD)
         END IF
         V = (4.D0*V)/1000.D0
         WRITE(4,120) LSTEP, PRESS, V
  120    FORMAT(3X,I3,10X,I5,10X,F8.3)
  130 CONTINUE
C
```

```
C     CLOSE FILES AND TERMINATE PROGRAM
C
      CLOSE(UNIT=1)
      CLOSE(UNIT=2)
      CLOSE(UNIT=3)
      CLOSE(UNIT=4)
C
      STOP
      END
```